NASA CONTRACTOR REPORT 177453

SOME DATA PROCESSING REQUIREMENTS FOR PRECISION NAP-OF-THE-EARTH (NOE) GUIDANCE AND CONTROL OF ROTORCRAFT

Warren F. Clement
Duane T. McRuer
Raymond E. Magdaleno

Systems Technology, Inc.
Mountain View, CA 94043

Prepared for
Ames Research Center
Under Contract NAS2-12364

National Aeronautics and
Space Administration

Ames Research Center
Moffett Field, California 94035

ABSTRACT

Nap-of-the-earth (NOE) flight in a conventional helicopter is extremely taxing for two pilots under visual conditions. Developing a single pilot all-weather NOE capability will require a fully automatic NOE navigation and flight control capability for which innovative guidance and control concepts have been examined. Constrained time-optimality provides a validated criterion for automatically controlled NOE maneuvers if the pilot is to have confidence in the automated maneuvering technique; this is one focus of this study. A second focus has been to organize the storage and real-time updating of NOE terrain profiles and obstacles in course-oriented coordinates indexed to the mission flight plan. A method is presented for using pre-flight geodetic parameter identification to establish guidance commands for planned flight profiles and alternates. A method is then suggested for interpolating this guidance command information with the aid of forward- and side-looking sensors within the resolution of the stored data base, enriching the data content with real-time information, and combining the stored and sensed data for real-time display, guidance, and control purposes. A third focus of this study defined a class of automatic anticipative guidance algorithms and necessary data preview requirements to follow the vertical, lateral, and longitudinal guidance commands dictated by the updated flight profiles and to address the effects of processing delays in digital guidance and control system candidates. The results of this three-fold research effort offer promising alternatives designed to gain pilot acceptance for automatic guidance and control of rotorcraft in NOE operations.

FOREWORD AND ACKNOWLEDGEMENTS

This report presents the results of Phase I of a Small Business Innovation Research (SBIR) program to develop fully automatic guidance for rotorcraft in nap-of-the-earth flight regimes.

The study was sponsored by the Flight Guidance and Navigation Branch (Code FSN), Flight Systems and Simulation Research Division, Aerospace Systems Directorate, Ames Research Center, National Aeronautics and Space Administration. Mr. Leonard McGee served as Project Monitor for the FSN Branch. The work was performed by Systems Technology, Inc., (STI), at Mountain View and Hawthorne, California. Mr. Warren F. Clement was the Project Engineer, and Mr. Duane T. McRuer, the Technical Director for STI. The authors gratefully acknowledge the digitized terrain data base furnished by the FSN Branch, the contributions by Mr. Wayne F. Jewell to the method for geodetic parameter identification to establish guidance commands for planned flight profiles, the cooperation and encouragement provided by FSN personnel, and the careful attention by Mrs. Sharon A. Duerksen of the Mountain View staff of STI in the production of the report.

TABLE OF CONTENTS

TABLE OF CONTENTS (CONTINUED)

TABLE OF CONTENTS (CONCLUDED)

LIST OF TABLES

LIST OF FIGURES

LIST OF FIGURES (Continued)

LIST OF FIGURES (Continued)

LIST OF FIGURES (Continued)

LIST OF FIGURES (Continued)

LIST OF FIGURES (Continued)

LIST OF FIGURES (Continued)

LIST OF FIGURES (Continued)

LIST OF FIGURES (Continued)

LIST OF FIGURES (Concluded)

LIST OF ABBREVIATIONS

AGL	Above ground level
DMA	Defense Mapping Agency
ETA	Estimated time of arrival
FCON	Frequency CONversion program
FFT	Finite Fourier transformation
FREDA	FREquency Domain Analysis program
IMC	Instrument meteorological conditions
LHX	Light helicopter experimental
NASA	National Aeronautics and Space Administration
NIPIP	Non-Intrusive Parameter Identification Program
NOE	Nap of the earth
OGE	Out of ground effect
PSD	Power spectral density
SFP	Stored flight plan
STI	Systems Technology, Inc.
TF/TA	Terrain following/terrain avoidance
VCHH	Vertical velocity command-height hold

LIST OF SYMBOLS

$\underline{c}$	Column-vector of c_j
$\underline{\hat{c}}$	Estimated value of $\underline{c}$
$c_0, c_1, c_2, \ldots, c_j$	Constant coefficients relating z and f_j
$C_E(s)$	Laplace transform of compensatory (i.e., error correcting) contribution to C(s)
C(s)	Laplace transform of summed controller's output to controlled element for guidance
$C_p(s)$	Laplace transform of pursuit feedforward contribution to C(s)
d	Differential operator
$d_0, d_1, d_2, \ldots, d_k$	Constant coefficients in Taylor series representing z(x)
D_{pe}	$V\tau_e$, compensatory data preview interval
D(s)	Laplace transform of disturbance
e,exp	Naperian base, 2.71828...
E	Error vector
E_T	Error threshold vector.
$f_1, f_2, \ldots, f_j$	Selected variables from the state vector $\underline{X}$ or explicit functions thereof
$\underline{F}$	Row-vector of f_j
g	Gravitational acceleration
G	Amplitude factor, p. 22
G_C^A	Collective to lateral cyclic crossfeed transfer function
G_C^B	Collective to longitudinal cyclic crossfeed transfer function
G_C^P	Collective to pedal crossfeed transfer function

LIST OF SYMBOLS (Continued)

G_P^A	Pedal to lateral cyclic crossfeed transfer function
G_P^B	Pedal to longitudinal cyclic crossfeed transfer function
G_P^C	Pedal to collective crossfeed transfer function
h	Perturbed height displacement
h_c	Height command
$\dot{h}_c$	Commanded vertical velocity
H	Matrix of adjoined measurements
I_x	Moment of inertia about the roll axis
I_y	Moment of inertia about the pitch axis
I_z	Moment of inertia about the yaw axis
j	$\sqrt{-1}$
k	Index denoting number of across-course coordinates $y_1, y_2, \cdots y_k$
$k!$	$k(k-1)(k-2)\cdots(1)$
K	Controlled element gain
K_c	High frequency gain of controlled element
K_e	Gain of compensatory (i.e., error correcting) guidance transfer function
$K_{\dot{h}}$	Height-to-collective control loop gain
K_{I_h}	Integral gain for height control
K_{I_x}	Integral gain for longitudinal displacement control
K_{I_y}	Integral gain for lateral displacement control
K_{I_ψ}	Integral gain for heading control
K_q	Pitch rate feedback gain

LIST OF SYMBOLS (Continued)

K_θ	Pitch attitude displacement feedback gain
K_ϕ	Roll attitude displacement feedback gain
L_x	Total length of route to be followed
L_{δ_A}	Derivative of rolling acceleration with respect to roll control displacement $(1/I_x)(\partial L/\partial \delta_A)$ rad/sec^2-% or -inch
m	Index representing number of c_j and f_j
M_q	Pitch damping, $(1/I_y)(\partial M/\partial q)$, rad/sec
M_{δ_B}	Derivative of pitching acceleration with respect to pitch control displacement, $(I/I_y)(\partial M/\partial \delta_B)$ rad/sec^2-% or -in
n	Index denoting each set of z and $\underline{F}$
n_h	Height measurement noise
n_x	Longitudinal displacement measurement noise
n_y	Lateral displacement measurement noise
n_ψ	Heading displacement measurement noise
N	Number of data points, p. 22
N_r'	Yaw damping $(1/I_z)(\partial N/\partial r)$ modified by one loop closure, rad/sec
$N_{r_{eff}}'$	Effective yaw damping (rad/sec)
N(s)	Laplace transform of measurement noise
NSC	Total number of sines and cosines, p. 22
N_{δ_p}	Derivative of yawing acceleration with respect to yaw control displacement $(1/I_z)(\partial N/\partial \delta_p)$ rad/sec^2-% or -inch
p	Index representing number of d_k; also rolling velocity, rad/sec

LIST OF SYMBOLS (Continued)

q	Pitching velocity, rad/sec
r	Yawing velocity, rad/sec
$r(s)$	Laplace transform of guidance course-and-profile command
$R(s)$	Laplace transform of guidance command
$R_f(s)$	Laplace transform of filtered guidance command
$\underline{R}_n$	nth guidance command vector from stored flight profile
$\hat{\underline{R}}_n$	nth vector representing sensed profile of terrain, obstacles, and threats with guidance offset requirements
$\underline{R}(\underline{X},t)$	Guidance command vector
s	Lapace transform operator
t	Time, sec
T_c	Characteristic time (sec) of controlled element damping; also time to complete rapid response phase
$T_h^{\cdot}$	Vertical velocity feedback gain
T_k	Characteristic time (sec) of first-order lead in controlled element transfer function
T_{L_h}	Characteristic time (sec) for first-order lead compensation in height control
T_{L_x}	Characteristic time (sec) for first-order lead compensation in longitudinal displacement control
T_{L_ψ}	Characteristic time (sec) for first-order lead compensation in heading control
T_p	Preview time interval
T_u	Characteristic time (sec) of the real zero in the numerator of the transfer function representing speed response to longitudinal cyclic control

LIST OF SYMBOLS (Continued)

$T_x^{\bullet}$	Longitudinal velocity feedback gain
$T_y^{\bullet}$	Lateral velocity feedback gain
T_{θ_1}	Characteristic time (sec) of the speed response of a pitch attitude-constrained aircraft, i.e., effective reciprocal surge damping with constrained attitude
T_{θ_2}	Characteristic time (sec) of the vertical velocity response of a pitch attitude-constrained aircraft, i.e., effective reciprocal heave damping with constrained attitude
T'_{θ_1}	T_{θ_1} modified by regulation of another control loop
T'_{θ_2}	T_{θ_2} modified by regulation of another control loop
T'_{ϕ_1}	Characteristic time (sec) of the lateral velocity response of a roll attitude-constrained rotorcraft, i.e., effective reciprocal sway damping with constrained attitude modified by regulation of another control loop
$T_{\psi}^{\bullet}$	Yaw rate feedback gain
u	Longitudinal velocity
U_o	Trimmed inertial velocity
v	Sideward or lateral velocity
$\underline{v}$	Vector representing difference between actual and estimated height of terrain and obstacles
V	Velocity
V_i	Inertial velocity
w	Heaving velocity
W	Half-width distance of lateral terrain coverage corresponding to field of view angle ξ_s
$W_h(s)$	Height measurement filter transfer function
$W_m(s)$	Response measurement filter tranfer function

LIST OF SYMBOLS (Continued)

$W_M(s)$	Laplace transform of measurement filter
$W_r(s)$	Command filter transfer function
$W_R(s)$	Laplace transform of command filter
$W_x(s)$	Longitudinal displacement measurement filter transfer function
$W_y(s)$	Lateral displacement measurement filter transfer function
$W_\psi(s)$	Heading displacement measurement filter transfer function
x	Along-course coordinate; perturbed longitudinal displacement
$\dot{x}$	Perturbed longitudinal velocity
x_c	Longitudinal displacement command
x_o	Reference coordinate for x
x_{ref}	Reference coordinate for x
X_α	$U_o X_w$, ft/sec^2
$\underline{X}$	State vector of independent variables
X_u	Surge damping, $(1/m)(\partial X/\partial u)$ 1/sec
X_w	Derivative of longitudinal acceleration with respect to heaving velocity $(1/m)(\partial X/\partial w)$ rad/sec
X_{δ_B}	Derivative of longitudinal displacement with respect to pitch control displacement, $(1/m)(\partial X/\partial \delta_B)$ rad/sec^2-% or -inch
X_{δ_c}	Derivative of longitudinal displacement with respect to collective control displacement, $(1/m)(\partial X/\partial \delta_c)$ rad/sec^2-% or -inch
y	Across-course coordinate; lateral displacement

LIST OF SYMBOLS (Continued)

$\dot{y}$	Lateral velocity
$Y_c(s)$	Controlled element transfer function
Y_c^p	Collective-to-pedal crossfeed describing function
$Y_d(s)$	Disturbance transfer function
Y_{e_h}	Height error reduction describing function
Y_E	Compensatory equalization for error reduction if $E \leq E_T$
Y_p	Pursuit feedforward guidance function
$Y_p(s)$	Pursuit feedforward guidance transfer function
Y_{RR}	Time optimal program for rapid response (RR) maneuvers if $E > E_T$
Y_v	Sway damping $(1/m)(\partial Y/\partial v)$ 1/sec
z	Height of terrain and obstacles; vertical displacement
$\underline{z}$	Vector representing height of terrain and obstacles
z_n	nth measurement of z
Z_w	Heave damping $(1/m)(\partial Z/\partial w)$ rad/sec
Z_α	$U_o Z_w$, ft/sec^2
Z_{δ_c}	Derivative of normal acceleration with respect to collective control displacement, $(1/m)(\partial Z/\partial \delta_c)$, ft/sec^2-% or -inch
α	$1/T_L - 1/T_c$ in the extended crossover model, rad/sec
δ_a, δ_A	Roll control displacement
δ_B	Pitch control displacement
δ_c, δ_{coll}	Collective or heaving control displacement percent
δ_p	Yaw control displacement

LIST OF SYMBOLS (Continued)

$\Delta''(s)$	Closed-loop determinant of height and airspeed regulation with constrained attitude
$\Delta\omega$	Incremental circular frequency bandwidth for smoothing power spectral densities based on FFT
ζ	Damping ratio
ζ_h''	Closed-loop height regulation damping ratio with simultaneous attitude and speed or position regulation
ζ_p'	Damping ratio of the phugoid oscillation modified by attitude regulation
ζ_u	Damping ratio of the complex zero in the numerator of the transfer function representing speed response to longitudinal cyclic control
η_{p_g}	Independent white noise source for representing stochastic variation in rolling gust velocity (i.e., span wise distribution of normal gust velocity)
η_{u_g}	Independent white noise source for representing stochastic variation in longitudinal gust velocity
η_{v_g}	Independent white noise source for representing stochastic variation in lateral gust velocity
η_{w_g}	Independent white noise source for representing stochastic variation in normal gust velocity
θ	Perturbed pitch attitude displacement
θ_c	Pitch attitude displacement command
λ	Angular argument of Fourier series
Λ	High frequency gain of $Y_d(s)$
ξ	Phase angle
ξ_s	Half-angle of lateral field of view for level sidestepping

LIST OF SYMBOLS (Continued)

ξ_t	Half-angle of lateral field of view for level turning
π	3.14159...
τ_c	Effective delay of controlled element
τ_e	Effective closed-loop compensatory time delay
τ_k	Effective time delay in controlled element transfer function
τ_m	Preview interval of measurement filter
τ_p	Preview time interval of the anticipative trajectory coupler
τ_r	Preview interval of command filter
τ_t	Time delay of transition phase preceding rapid response phase
τ'_θ	Effective time delay for regulation of pitch attitude modified by regulation of another control loop
τ''_θ	Effective time delay for regulation of pitch attitude modified by regulation of two other control loops
τ'_ϕ	Effective time delay for regulation of roll attitude modified by regulation of another control loop
τ''_ϕ	Effective time delay for regulation of roll attitude modified by regulation of two other control loops
ϕ	Perturbed roll attitude displacement; roll angle, rad or deg
ϕ_c	Roll command, rad or deg
ϕ_s	Bank angle for level sidestepping
ϕ_t	Bank angle for level turning
$\Phi_{ii}(\omega)$	Power spectral density of input i (units of $i)^2/(rad/sec)$
ψ	Heading displacement angle, rad or deg

LIST OF SYMBOLS (Concluded)

$\dot{\psi}$	Heading angular velocity, rad/sec
$\dot{\psi}_c$	Commanded heading angular velocity, rad/sec
$\omega_1, \omega_2, \ldots, \omega_m$	Frequencies representing predominant spectral content in FFT
ω''_{c_u}	Crossover frequency for speed regulation with regulated attitude and height while traveling
ω''_h	Closed-loop undamped natural frequency for height regulation with simultaneous attitude and speed or position regulation
ω_{i_e}	Equivalent rectangular bandwidth of input i, p. 89
ω_n	Undamped natural frequency (rad/sec)
ω'_p	Undamped natural frequency of the phugoid oscillation modified by attitude regulation
ω_u	Undamped natural frequency of the complex zero in the numerator of the transfer function representing speed response to longitudinal cyclic pitch control
ω''_u	Closed-loop airspeed regulation subsidence with regulated attitude and height
$\partial D(s)/\partial M(s)$	Response correlated disturbance gradient
$\partial u_g/\partial h$	Longitudinal component of shear gradient with respect to a change in height
$\partial u_g/\partial x$	Longitudinal component of shear gradient with respect to a change in longitudinal displacement

SECTION I

BACKGROUND AND INTRODUCTION

A. BACKGROUND

The U.S. Army and helicopter manufacturers are vitally interested in automatic nap-of-the-earth (NOE) flight. The more perceptive of these believe that most of the guidance and control problems associated with Light Helicopter Experimental (LHX) and AH-64X rotorcraft operations have at least interim solutions using a mixture of manual and automatic resources. There is some promise that the range of automatic operations can be extended further to include automatic NOE flight. Before this can be accomplished, however, there are at least three major issues that must be resolved:

1. Interpolating within the resolution of a stored NOE data base with the aid of forward- and side-looking sensors, enriching the data content with real-time information, and combining the stored and sensed data for real-time display, guidance, and control purposes.

2. Development of path and attitude command signals from this data array that are appropriate to command safe NOE flight of a three-dimensional helicopter (in contrast to a point mass helicopter).

3. Pilot acceptance of automatic NOE flight.

In the past, the path toward full automation of dangerous mission-critical elements that could, in principle, be accomplished by the pilot has been difficult and fraught with subtle misunderstandings between the piloting and engineering communities. Automatic landing is perhaps the best example of this. Ultimately successful systems required the development not only of guidance and control systems that could do the job with acceptable performance and fail-operational reliability, but they also required:

- Displays presenting status and back-up command information with which the pilot could monitor the progress of operations, the automatic equipment, etc., with the option of instantaneous takeover

- Control laws that, to a very large extent, mimicked the operations of a pilot when following the same guidance information.

The last point above is indeed quite subtle, because it implies that a key factor in pilot acceptance of automatic equipment to fly complex maneuvers is that "it flies the airplane as a pilot would."

For the automatic equipment to fly the helicopter as a pilot would, an automatic system is required that emulates not only the error-correcting features of ordinary feedback control processes but also a system that has predictive and anticipative properties. In terms of the classical modes of pilot control behavior, the automatic equipment should incorporate so-called "pursuit" and, for some maneuvers, "precognitive" elements in addition to the "compensatory" (error correcting) feedback control system behavioral aspects common to both automatic and manual control systems. These higher-order modes of control behavior are not easily mechanized in typical guidance systems, because they require prediction and anticipation. The pilot develops the higher-level behavioral modes by discerning more cues (e.g., via preview) than are conventionally available to monometric single-quantity sensors and by virtue of operations as a dual-mode controller when the input command is appropriate. Thus the pilot in higher level control is very sensitive to the total command as well as any errors, while most automatic equipment is largely error driven.

B. INTRODUCTION

Contemporary technology has provided automated guidance systems for up-and-away flight between stored waypoints using inertial, Doppler, Loran, TACAN, VOR/DME, VORTAC, Omega, and Global Positioning Systems (GPS). Contemporary technology has also provided independent automatic

terrain following/terrain avoidance (TF/TA) and course-keeping systems for low altitude flight using forward looking radar.

Piloted guidance technology for rotorcraft, furthermore, has now provided passive FLIR and SLIR sensors and image converters. This technology could be adapted with additional processing of the converted images, e.g., as suggested in Ref. 1, in order to develop an innovative form of automatic guidance and control which is compatible with piloted guidance. We shall, however, adopt a somewhat different approach here, based on the proposal in Ref. 2.

Automatic nap-of-the-earth (NOE) operations based on stored knowledge of terrain, obstacles, threats, and targets will require advancements in two related technologies. The first is the creation of accurate geodetic bases for navigation, threats, and targets in any theater of operation. The second is the development of storage and display media for real-time use of the data bases in flight. The geodetic bases must cover wide areas in order to allow for versatile mission planning; this will require data storage media more compact than now available (Ref. 3).

For flight planning and in-flight uses, however, the pilot usually prefers that the terrain profiles, obstacles, threats, and targets be presented in course-oriented coordinates for monitoring automatic guidance as well as for manual backup guidance. Although the adoption of course-oriented coordinates will inherently contribute significant compression of terrain data storage requirements for a specific mission, additional data compression is desirable based on the properties of the terrain itself. This issue is addressed in Refs. 4 and 5 and in Section II, "Task I: Storage and Updating of Terrain Profiles and Obstacles," which describes our innovative method for organizing the storage and realtime retrieval of terrain profiles, sensed obstacles, threats, and targets in course-oriented coordinates indexed to a defined flight profile.

Some of the consequential guidance and control data processing issues associated with the automation of following defined flight profiles in NOE operations are discussed in Section III, "Task II: Automatic Guidance for Following Flight Profiles," and in Section IV, "Task III: Automatic

Guidance for Aggressive NOE Maneuvers." Both of these sections have supporting appendices.

Section V presents a summary of pilot-centered considerations for monitoring automatically controlled NOE flight. These considerations include automatic-manual control response compatibility, status displays, and decoupled control responses, all of which are essential for pilot acceptance of automatic NOE flight.

Finally, Section VI presents a summary of the principal findings for each of the tasks that constitute this phase of the study.

SECTION II

TASK I: STORAGE AND UPDATING OF TERRAIN PROFILES AND OBSTACLES

On future U.S. Army helicopters, such as the Light Helicopter-Experimental (LHX), the entire scout or attack mission may be accomplished in instrument meteorological conditions (IMC) with a single pilot. Consequently, if the LHX concept of a single-place attack (or even a scout) mission is to be viable, many of the elements in a typical sequence would have to be handled by automatic equipment.

Virtually all functions of scout/attack rotorcraft depend on maintaining the planned flight profile as a function of time. Other mission functions--such as threat warning and countermeasures, target detection and acquisition, and weapon delivery and fire control--are intimately related to the flight guidance function. Therefore, it is logical to consider automatic navigation and flight control as "core functions" for automating the flight guidance functions.

In an automated guidance system for rotorcraft, a computer-assisted briefing system should augment or supplant the verbal transmission of mission data. An important part of an automated guidance system would be a prepared portable storage medium that would permit automatic loading of all mission-required data into the rotorcraft's guidance system. The mission data required would include (from Ref. 3):

- Routes, waypoints, initial points, targets
- Terrain profiles
- Obstacle types and locations
- Threat types and locations
- Target characteristics
- Weapons complements.

It would be necessary to update automatically this pre-flight data base with information from scouts and other airborne warning and control systems via a secure data transfer link.

Automatic NOE operations based on stored knowledge of terrain, obstacles, threats, and targets will require advancements in three related technologies. The first of these is the creation of accurate geodetic bases with sufficient resolution for navigation, threats, and targets in any theater of operation. The second technology is the development of storage and display media for real-time use of the data bases in flight. The geodetic bases must cover wide areas in order to allow for versatile mission planning; this will require data storage media more compact than are now available (Ref. 3). The third technology is the interpolation within and enrichment in real time of the stored data base with a sensed data base of obstacles and threats acquired from forward- and side-looking sensors.

For flight planning and in-flight uses, however, the pilot usually prefers that the terrain profiles, obstacles, threats, and targets be presented in course-oriented coordinates for monitoring automatic guidance. (Airborne radar, lidar, and infrared sensors can also be directed to scan in course-oriented coordinates.) Part 1 of Table 1 shows that U.S. Army standards for scout/attack terrain flight training require navigation within 1500 m left or right of the preselected course. Thus one innovation which we have begun to investigate is to organize the storage and real-time retrieval of terrain profiles, sensed obstacles, threats, and targets in course-oriented coordinates which are indexed to the defined flight profile. Besides condensing the data storage requirements, this arrangement will simplify the coordinate conversion and identification required for compatible processing of real-time data from on-board forward-looking and side-looking terrain/obstacle/threat sensors. This processed real-time data will be applied subsequently in a coordinate estimation algorithm to update the defined flight profile and the guidance commands derived therefrom for use by the automatic guidance algorithms. The automatic guidance algorithms will employ estimates of predicted vertical, lateral, and longitudinal deviation commands required

TABLE 1. U.S. ARMY STANDARDS FOR ATTACK/SCOUT TERRAIN FLIGHT TRAINING

	TERRAIN FLIGHT MODE		
	LOW LEVEL	CONTOUR	NOE
1. TERRAIN FLIGHT NAVIGATION			
• Know enroute location within:	100 M	500 M	500 M
• Navigate within left or right of preselected course		1500 M	1500 M
• Locate final objective within:	100 M	100 M	100 M
• Navigate – perform tactical NAV for:	40 KM	40 KM	10 KM for AH-1 20 KM for UH-58
2. TASK PERFORMANCE			
• Maintain altitude within:	± 25 ft	Safe obstacle clearance	As close to earth as vegetation and obstacles permit
• Maintain airspeed within:	± 10 kt	Commensurate with terrain	Commensurate with terrain
• Arrive at checkpoints within:	± 2 min of ETA	Report all checkpoints	Report all checkpoints
• Negotiate wire obstacles		Overfly at poles or underfly with hover ht + 25 ft at hover speed	Overfly at poles or underfly at hover ht + 25 ft (AH-1) or 17 20 ft (Scouts)
• NOE Deceleration			
– Maintain heading within:	± 10 deg	–	–
– Decel & stop within:	± 50 ft		
– Tail rotor	Clear of all obstacles	Clear of all obstacles	Clear of all obstacles
• Masking/Unmasking			
– Unmasked exposure not to exceed	10 seconds	10 seconds	10 seconds
– Location	Move to new loc prior to subsequent unmask	Move prior to 2nd unmask	Move prior to 2nd unmask
– Hover unmasking	–	–	• Power check before unmask • Prefer lateral to vertical unmasking
– Acft clearance	–	Clear of all obstacles	Clear obstacles, especially beneath or in flight path
• Terrain Flt Approach			
– Approach angle 0–90°			Maintain constant angle
– Heading within:			± 10 degrees
• Hover OGE check/before terrain flt			
– Maintain altitude			50 ft AGL ± 5 ft (AH 1/OH-58) 35 ft AGL ± 5 ft (OH-6)
– Required maneuver to determine excess torque available			360° LT turn/90° in 4 sec

to follow the updated path, course, and schedule, respectively, with feedforward command compensation. Preview of both stored and sensed terrain and obstacles is therefore essential. Novel approaches to setting both compensatory and pursuit feedforward preview distances are recommended subsequently for minimizing the guidance error in the presence of atmospheric disturbances which may be correlated with the terrain and obstacles.

A. A METHOD FOR PREFLIGHT GEODETIC PARAMETER IDENTIFICATION TO ESTABLISH GUIDANCE COMMANDS FOR PLANNED FLIGHT PROFILES

This method involves the assumption of a mathematical structural model of flight profile guidance commands with undetermined coefficients, and it determines the coefficients of the required guidance command strategy by recursively matching the model to the sensed obstacle and terrain data using a running least-squares estimation technique (i.e., a multiple linear regression). Initially, the coefficients of the model are defined by the guidance commands for the a priori flight plan. (In flight, the guidance commands will be updated in real time from a sensed data base using a procedure to be discussed in a subsequent subtopic.)

The guidance command vector, $\underline{R}(\underline{X},t)$, will be a function of the state vector, $\underline{X}$. Both $\underline{R}$ and $\underline{X}$ will have along-course, across-course, and elevation components. The guidance command vector, $\underline{R}(\underline{X},t)$ will also be a function of events in real-time coordinate, t, detected by the terrain and obstacle sensors or communicated by data link. In the mathematical model that we have investigated, $\underline{R}(\underline{X},t)$ will be represented by a combination of polynomial and harmonic functions of along-course and across-course coordinates, i.e., a vector of truncated Taylor and Fourier series.

The numerical analysis concept central to the procedure consists of applying a running least-squares estimation technique using a moving data "window." A specific example of least-squares estimation occurs in curve-fitting problems where it is desired to obtain a functional form of some chosen order that best fits a given set of discrete measurements. Thus the least-squares problem that we have investigated consists of

correlating a dependent variable, z, e.g., the elevation component of $\underline{R}(\underline{X},t)$, with one or more elements of an independent variable vector, $\underline{X}$. It is assumed that z and $\underline{X}$ are related by an expression of the form

$$z = f_1c_1 + f_2c_2 + \ldots + f_jc_j \ldots + f_mc_m \qquad (1)$$

$$z = [f_1, f_2, \ldots f_m][c_1, c_2, \ldots c_m]^T$$

or

$$z \equiv \underline{F}\,\underline{c} \qquad (2)$$

where f_1, f_2, ... are selected variables from the state vector $\underline{X}$ or explicit functions thereof, and the c_j's are constant coefficients relating y and f_j. In Eq. 2 $\underline{F}$ is a row-vector of the f_j, and $\underline{c}$ is a column-vector of the c_j. For example, $\underline{z} = \underline{F}\,\underline{c}$ will include the following forms for Fourier and Taylor series in one dimension.

Fourier Series

$$z(\lambda,\xi) = c_0 + \sum_{j=1}^{m} c_j \cos\left(\lambda_j - \xi_i\right) \text{ where the } c_j \text{ are real}$$

or

$$z(\lambda) = \sum_{j=-n}^{n} c_j \exp\left(i\lambda_j\right) \text{ where the } c_j \text{ are complex}$$

Taylor Series

$$z(x) = d_o + \sum_{k=1}^{p} d_k \frac{\left(x-x_{ref}\right)^k}{k!} \quad \text{where } d_k = z^{(k)}\left(x_{ref}\right)$$

For a terrain model, however, z is also a function of across-course coordinate y, i.e., $z = z(x,y_k)$ as shown in Table 2 for truncated Fourier and Taylor series representations.

TABLE 2. TERMS FROM TRUNCATED FOURIER AND TAYLOR SERIES FOR TERRAIN MODEL

FOURIER SERIES

Assume the Fourier series in the form of a sum of cosines and sines with undetermined coefficients and given periods for f_{km}:

Define:

$$c_{km} f_{km} = \frac{2c_{km}}{L_x} \cos \frac{2m\pi x}{L_x} + \frac{2d_{km}}{L_x} \sin \frac{2m\pi x}{L_x} ; \begin{cases} m = 0, 1, 2, 3, \ldots M \\ k = 1, 2, 3, \ldots K \end{cases}$$

Height of Terrain and Obstacles — Across Course Coord. — Along Course Coord. — Average Height

$$\begin{aligned} z = z(x, y_1) &= c_{10} + f_{11} c_{11} + f_{12} c_{12} + f_{13} c_{13} + \ldots + f_{1m} c_{1m} \\ &= z(x, y_2) = c_{20} + f_{21} c_{21} + f_{22} c_{22} + f_{23} c_{23} + \ldots + f_{2m} c_{2m} \\ &= z(x, y_3) = c_{30} + f_{31} c_{31} + f_{32} c_{32} + f_{33} c_{33} + \ldots + f_{3m} c_{3m} \\ &\vdots \qquad\quad \vdots \qquad\quad \vdots \qquad\quad \vdots \qquad\quad \vdots \\ &= z(x, y_k) = c_{k0} + f_{k1} c_{k1} + f_{k2} c_{k2} + f_{k3} c_{k3} + \ldots + f_{km} c_{km} \end{aligned}$$

Estimate the kth set of c_{km} using $y = y_k$ and 2M values of x to determine $f(x, y_k)$

Model requires 2M*K values of z corresponding to 2M values of x at K values of y to estimate $c_{km}(y_k)$ and $d_{km}(y_k)$

TAYLOR SERIES

In particular situations it will be necessary also to incorporate terms from truncated Taylor's series:

$$f_{(k+1)(m+1)} C_{(k+1)(m+1)} = (x - x_o) C_{(k+1)(m+1)} \text{ for linear slope}$$

$$f_{(k+2)(m+2)} C_{(k+2)(m+2)} = (x - x_o)^2 C_{(k+2)(m+2)} \text{ for curvature}$$

An example of the array of undetermined coefficients for coordinate $z(x,y_k)$ for a terrain model (and for a corresponding guidance command model) is shown in Table 3, with m harmonics along-course and k coordinates across-course. Examples of the specific number $(1 + 2m)k$ of numerical coefficients required to represent a 3 km × 30 km terrain model of a route having a particular x-y coordinate resolution are listed in Table 4. The present study investigated the representation of profiles from a 5 km × 5 km digitized terrain model furnished by NASA and having 10 m resolution shown in Fig. 1.

The number of coefficients of the terrain model (and corresponding guidance command model) required for a truncated Fourier series representation can be estimated in advance by preprocessing sections of the terrain for the intended route with a finite Fourier transformation (FFT). The significant harmonic content for guidance can be estimated from the effective spatial bandwidth of the terrain over the route to be followed by the rotorcraft. Figure 2 provides a convenient graph for relating spatial bandwidth of the terrain or route to the temporal bandwidth of a guidance and control system at three forward speeds. At 20 kts, spatial bandwidth in radians per decameter (rad/dm) and temporal bandwidth in radians per second (rad/sec) are virtually identical numbers. The sections of terrain in Fig. 1 for which FFTs were obtained exhibited effective spatial bandwidths of about 0.2 rad/dm. Thus we can expect a typical guidance and control system to follow an offset profile over these samples with good precision at 20 to 40 kts forward speed.

The STI proprietary computer program for obtaining FFTs from digitized samples of data is called FREquency Domain Analysis (FREDA). The NASA-STI computer program for parameter identification using a running least squares estimation is called Non-Intrusive Parameter Identification Program (NIPIP). These acronyms will recur in subsequent text. Before we present some of the results using FREDA and NIPIP, we shall digress to summarize the steps in the procedure used in NIPIP to obtain least-squares estimates for the undetermined coefficients in the terrain model.

TABLE 3. TERRAIN MODEL ARRAY OF $c_{km}(y_k)$, $d_{km}(y_k)$
AS SHOWN WITH (1+2M)K COEFFICIENTS

$c_{10}(y_1)$	$c_{11}(y_1),d_{11}(y_1)$	$c_{12}(y_1),d_{12}(y_1)$	$c_{13}(y_1),d_{13}(y_1)$ ...	$c_{1m}(y_1),d_{1m}(y_1)$
$c_{20}(y_2)$	$c_{21}(y_2),d_{21}(y_2)$	$c_{22}(y_2),d_{22}(y_2)$	$c_{23}(y_2),d_{23}(y_2)$ ...	$c_{2m}(y_2),d_{2m}(y_2)$
$c_{30}(y_3)$	$c_{31}(y_3),d_{31}(y_3)$	$c_{32}(y_3),d_{32}(y_3)$	$c_{33}(y_3),d_{33}(y_3)$ ...	$c_{3m}(y_3),d_{3m}(y_3)$
⋮	⋮	⋮	⋮	⋮
$c_{k0}(y_k)$	$c_{k1}(y_k),d_{k1}(y_k)$	$c_{k2}(y_k),d_{k2}(y_k)$	$c_{k3}(y_k),d_{k3}(y_k)$ ...	$c_{km}(y_k),d_{km}(y_k)$

Options: (1) Store coefficients as an array for interpolation and recall or

(2) Derive a least squares estimate for each column of $c_{km}(y_k)$ and $d_{km}(y_k)$ using polynomials with undetermined coefficients on Fourier series to provide a basis for interpolating $c_{km}(y_k)$ and $d_{km}(y_k)$

TABLE 4. EXAMPLE OF ROUTE MAP

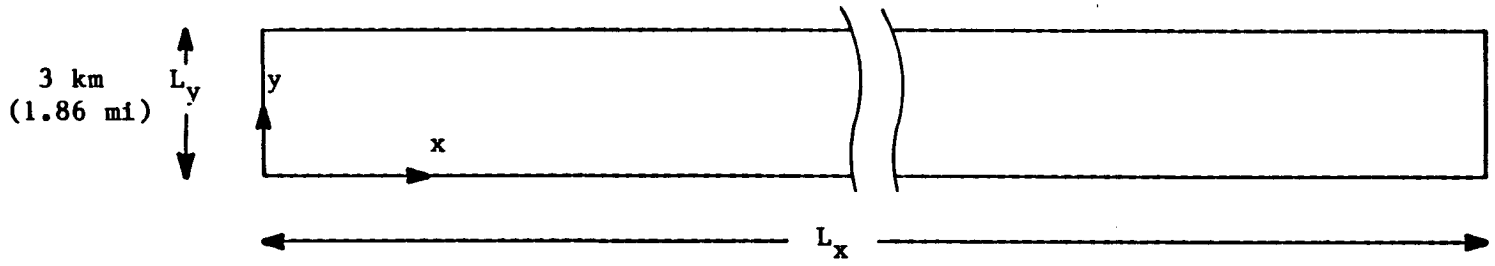

30 km (18.6 mi)
Requires 10 sets to cover 300 km in x

Courses 6201(PA), 9998(MT)

Present Study

DMA

NOTS course 10(CA)

x-y Resolution (m)	1	3	10	30	100	175	300	1000
x-y Resolution (km):	0.001	0.003	0.01	0.03	0.1		0.3	1
2M if L_x = 30 km	30000	10000	3000	1000	300		100	30
K if L_y = 3 km	3000	1000	300	100	30		10	3
(1+2M)K =	0.9E8+3000	1E7+1000	0.9E6+300	1E5+100	0.9E4+30		1E3+10	93

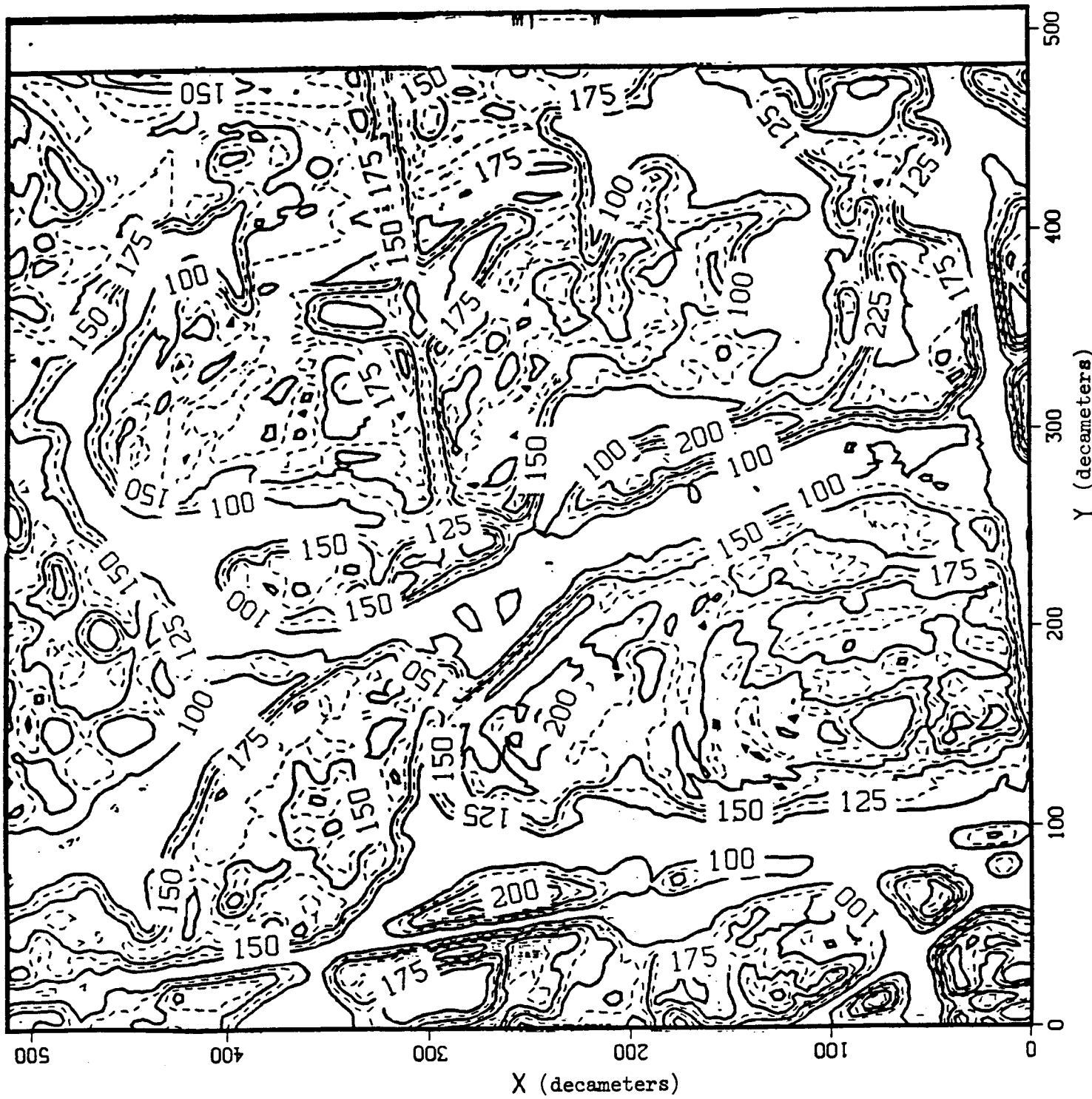

Figure 1. Contour Map for Example of Terrain Data Base

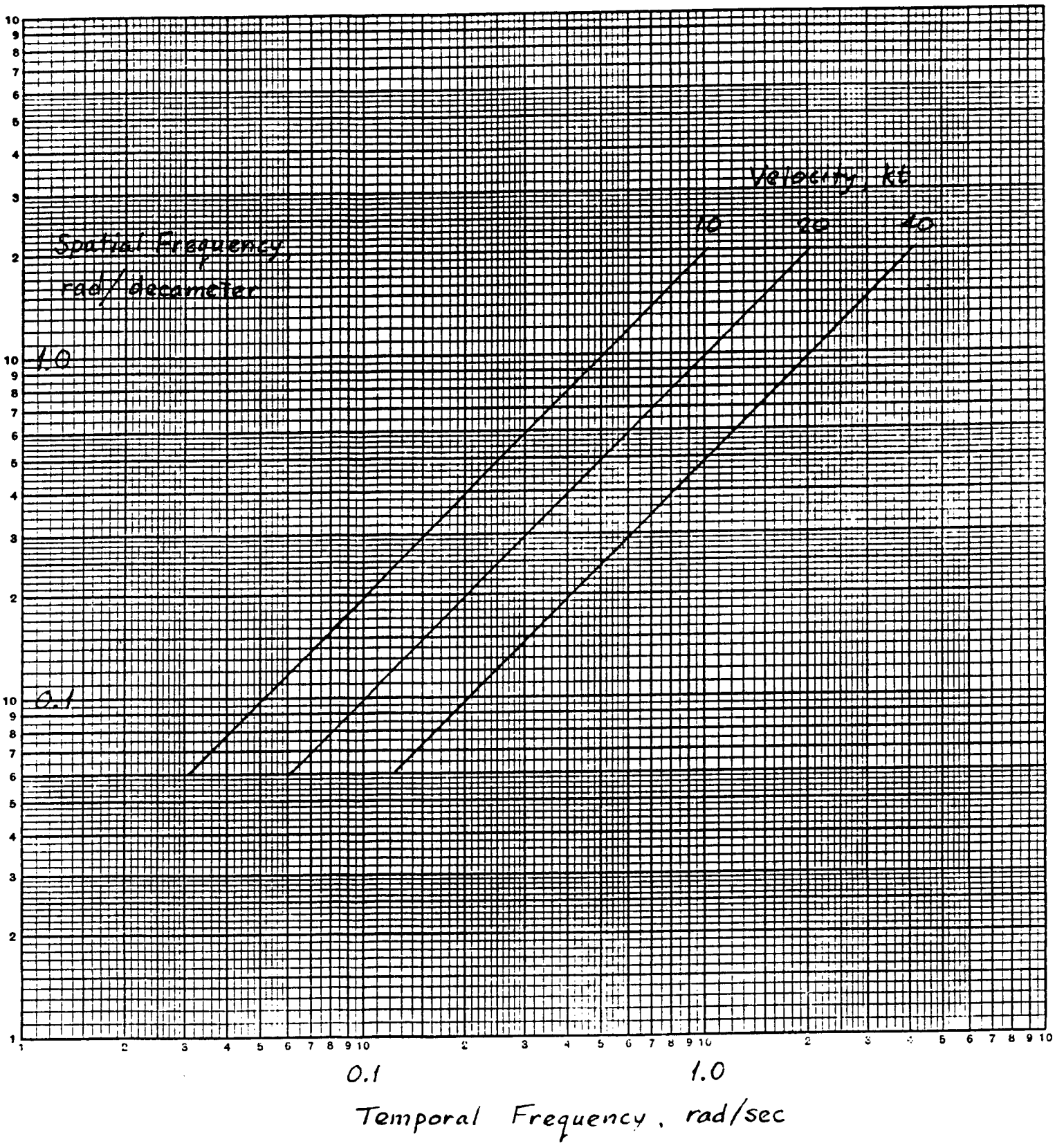

Figure 2. Relationships Between Temporal and Spatial Frequencies at Three Forward Speeds

Procedure for Obtaining Least-Squares Estimate For Undetermined Terrain Model Coefficients

If there exist sets of discrete measurements for z and $\underline{F}$ from the terrain and obstacle sensors and navigation systems and the difference between the actual guidance profile required to avoid terrain and obstacles and the output of the assumed model given by Eq. 1 is given by v, then

$$z_n = \underline{F}_n \hat{\underline{c}} + v_n$$

where $\hat{\underline{c}}$ is the estimated value of $\underline{c}$ given by Eq. 1, and the subscript n is used to denote each set of y and $\underline{F}$. It is assumed that there exists a $\hat{\underline{c}}$ which will relate all values of z_n to the $\underline{F}_n$.

To arrive at an estimate for $\hat{\underline{c}}$, at least m sets of measurements are required (where m is the number of degrees of freedom in Eq. 1). The solution for $\hat{\underline{c}}$ is found by adjoining these sets of discrete measurements as follows,

$$\begin{bmatrix} z_1 \\ z_2 \\ \vdots \\ z_N \end{bmatrix} = \begin{bmatrix} \underline{F}_1 \\ \underline{F}_2 \\ \vdots \\ \underline{F}_N \end{bmatrix} \hat{\underline{c}} + \begin{bmatrix} v_1 \\ v_2 \\ \vdots \\ v_N \end{bmatrix} \qquad (3)$$

where N is the number of measurements and $N > m$. Equation 3 can be written more concisely in a matrix notation as

$$\underline{z} = H \hat{\underline{c}} + \underline{v} \qquad (4)$$

where $\underline{z}$, H, and $\underline{v}$ are defined by inspection. Note that H is an N by m matrix.

The derivation of the least-squares estimate for the unknown coefficients, $\hat{\underline{c}}$, is obtained by minimizing the sum of the squares of $\underline{v}$ where

$$\underline{v} = \underline{z} - H\hat{\underline{c}} \tag{5}$$

The complete derivation is given in Ref. 2.

The recursive least-squares estimate for $\hat{\underline{c}}$ is given as

$$\hat{\underline{c}} = \left(\sum_{n=1}^{N} \underline{F}_n^T \underline{F}_n \right)^{-1} \sum_{n=1}^{N} \underline{F}_n^T z_n \tag{6}$$

where N is the number of data points up to the given point in time where the sum is truncated.

The following features of this solution can be noted. First, the main computational task consists of updating summations of products of the m by m matrix $\underline{F}^T\underline{F}$. The only storage requirement is that these summations alone be saved, not all of the accumulated data as with a batch processing scheme. Second, the most complex computational task is the inversion of the $\sum_{n=1}^{N} \underline{F}_n^T \underline{F}_n$ matrix.

This completes our digression to describe the way in which the least-squares estimate is performed by NIPIP (more details on NIPIP can be found in Refs. 6, 7, and 8). We shall now return to describe the results of using FREDA and NIPIP to model terrain using Fourier series descriptors.

B. RESULTS OF TERRAIN MODELING USING FOURIER SERIES DESCRIPTORS

Recall that the purpose of this effort is to evaluate various ways of arriving at a terrain model (and corresponding offset guidance command model) that uses a Fourier-series-like structure, but with a reduced

number of components. The example terrain data base consists of a set of altitudes over an x-y grid. Figure 1 (on p. 14) shows a contour plot for the example data base. This data set is available on a MICRO-VAX II as discrete altitude in units of decameters (dm) stored as an array having a discrete x-y grid of 512 × 512 dm. Six slices along y = 110, 185, 199, 200, 201, and 440 dm were unpacked and stored as IBM PC files for subsequent analysis using FREDA and NIPIP. STI's Frequency CONversion program FCON was used to produce the binary input file format for entry into FREDA.

FREDA can provide results only at frequencies that are harmonics of a cycle per run length. NIPIP is more general, in that it can use non-harmonics in its fitting process, albeit at a cost of larger matrices and slower execution in storing all of the cross-products required. Thus, our procedure is to use FREDA to determine bandwidth and provide insight into those spatial frequencies having predominant power in order to guide the selection of a reduced number of frequency components for use in NIPIP.

1. FREDA Results

Figure 3 shows plots of the spatial history and power spectral density (PSD) of elevation along the slice at y = 200 dm. The spatial history includes the average value that was removed during the PSD analysis. The logarithmically-spaced bin selection technique was chosen so that the first 24 PSD results (Fig. 3) would have a bandwidth of one cycle per run length (expressed in rad/dm) and center frequencies at multiples of the first one, which is $2\pi/512 = 0.0123$ rad/dm. Above the first 24 components, the PSD is binned using an approximate log-spacing technique up to the maximum available frequency (π rad/dm in Fig. 3). Figures 4 and 5 show results for y = 440 and 110 dm, respectively. While the detailed spatial histories are different, there is a second-order roll-off in power (first-order roll-off in amplitude) above the effective bandwidth of about 0.2 rad/dm in all three PSDs.

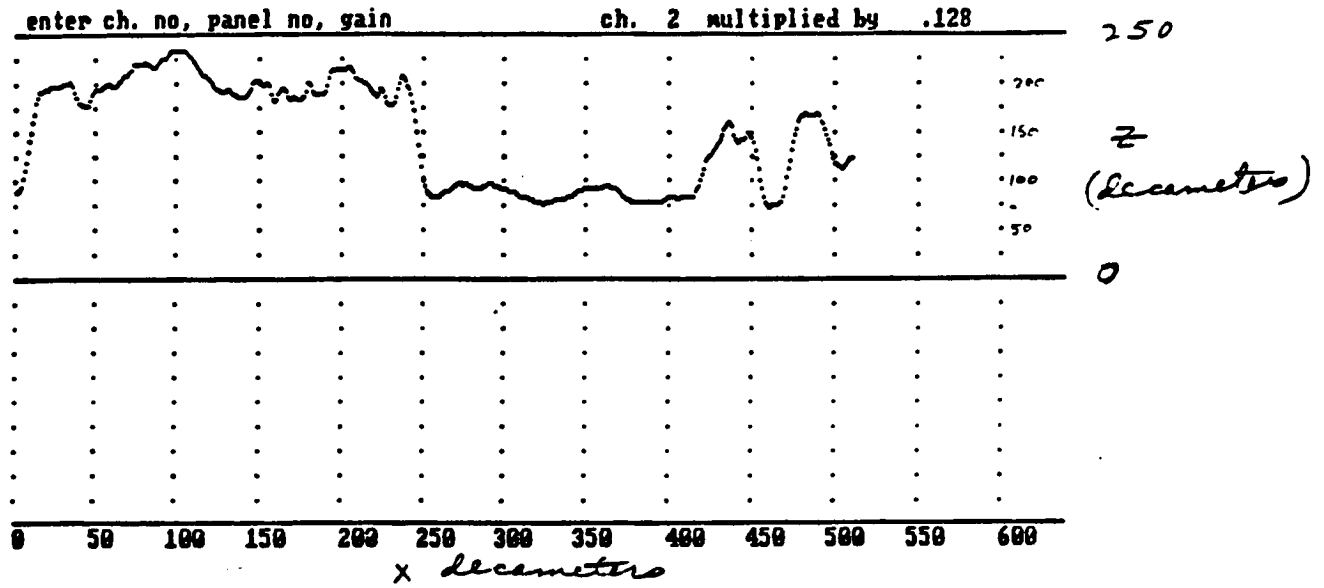

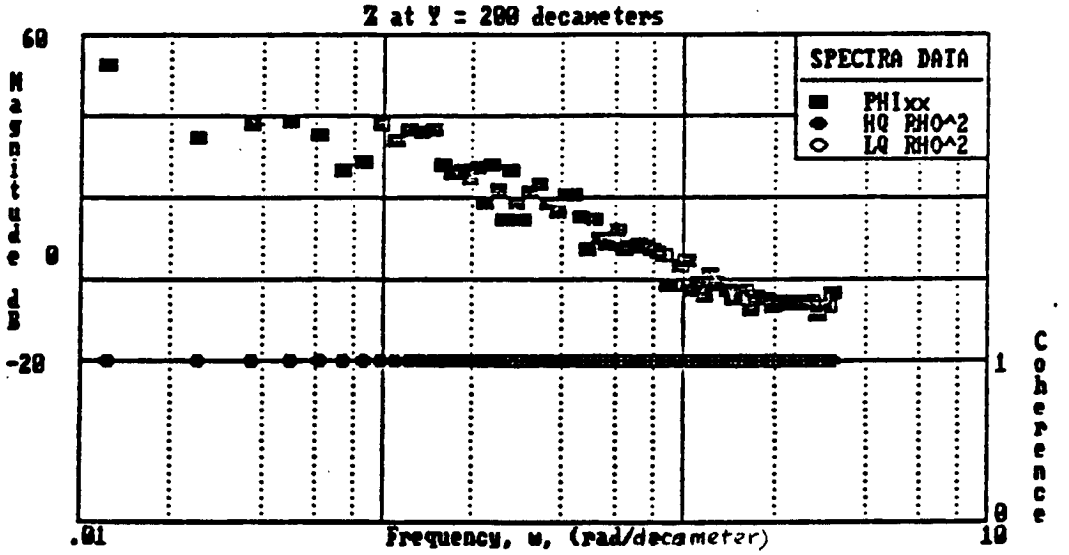

$\frac{2\pi}{512}$ = 0.0123 rad/dm

Mean Terrain Height 150.192 dm
Root Mean Squared Height 54.3 dm
Mean Squared Height 2946.9 $(dm)^2$
Effective Spatial Bandwidth 0.2 rad/dm

Figure 3. FREDA Output for y = 200 dm

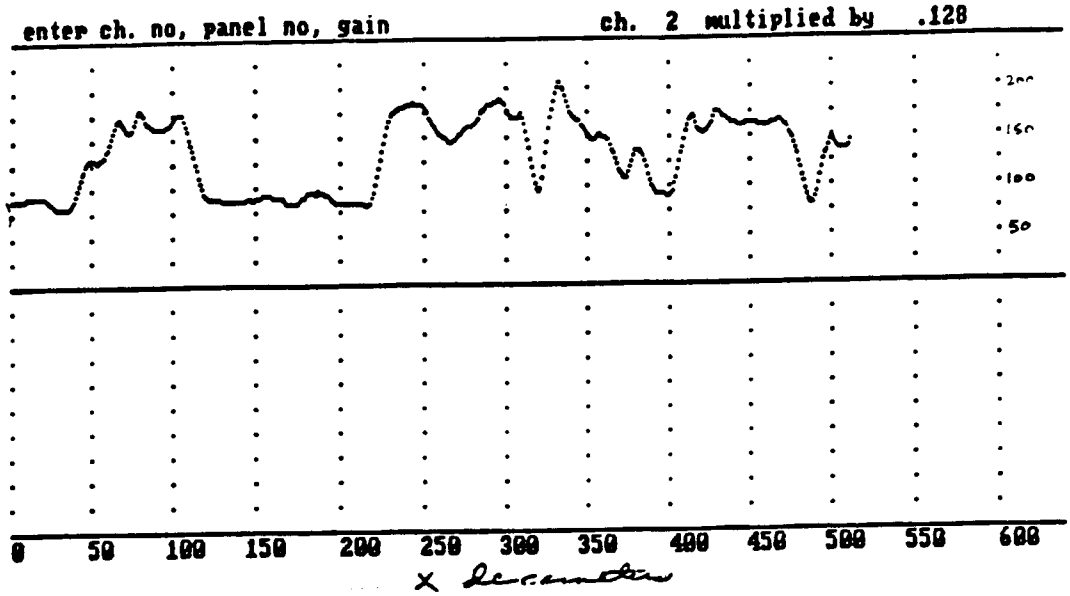

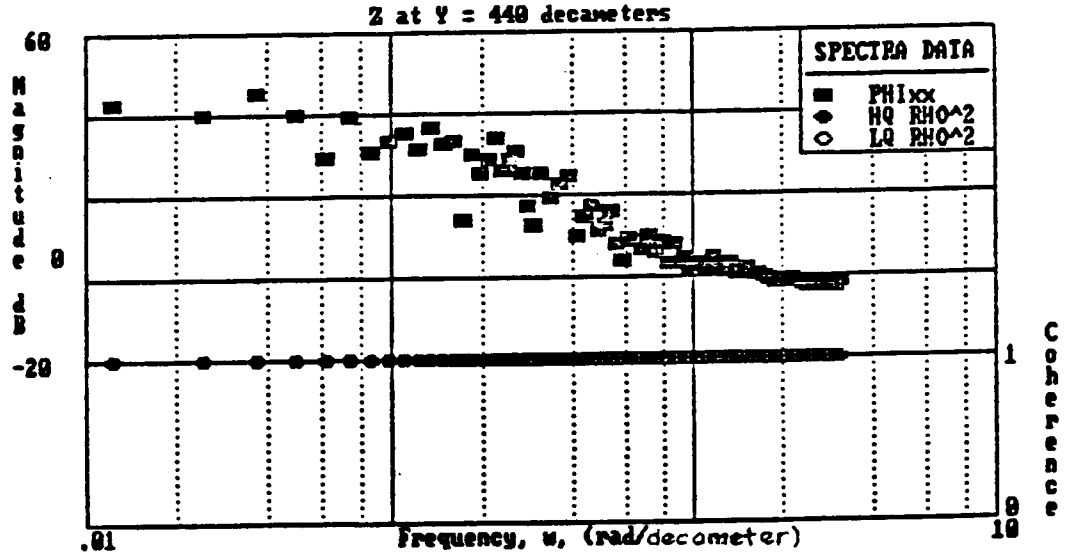

$\frac{2\pi}{512}$ = 0.0123 rad/dm

Mean Terrain Height 135.706 dm
Root Mean Squared Height 36.7 dm
Mean Squared Height 1343.4 $(dm)^2$
Effective Spatial Bandwidth 0.2 rad/dm

Figure 4. FREDA Output for y = 440 dm

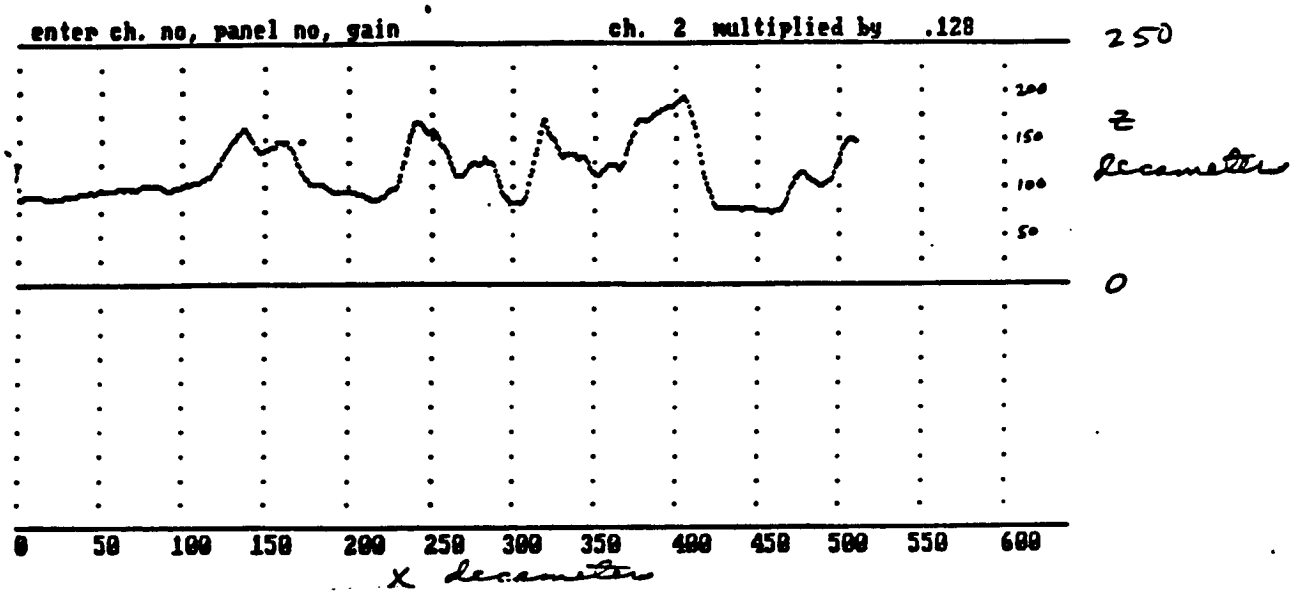

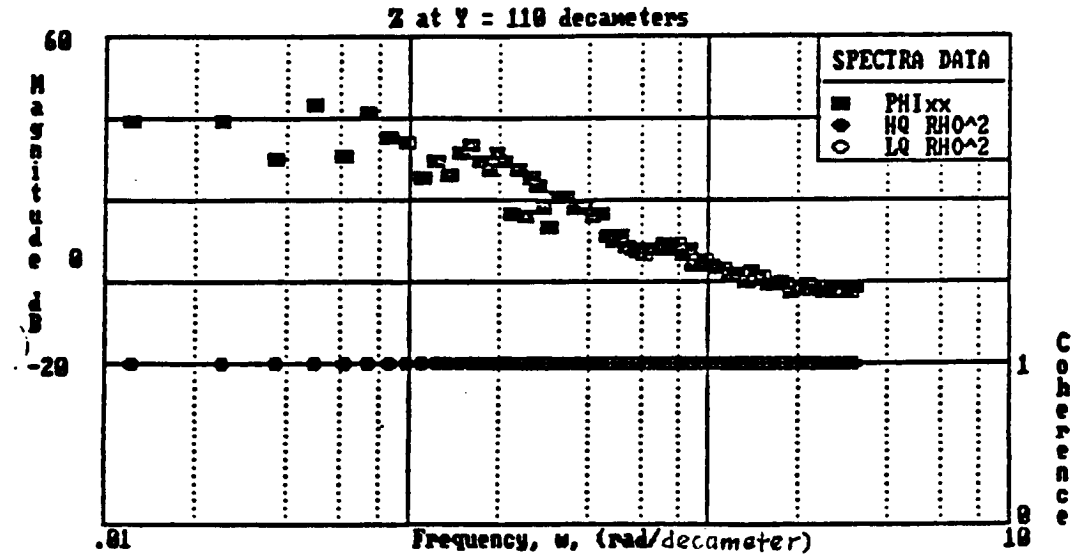

$\frac{2\pi}{512}$ = 0.0123 rad/dm

Mean Terrain Height 119.009 dm
Root Mean Squared Height 29.6 dm
Mean Squared Height 875.47 $(dm)^2$
Effective Spatial Bandwidth 0.2 rad/dm

Figure 5. FREDA Output for y = 110 dm

2. NIPIP Results

The NIPIP program was adapted to the IBM PC in a standard version. A special version was then set up to allow it to identify the amplitudes of a sum of sines and cosines to represent terrain data. Some additional enhancements were needed for dynamic range scaling of the matrices to prevent overflows that can occur for a long data window and a large number of sines and cosines. These enhancements reflect the results of an insightful review of the similarity of the NIPIP and FREDA formulations for the special case of sine waves that have an integer number of cycles in a data window or run length. For this case, the determinant of a key NIPIP matrix is bounded by N*(0.5*N*G*G)**NSC, where N is the number of data points, G is the amplitude factor, and NSC is the total number of sines and cosines. In the future, this relationship can be incorporated into NIPIP to scale the calculations automatically.

Figure 6 shows the output file from NIPIP with 20 harmonics, and it compares some of the peak amplitudes of the sine (AS_i) and cosine (AC_i) components with those found using FREDA. The results are virtually identical. Figure 7a compares the 20-harmonic fit to the y = 200 dm slice (the smoother curve is the fit). The data compression ratios are shown in each caption.

In Fig. 7a, the resulting extreme deviations of the approximation are within 10 dm with three exceptions: the initial valley at X = 0 is under-estimated by 12 dm, the valley at x = 225 dm is under-estimated by 15 dm, and the mesa at x = 512 dm is under-estimated by 20 dm. Obviously, under-estimation of the peaks is unsafe, but the extreme deviations of peaks can be more confidently predicted by sensed information; whereas, the valleys are usually shielded from forward-looking sensors by intervening peaks. Thus the procedure is at least on the safe side (with respect to terrain) in under-estimating the valleys, because the affected flight profile commands, based on the stored knowledge of terrain, will be updated in real time by coordinate identification using sensed obstacle and terrain data. This will provide the capability to interpolate within

```
MS-DOS 3.10  Thu  8-21-1986 17:06:59.7(
(C)
  20,  .1500 ,  ASi      ,  ACi      ,
   .1227E-01,   447.8    ,   84.59    ,
   .2454E-01,  -51.03    ,  -25.49    ,
   .3682E-01,   73.68    ,  -41.59    ,
   .4909E-01,  -60.94    ,  -68.14    ,
   .6136E-01,   52.99    ,   29.66    ,
   .7363E-01,   18.07    ,  -13.94    ,
   .8590E-01,   3.167    ,   26.89    ,
   .9817E-01,  -52.65    ,  -64.18    ,
   .1104    ,  -19.74    ,  -48.81    ,
   .1227    ,  -24.63    ,  -68.52    ,
   .1350    ,   37.79    ,  -55.49    ,
   .1473    ,   8.414    ,  -69.62    ,
   .1595    ,   26.00    ,   4.085    ,
   .1718    ,   5.838    ,  -20.72    ,
   .1841    ,   6.596    ,   21.92    ,
   .1963    ,   2.030    ,  -18.17    ,
   .2086    ,  -6.773    ,   22.54    ,
   .2209    ,  -6.982    ,  -5.640    ,
   .2332    ,  -21.74    ,   13.38    ,
   .2454    ,  -9.065    ,  -10.16    ,
   .0000    ,   150.2    ,

MS-DOS 3.10  Thu  8-21-1986 17:07:01.66
(C)

MS-DOS 3.10  Thu  8-21-1986 17:07:01.88
(C)
```

F20.15 - amplitude scale factor

= .15 $\sqrt{AS_i^2 + AC_i^2}$

Peak ← Peak via FREDA

68.36 68.39

12.69 12.68

7.9 7.87

3.83 3.86

2.04 2.02

150.19

Figure 6. NIPIP Output File

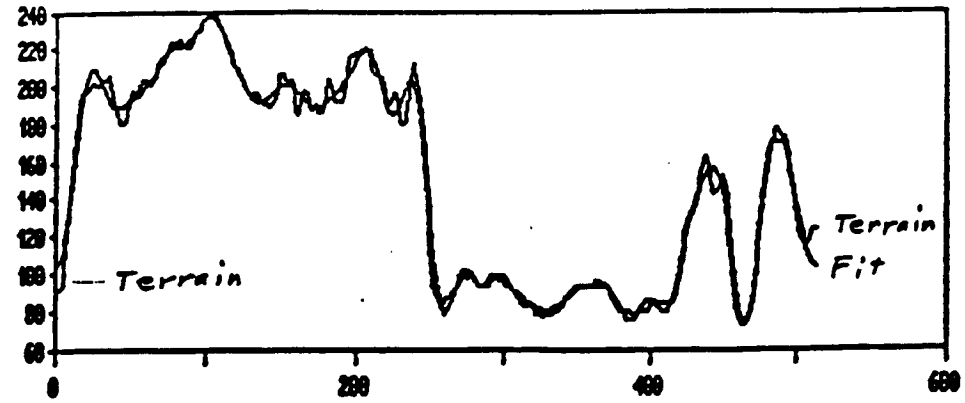

a) First 20 Harmonics. Data Compression Ratio 512:[1+20(3)], i.e., 512:61 or 8.39:1

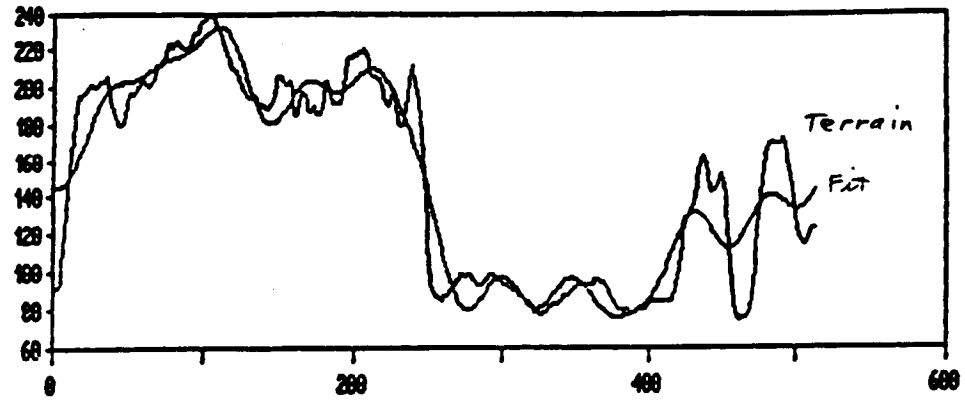

b) First Five Harmonics Plus Two Non-Harmonics at 0.1 and 0.14 rad/dm. Data Compression Ratio 512:[1+7(3)], i.e., 512:22 or 23.3:1

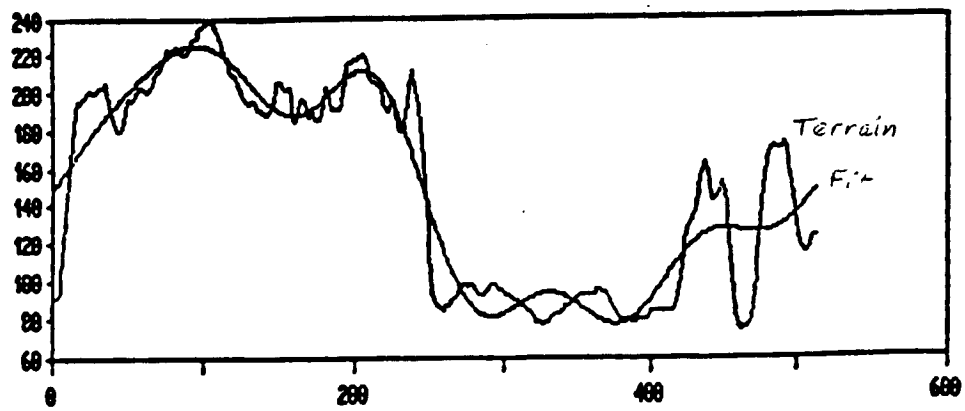

c) First Five Harmonics. Data Compression Ratio 512:[1+5(3)], i.e., 512:16 or 32:1

Figure 7. Effect of Number of Harmonics on Terrain Fits for y = 200 dm

geodetic data bases having a coarse quantization of terrain, such as the Defense Mapping Agency (DMA) 10 dm data base.

Figure 7c shows the effect of reducing the frequencies to the first five harmonics; whereas, Fig. 7b shows the effect of adding two non-harmonic frequencies (0.1 and 0.14 rad/dm) above the first five. These preliminary efforts show that about 20+ frequencies are needed if the peaks are to be accurately described. Finally, Fig. 8 shows the fit for the first 206 dm using the same seven frequencies used in Fig. 7b. This case is included here to give some initial insight into what can be achieved with non-harmonic frequencies selected from inspection of the PSD, since the fit is clearly superior for the same region.

These results suggest that the techniques examined can achieve practical data compression ratios between 8:1 and 10:1 for the samples of vertical profiles from the terrain data base in Fig. 1. The resulting recommendations for compressing flight profile data storage requirements are summarized in Table 5.

This completes our discussion of the results of terrain modeling for the purpose of representing off-set guidance commands using Fourier series descriptors. In the next subtopic, we shall describe a procedure for updating and modifying the stored flight profile guidance commands in real time using a data base derived from forward- and sideward-looking sensors and having a (navigation) reference system in common with that for the stored data base.

C. REAL-TIME MODIFICATION OF THE FLIGHT PLAN TO ACCOMMODATE SENSED TERRAIN AND OBSTACLES

Figure 9 illustrates a procedural flow diagram for updating and modifying the stored guidance command flight profiles in real time to provide unexpected obstacle avoidance. Two data bases having a common navigational reference system (which provides state vector $\underline{X}$) are identified at the top of the diagram: the stored flight profiles (vector $\underline{R}_n$) at the upper left and the sensed profile of terrain, obstacles, and threats, together with offset bias requirements for safety at the upper right (vector $\hat{\underline{R}}_n$).

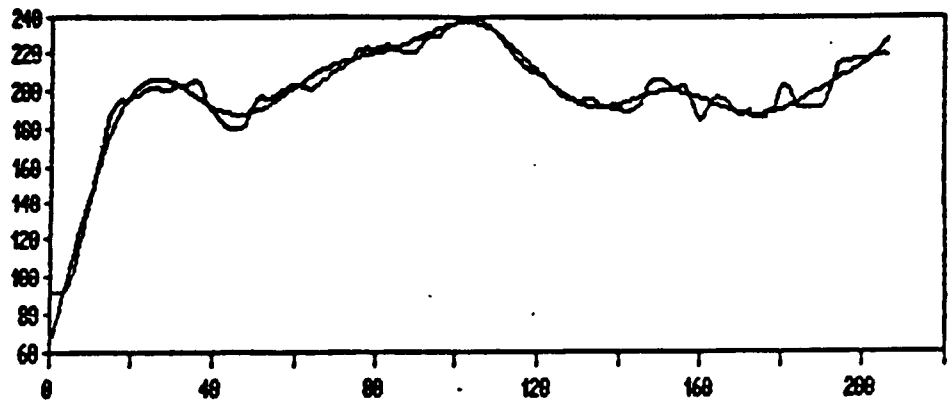

Figure 8. Seven Frequency Fit to the First 206 dm Portion of the y = 200 dm Slice with Non-Harmonically Related Frequencies. Data Compression Ratio 206:[1+7(3)], i.e., 206:22 or 9.36:1

TABLE 5

RECOMMENDATIONS FOR COMPRESSING FLIGHT PROFILE DATA STORAGE REQUIREMENTS

- Preprocess flight profile with FFT program, e.g., FREquency Domain Analysis (FREDA) Program
- Identify mean bias, slope, and curvature in planned flight profile
- Identify special patterned features such as step functions, square waves, trapezoidal waves, triangular waves, and sawtooth waves, which require extraordinary spatial frequency bandwidth to represent harmonically
- Estimate predominant spatial harmonic content in planned flight profile after identifying, defining, and removing mean bias, slope, curvature, and special patterned features which can otherwise be represented by truncated polynomials and simpler unique functions
- Define criteria for adjusting $\Delta\omega$ to smooth raw spectra
- Select only those frequencies among ω_m (m = 1, 2, ..., m) that represent predominant power in the FFT of the flight profile
- Omit many of the higher frequencies with low power, and use non-harmonically related frequencies in selected regions
- Use only the selected frequencies in the vector of Fourier series with undetermined coefficients
- Reduce the number of undetermined coefficients to be stored
- Modify parameter identification program (NIPIP) for automatic self-scaling
- Consider shorter run lengths, although this will require transition logic to blend the ends during reconstruction

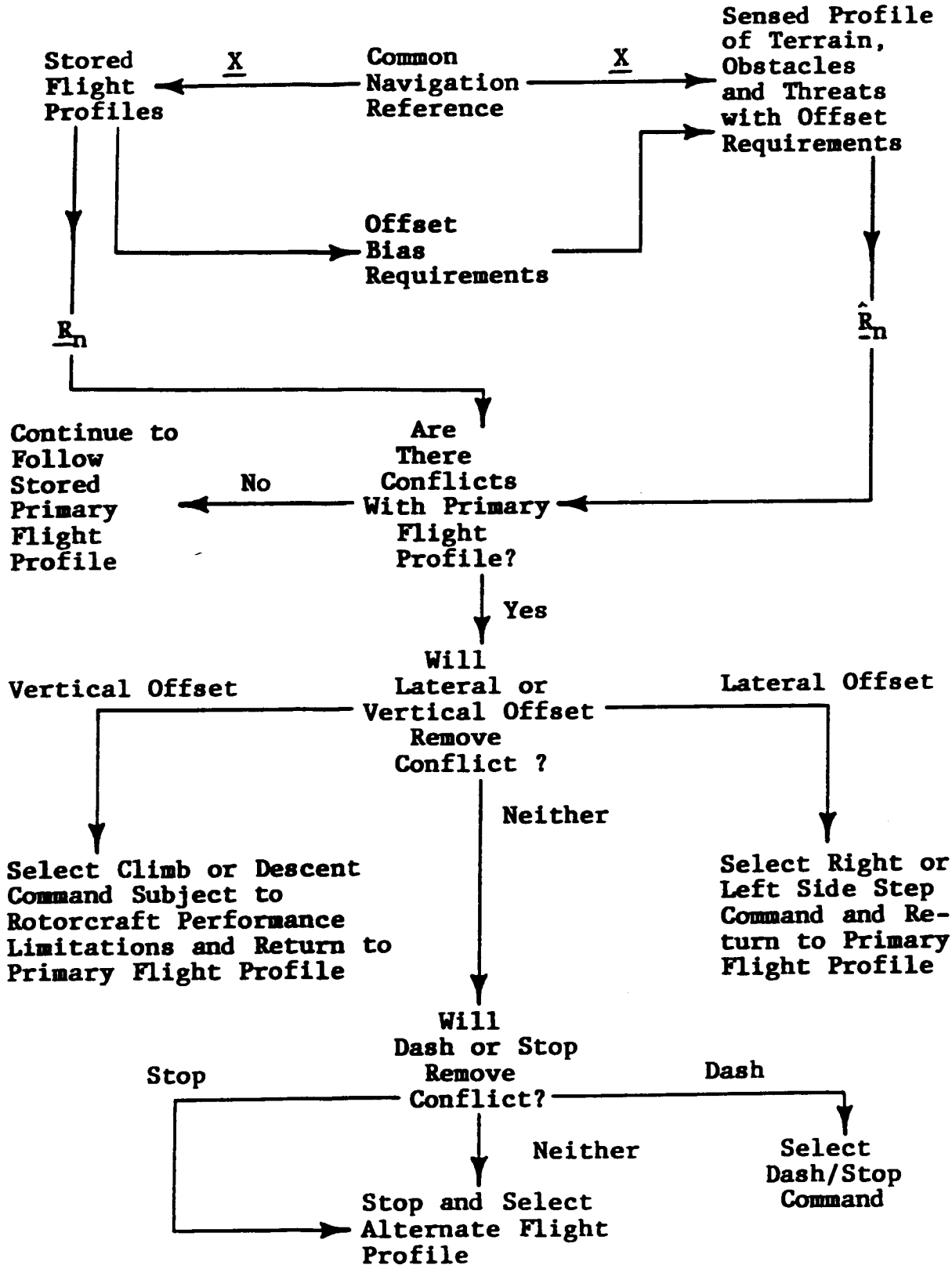

Figure 9. Procedural Flow Diagram for Unexpected Obstacle Avoidance in Real Time

In principle, it is necessary to compare $\hat{\underline{R}}_n$ with $\underline{R}_n$ in real time and resolve any conflicts with the planned flight profile by automatically selecting the indicated lateral or vertical offset maneuvers and returning to the planned flight profile where possible. If lateral or vertical offset maneuvers will not remove a conflict between $\hat{\underline{R}}_n$ and $\underline{R}_n$, it may be necessary to accelerate or decelerate or stop and let the pilot select another flight plan. The automatic obstacle avoidance maneuvers will be selected from the constrained time-optimal repertory to be discussed subsequently in connection with Task III. A practical method for comparing $\hat{\underline{R}}_n$ and $\underline{R}_n$ is described briefly in the following paragraphs.

A three-dimensional safety margin envelope is defined mathematically in the form of a cylinder which encompasses the extremities of the rotorcraft with room to spare, governed by safety margins. This cylindrical envelope is mathematically centered on the planned course and vertically offset profile. When the rotorcraft is hovering, the cylindrical envelope is centered on the present position of the rotorcraft. When the rotorcraft is translating, an hemicylindrical envelope bisected by the direction of the inertial velocity (V_i) advances mathematically ahead of the rotorcraft's present position a distance $V_i \tau_p$, where τ_p is the preview time interval of the anticipative trajectory coupler discussed in Section III with respect to Task II.

If the sensed profile of terrain, obstacles, and threats (i.e., the sensed data base) mathematically penetrates the anticipative hemicylinder, a conflict exists along the planned flight course-and-profile. This conflict must be detected in real time by coordinate identification and comparison over the leading surface of the anticipative hemicylinder using sensed terrain and obstacle data. It remains to develop in Phase II of this study a rationale and procedure for correcting the conflict and returning to the flight plan safely by means of transition logic between the anticipative trajectory coupler (discussed in Section III) and the constrained time-optimal maneuvers for avoiding the obstacles (discussed in Section IV).

SECTION III

TASK II: AUTOMATIC GUIDANCE FOR FOLLOWING FLIGHT PROFILES

A. GUIDANCE AND CONTROL DATA PROCESSING

Automatic processing of stored and sensed terrain and obstacle data will involve sampling, interpolation, extrapolation, smoothing, and comparison of spatial and temporal series of data coupled with priority logic for use of the processed data by the automatic guidance algorithms. An example of a first level of priority logic for unexpected obstacle avoidance using discrete maneuvers was illustrated in the flow diagram, Fig. 9 (p. 28). The automatic guidance algorithms will employ estimates of predicted (i.e., previewed or time-advanced) vertical, lateral, and longitudinal deviation commands required to follow the desired path, course, and schedule, respectively, with feedforward command compensation. Preview of both stored and sensed terrain and obstacle data is therefore essential in order to compensate for the inevitable (and predictable) processing delays and rotorcraft response lags.

A novel approach to setting the (stored and sensed terrain data) preview distance has been developed in which the best command-following flight guidance and control system is synthesized, and its equivalent closed-loop time delay, τ_e, for low-frequency inputs is determined. The data preview distance, D_{pe} , is then set to read (stored and sensed) terrain at $D_{pe} = V\tau_e$ ahead of the rotorcraft in the direction of travel at velocity, V. (Alternatively, in the time domain, the data preview interval $T_p \triangleq D_{pe}/V = \tau_e$.)

Precision NOE guidance and control, however, imposes a number of other requirements on data processing in real time. Consider, for example, the vector block diagram representing a multiloop guidance and control system in Fig. 10 which is subject to response-correlated disturbances, $\partial D(s)/\partial M(s)$. Each vector and matrix will be represented in operational rotation as a function of the Laplace transformation operator, s. (The

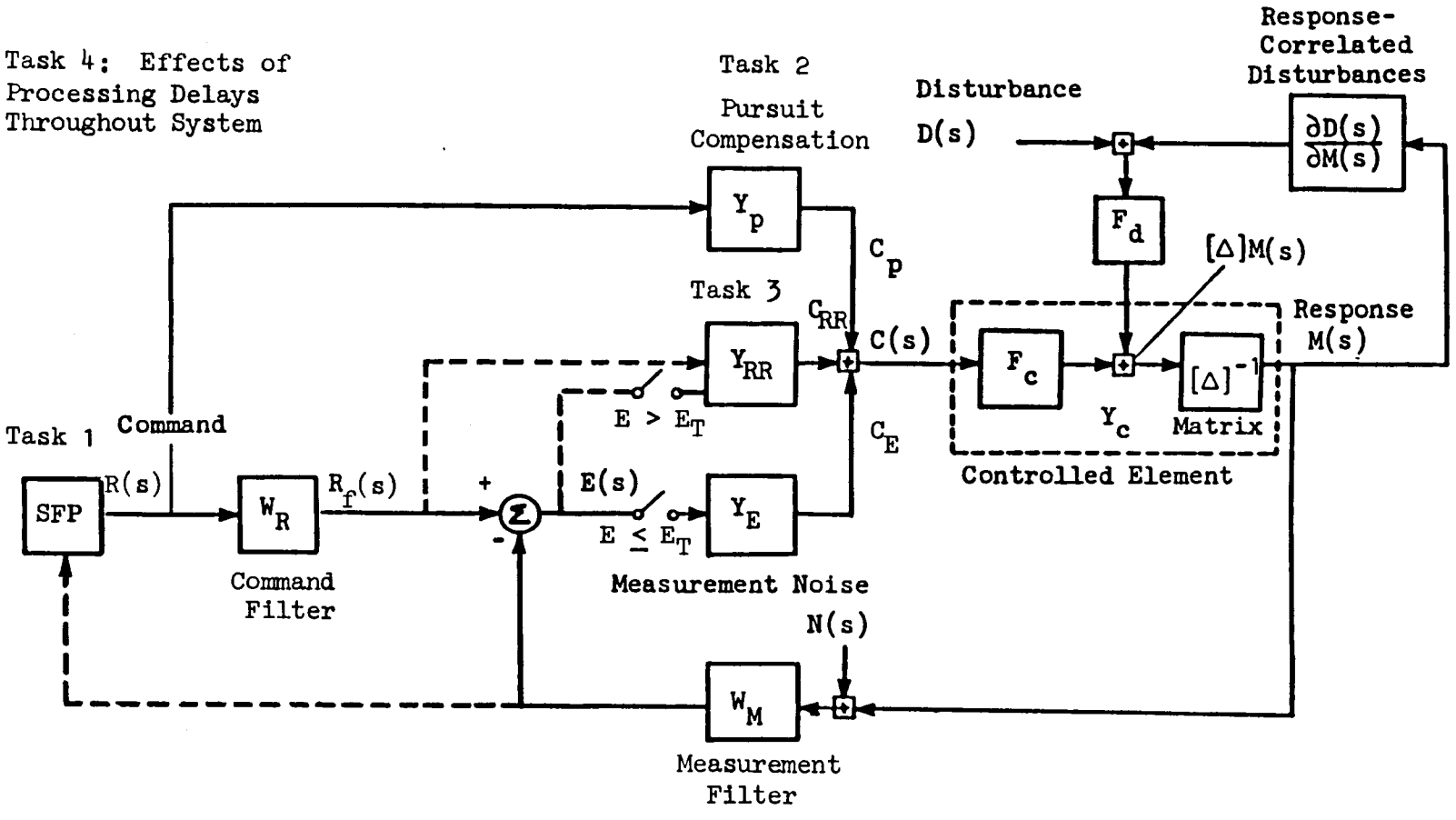

Figure 10. Vector Block Diagram for Multiloop Guidance and Control System
Studies on Contract NAS2-12361

SFP = Stored flight plan and compressed data for terrain model

Y_{RR} = Time Optimal Program for Rapid Response (RR) Maneuvers if $E > E_T$

Y_E = Compensatory Equalization for Error Reduction if $E \leq E_T$

E_T = Error Threshold

various parts of the block diagram that have been addressed by tasks in Phase I are identified in Fig. 10 with Arabic task numbers rather than Roman.) The stored flight plan (SFP) and compressed data for the guidance command R(s) based on the terrain model investigated in Task 1 is shown at the extreme left-side of the figure. The command R(s) is applied (with preview) to the pursuit compensation (Task 2) at the top of the figure. A filtered command $R_f(s)$ is applied to the compensatory error-correcting feedback loop including error processing and equalizing element Y_E and measurement filter W_M with injected measurement noise N(s) added to response M(s). A constrained time-optimal program (Task 3) for rapid response (RR) maneuvers if error E is greater than threshold E_T is vested in element Y_{RR}. The summed control output C(s) from the three levels of guidance, viz., compensatory, pursuit, and programmed rapid response, is applied to the controlled element at the right side of the diagram. The preferred controlled element for this application will be a decoupled velocity command-position hold flight control system-and-rotorcraft.

When each vector consists of only one component, the system error relationships reduce to the following conventional transfer functions

$$e(s) = \frac{\left[W_r\left(1 - Y_d \frac{\partial d}{\partial m}\right) - W_m Y_c Y_p\right] r(s) - \left(1 - Y_d \frac{\partial d}{\partial m}\right) W_m n(s) - W_m Y_d d(s)}{\Delta(s)}$$

and the system response relationships become

$$m(s) = \frac{\left(W_r Y_e + Y_p\right) Y_c r(s) - W_m Y_c Y_e n(s) + Y_d d(s)}{\Delta(s)}$$

Stabilization and bandwidth requirements vested in $\Delta(s)$ are subject to alteration by response-correlated disturbance gradients $\partial d/\partial m$. Characteristic singularities of $\Delta(s)$ are given by the roots of

$$\Delta(s) = \left\{1 + W_m Y_c Y_e - Y_d \frac{\partial d}{\partial m}\right\} = 0$$

Processing delays τ_e (computer frame time, data skewness, algorithmic delays) in Y_e and higher frequency lags represented by effective delay τ_c in controlled element Y_c can be at least partially compensated for their effects on stability by lead compensation (or prediction) in W_m and wholly compensated for their effects on response delay by command preview in W_r. [Approximate the measurement prediction filter by the ideal form: $W_m \doteq \exp(\tau_m s)$ and the command preview filter by the form: $W_r \doteq \exp(\tau_r s)$]

Response-correlated disturbance gradients $\partial d/\partial m$ act to increase or decrease the effective open-loop gain of the guidance and control system and may even be so great as to compromise stability in the presence of delay or to compromise bandwidth regardless of delay. For example, if

$$Y_c = \frac{K_c}{s\left(s + \frac{1}{T_c}\right)} \exp(-\tau_c s) \; ; \; Y_e = K_e \exp(-\tau_e s) \; ; \text{ and } Y_d = \frac{\Lambda}{s\left(s + \frac{1}{T_c}\right)} \; ;$$

the closed-loop guidance bandwidth and stability will be governed by the characteristic roots of

$$\Delta(s) = s\left(s + \frac{1}{T_c}\right) + K_c K_e \exp\left[\left(\tau_m - \tau_c - \tau_e\right)s\right] - \Lambda \frac{\partial d}{\partial m} = 0$$

Examples of the complex root loci without and with delay appear in Figs. 11a and 11b, respectively.

That part of the guidance error (e) associated with commands ($r_f = W_r r$) may be reduced by the ideal pursuit guidance adjustment

$$W_r\left(1 - Y_d \frac{\partial d}{\partial m}\right) - W_m Y_c Y_p = 0$$

$$\Delta(s) = s(s + 1/T_c) + K_c K_e \exp[(\tau_m - \tau_c - \tau_e)s] - \Lambda(\partial d/\partial m) = 0$$

A) Without Delay

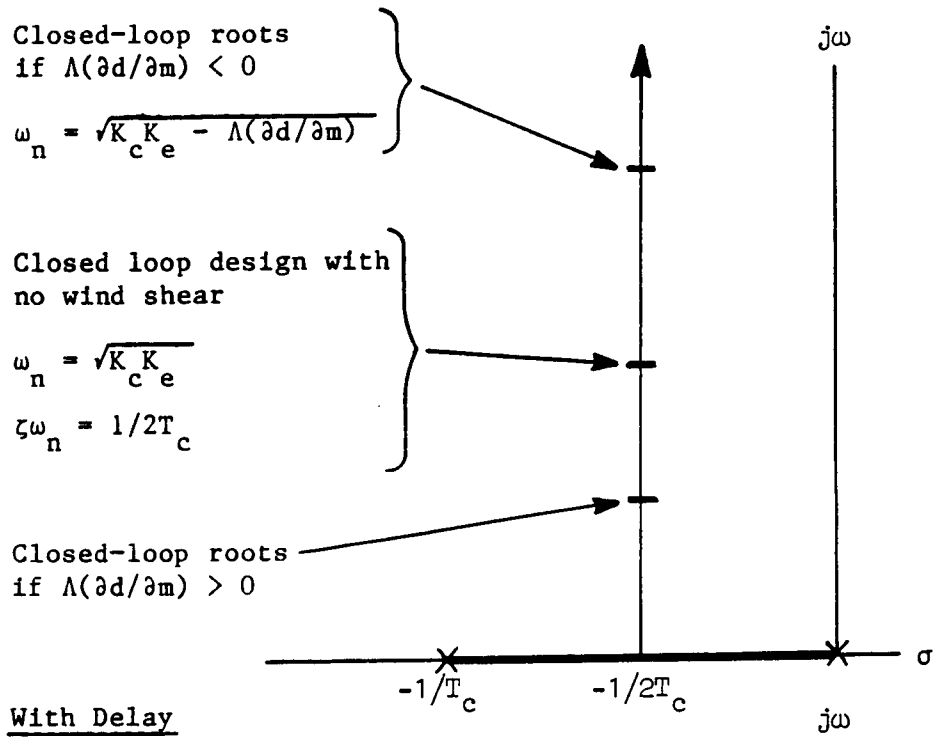

B) With Delay

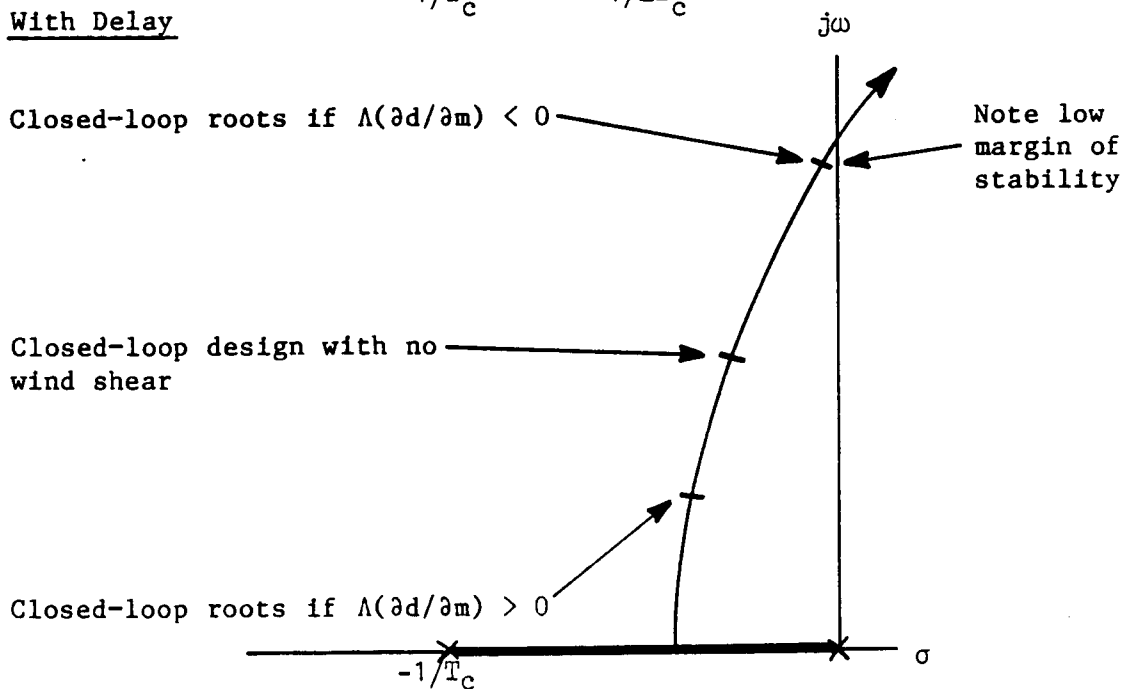

Figure 11. Effect of Response-Correlated Disturbance Gradients (e.g., Wind Shear) on Closed-Loop Roots for Height or Position Guidance and Control Without and With Processing Delay

which requires that

$$Y_p = \frac{W_r}{W_m Y_c}\left(1 - Y_d \frac{\partial d}{\partial m}\right)$$

If $\partial d/\partial m = 0$ or if $\partial d/\partial m$ is estimated by $\overline{\partial d/\partial r}$, Y_c by $\overline{Y}_c$, and Y_d by $\overline{Y}_d$ such an adjustment is quite practical for

$$\overline{Y}_c \triangleq \frac{K_c}{s\left(s + \frac{1}{T_c}\right)} \exp\left(-\tau_c s\right) \; ; \text{ and } \overline{Y}_d = \frac{\Lambda}{s\left(s + \frac{1}{T_c}\right)}$$

which represent the physical translation dynamics of the attitude stabilized, velocity-command-augmented, and decoupled rotorcraft. [Denominator factor $(s+1/T_c)$ in Y_c represents (augmented) heave damping (z-axis), sway damping (y-axis), surge damping (x-axis), or yaw damping.]

The practical adjustment requires a pursuit guidance command $C_p(s) = Y_p r(s)$, which becomes

$$C_p(s) = \frac{1}{K_c}\left[s\left(s + \frac{1}{T_c}\right) - \Lambda \frac{\partial d}{\partial r}\right] \frac{W_r}{W_m} r(s)$$

This pursuit adjustment requires a weighted linear combination of the acceleration, velocity, and displacement of the guidance course-and-profile command r(s). Commanded velocity must, however, be limited in accordance with propulsion constraints (e.g., rotor torque and speed limits, blade-stall limits, best-climb rationships between collective and cyclic blade pitch), attitude and heading limits near terrain and obstacles (e.g., main and tail rotor strikes), and control authority. Commanded acceleration must also be limited in accordance with rotor flapping limitations, attitude limits, and control rate limits.

The human operator will adopt at least the first two terms, $[sr(s)/K_cT_c]$ and $[s^2r(s)/K_c]$, of this pursuit adjustment in following a fluctuating curved course if sufficient preview of the course slope and curvature are available to the operator (Ref. 9). (The operator infers the first derivative of the course command from the visible slope and the second derivative, from the visible curvature.) In addition, the operator may adopt the third term, $(\Lambda/K_c)(\partial d/\partial r)$, if he has knowledge of or prior experience with the wind shear field on the particular course being flown. If incorporated in automatic guidance, this practical pursuit adjustment will be consistent with piloting technique, given sufficient visual preview and will therefore enhance pilot acceptance of automatic guidance in following NOE flight profiles with precision. A stored data base for the flight profile will provide a practical basis for this pursuit command in automatic guidance.

If this practical adjustment is incorporated, the transfer function for the part of the closed-loop system response to command r(s) becomes

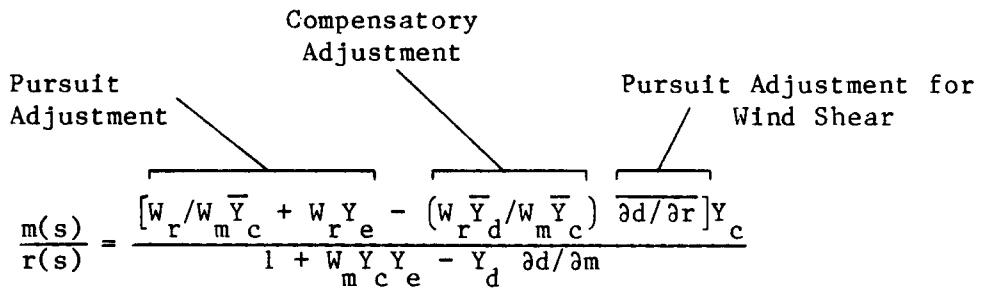

The effect of the response-correlated disturbance gradient $\partial d/\partial m$ can be approximately compensated by introducing estimated command-correlated disturbance gradient $\overline{\partial d/\partial r} \doteq \partial d/\partial m$ in the pursuit adjustment, and the overall command response fidelity and delay can be compensated by introducing preview in command filter $W_r = \exp(\tau_r s)$, where $\tau_r = \tau_m$, if $W_m = \exp(\tau_m s)$. A stored data base for the flight profile will provide a practical basis for this preview requirement, where the pursuit data preview distance will be $V_i\tau_r = V_i\tau_m$ in the direction of travel at inertial velocity V_i.

If the pursuit adjustment is not incorporated or fails, the transfer function for the part of the closed-loop system response to r(s) reduces to that for compensatory guidance:

$$\frac{m(s)}{r(s)} = \frac{W_r Y_e Y_c}{1 + W_m Y_c Y_e - Y_d \frac{\partial d}{\partial m}}$$

The compensatory response delay in $Y_e Y_c$, i.e., $\tau_e + \tau_c$, can now be approximately compensated by introducing a different preview in the command filter $W_r = \exp(\tau_r s)$, where $\tau_r = \tau_e + \tau_c$.

A significant degree of immunity from wind shears and turbulence is provided by automatic velocity-command-position-hold guidance and control systems (Ref. 10) whose low order effective controlled element forms are given in Table 6. With the exception of the forms for the hover turn, the forms for the other maneuvers are valid at translational velocities typical of NOE operations. The revised form for heading regulation when the translational velocity is not zero is given at the end of Table 6. Each of these controlled elements has the generic form

$$Y_c = \frac{K_c\left(s + \frac{1}{T_K}\right)e^{-\tau_k s}}{s\left[s^2 + 2\zeta\omega_n s + \omega_n^2\right]} \tag{7}$$

for a displacement response to a velocity command. If we postulate this generic form for Y_c, representing vehicle displacement response to a velocity command, the ideal pursuit feedforward guidance function $Y_p \doteq [\exp(\tau_m s)]/Y_c$ which operates on guidance command r, becomes

$$Y_p = \left[\exp\left(\tau_m + \tau_k\right)s\right] \frac{s\left[s^2 + 2\zeta\omega_n s + \omega_n^2\right]}{K_c\left(s + \frac{1}{T_K}\right)} \tag{8}$$

$$= \frac{\left[\exp\left(\tau_m + \tau_K\right)s\right]}{K_c} \left\{s^2 + \left(2\zeta\omega_n - \frac{1}{T_K}\right)s + \left[\omega_n^2 - \frac{2\zeta\omega_n}{T_K} + \frac{1}{T_K^2}\right] \frac{s}{\left(s + \frac{1}{T_K}\right)}\right\}$$

TABLE 6

PRACTICAL EXAMPLES OF LOW-ORDER EFFECTIVE CONTROLLED ELEMENTS FOR FIVE NOE MANEUVERS IN ROTORCRAFT

(Symbols are defined in Ref. 24)

MANEUVER	LOW-ORDER TRANSFER FUNCTION FOR EFFECTIVE CONTROLLED ELEMENT
Bob-Up or -Down (Vertical Unmask-Remask)	
With Constrained Attitude	$\left.\frac{h(s)}{\delta_c(s)}\right\|_{\substack{\theta \to \delta_B \\ \phi \to \delta_A}} = \frac{-Z_{\delta_c}}{s\left(s + 1/T_{\theta_2}\right)}\ ;\ \frac{1}{T_{\theta_2}} \doteq -Z_w$
With Vertical Velocity Command-Height Hold as in Section III, Fig. 32	$\frac{h(s)}{\dot{h}_c(s)} \doteq \frac{-Z_{\delta_c} K_{I_h} K^{\bullet}_{h_c}\left(s + 1/K^{\bullet}_{h_c}\right)}{s\left(s - Z_{\delta_c} K_{I_h} T^{\bullet}_h\right)\left(s + 1/T^{\bullet}_h\right)}$, if $\frac{1}{T^{\bullet}_h} \doteq \frac{1}{T_{\theta_2}}$
Hover Turn	
With Constrained Attitude	$\left.\frac{\psi(s)}{\delta_p(s)}\right\|_{\substack{\theta \to \delta_B \\ \phi \to \delta_A}} \doteq \frac{N'_{\delta_p}\left(s - Y_v + \frac{Y_{\delta_p}}{N'_{\delta_p}} N'_v\right)}{s\left(s - N'_r\right)\left(s - Y_v\right)} \doteq \frac{N'_{\delta_p}}{s\left(s - N'_r\right)}$
With Rate Command-Heading Hold as in Section III, Fig. 33	$\frac{\psi(s)}{\dot{\psi}_c(s)} \doteq \frac{N_{\delta_p} K_{I_\psi} K^{\bullet}_{\psi_c}\left(s + 1/K^{\bullet}_{\psi_c}\right)}{s\left(s + N_{\delta_p} K_{I_\psi} T^{\bullet}_{\psi}\right)\left(s + 1/T^{\bullet}_{\psi}\right)}$, if $\frac{1}{T^{\bullet}_{\psi}} \doteq -N'_r$

TABLE 6 (CONTINUED)

MANEUVER	LOW-ORDER TRANSFER FUNCTION FOR EFFECTIVE CONTROLLED ELEMENT
Dash-Quickstop (Accel/Decel)	
With Constrained Roll Attitude and and Heading	$\left.\frac{x(s)}{\theta_c(s)}\right\|_{\substack{\theta,q \to \delta_B \\ \phi \to \delta_A \\ \psi \to \delta_p}} \doteq \frac{K_\theta X_{\delta_B}\left[s^2 - M_q s - \frac{g}{X_{\delta_B}} M_{\delta_B}\right] e^{-\tau_r s}}{s\left(s + 1/T'_{\theta_1}\right)\left[s^2 + \left(K_q M_{\delta_B} - M_q\right)s + K_\theta M_{\delta_B}\right]}$ τ_r represents an effective rotor delay $\doteq \frac{-ge^{-\tau'_\theta s}}{s\left(s + 1/T'_\theta\right)}$, if $s^2 \ll K_\theta M_{\delta_B}$; where $0 < 1/T'_{\theta_1} < -X_u$
With Velocity Command-Position Hold as in Section III, Fig. 32	$\frac{x(s)}{\dot{x}_c(s)} \doteq \frac{-gK_{I_x}\left(K_{\dot{x}_c} s + 1\right)e^{-\tau''_\theta s}}{s\left[s^2 + \left(1/T'_{\theta_1} - gK_{I_x} T_{\dot{x}}\right)s - gK_{I_x}\right]}$ where $\frac{1}{K_{\dot{x}_c}} = \sqrt{-gK_{I_x}}$; $T_{\dot{x}} \sqrt{-gK_{I_x}} > \sqrt{2}$ $\doteq \frac{\sqrt{-gK_{I_x}}\, e^{-\tau''_\theta s}}{s\left(s + \sqrt{-gK_{I_x}}\right)}$ if $\frac{1}{K_{\dot{x}_c}} \doteq \sqrt{-gK_{I_x}}$; $T_{\dot{x}} \sqrt{-gK_{I_x}} \doteq 2$

TABLE 6 (Continued)

MANEUVER	LOW-ORDER TRANSFER FUNCTION FOR EFFECTIVE CONTROLLED ELEMENT
Sidestep	
With Constrained Heading and Pitch Attitude	$\left.\frac{y(s)}{\phi_c(s)}\right\|_{\substack{\phi,p \to \delta_a \\ \theta \to \delta_B \\ \psi \to \delta_p}} \doteq \frac{K_\phi Y_{\delta_A}\left[s^2 - L_p s + g/Y_{\delta_A} L_{\delta_A}\right]e^{-\tau_r s}}{s\left(s + 1/T'_{\phi_1}\right)\left[s^2 + \left(K_p L_{\delta_A} - L_p\right)s + K_\phi L_{\delta_A}\right]}$ τ_r represents an effective rotor delay
	$\left.\frac{y(s)}{\phi_c(s)}\right\|_{\substack{\psi \to \delta_p \\ \phi \to \delta_a \\ \theta \to \delta_B}} \doteq \frac{g e^{-\tau'_\phi s}}{s\left(s + 1/T'_{\phi_1}\right)}$, if $s^2 \ll K_\phi L_{\delta_A}$; where $0 < 1/T'_{\phi_1} < -Y_v$
With Velocity Command-Position Hold as in Section III, Fig. 33	$\frac{y(s)}{\dot{y}_c(s)} \doteq \frac{gK_{I_y}\left(K_{\dot{y}_c} + 1\right)e^{-\tau''_\phi s}}{s\left[s^2 + \left(1/T'_{\phi_1} + gK_{I_y} T_{\dot{y}}\right)s + gK_{I_y}\right]}$ where $\frac{1}{K_{\dot{y}_c}} \doteq \sqrt{gK_{I_y}}$; $T_{\dot{y}} \sqrt{gK_{I_y}} > \sqrt{2}$ $\doteq \frac{\sqrt{gK_{I_y}}\, e^{-\tau''_\phi s}}{s\left(s + \sqrt{gK_{I_y}}\right)}$ if $\frac{1}{K_{\dot{y}_c}} \doteq \sqrt{gK_{I_y}}$; $T_{\dot{y}} \sqrt{gK_{I_y}} \doteq 2$

TABLE 6 (Concluded)

MANEUVER	LOW-ORDER TRANSFER FUNCTION FOR EFFECTIVE CONTROLLED ELEMENT
Heading Regulation While Traveling Forward ($U_o > 0$) or Rearward ($U_o < 0$) With Constrained Attitude	$\frac{\psi(s)}{\delta_p(s)} = \frac{N'_{\delta_p}\left(s - Y_v + \frac{Y_{\delta_p}}{N'_{\delta_p}} N'_v\right)}{s\left[s^2 - (N'_r + Y_v)s + U_o N'_v + N'_r Y_v\right]}$ where U_o is inertial velocity

This ideal guidance adjustment requires prediction over time interval $\tau_m + \tau_k$ of weighted commanded acceleration s^2r/K_c, weighted commanded velocity

$$\frac{\left(2\zeta\omega_n - \frac{1}{T_K}\right)}{K_c} sr$$

and weighted washed-out commanded displacement

$$\frac{1}{K_c}\left[\omega_n^2 - \frac{2\zeta\omega_n}{T_K} + \frac{1}{T_K^2}\right] \frac{sr}{\left(s + \frac{1}{T_K}\right)}$$

If the damping ratio $\zeta = 1$, the weighted washed-out commanded displacement becomes

$$\frac{1}{K_c}\left(\omega_n - \frac{1}{T_K}\right)^2 \frac{sr}{\left(s + \frac{1}{T_K}\right)}$$

and the weighted commanded velocity becomes

$$\frac{\left(2\omega_n - \frac{1}{T_K}\right)}{K_c} sr$$

If, in addition to $\zeta = 1$, $\omega_n = 1/T_K$ (the best design practice regardless of damping ratio), the controlled element in Eq. 7 reduces to

$$Y_c = \frac{K_c e^{-\tau_k s}}{s\left(s + \frac{1}{T_k}\right)} \qquad (9)$$

for displacement response to a velocity command. The weighted washed-out commanded displacement is unnecessary (except for improving immunity to wind shear), and the weighted commanded velocity reduces to sr/K_cT_K. The

required weighted linear combination of predicted commanded acceleration, velocity (and washed-out displacement, if needed) can be readily derived with a low noise level from the stored flight profile format discussed previously as part of Task I (Refs. 4 and 5), since continuous functions with continuous first and second derivatives are used to represent the required flight profile(s), whereas, the discrete maneuver logic in Fig. 9 will be invoked to cope with unexpected obstacle avoidance.

B. FIELD OF COVERAGE FOR SENSED TERRAIN AND OBSTACLES

Other characteristics of the stored and sensed data which affect processing and must be defined are field of coverage, resolution or quantization, and update rate. Relationships among horizontal field of coverage, preview interval, velocity, and bank angle in both coordinated level turns and uncoordinated level side stepping have been examined in Ref. 11. Two relationships are plotted in Fig. 12 for a fixed preview interval of 3 sec. The upper figure is for coordinated level turning; the lower, for level side stepping. Both relationships are practically the same for half-fields of coverage less than 30 deg. A 60-deg half-field angle (120 deg field of coverage), on the other hand, will accommodate banking at 60 deg for a 2 g level turn at 50 kt and a 2 g level side step at 30 kt. Reference 11, however, suggests that 60-deg bank angles are rarely used in NOE operations. Instead, reduced bank angles are likely at lower speeds--possibly in accord with the "hypothesized NOE boundary" in the lower graph in Fig. 11 corresponding to the 60-deg half-field angle down to a bank angle of 20 deg. The cut-off at a bank angle of 20 deg represents a typical hovering bank angle requirement based on needs for wind-proofing and has nothing to do with horizontal field of data coverage. Larger bank angles than those implied by the "hypothesized NOE boundary" are probably not used, because the resulting horizontal accelerations cannot be effectively managed in close quarters. Thus, if the preview interval is 3 sec, it is likely that a horizontal field of data coverage greater than 120 deg can seldom be used in NOE operations involving forward flight. (Clearly, if automatic side stepping maneuvers

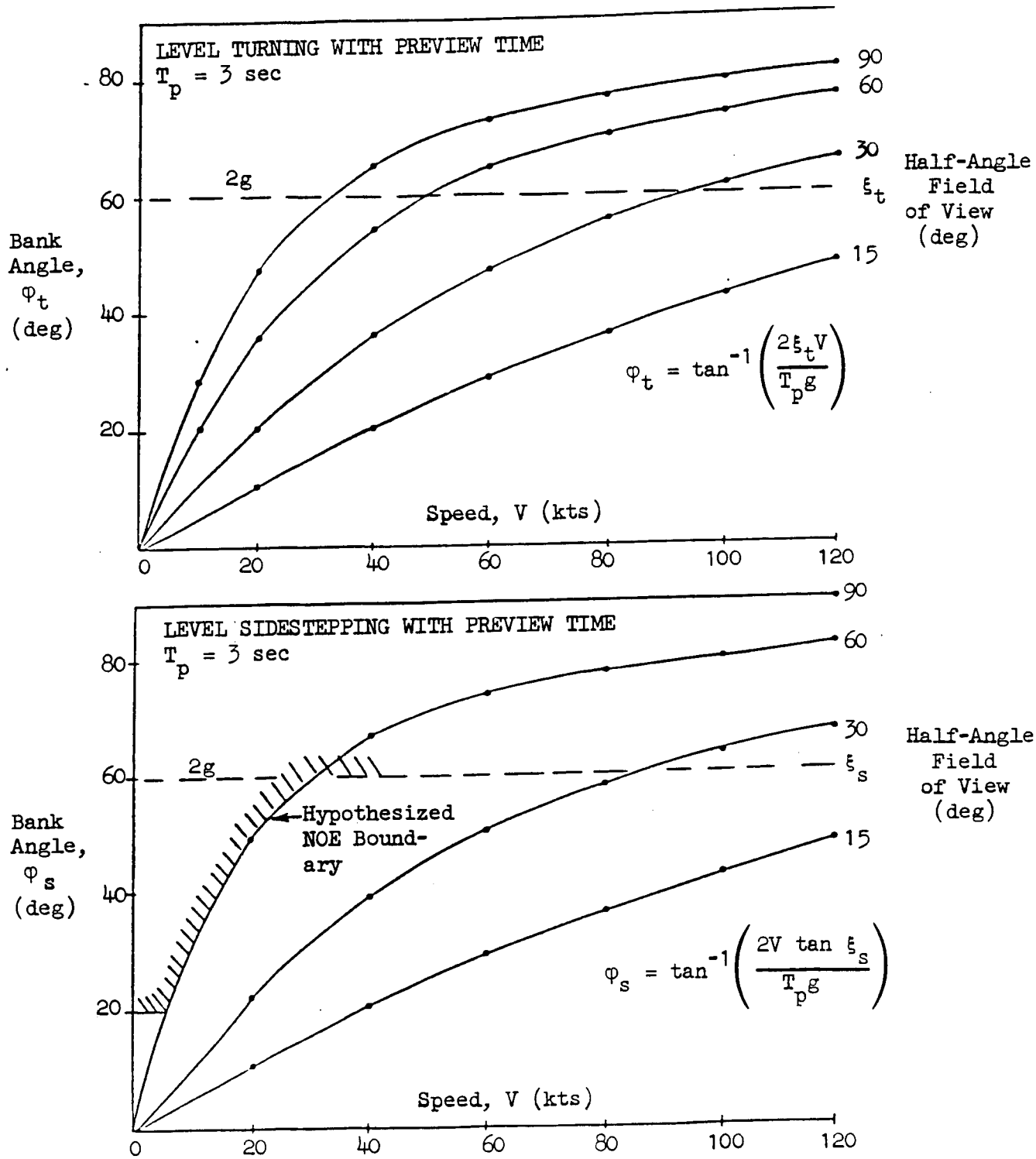

Figure 12. Required Half-Angle Field of View as Functions of Allowable Level Turn and Sidestepping Bank Angle Versus Speed for a Preview Time of 3 Seconds

from hovering flight are required in exceptional instances, the defined half-field angle of coverage must exceed 90 deg by virtue of a side-looking sensor.)

Conversion of the horizontal half-field angle of coverage to the half-width distance, W, of terrain coverage gives $2W = T_p^2 g \tan \phi_s$. If the preview interval is 3 sec and the bank angle does not exceed 60 deg, the required half-width of terrain coverage to initiate the sidestepping maneuver in forward flight will be 76 m (251 ft) left or right of the preselected course at commencement of the maneuver. This half-width, W, is only about 5 percent of the Army standard 1500 m, listed in Part 1 of Table 1 for navigating left or right of the preselected course in terrain flight training. Thus there is ample margin in this example for continuing the maneuver or increasing the preview interval while retaining the 60 deg bank angle limitation.

C. EFFECT OF GUIDANCE AND CONTROL DELAY ON HEIGHT CONTROL WHILE TRAVELING IN "DOLPHIN" MANEUVERS

The first and most fundamental effect of discrete data processing to be considered in a digital guidance and control system is time delay, the cause of which may be vested in a particular algorithm, in the overall computational frame time or update rate, in data acquisition by a scanning and sampling sensor, or in data conversion from digital to analog form and vice versa.

Another form of delay is peculiar to data multiplexing. When data is acquired sequentially, converted from analog to digital form and vice versa, or when discrete data is passed between computers serially, some data will inevitably be "skewed" (i.e., delayed) in time with respect to other data. Thus there will be a progressive "staleness" associated with skewed samples of data; sometimes the effect of this staleness can be significant, although it is usually much less than the processing delay discussed above.

A third form of delay is called computation "frame slip" and is associated with data transfer between two or more independent asynchronous digital processors. Each independent processor may have a slightly different frame time from the others in the network. For example, one processor might have a frame time of 40 ms and another, 39 ms. Every so often (about every 1.56 sec), the faster processor will have executed one more full frame than the slower processor. This constitutes the effect called "frame slip," which can produce undesirable transport delay jump phenomena in the dynamic system.

Effects of data sampling, quantization, and control roughness or intersample ripple in digital guidance and flight control systems can be treated by means of an innovative direct digital design procedure evolved and applied in Refs. 12 through 20.

The effects of delays involving processing and higher frequency rotorcraft lags on the closed-loop bandwidth of height control while traveling in "dolphin" maneuvers will be first illustrated using numerical characteristics of the UH-1H helicopter at 20 kts, sea level, 8000 lbs weight, with a mid-c.g. location. Subsequently, it will be possible to normalize the time delay, the required open-loop compensation, and the closed-loop bandwidth of height regulation in terms of the heave damping and collective control effectiveness of the rotorcraft and thus to provide more general design requirements to counteract the effects of time delay in any similar rotorcraft height, heading, or position guidance and control system.

Figure 13 presents a complex root locus showing the effects of varying the height-to-collective control high-frequency gain $K_h^{\bullet}$ with a constant lead compensation $1/T_{L_h}$ = 1.13 rad/sec and a constant value of the airspeed-to-pitch attitude control high frequency gain K_u = -0.01 rad θ_c/ft/sec designed to provide a closed-loop speed regulation subsidence $1/T_{\theta_1}'$ = 0.3 rad/sec. There is no delay represented in the results of Fig. 12. Closed-loop characteristics are shown for two values of $K_h^{\bullet}$, 0.0245 and 0.0923 in/ft/sec. The closed-loop damping ratio in both cases is at least 0.7; the larger closed-loop undamped natural frequency is 1 rad/sec, and the smaller is about half of the larger value.

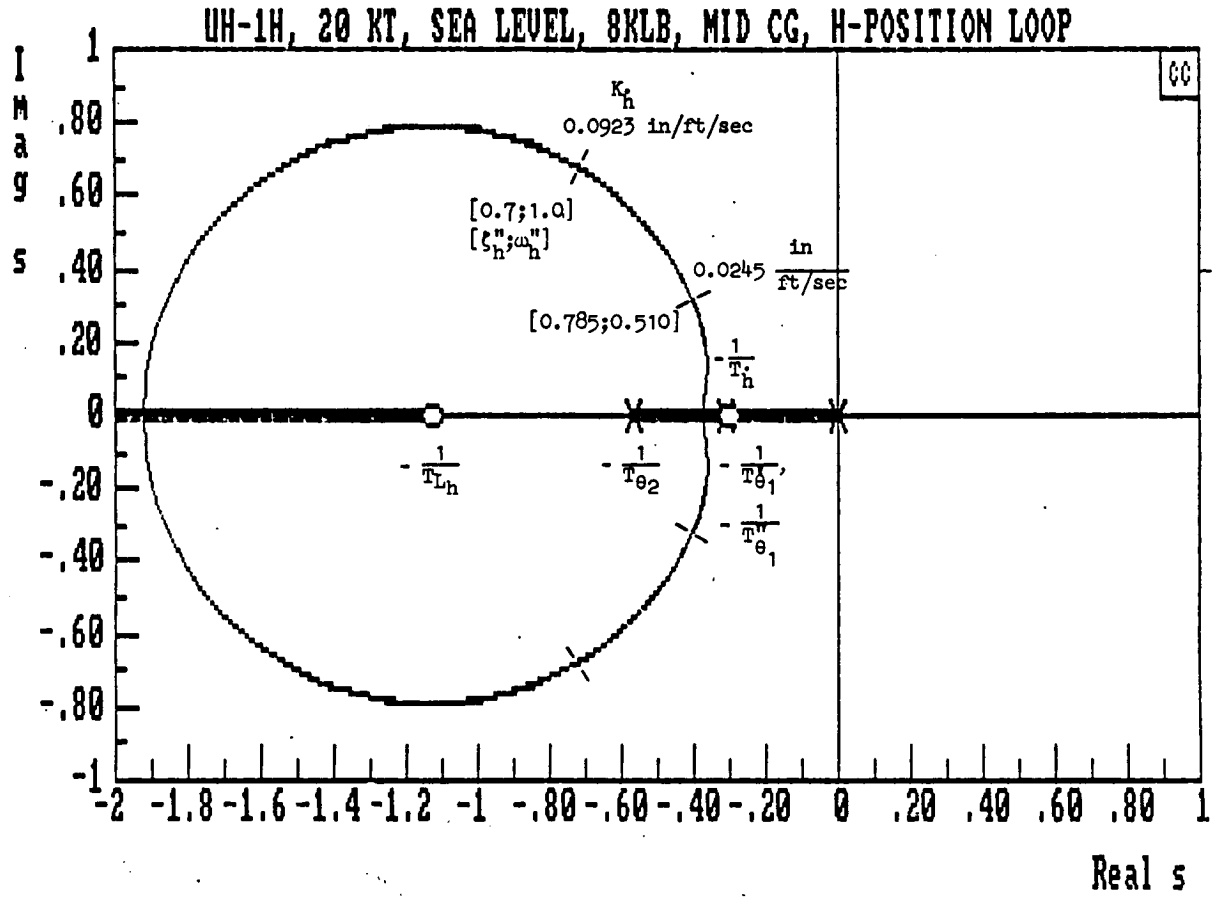

Complex Root Locus of Characteristic Values for the Closed-Loop Determinant $\Delta''(s)$ of Height and Airspeed Control Equations While Traveling

$$\Delta''(s) = s(s + 1/T_{\theta_1})(s + 1/T_{\theta_2}) - Z_{\delta_c} K_h^{\cdot}(s + 1/T_{L_h}) \cdot$$

$$\cdot \{s - X_u + (X_{\delta_c}/-Z_{\delta_c})Z_u + K_u[X_\alpha - g + (X_{\delta_c}/-Z_{\delta_c})Z_\alpha]\}$$
$$\underbrace{\qquad\qquad\qquad\qquad (s + 1/T_h^{\cdot})}$$

$$+ K_u(X_\alpha - g)s[s - Z_w + (X_w Z_\alpha/X_\alpha - g)]$$
$$\underbrace{\doteq 1/T_{\theta_1}'} \qquad \underbrace{\doteq (s + 1/T_{\theta_2})}$$

Figure 13. Effects of Varying Height-to-Collective Control Loop Gain $K_h^{\cdot}$ with Lead Compensation $1/T_{L_h} = 1.13$ rad/sec and Airspeed-to-Pitch Attitude Control Gain $K_u \doteq -0.01$ rad θ_c/ft/sec

The effect of a 0.5 sec time delay involving processing and higher-frequency lags is shown in Fig. 14. The lead compensation remains at 1.13 rad/sec, and the airspeed-to-pitch attitude control loop gain remains the same at -0.01 rad θ_c/ft/sec. At the lower value of $K_h^\bullet$ = 0.0245 in/ft/sec, the closed-loop characteristics remain approximately the same. The damping ratio is 0.69, and the closed-loop undamped natural frequency is 0.54 rad/sec. At the higher value of gain required to achieve an undamped natural frequency of 1 rad/sec, the damping ratio is reduced to 0.54 with 0.5 sec time delay. Figure 15 shows that the closed-loop damping ratio can be restored to about 0.7 with an 0.5 sec delay by reducing the frequency of the lead compensation, $1/T_{L_h}$, to a value of 0.89 rad/sec and reducing the high frequency gain $K_h^\bullet$ to a value of 0.074 in/ft/sec.

The effect of a 1.0 sec time delay involving processing and higher-frequency lags is shown in Fig. 16. The lead compensation is back at 1.13 rad/sec, and the airspeed-to-pitch attitude control loop gain remains the same at -0.01 rad θ_c/ft/sec. If $K_h^\bullet$ = 0.0205 in/ft/sec, the closed-loop damping ratio is 0.61, and the closed-loop undamped natural frequency is 0.50 rad/sec--only slightly degraded with respect to corresponding values for 0.5 sec delay. At the higher value of gain ($K_h^\bullet$ = 0.0693 in/ft/sec) required to achieve an undamped natural frequency of 1 rad/sec, however, the damping ratio is reduced to 0.19 with 1.0 sec time delay. Figure 17 shows that the closed-loop damping ratio can be restored to about 0.7 with a 1.0 sec delay by reducing the frequency of the lead compensation, $1/T_{L_h}$, to a value corresponding to the heave damping $1/T_{\theta_2}$.

All of the foregoing effects and requirements for compensation of time delay in height guidance and control systems can be summarized as shown in Fig. 18 for a specific value of heave damping $1/T_{\theta_2}$ = 0.567 rad/sec in the illustrative rotorcraft flight condition. Plotted in Fig. 18 as functions of the time delay, τ_h, are the lead compensation frequency, $1/T_{L_h}$, and the high frequency gain, $-K_h^\bullet Z_{\delta_c}$ required to provide two closed-loop characteristic height control frequency bandwidths expressed in terms of

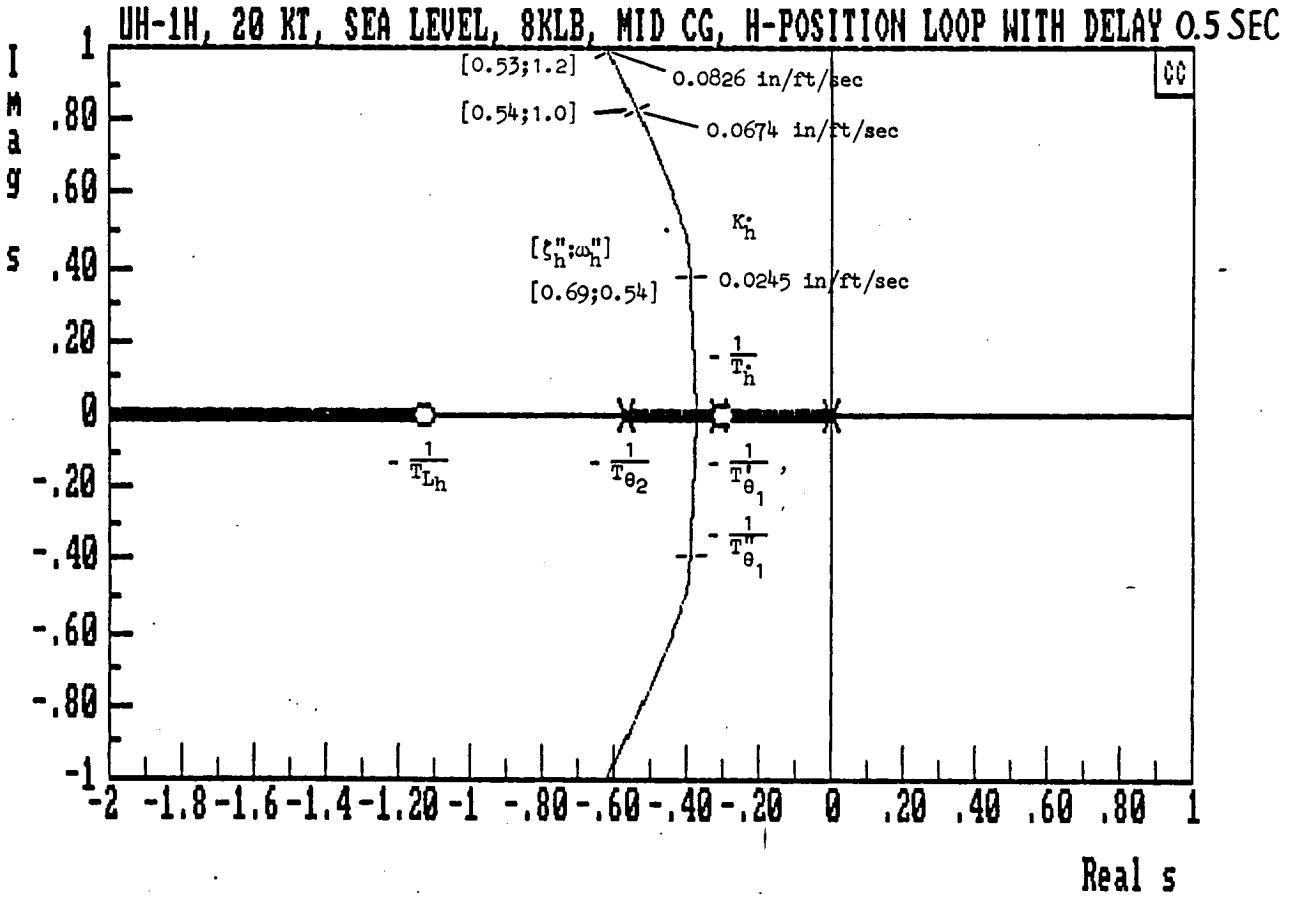

Complex Root Locus of Characteristic Values for the Closed-Loop Determinant $\Delta''(s)$ of Height and Airspeed Control Equations While Traveling

$$\Delta''(s) = s(s + 1/T_{\theta_1})(s + 1/T_{\theta_2}) - Z_{\delta_c} K_h^* [\exp(-0.58)](s + 1/T_{L_h}) \cdot$$

$$\cdot \{s - X_u + (X_{\delta_c}/-Z_{\delta_c}) Z_u + K_u[X_\alpha - g + (X_{\delta_c}/-Z_{\delta_c}) Z_\alpha]\}$$

$$\underbrace{\qquad\qquad\qquad\qquad (s + 1/T_h^*)}$$

$$+ K_u(X_\alpha - g)s[s - Z_w + (X_w Z_\alpha / X_\alpha - g)]$$

$$\underbrace{\doteq 1/T'_{\theta_1}} \qquad \underbrace{\doteq (s + 1/T_{\theta_2})}$$

Figure 14. Effects of 0.5 sec Time Delay and Varying Height-to-Collective Control Loop Gain K_h^* with Lead Compensation $1/T_{L_h} = 1.13$ rad/sec and Airspeed-to-Pitch Attitude Control Gain $K_u \doteq -0.01$ rad θ_c/ft/sec

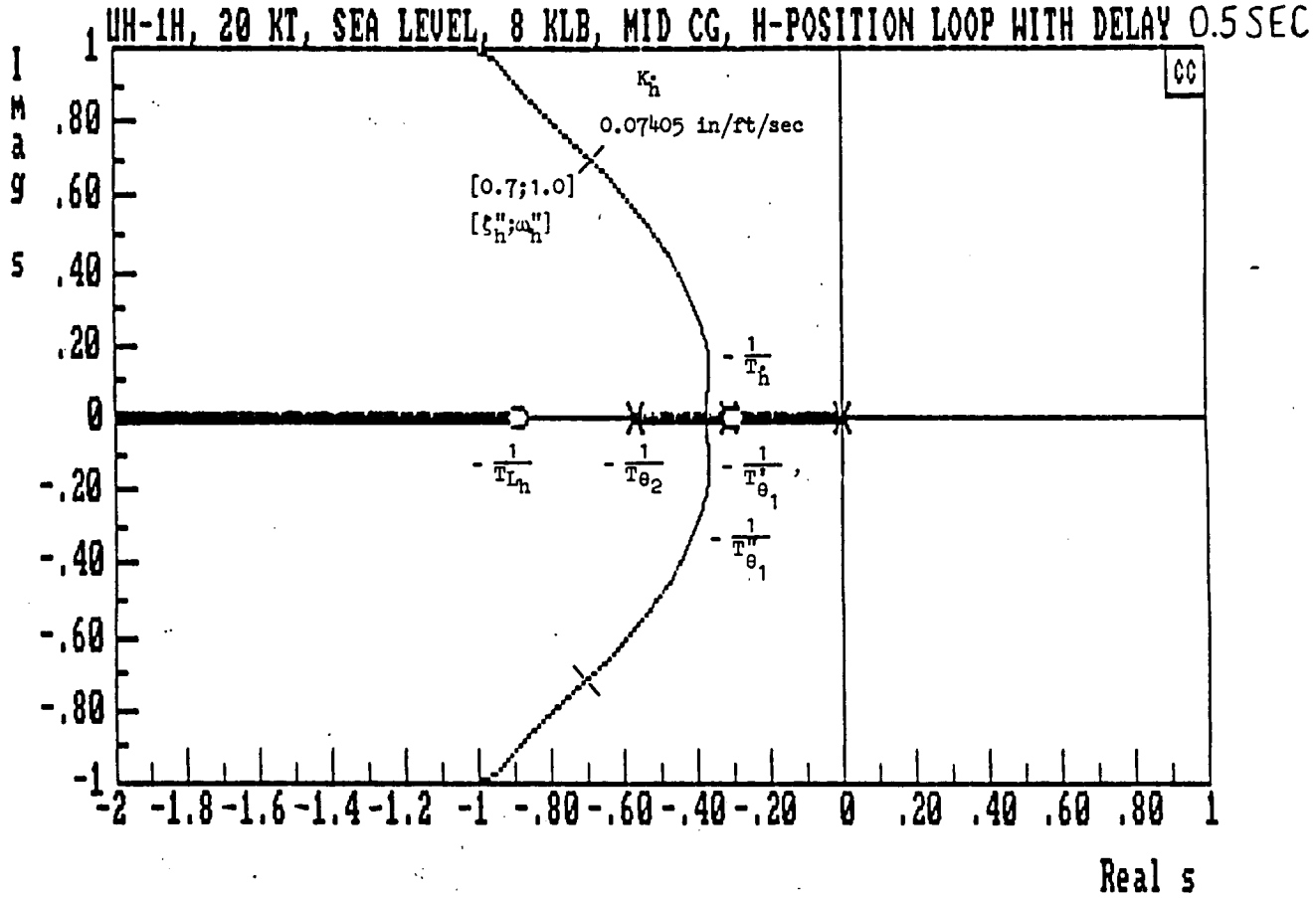

Complex Root Locus of Characteristic Values for the Closed-Loop Determinant $\Delta''(s)$ of Height and Airspeed Control Equations While Traveling

$$\Delta''(s) = s(s + 1/T_{\theta_1})(s + 1/T_{\theta_2}) - Z_{\delta_c} K_h^* [\exp(-0.58)](s + 1/T_{L_h}) \cdot$$

$$\cdot \underbrace{\{s - X_u + (X_{\delta_c}/-Z_{\delta_c})Z_u + K_u[X_\alpha - g + (X_{\delta_c}/-Z_{\delta_c})Z_\alpha]\}}_{(s + 1/T_h^*)}$$

$$+ K_u(X_\alpha - g)s[s - Z_w + (X_w Z_\alpha / X_\alpha - g)]$$

$$\underbrace{\hat{=} 1/T'_{\theta_1}}_{} \qquad \underbrace{\hat{=} (s + 1/T_{\theta_2})}_{}$$

Figure 15. Effects of 0.5 sec Time Delay and Varying Height-to-Collective Control Loop Gain K_h^* with Lead Compensation $1/T_{L_h} = 0.89$ rad/sec and Airspeed-to-Pitch Attitude Control Gain $K_u = -0.01$ rad θ_c/ft/sec

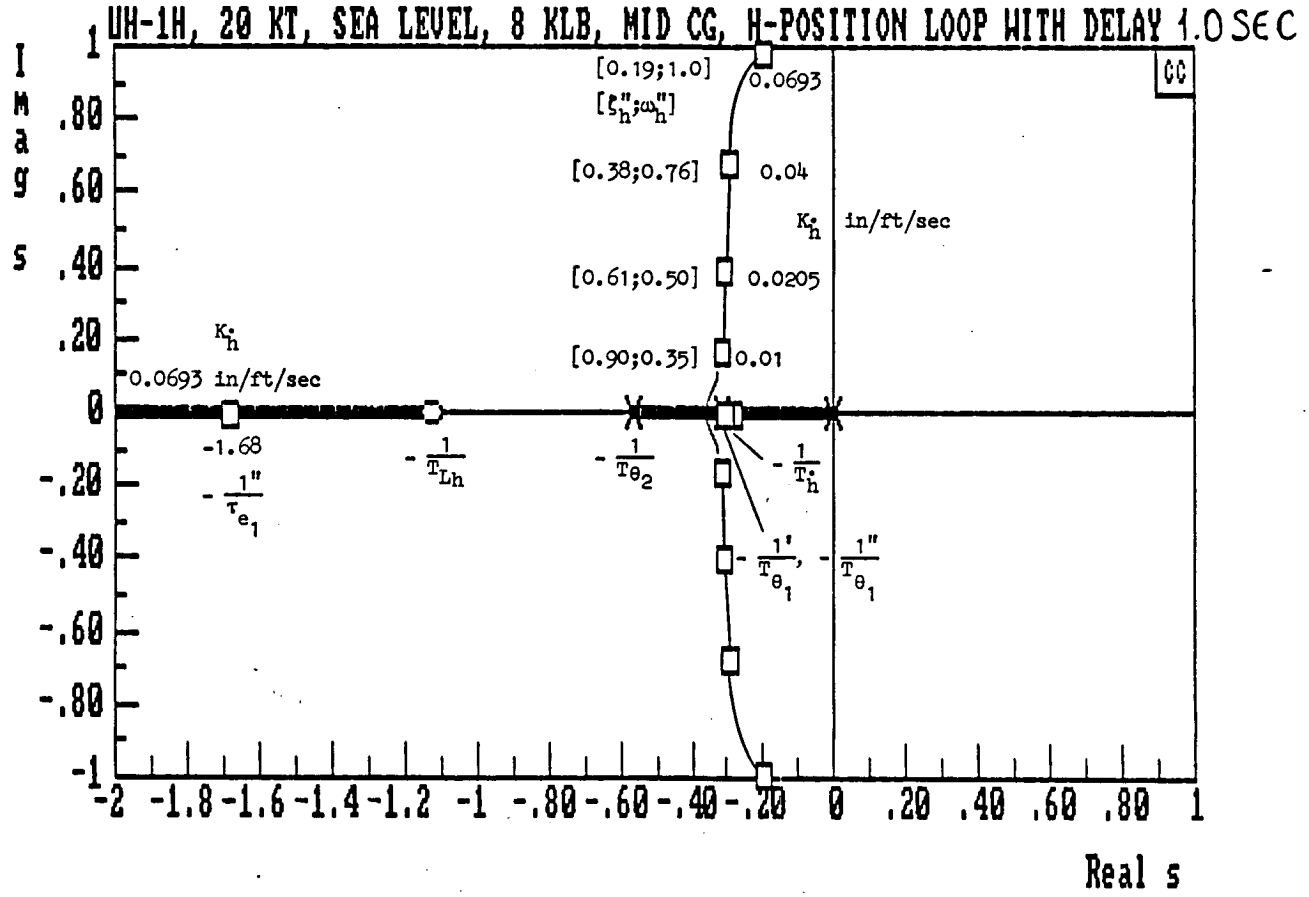

Complex Root Locus of Characteristic Values for the Closed-Loop Determinant Δ"(s) of Height and Airspeed Control Equations While Traveling

$$\Delta''(s) = s(s + 1/T_{\theta_1})(s + 1/T_{\theta_2}) - Z_{\delta_c} K_h^{\bullet}[\exp(-1.0s)](s + 1/T_{L_h}) \cdot$$

$$\cdot \{s - X_u + (X_{\delta_c}/-Z_{\delta_c})Z_u + K_u[X_\alpha - g + (X_{\delta_c}/-Z_{\delta_c})Z_\alpha]\}$$

$$\underbrace{\qquad\qquad\qquad\qquad\qquad\qquad (s + 1/T_h^{\bullet})\qquad\qquad\qquad\qquad\qquad\qquad}$$

$$+ K_u(X_\alpha - g)s[s - Z_w + (X_w Z_\alpha / X_\alpha - g)]$$

$$\underbrace{\doteq 1/T'_{\theta_1}} \qquad \underbrace{\doteq (s + 1/T_{\theta_2})}$$

Figure 16. Effects of 1.0 sec Time Delay and Varying Height-to-Collective Control Loop Gain $K_h^{\bullet}$ with Lead Compensation $1/T_{L_h}$ = 1.13 rad/sec and Airspeed-to-Pitch Attitude Control Gain K_u = -0.01 rad θ_c/ft/sec

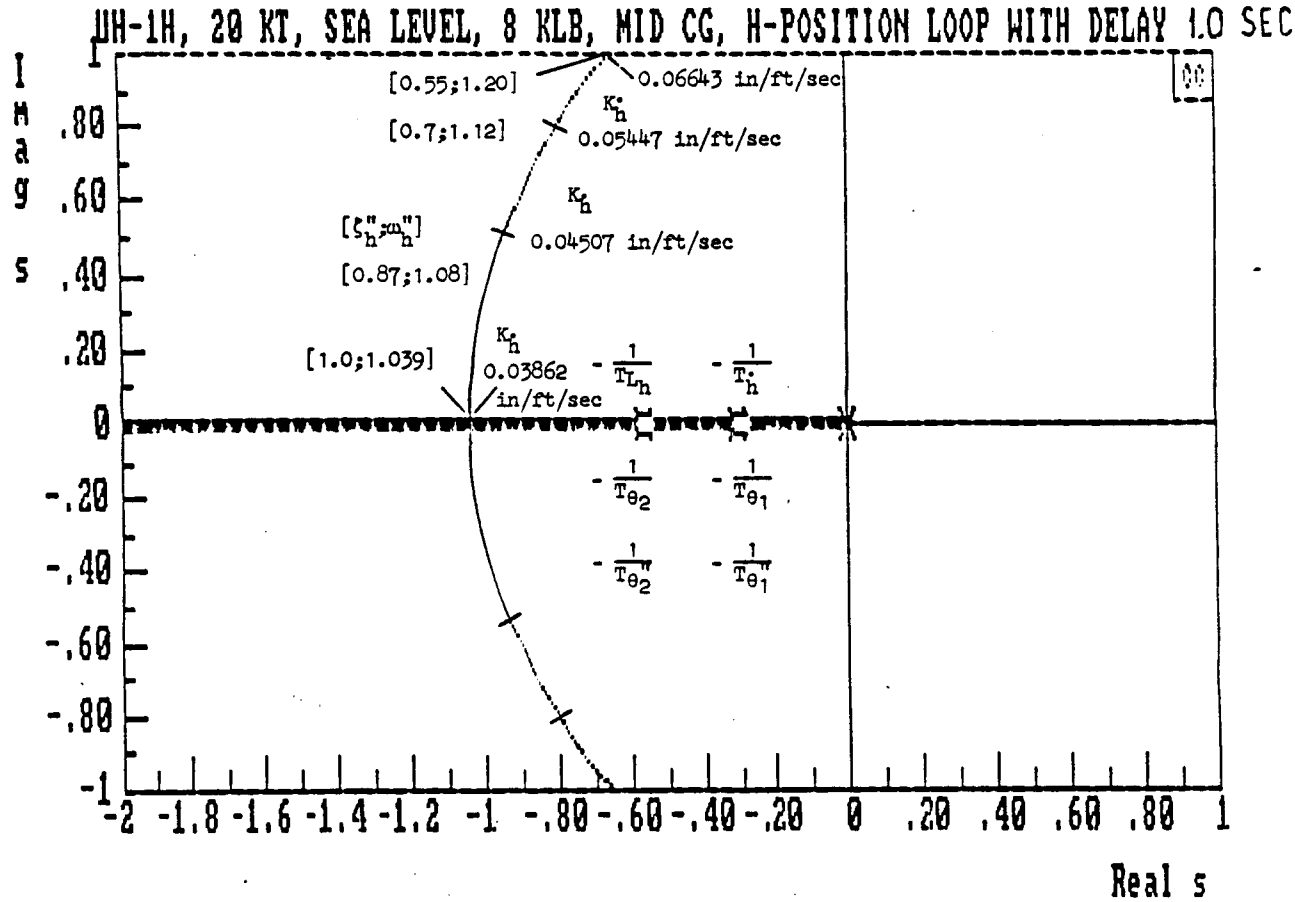

Complex Root Locus of Characteristic Values for the Closed-Loop Determinant $\Delta''(s)$ of Height and Airspeed Control Equations While Traveling

$$\Delta''(s) = s(s + 1/T_{\theta_1})(s + 1/T_{\theta_2}) - Z_{\delta_c} K_h^{\cdot}[\exp(-1.0s)](s + 1/T_{L_h}) \cdot$$

$$\cdot \{s - X_u + (X_{\delta_c}/-Z_{\delta_c})Z_u + K_u[X_\alpha - g + (X_{\delta_c}/-Z_{\delta_c})Z_\alpha]\}$$

$$\underbrace{\qquad\qquad\qquad\qquad\qquad\qquad}_{(s + 1/T_h^{\cdot})}$$

$$+ K_u(X_\alpha - g)s[s - Z_w + (X_w Z_\alpha/X_\alpha - g)]$$

$$\underbrace{\doteq 1/T_{\theta_1}'}_{} \qquad \underbrace{\doteq (s + 1/T_{\theta_2})}_{}$$

Figure 17. Effects of 1.0 sec Time Delay and Varying Height-to-Collective Control Loop Gain $K_h^{\cdot}$ with Lead Compensation $1/T_{L_h} = 0.56$ rad/sec and Airspeed-to-Pitch Attitude Control Gain $K_u = -0.01$ rad θ_c/ft/sec

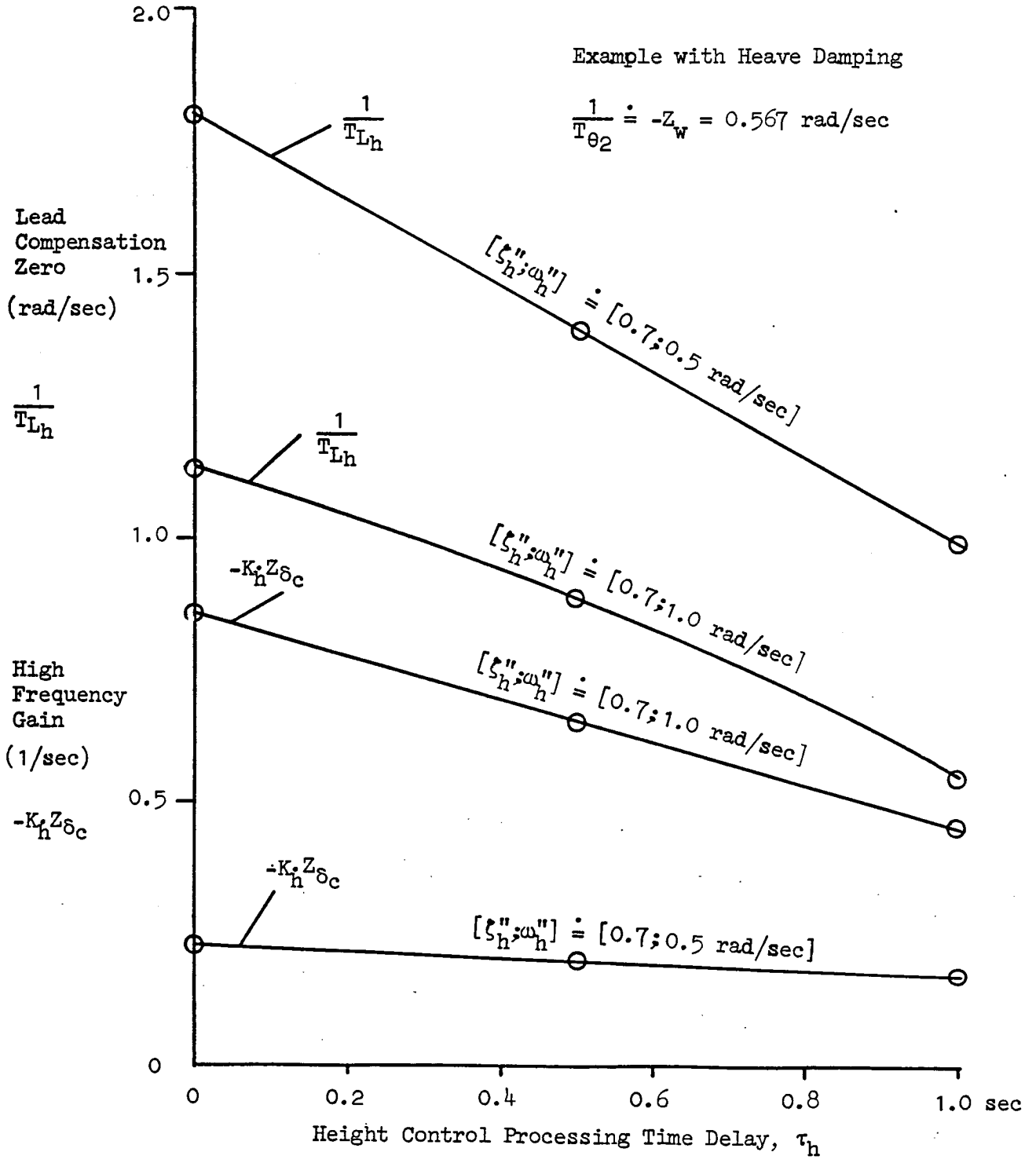

Figure 18. Compensatory Height Control High Frequency Gain, and Lead Equalization Requirements as Functions of Processing Time Delay, Heave Damping, and Collective Control Effectiveness Required to Maintain Constant Closed-Loop Characteristics

Example with Heave Damping $1/T_{\theta_2} = 0.567$ rad/sec

ω_h'', the undamped natural frequency of height regulation, each with closed-loop damping ratio, $\zeta_h'' \doteq 0.7$. The two sets of closed-loop characteristics are represented by $[\zeta_h''; \omega_h''] \doteq [0.7;0.5]$ and $[0.7;1.0]$. The effects on these closed-loop characteristics of a headwind-to-tailwind shear with decreasing altitude will be discussed subsequently. Because all of the results in Fig. 18 scale with heave damping, $1/T_{\theta_2}$, of the rotorcraft, they can be normalized by $1/T_{\theta_2}$ and presented in the more general form depicted in Fig. 19 for the purpose of design.

Furthermore, since the form of the rotorcraft's controlled element in hover turns is analogous to that for height control, as shown in Table 6, the same results, with appropriately revised notation, can be applied to hover turn guidance and control with delay as shown in Fig. 20 (normalized) and Fig. 21 (specialized for effective yaw damping, $-N'_{r_{eff}} = 0.567$ rad/sec).

C. EFFECTS OF HORIZONTAL WIND SHEAR GRADIENT ON HEIGHT CONTROL WHILE TRAVELING IN "DOLPHIN" MANEUVERS

The effects on closed-loop characteristics of a headwind-to-tailwind shear gradient, $\partial u_g/\partial h < 0$, with decreasing altitude are shown in Figs. 22 through 25. The airspeed regulation subsidence, $\omega_u'' = 0.3$ rad/sec, corresponds with a velocity-to-pitch attitude control high frequency gain $K_u = -0.01$ rad θ_c/ft/sec in both sets of figures. Figures 22 and 23 represent the effects with the lower value of height-to-collective control high-frequency gain $K_h^{\bullet} = 0.0245$ in/ft/sec (damping ratio 0.785; undamped natural frequency 0.51 rad/sec); Figs. 24 and 25 represent the effects for a higher value of $K_h^{\bullet} = 0.0923$ in/ft/sec (damping ratio 0.7; undamped natural frequency 1.0 rad/sec). The shear gradient $\partial u_g/\partial h$ varies along the complex and real root loci in Figs. 22 and 24 as shown in the corresponding logarithmic Sigma-Bode root loci, Figs. 23 and 25. The results in Figs. 22 through 25 are further expanded in Appendix B to represent the effects of two other values of airspeed regulation subsidence, $\omega_u'' = 0.15$ and 0.6 rad/sec, corresponding respectively to two other values of velocity-to-pitch attitude control high-frequency gain,

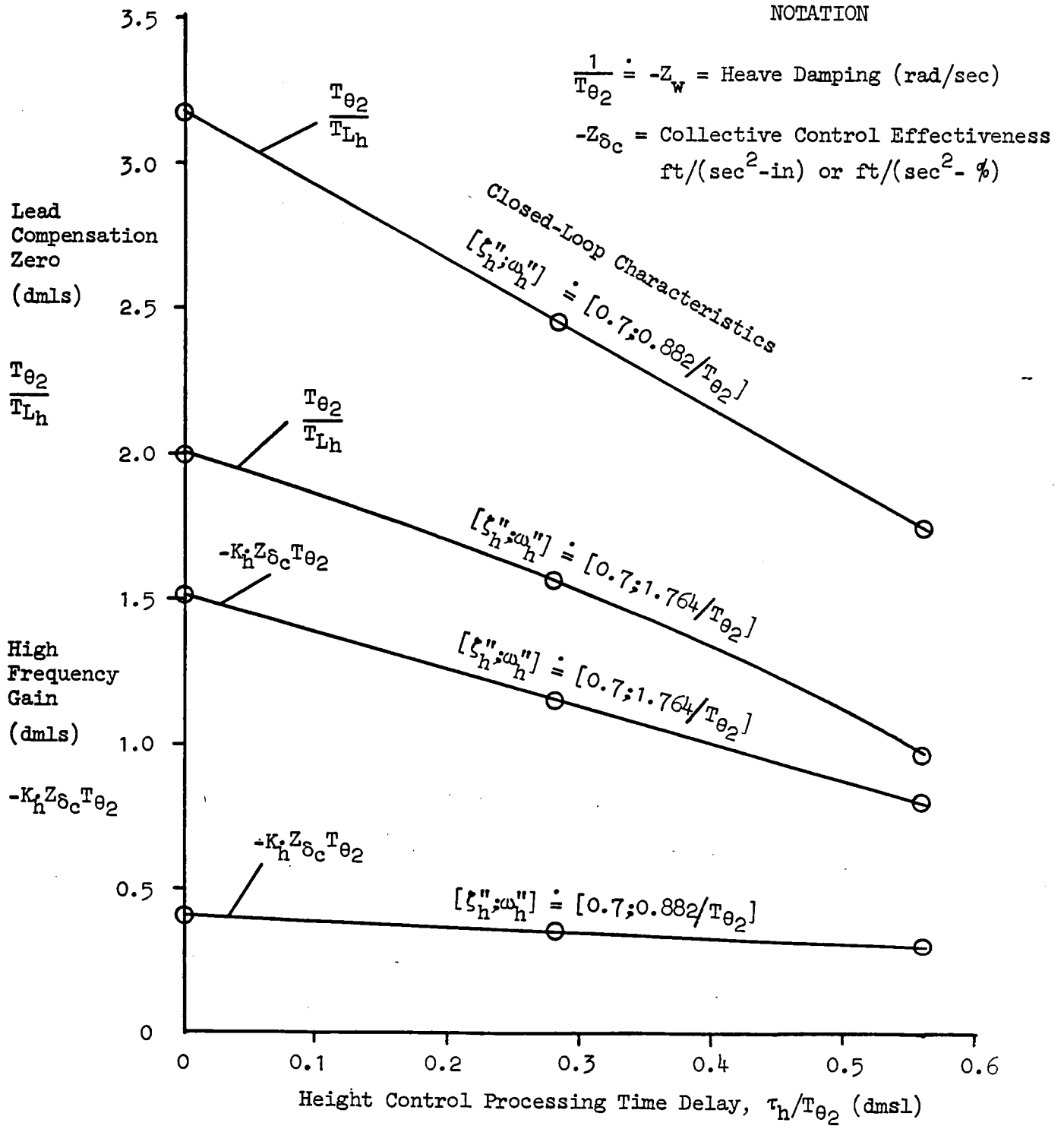

Figure 19. Compensatory Height Control High Frequency Gain, and Lead Equalization Requirements as Functions of Processing Time Delay, Heave Damping, and Collective Control Effectiveness Required to Maintain Constant Closed-Loop Characteristics

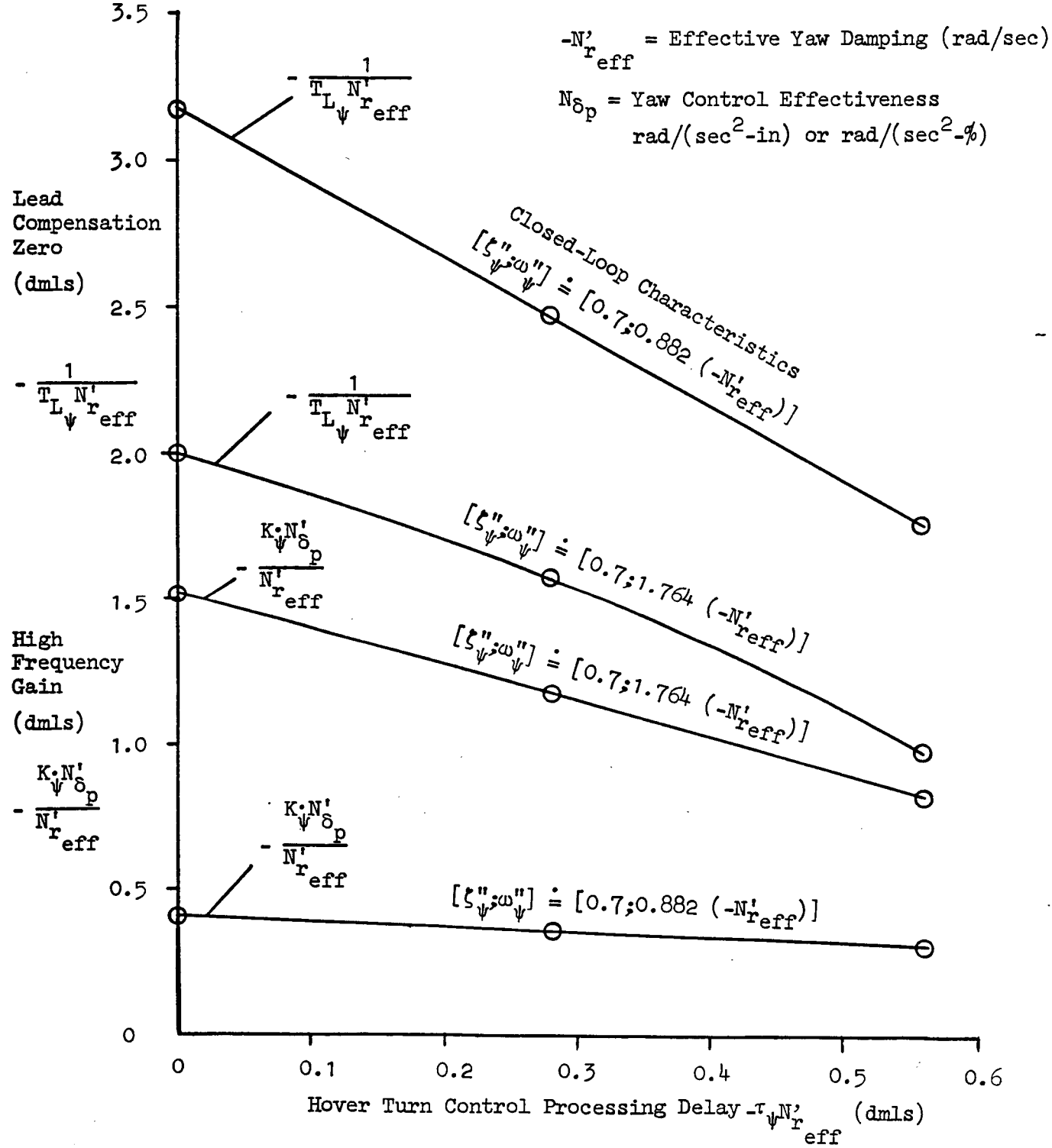

Figure 20. Compensatory Hover Turn Control High Frequency Gain and Lead Equalization Requirements as Functions of Processing Time Delay, Yaw Damping, and Yaw Control Effectiveness Required to Maintain Constant Closed-Loop Characteristics

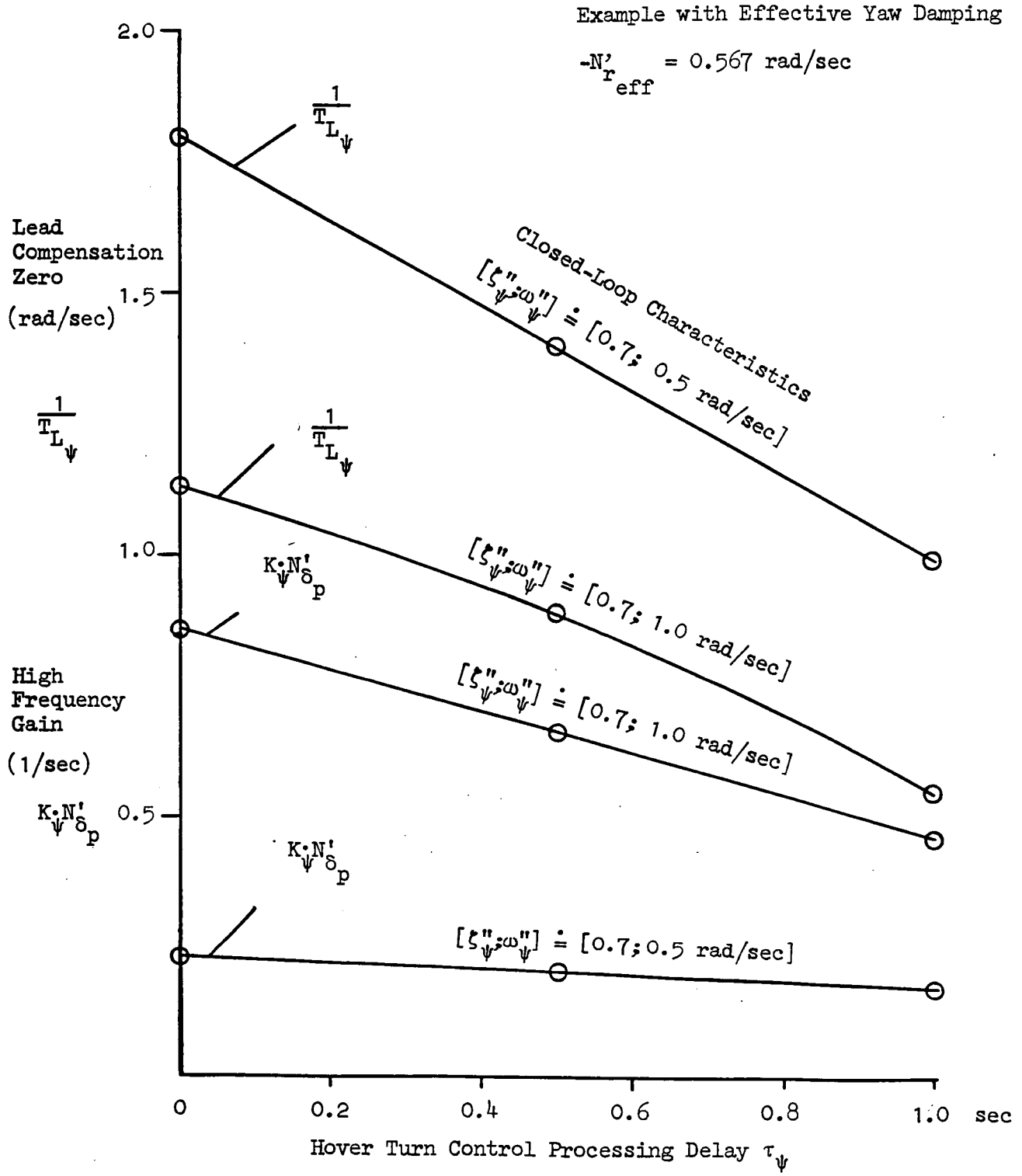

Figure 21. Compensatory Hover Turn Control High Frequency Gain and Lead Equalization Requirements as Functions of Processing Time Delay, Yaw Damping, and Yaw Control Effectiveness Required to Maintain Constant Closed-Loop Characteristics

Example with Effective Yaw Damping $-N'_{r_{eff}}$ = 0.567 rad/sec

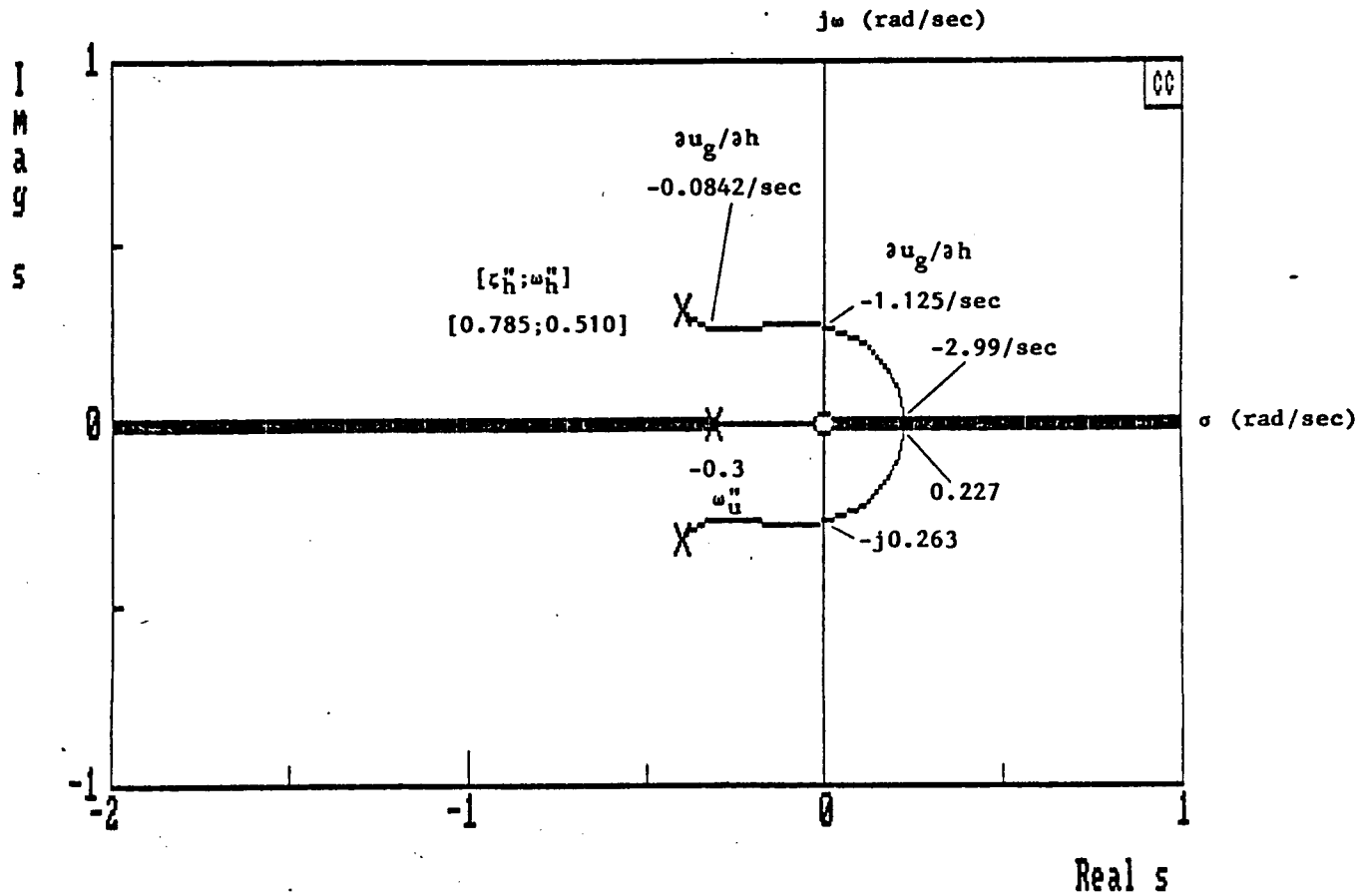

Complex Root Locus of Characteristic Values for the Closed-Loop Determinant Δ"(s) of Height and Airspeed Control Equations While Traveling

$$\Delta''(s) \doteq \left[s + 1/T_{\theta_1} + K_u(X_\alpha - g)\right]$$
$$\left[s^2 + (1/T_{\theta_2} - Z_{\delta_c} K_h^{\bullet})s - (Z_{\delta_c} K_h^{\bullet}/T_{L_h})\right]$$
$$- (\partial u_g/\partial h)s(Z_u - K_u Z_\alpha)$$

$\partial u_g/\partial h < 0$, UH-1H at 20 kt, Sea Level, 8000 lb, mid cg, $K_h^{\bullet} = 0.0245$ in/ft/sec

$-Z_w = 0.567$ rad/sec $-Z_{\delta_c} = 9.29$ ft/sec^2-in $-X_u = 0.005$ rad/sec

$-Z_u = 0.198$ rad/sec $(X_\alpha - g)K_u \doteq \omega_{c_u}'' \doteq 0.3$ rad/sec $1/T_{L_h} = 1.13$ rad/sec

Figure 22. Complex Root Locus of Characteristic Values for the Closed-Loop Determinant of Height and Airspeed Control Equations While Traveling Showing Effects of Headwind-to-Tailwind Shear with Decreasing Altitude

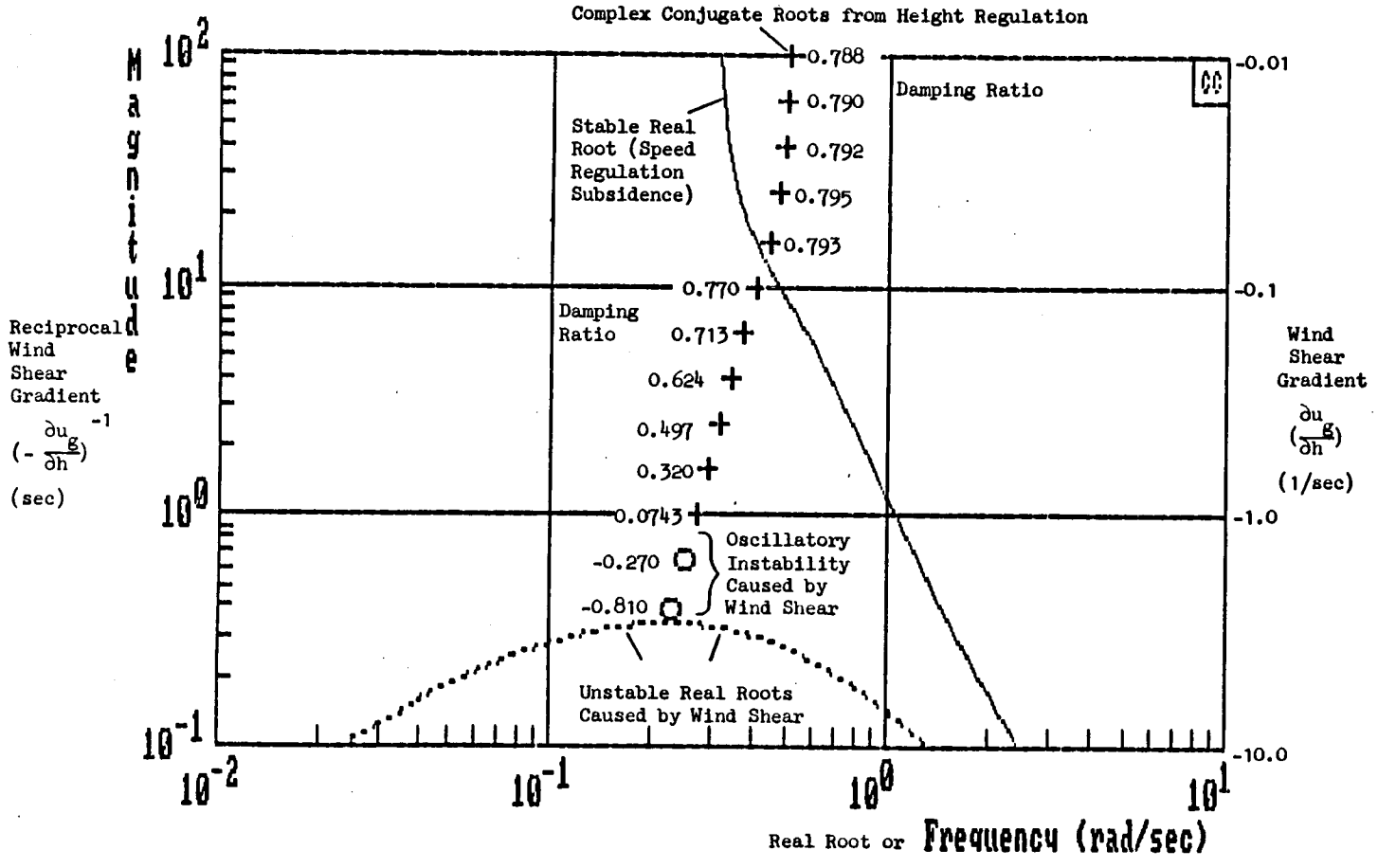

$\partial u_g/\partial h < 0$, UH-1H at 20 kt, Sea Level, 8000 lbs, mid c.g. Height Regulation Loop Closed Via Collective Control with Lead Compensation $1/T_{L_h}$ = 1.13 rad/sec Without Delay and High Frequency Gain $K_h^{\bullet}$ = 0.0245 in/ft/sec. Speed Regulation Loop Closed Via Pitch Attitude Without Delay and High Frequency Gain K_u = -0.01 rad θ_c/ft/sec

Figure 23. Sigma-Bode Root Locus of Characteristic Values for the Closed-Loop Determinant $\Delta''(s)$ of Height and Airspeed Control Equations While Traveling

$$\Delta''(s) \doteq \left[s + 1/T_{\theta_1} + K_u(X_\alpha - g)\right]\left[s^2 + \left(1/T_{\theta_2} - Z_{\delta_c}K_h^{\bullet}\right)s - \left(Z_{\delta_c}K_h^{\bullet}/T_{L_h}\right)\right] - \left(\partial u_g/\partial h\right)s\left(Z_u - K_u Z_\alpha\right)$$

Showing Effect of Headwind-to-Tailwind Shear with Decreasing Altitude

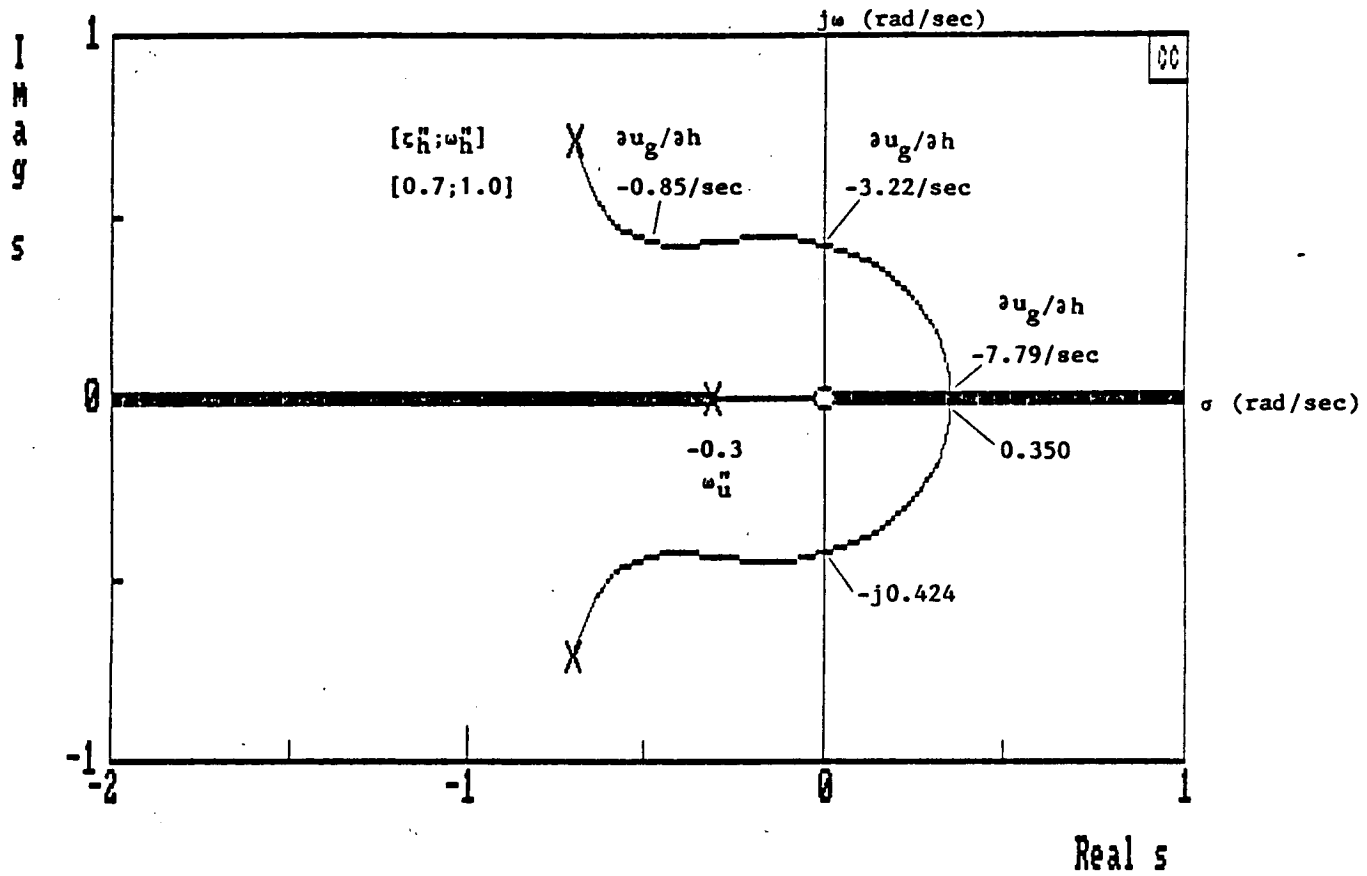

Complex Root Locus of Characteristic Values for the Closed-Loop Determinant Δ"(s) of Height and Airspeed Control Equations While Traveling

$$\Delta''(s) \doteq \left[s + 1/T_{\theta_1} + K_u(X_\alpha - g)\right]$$
$$\left[s^2 + \left(1/T_{\theta_2} - Z_{\delta_c} K_h^{\cdot}\right)s - \left(Z_{\delta_c} K_h^{\cdot}/T_{L_h}\right)\right]$$
$$- \left(\partial u_g/\partial h\right)s\left(Z_u - K_u Z_\alpha\right)$$

$\partial u_g/\partial h < 0$, UH-1H at 20 kt, Sea Level, 8000 lb, mid cg, $K_h^{\cdot} = 0.0923$ in/ft/sec

$-Z_w = 0.567$ rad/sec $-Z_{\delta_c} = 9.29$ ft/sec^2-in $-X_u = 0.005$ rad/sec

$-Z_u = 0.198$ rad/sec $(X_\alpha - g)K_u \doteq \omega''_{c_u} \doteq 0.3$ rad/sec $1/T_{L_h} = 1.13$ rad/sec

Figure 24. Complex Root Locus of Characteristic Values for the Closed-Loop Determinant of Height and Airspeed Control Equations While Traveling Showing Effects of Headwind-to-Tailwind Shear with Decreasing Altitude

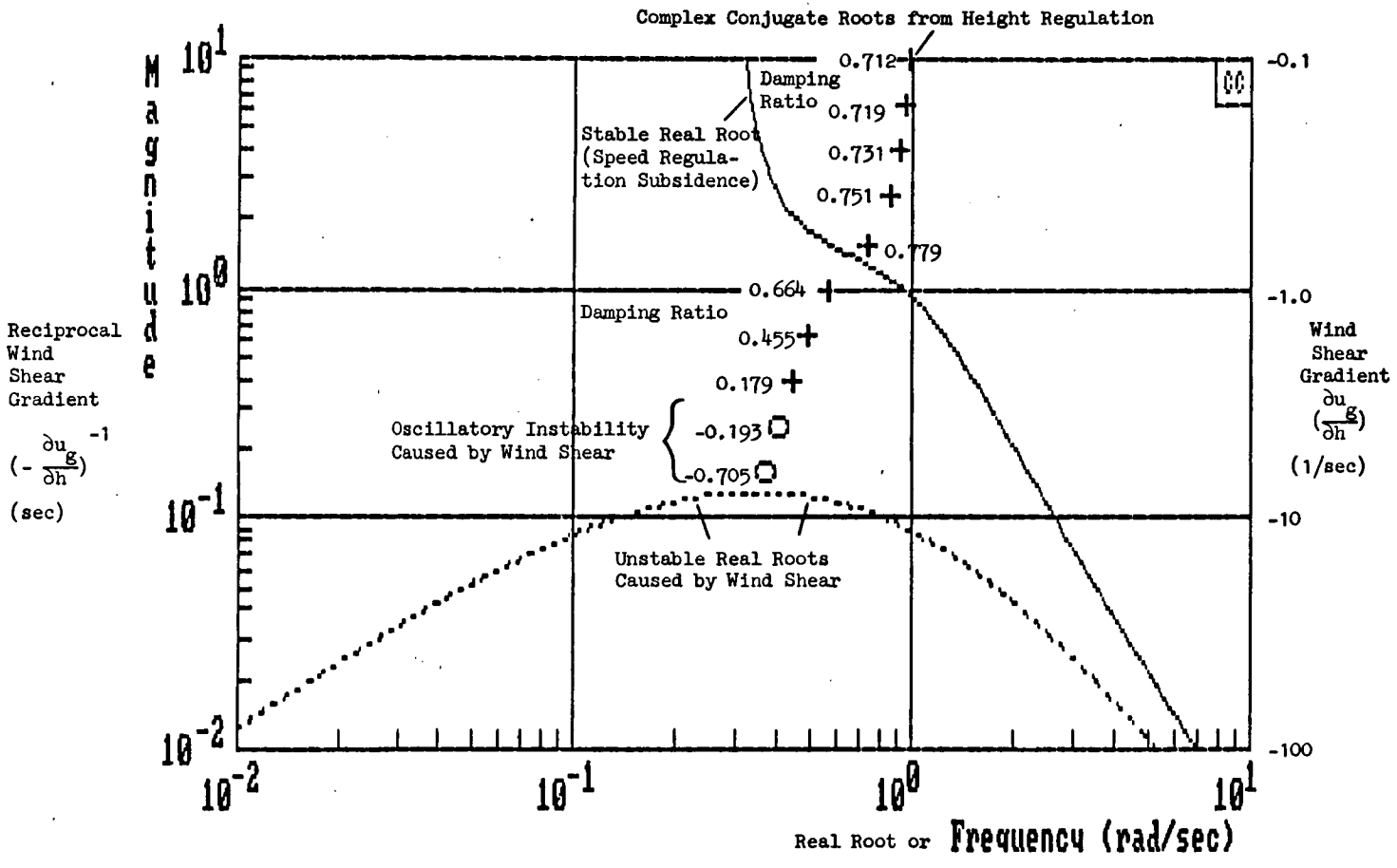

$\partial u_g/\partial h < 0$, UH-1H at 20 kt, Sea Level, 8000 lbs, mid c.g. Height Regulation Loop Closed Via Collective Control with Lead Compensation $1/T_{L_h}$ = 1.13 rad/sec Without Delay and High Frequency Gain $K_h^{\cdot}$ = 0.0923 in/ft/sec. Speed Regulation Loop Closed Via Pitch Attitude Without Delay and High Frequency Gain K_u = -0.01 rad θ_c/ft/sec

Figure 25. Sigma-Bode Root Locus of Characteristic Values for the Closed-Loop Determinant $\Delta''(s)$ of Height and Airspeed Control Equations While Traveling

$$\Delta''(s) \doteq \left[s + 1/T_{\theta_1} + K_u(X_\alpha - g)\right]\left[s^2 + (1/T_{\theta_2} - Z_{\delta_c} K_h^{\cdot})s - (Z_{\delta_c} K_h^{\cdot}/T_{L_h})\right] - (\partial u_g/\partial h)s(Z_u - K_u Z_\alpha)$$

Showing Effect of Headwind-to-Tailwind Shear with Decreasing Altitude

viz., K_u = -0.005 and -0.02 rad θ_c/ft/sec. Appendix D provides a discussion of airspeed regulation via pitch attitude control and of some of the issues affecting the choice of gain K_u.

Not surprisingly, the higher height control bandwidth in Figs. 24 and 25 provides a higher threshold of instability caused by the wind shear gradient. Although the height control bandwidth in Figs. 24 and 25 is only doubled with respect to that in Figs. 22 and 23, the wind shear gradient required to cause instability is between 2-1/2 and 3 times greater in Figs. 24 and 25, depending on the speed regulation subsidence.

The results from the six examples in Appendix B are summarized in Figs. 26 through 28.

The gradient of the headwind-to-tailwind shear, $\partial u_g/\partial h < 0$, is represented on the (inverted) ordinate, and the closed-loop speed subsidence ω_u'' (rad/sec) in the absence of wind shear is represented on the abscissa of Figs. 26 through 28. The closed-loop height control characteristics provide damping ratio ζ_h'' = 0.785 and undamped natural frequency ω_h'' = 0.51 in the absence of wind shear in Fig. 26 and ζ_h'' = 0.7, ω_h'' = 1.0 without wind shear in Fig. 27. Each figure shows a family of curves for the relative shear-induced damping ratio and the relative shear-induced undamped natural frequency (i.e., height control bandwidth) expressed as a percentage of the respective values without wind shear. The shear-induced limit of closed-loop stability is represented by the loci for ζ_h'' = 0. The higher degree of immunity from the compromising effects of the wind shear gradient provided by the higher height control bandwidth in Fig. 27 is readily apparent. Both Figs. 26 and 27 also demonstrate that a higher closed-loop speed subsidence (which provides tighter speed regulation) causes the compromised closed-loop height damping ratio to be more sensitive to the wind shear gradient than the compromised closed-loop height bandwidth; whereas, a lower closed-loop speed subsidence (which provides looser speed regulation) causes the compromised closed-loop height bandwidth to be more sensitive to the wind shear gradient than the compromised closed-loop height damping ratio. Thus an intermediate value of the closed-loop speed subsidence will provide a balanced compromise among the requirements for speed regulation and immunity from the effects of the wind shear on height regulation.

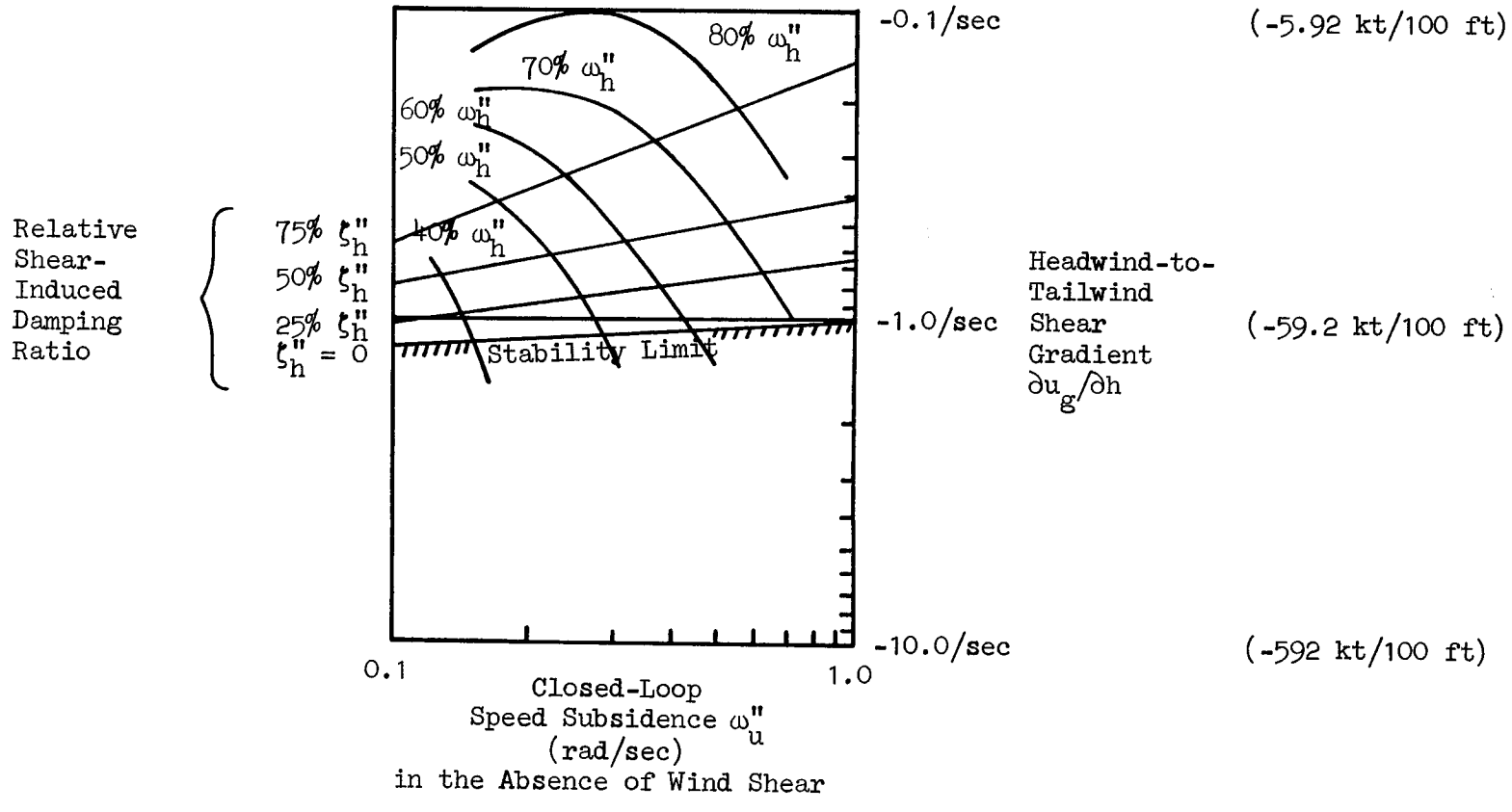

Figure 26. Relative Shear-Induced Closed-Loop Bandwidth and Damping Ratio for Height Control as a Function of Headwind-to-Tailwind Shear Gradient and Closed-Loop Speed Subsidence, if Closed-Loop Height Control Characteristics Provide $[\zeta_h''; \omega_h''] = [0.785; 0.51$ rad/sec) Without Wind Shear

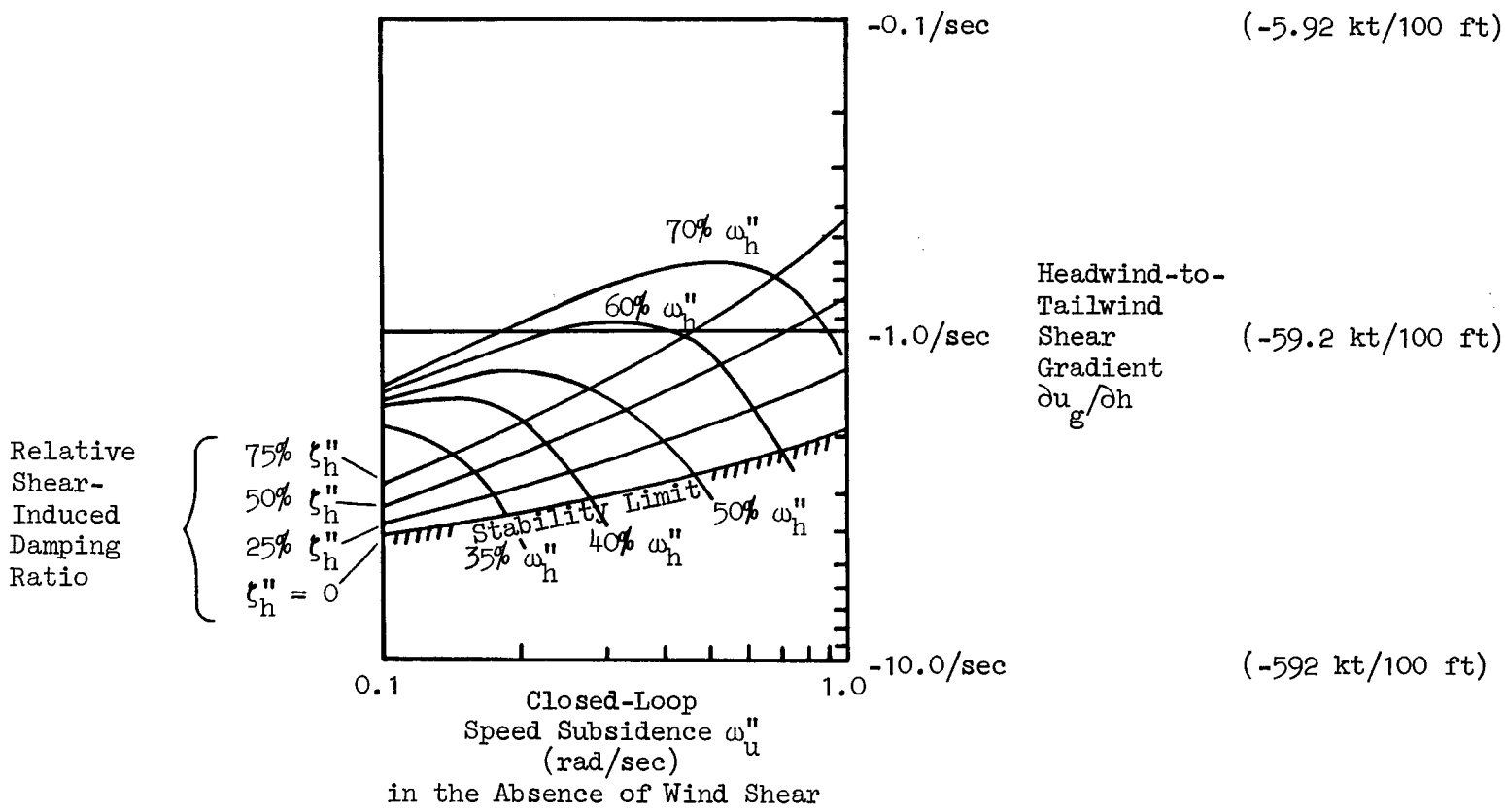

Figure 27. Relative Shear-Induced Closed-Loop Bandwidth and Damping Ratio for Height Control as a Function of Headwind-to-Tailwind Shear Gradient and Closed-Loop Speed Subsidence, if Closed-Loop Height Control Characteristics Provide $[\zeta''_h;\omega''_h]$ = [0.7;1.0 rad/sec] Without Wind Shear

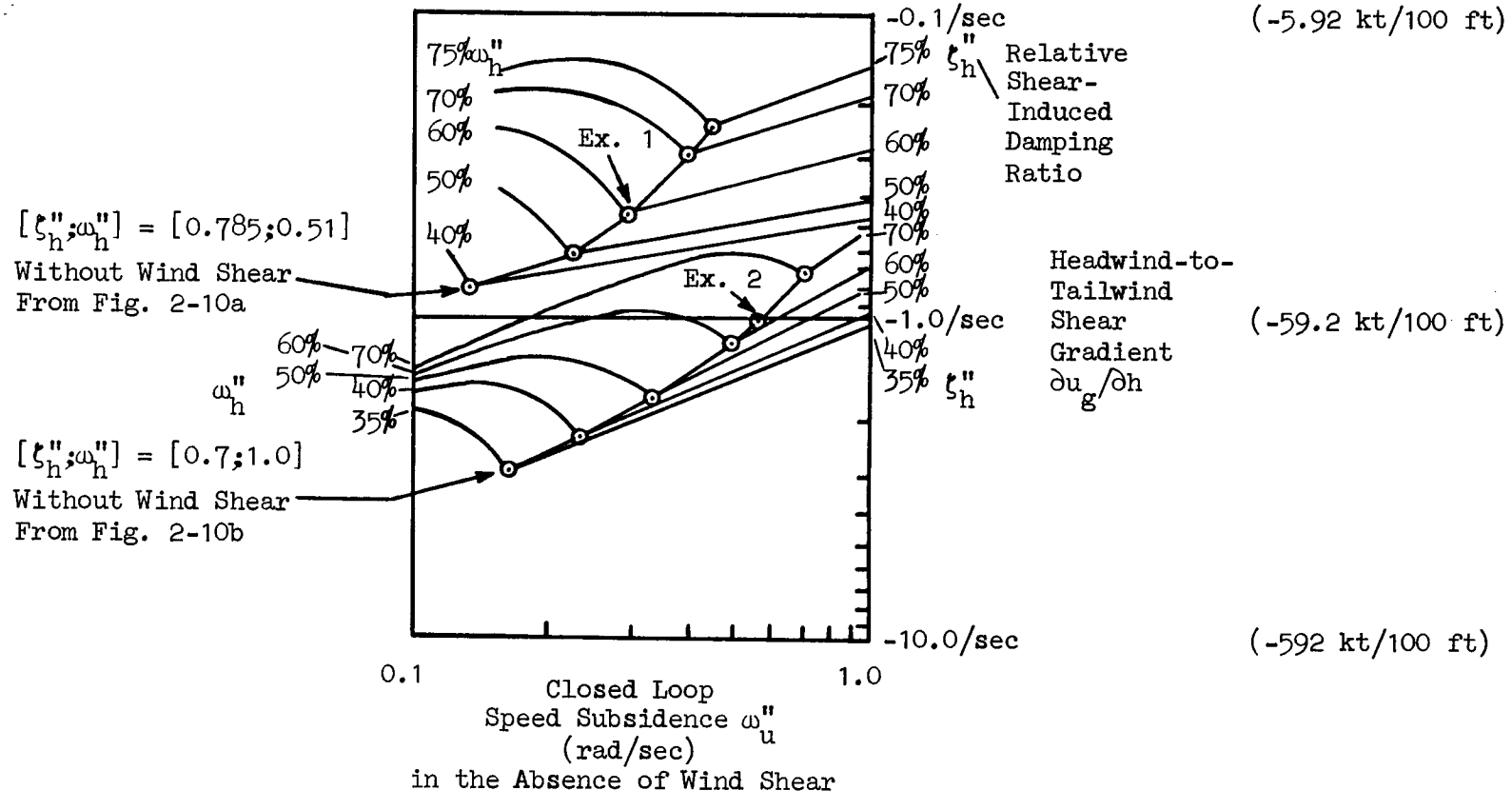

Figure 28. Loci of Equal-Percentages of Relative Closed-Loop Damping Ratio and Bandwidth, Whichever is Less, Induced by Wind Shear for Two Different Closed-Loop Height Control Characteristics

To aid in the interpretation of these results and in their use in design, we have prepared in Fig. 28 the loci for paired equal percentages of relative closed-loop damping ratio and bandwidth, whichever is less, induced by the wind shear for the two sets of height control characteristics. Two concluding examples will illustrate the use of Fig. 28.

Example 1: Closed-Loop Height Control Characteristics $[\zeta_h'';\omega_h''] = [0.785;0.51]$ Without Wind Shear. If one wishes to accept no less than 60 percent ζ_h'' and 60 percent ω_h'' caused by the wind shear, what speed subsidence ω_u'' should be selected in the absence of wind shear and how large a gradient $\partial u_g/\partial h < 0$ can be tolerated? The speed subsidence $\omega_u'' = 0.29$ rad/sec in the absence of wind shear and $\partial u_g/\partial h$ can be at most -0.45/sec (-26.6 kt/100 ft).

Example 2: Closed-Loop Height Control Characteristics $[\zeta_h'';\omega_h''] = [0.7;1.0]$ Without Wind Shear. If one wishes to provide a degree of height control immunity against a wind shear gradient up to $\partial u_g/\partial h = -1.0$/sec (-59.2 kt/100 ft), what is the largest speed subsidence ω_u'' which will provide balanced relative immunity in closed-loop damping ratio ζ_h'' and bandwidth ω_h''? The speed subsidence $\omega_u'' = 0.55$ rad/sec and the balanced relative level of height control immunity will be not less than 63 percent ζ_h'' and 63 percent ω_h''.

The conclusion at this point is that a closed-loop height-to-collective control characteristic having a damping ratio of at least 0.7 and a bandwidth of at least 0.5 rad/sec will provide insufficient margin of immunity against a headwind-to-tailwind shear gradient with decreasing altitude in excess of -50 kts/100 ft, although a closed-loop height bandwidth of 1.0 rad/sec will provide superior immunity. An intermediate range of closed-loop speed subsidence of 0.3 to 0.5 rad/sec in the absence

of wind shear provides a more favorably balanced immunity than a high subsidence in excess of 0.6 rad/sec, because the wind shear gradient $\partial u_g/\partial h < 0$ will itself cause the speed subsidence to increase.

SECTION IV

TASK III: AUTOMATIC GUIDANCE FOR AGGRESSIVE NOE MANEUVERS

A. A TIME-OPTIMAL MODEL FOR AGGRESSIVE NOE MANEUVERS

Four distinctive multiaxis NOE maneuvers, each involving primarily one of the four rotorcraft controls as a commanded input, are critical to the success of most NOE missions. These maneuvers include the (1) bob-up and -down, (2) hover turn, (3) dash-quickstop, and (4) sidestep. Recent Black Hawk (UH-60A) flight tests and simulation tests for the purpose of assessing the fidelity of simulated NOE maneuvers (Refs. 21 through 24) have shown that experienced pilots can perform nearly time-optimal bob-ups, hover turns, dash-quickstops, and sidesteps when circumstances require aggressive maneuvers. Time optimality therefore provides a well-defined and validated criterion for corresponding automatically controlled NOE maneuvers, if the pilot is to have confidence in the automated maneuvering technique.

Instructions given to the pilots for performing the rapid response phase of the bob-ups or -down and hover turns described in Refs. 21 through 24 were intended to instill a sense of urgency approaching a step function for the internal height or heading command while the pilot was otherwise engaged in steady-state regulation of his attitude, heading, height, and position in the presence of atmospheric turbulence. It has been found (Ref. 25 and Appendix A herein) that such combined transient and steady-state situations can be represented adequately with a single input dual-path structure such as that shown in the simplified diagram of Fig. 29. To represent a multiloop situation, the signals shown in this block diagram could be considered as vector quantities. The quasi-linear steady-state path is the one used for regulating errors caused by random inputs or disturbances and illustrated previously in Fig. 10 with the symbol Y_E. It operates when the error (e) has been reduced within a tolerance acceptable to the pilot for the task of regulation. The

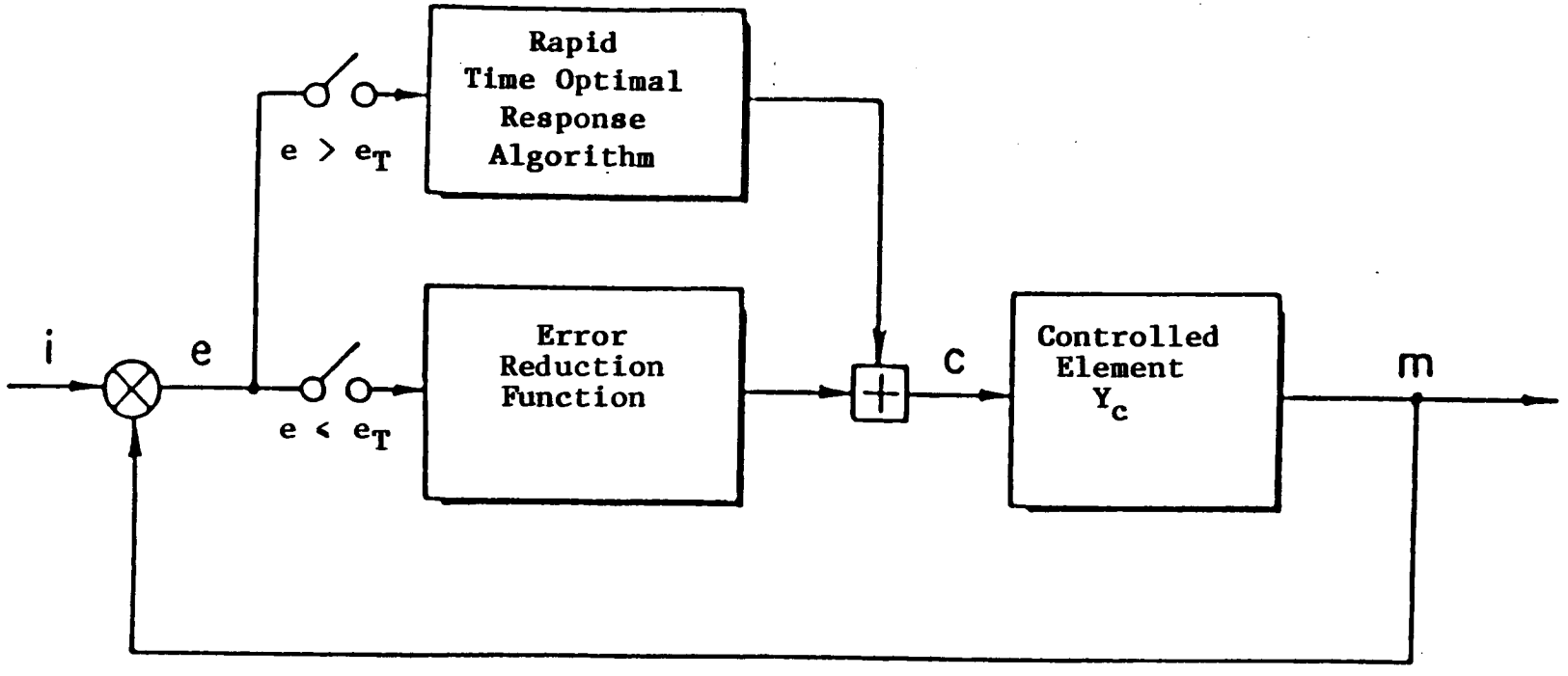

For the bob-up maneuver, e_T is height error threshold, i = h_i, e = h_e, c = δ_{COLL}, m = h, and the error reduction function is Y_{e_h}

Figure 29. Structure of the Dual-Mode Model

feedforward element in Fig. 29 operates on the large transient errors induced by the pilot's internal command or desire to initiate the bob-up or -down or hover turn. This feedforward element has been embedded in the context of Fig. 10 by the block identified with the symbol Y_{RR} (denoting rapid response).

The roles of the switching and the feedforward element are, in the simplest terms, such as to partition the pilot's control strategy into three phases, each having a different system organization. As an elementary example, consider the typical system step response shown in Fig 30. In terms of the three phases, the operation of the dual path model can be expressed in the following terms:

- Transition from quasi-linear path to feedforward path, corresponding to the time delay phase of duration τ_t.
- Patterned feedforward response, corresponding to the rapid response phase of duration T_c.
- Return to the quasi-linear path, corresponding to the error reduction phase of indefinite duration.

The time delay phase is observable only when the transient forcing function is imposed on the pilot unexpectedly from an external source.

B. HEIGHT CONTROL IN THE BOB-UP OR -DOWN RAPID RESPONSE PHASE

The bob-up or -down rapid response phase begins at the point in time that the pilot mentally defines the magnitude of the change in altitude required to reach a desired height and decides to displace the collective control to begin the maneuver. This is essentially an open-loop command which is designed by the pilot to obtain a rate-of-climb or -descent as soon as possible while keeping within safe torque limitations and within the capability of the rotor speed governor. Initially, no attention is given to the problem of stabilizing at the new altitude.

The most important aspect of the rapid response phase is the pulse-like "bang-bang" nature of the control movements, albeit with practical

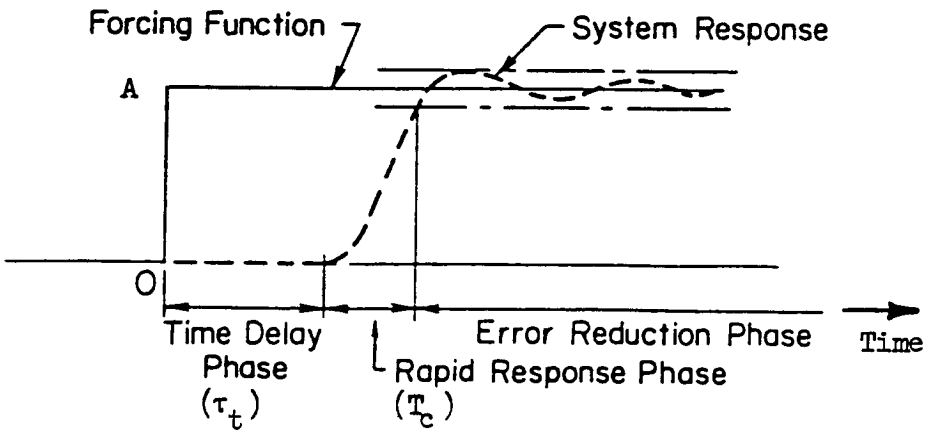

Figure 30. Typical System Step Response

rate limitations. In fact, the pilot's control displacement (c) is a remarkably good approximation to the controller properties of the single-input, single-output, time-optimal control system with $|c(t)| \leq M$. Here, the bound (M) may represent either a physical limit on the control deflection or the velocity command or, more likely in the piloted case, an implicit restraint imposed by the pilot for the given situation for keeping within safe torque and rotorspeed limitations.

The output of the feedforward element representing the rapid response technique for a skilled pilot is peculiar to each controlled element form. For the helicopter, the controlled element transfer function, $Y_c(s)$, representing height response to collective control displacement is given with good approximation for our purposes by $Y_c(s) = K_c/s(s + a)$ where $K_c = -Z_{\delta_c}$, the collective control acceleration effectiveness and $a = -Z_w$, the heave damping. Ideal time-optimal traces for comparison with the actual piloted responses are shown in Figure 31. (Those for $Y_c(s) = K_c/s$ and K_c/s^2 are from Ref. 25 and Appendix A.) The optimal control pulse intervals are unequal in duration for controlled element $K_c/s(s + a)$; the starting pulse is longer than the final pulse when the damping coefficient a is substantial. Suboptimal control techniques by pilots in Refs. 21 through 24 are evidenced by irregular trapezoidal control, attitude, or command pulses of long duration and unequal amplitude. Usually the starting pulse is greater in amplitude than the final pulse. Practical examples of $Y_c(s) = K_c/s(s + a)$ and other controlled elements are listed in Table 6. Note that the form $Y_c(s) = K_c/s(s + a)$ applies to the heading response-to-pedal inputs in a hover turn with constrained attitude as well as to all four maneuvers with the velocity command-displacement hold control systems typically required for automatic NOE maneuver control. The controlled elements for displacement response to attitude commands at low frequencies in the dash-quickstop and the sidestep are given approximately by the form $Y_c(s) = K_c/s^2$, because surge damping and sway damping are usually very small in rotorcraft at the low speeds which prevail in NOE maneuvers.

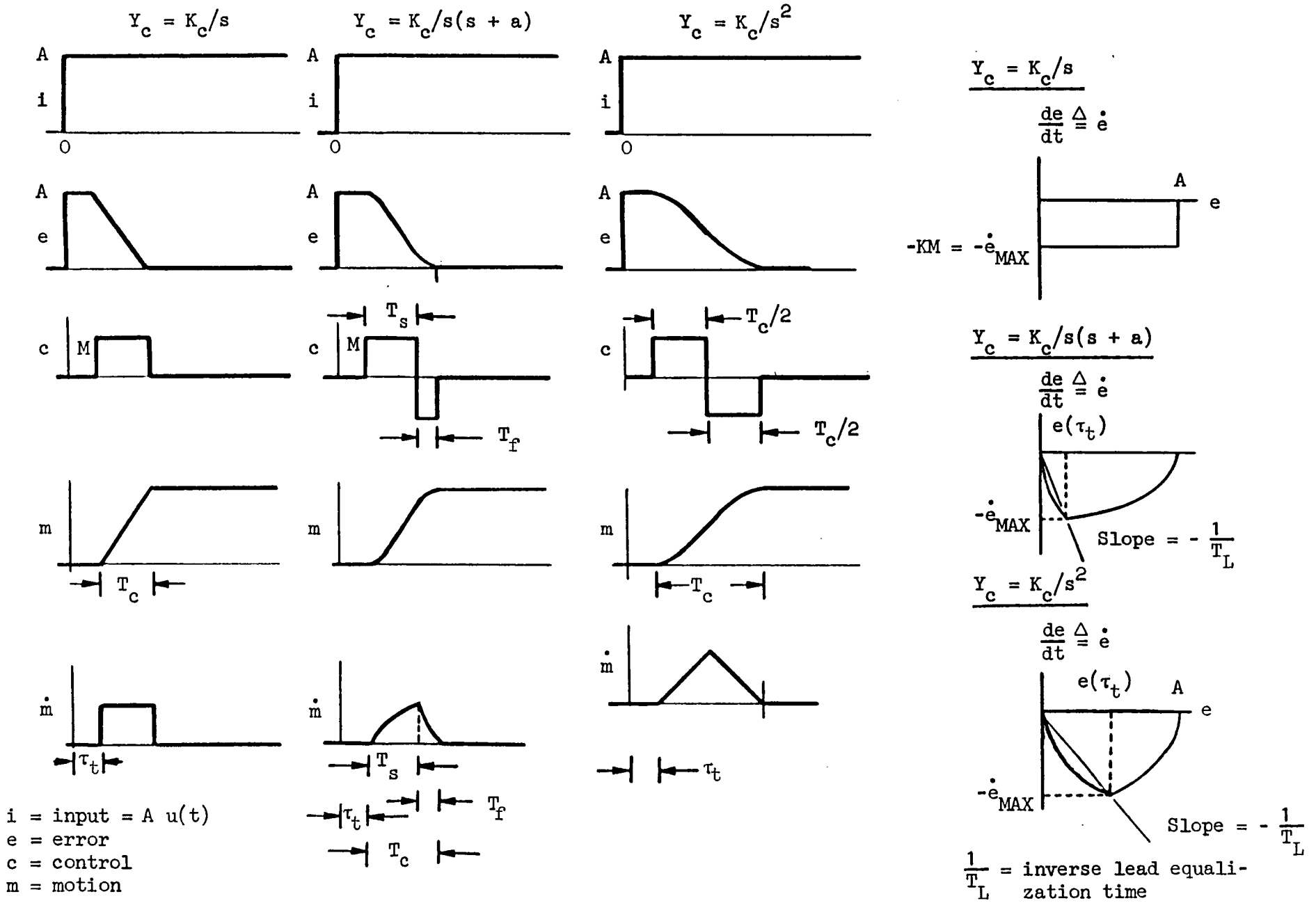

Figure 31. Ideal Time-Optimal Response Characteristics
(T_c = Time to Complete Control Program)

1. Height Control With Vertical Velocity Command-Height Hold (VCHH)

During the rapid response phase of the vertical maneuver with velocity command-height hold capability in Fig. 32, the reference for the compensatory height regulation loop via the controller is slewed by the velocity command integration while the height feedback loop remains closed to provide a measure of immunity against disturbances--especially the destabilizing effect of a headwind-to-tailwind shear gradient with decreasing altitude: $\partial u_g/\partial h < 0$. Concurrently, the three other compensatory loops for longitudinal (Fig. 32) and lateral stationkeeping (Fig. 33) and heading-hold are closed via the controller throughout the rapid response phase of the vertical maneuver. To simplify the subsequent analysis, we shall consider only the vertical and longitudinal motions by assuming that the controller decouples the lateral-directional motions during the vertical maneuver by means of the methods described, for example, in Ref. 26. The mathematical details of the following analysis appear in Appendix C. Equations C-1 through C-4 and the accompanying text (pp. C-1 through C-3) form prerequisites for interpreting the motion and control responses in terms of the symbols in the block diagram of Fig. 32. The first subtopic (a) following is expanded in Appendix C, pp. C-3 and C-4 using Eqns. C-5 and C-6.

a. Example of design for a special case of VCHH with preservation of inherent heave damping, i.e., $1/K^{\bullet}_{h_c} \triangleq 1/T_{L_{hc}} \doteq 1/T_{L_h} \triangleq 1/T^{\bullet}_h \doteq 1/T_{\theta_2}$ and no wind shear, i.e., $\partial u_g/\partial h = 0$

The analysis in Appendix C shows that the special case of VCHH with preservation of heave damping in the absence of wind shear leads to the following design constraints

$$-Z_{\delta_c} K^{\bullet}_{h_c} \doteq - Z_{\delta_c} K^{\bullet}_h \doteq \omega''_h \doteq 1/T_{\theta_2}$$

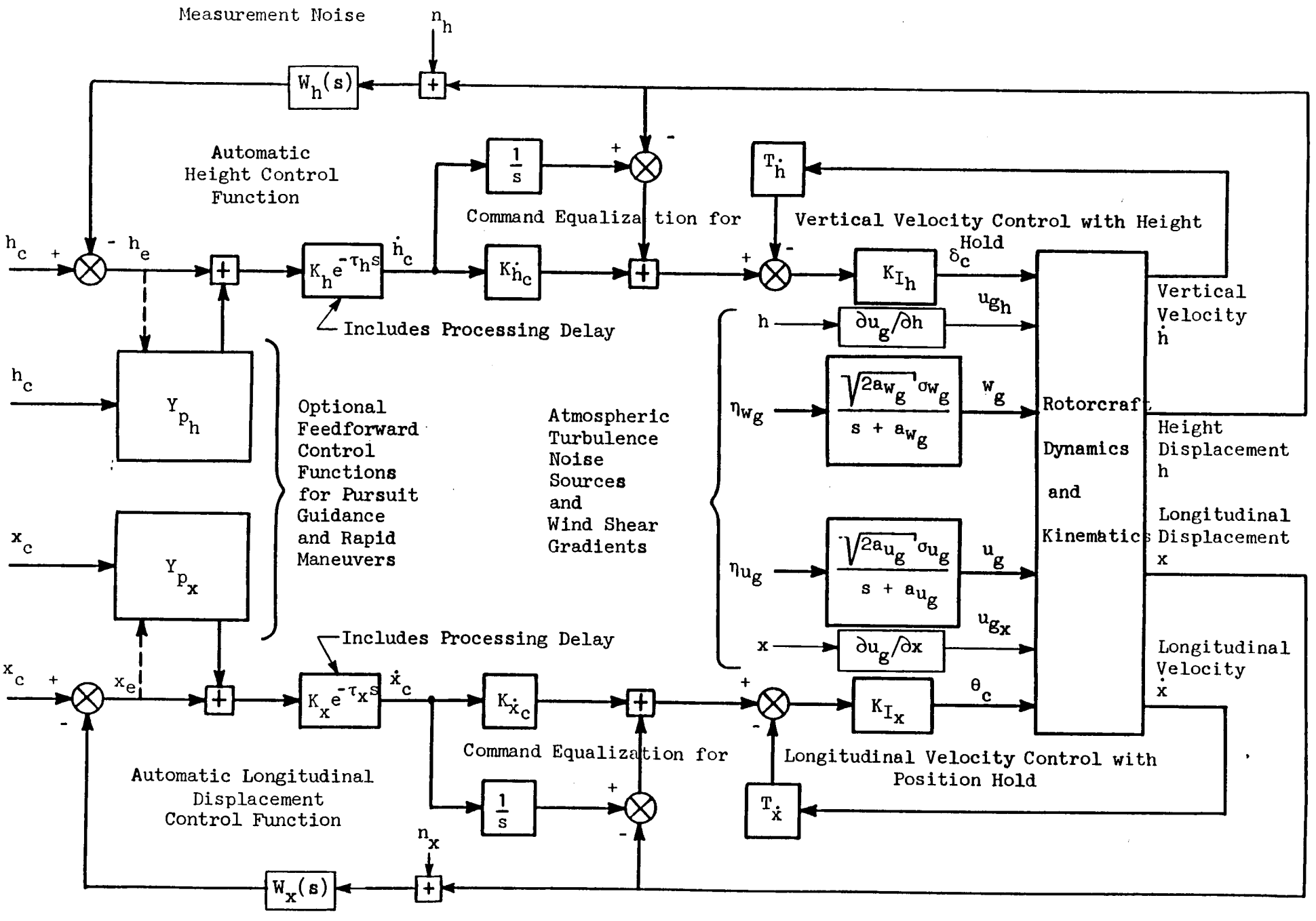

Figure 32. Block Diagram of Mathematical Models for Covariance Estimation in Height Control and Longitudinal Control Tasks

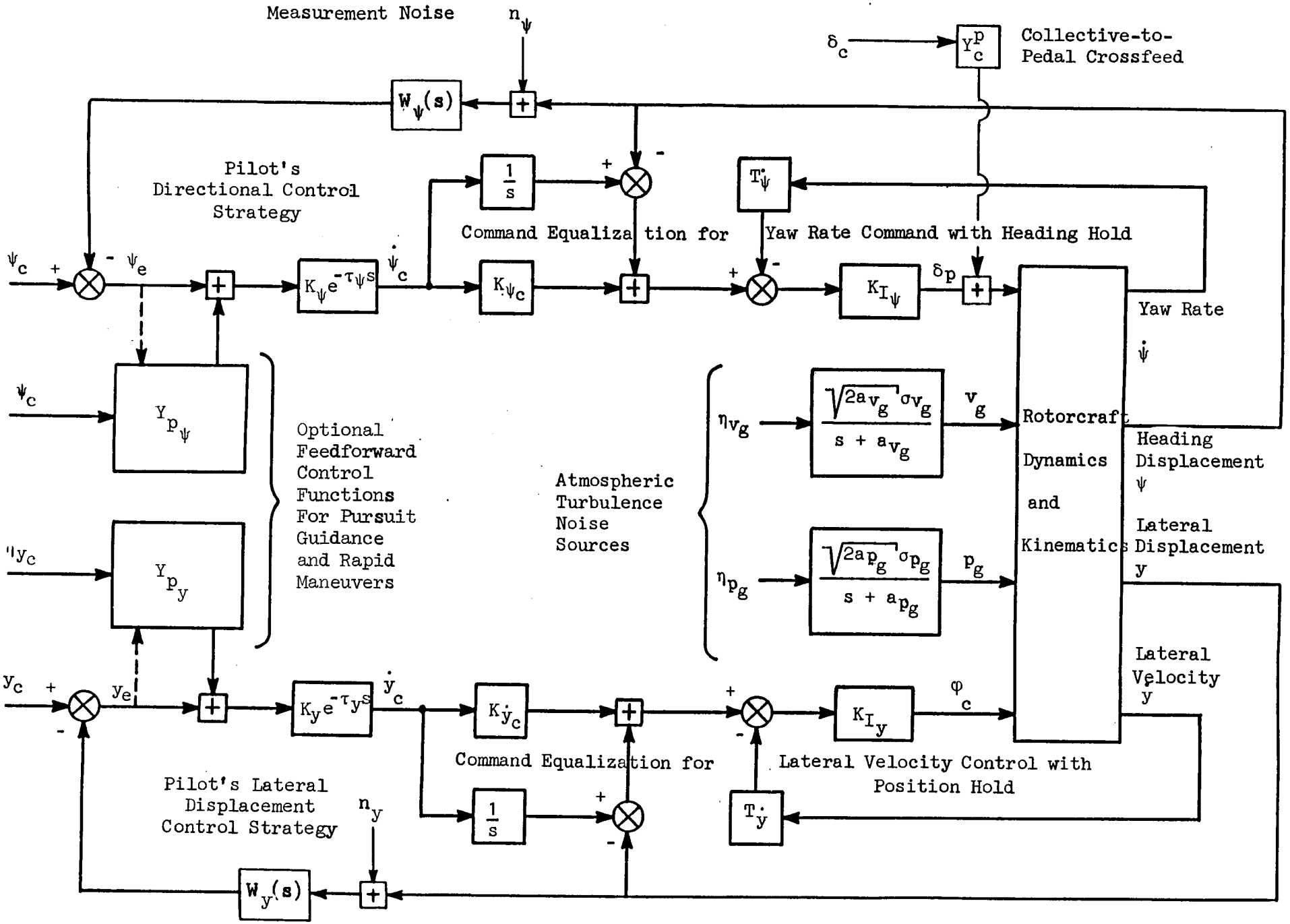

Figure 33. Block Diagram of Mathematical Models for Covariance Estimation in Directional Control and Lateral Control Tasks

or, in terms of symbols in the block diagram of Fig. 32,

$$-Z_{\delta_c} K_{I_h} K_{\dot{h}_c} \doteq -Z_{\delta_c} K_{I_h} T_h^{\bullet} \doteq \omega_h'' \doteq 1/T_{\theta_2}$$

where $1/T_{\theta_2}$ is the inherent heave damping, $-Z_{\delta_c} K_{\dot{h}_c} \doteq -Z_{\delta_c} K_{\dot{h}}^{\bullet} \doteq \omega_h'' \doteq 1/T_{\theta_2}$, where $1/T_{\theta_2}$ is the inherent heave damping, a function of main rotor properties, disc loading, geometry and true airspeed, and Z_{δ_c}, the collective control effectiveness, is also a function of main rotor properties, disc loading, geometry, and true airspeed. Equation C-5 in Appendix C, p. C-3, approximates the controlled element form $Y_c = K_c/s(s + a)$ with $K_c = a$ for which the generic time-optimal velocity command and rapid height response to a step command in height has already been described. Equation C-6 in Appendix C, p. C-4, shows that the required collective control displacement will be proportional to and in phase with the vertical velocity command time history.

b. Examples of transient responses during a time-optimal bob-down for the special Case (a) in the absence of wind shear

For a time-optimal 50 ft bob-down, define amplitude A = 50 ft (in a negative sense) and select the dimensionless inverse maneuver urgency factor, $a^2A/K_cM = 1.0$ in Appendix E, Table E-1, p. E-2, where $K_c = a = 1/T_{\theta_2} = 0.567$ rad/sec for this example, and M represents the absolute magnitude of the vertical velocity command, $\pm |\dot{h}_c|$. Therefore, $M = |\dot{h}_c| = A/T_{\theta_2} = 28.35$ ft/sec, and Appendix E, Table E-1, gives the starting descent velocity command pulse time interval $T_s = 1.61\ T_{\theta_2} = 2.84$ sec, and the final opposite arresting velocity command pulse time interval $T_F = 0.511\ T_{\theta_2} = 0.901$ sec. Thus the time to complete the 50 ft descent will be $T_c = T_s + T_F = 2.12\ T_{\theta_2} = 3.74$ sec. Time histories of the ideal optimal velocity command, the change in collective control displacement from trim, the change in height, and the vertical velocity are plotted in Figs. 34 through 37, respectively. The

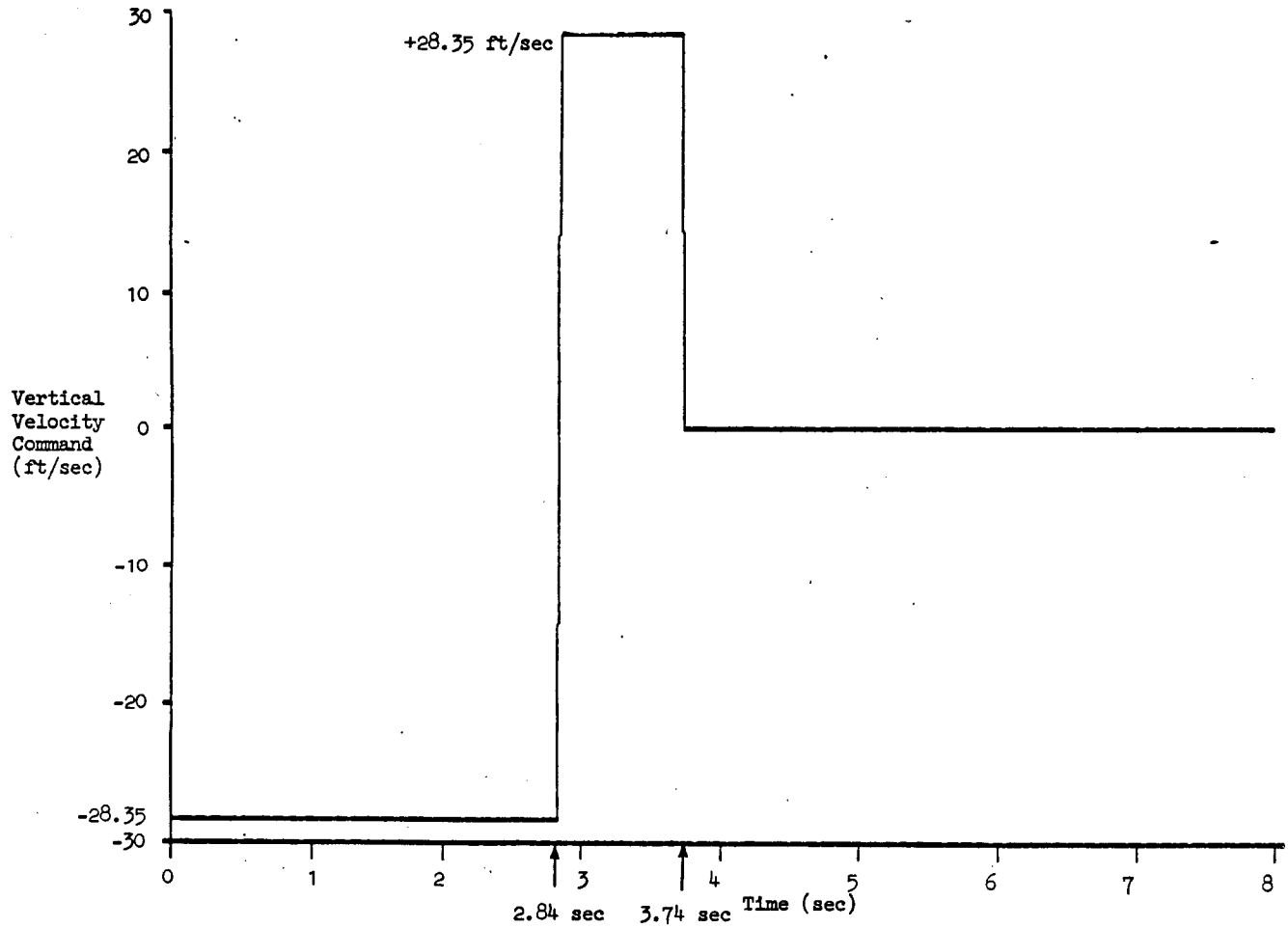

Figure 34. Programmed Time-Optimal Time History of Vertical Velocity Command for 50-ft Descent with a Vertical Velocity Command-Height Hold Control System Having an Effective Controlled Element Transfer Function

$$Y_c(s) = \left[h(s)/\dot{h}_c(s)\right] = [0.567/s(s + 0.567)] \text{ sec}$$

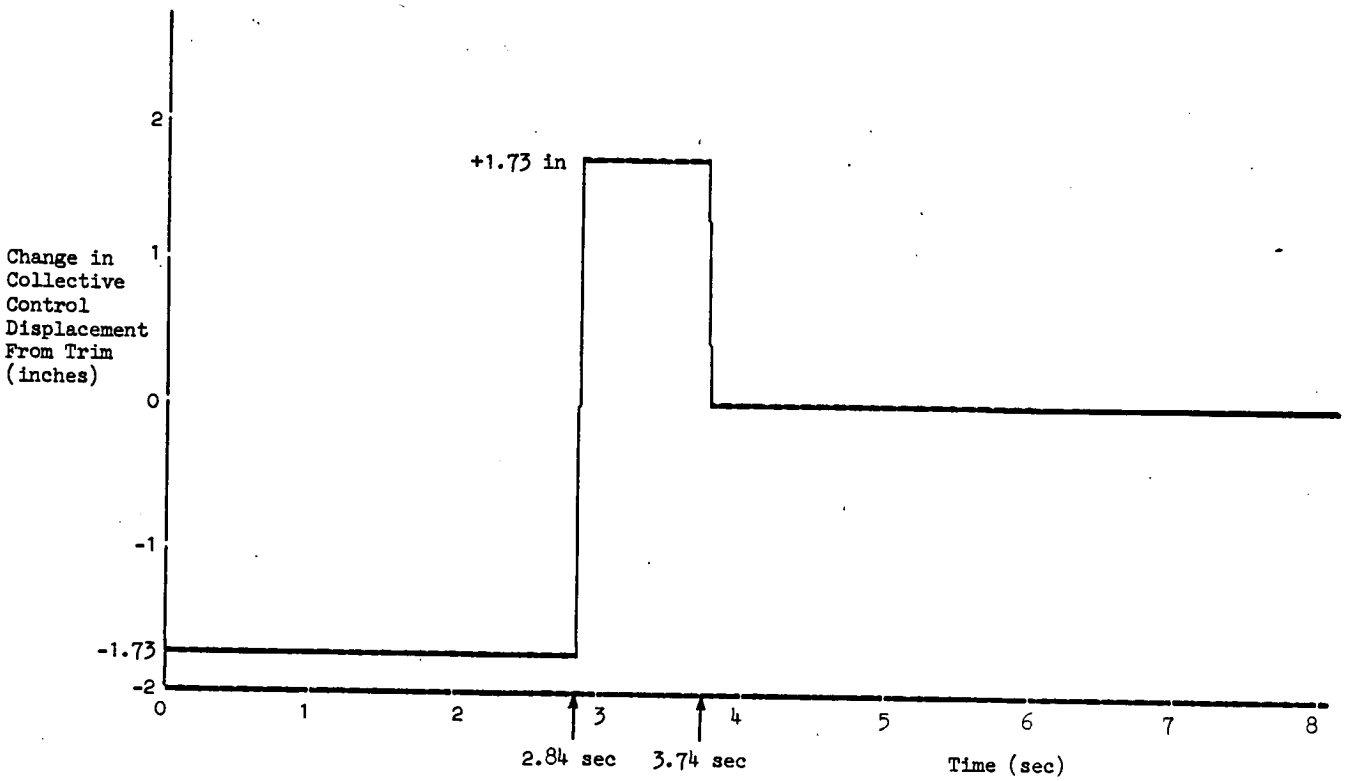

VCHH for the UH-1H; no Shear; 20 kts

Figure 35. Programmed Optimal Time History of Collective Control for 50-ft Descent with a Vertical Velocity Command-Height Hold Control System Having an Effective Controlled Element Transfer Function

$$Y_c(s) = [h(s)/\dot{h}_c(s)] = [0.567/s(s + 0.567)] \text{ sec}$$

$$[\delta_{coll}(s)/\dot{h}_c(s)] \doteq \frac{0.567}{9.29} = 0.0610 \text{ in/ft/sec}$$

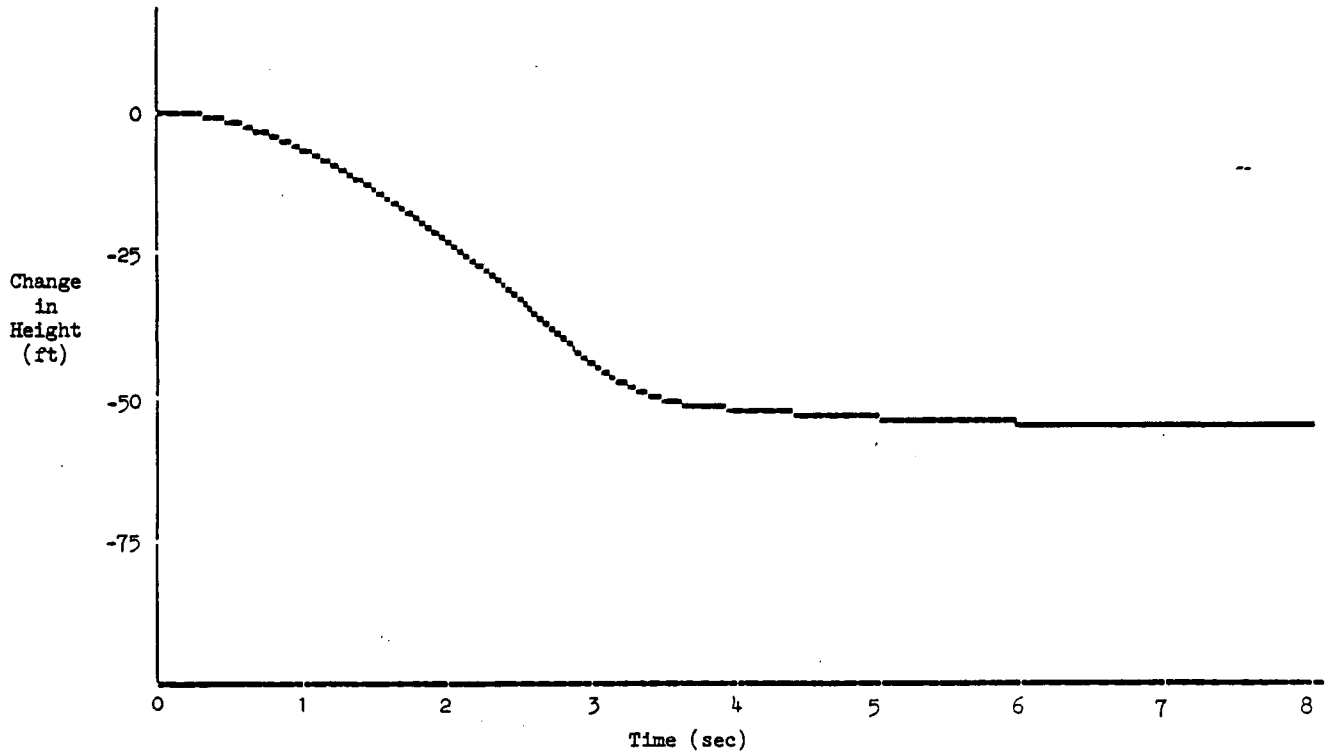

VCHH for the UH-1H; no Shear; 20 kts

Figure 36. Time-Optimal Descent of 50 ft with Programmed Vertical Velocity Command-Height Hold Control for Controlled Element Transfer Function

$$Y_c(s) = \left[h(s)/\dot{h}_c(s)\right] = [0.567/s(s + 0.567)] \text{ sec}$$

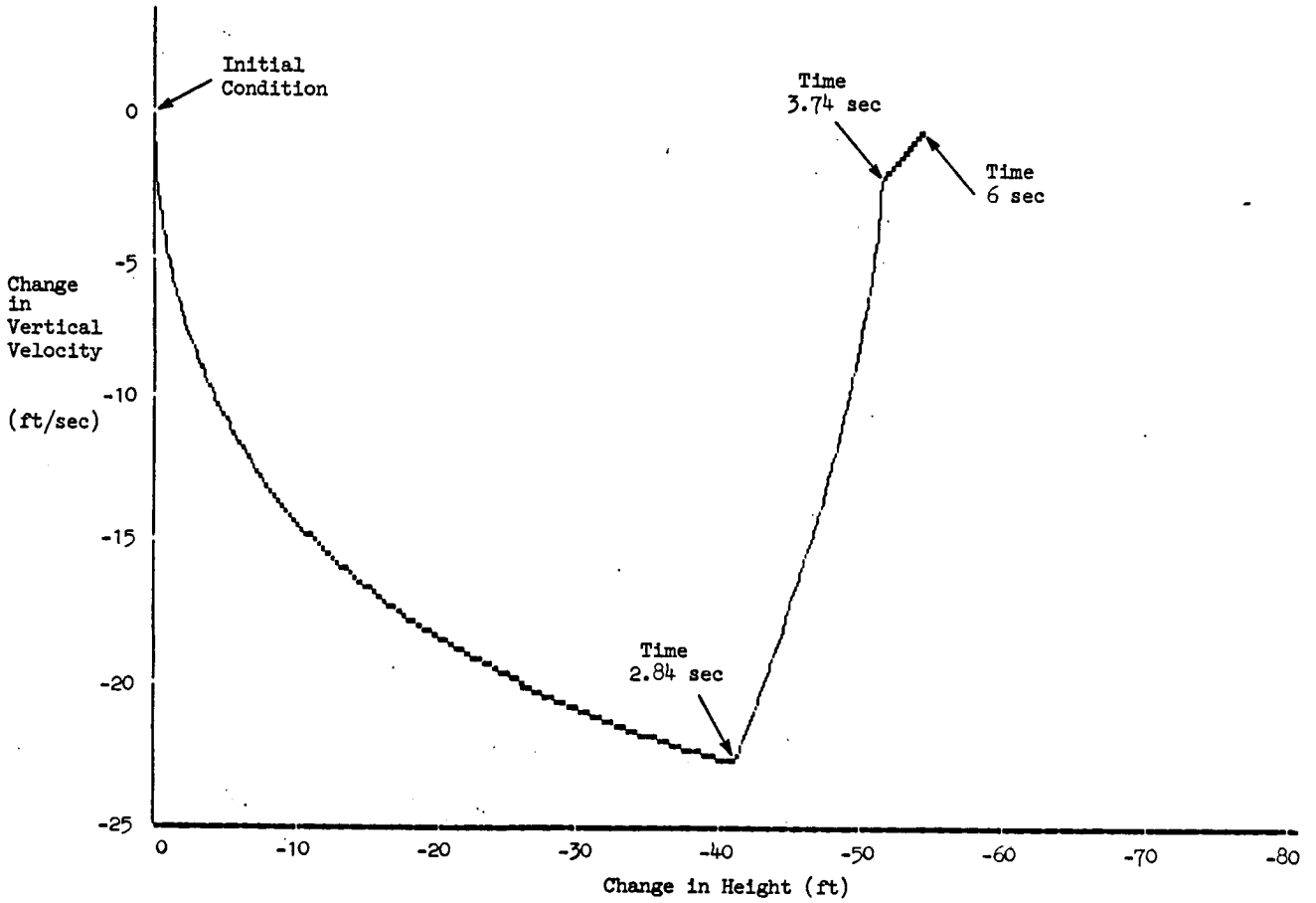

VCHH for the UH-1H; no Shear; 20 kts

Figure 37. Phase Plane for Time-Optimal Descent of 50 ft with Programmed Vertical Velocity Command-Height Hold Control for Controlled Element Transfer Function

$$Y_c(s) = [h(s)/\dot{h}_c(s)] = [0.567/s(s + 0.567)] \text{ sec}$$

required collective displacement authority if $-Z_{\delta_c} = 9.29$ ft/sec^2-in will be $\pm |\delta_{coll}| = \pm |\dot{h}_c|/-Z_{\delta_c} T_{\theta_2} = \pm 1.73$ inches out of a total of 10.7 inches or ± 16.2 percent with respect to the trim displacement which is [(13.57-7.25)deg]/0.15 deg/percent = 42.1 percent of main rotor collective authority for the UH-1H helicopter at 20 kts.

c. Example of VCHH design Case (a) in a wind shear gradient $\partial u_g/\partial h = -1.0$/sec (-59.2 kt/100 ft)

Equation C-2 in Appendix C shows that a head-to-tailwind shear gradient with decreasing altitude ($\partial u_g/\partial h < 0$) in the bob-down will reduce the closed-loop characteristic undamped natural frequency ω_h'', if $Z_u < 0$, which is the usual case for rotorcraft in forward level flight at speeds below that for minimum power required*. Figure 38 shows a Sigma-Bode root locus of this effect on the pair of characteristic poles in Example a above, the special case of VCHH where $\omega_h'' \triangleq 1/T_{\theta_2}$ and $\zeta_h'' = 1$ in the absence of wind shear. If $\partial u_g/\partial h = -1.0$/sec, the poles remain stable subsidences, but the value of the more critical factor decreases from $1/T_{\theta_2} = 0.567$ rad/sec to 0.12 rad/sec, and the value of the other factor increases from $1/T_{\theta_2} = 0.567$ rad/sec to 1.0 rad/sec.

Equation C-4 in Appendix C shows that a head-to-tailwind shear gradient with decreasing altitude ($\partial u_g/\partial h < 0$) in the bob-down will also alter the singularities in the numerator of the collective control response. Figure 39 shows a Sigma-Bode root locus of the effect on the zeroes of this numerator in Example a above. If $\partial u_g/\partial h = -1.0$/sec, the zero at the origin of the real axis in the complex plane moves to the right half plane and remains real at 0.244 rad/sec (factor is -0.244 in Fig. 39), and the value of the real zero in the left half plane at $-1/T_{\theta_2} = -0.567$ rad/sec increases (in a negative sense) to -0.811 rad/sec (factor is 0.811 in Fig. 39).

---

*Reference 27 lists Z_u for five helicopters. In forward level flight, the largest negative values of Z_u occur at 20 kt for four and 30 kt for one of the helicopters.

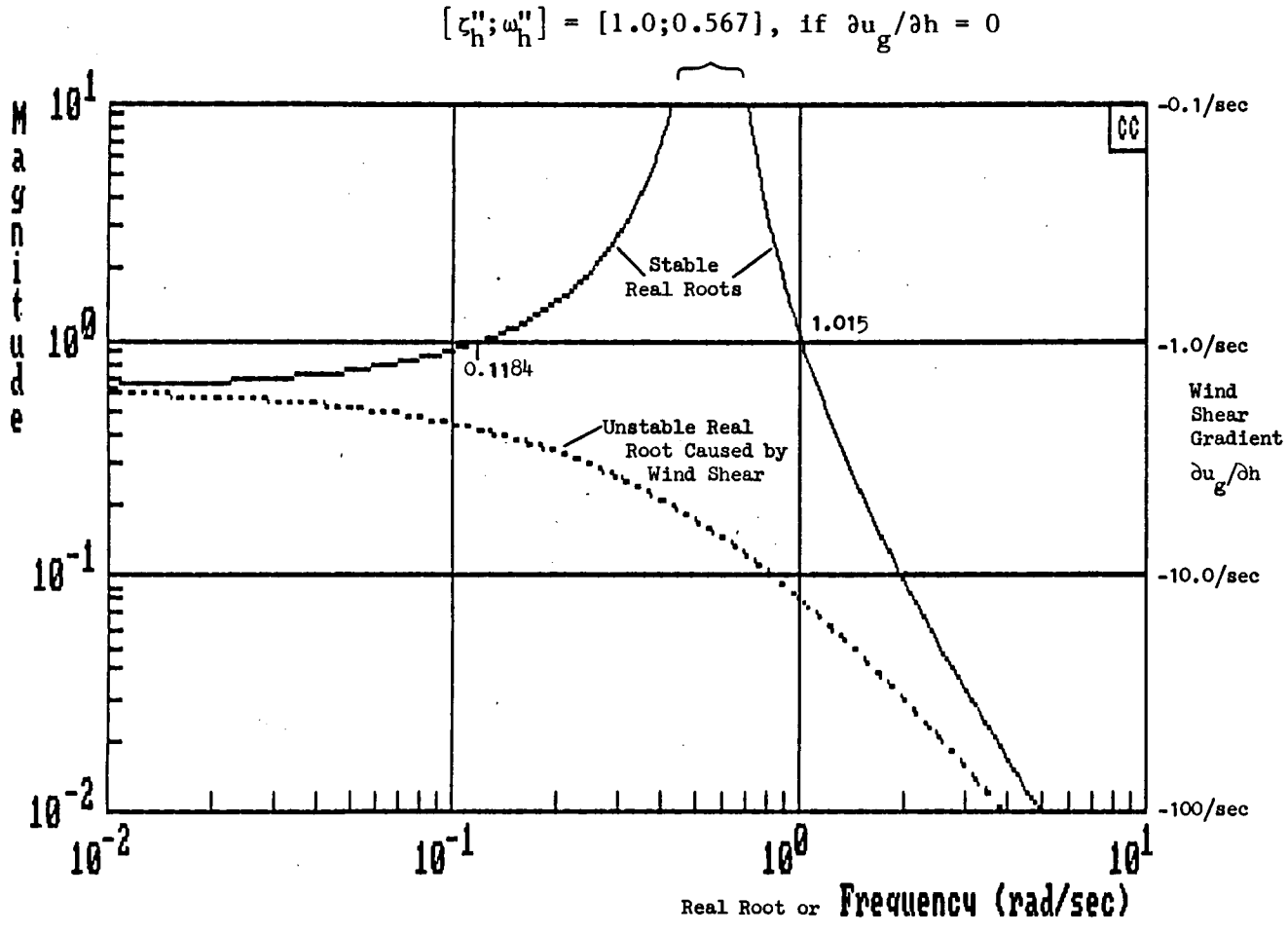

Figure 38. Sigma Bode Root Locus Showing Effect of Headwind-to-Tailwind Shear with Decreasing Altitude: $\partial u_g/\partial h > 0$ on Characteristic Poles for Vertical Velocity Command-Height Hold (VCHH) Control. Longitudinal Position Loop Closed Via Pitch Attitude With Lead Compensation $1/T_x = 0.3$ rad/sec and High Frequency Gain $K_x^* = -0.02$ rad θ_c/ft/sec (Complex Conjugate Roots From Stationkeeping Dipole Not Shown at $[\zeta''_x;\omega''_x] = [0.7;0.43]$

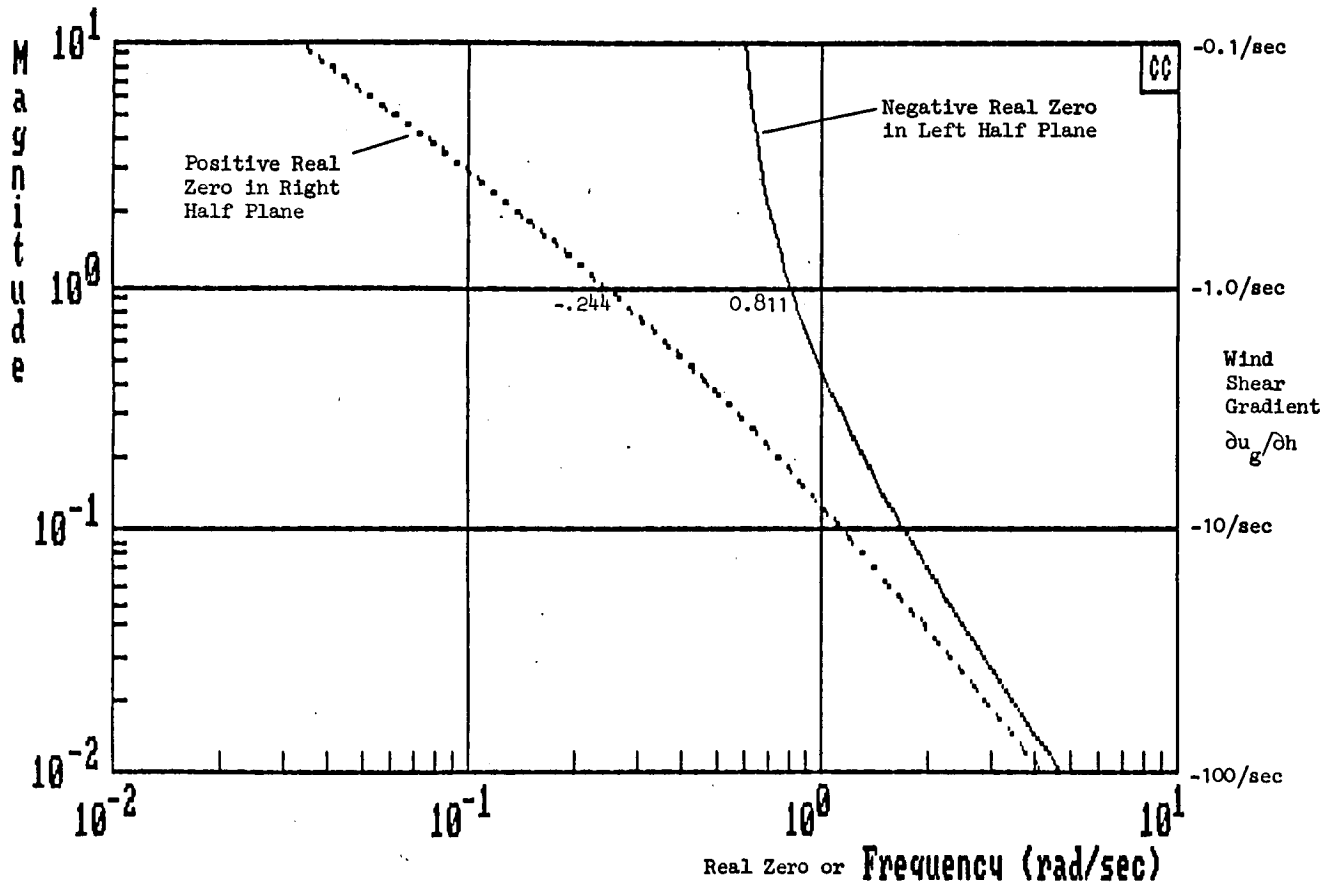

Figure 39. Sigma Bode Root Locus Showing Effect of Headwind-to-Tailwind Shear with Decreasing Altitude: $\partial u_g/\partial h > 0$ on Zeros of Numerator $N^{\delta_{COLL}}_{h_c/s}$ for Vertical Velocity Command-Height Hold (VCHH) Control. Longitudinal Position Loop Closed Via Pitch Attitude With Lead Compensation $1/T_x$ = 0.3 rad/sec and High Frequency Gain K_x^* = -0.02 rad θ_c/ft/sec (Complex Conjugate Roots From Stationkeeping Dipole Not Shown at $[\zeta_x'';\omega_x'']$ = [0.7;0.43]

d. Examples of transient responses for VCHH Case (a) in a wind shear gradient, $\partial u_g/\partial h = -1.0/\text{sec}$ (-59.2 kt/100 ft)

Figures 40, 41, and 42 show the transient responses for collective displacement, height displacement, and vertical velocity, respectively, for the 50 ft bob-down with VCHH Case (a) in a wind shear gradient $\partial u_g/\partial h = -1.0/\text{sec}$. The velocity command remains as in Fig. 34 (p. 78). The result is, of course, not time optimal, because the gain of the steady-state closed-loop vertical velocity response exceeds unity (it is 2.68), and the effective bandwidth of the height-hold loop is reduced to 0.12 rad/sec instead of 0.567 rad/sec. Thus the change in height overshoots -50 ft during the rapid response phase of 3.74 sec and continues to drift downward to approach -130 ft in about 24 sec because of the sluggish height-hold loop caused by the wind shear gradient in the absence of integral control during the height error reduction phase. In practice, this effect of the wind shear might be counteracted by switching to a higher gain compensatory error reduction loop at the end of the rapid response phase or by predicting or measuring the wind shear itself, the last two of which alternatives are difficult. Thus it is preferable to redesign the VCHH capability in Case (a) to provide more tolerance to such a severe wind shear gradient.

e. Example of redesign of VCHH system to increase tolerance to a wind shear gradient $\partial u_g/\partial h = -1.0/\text{sec}$ (-59.2 kt/100 ft)

(See Appendix C, pp. C-4 and C-5.)

f. Redesigned example Case (e) in the absence of wind shear ($\partial u_g/\partial h = 0$)

The analysis for this topic begins on p. C-6 in Appendix C. In the absence of wind shear, the effective controlled element in Eq. C-11 in Appendix C, p. C-6, is still approximately of the form $Y_c = K_c/s(s + a)$,

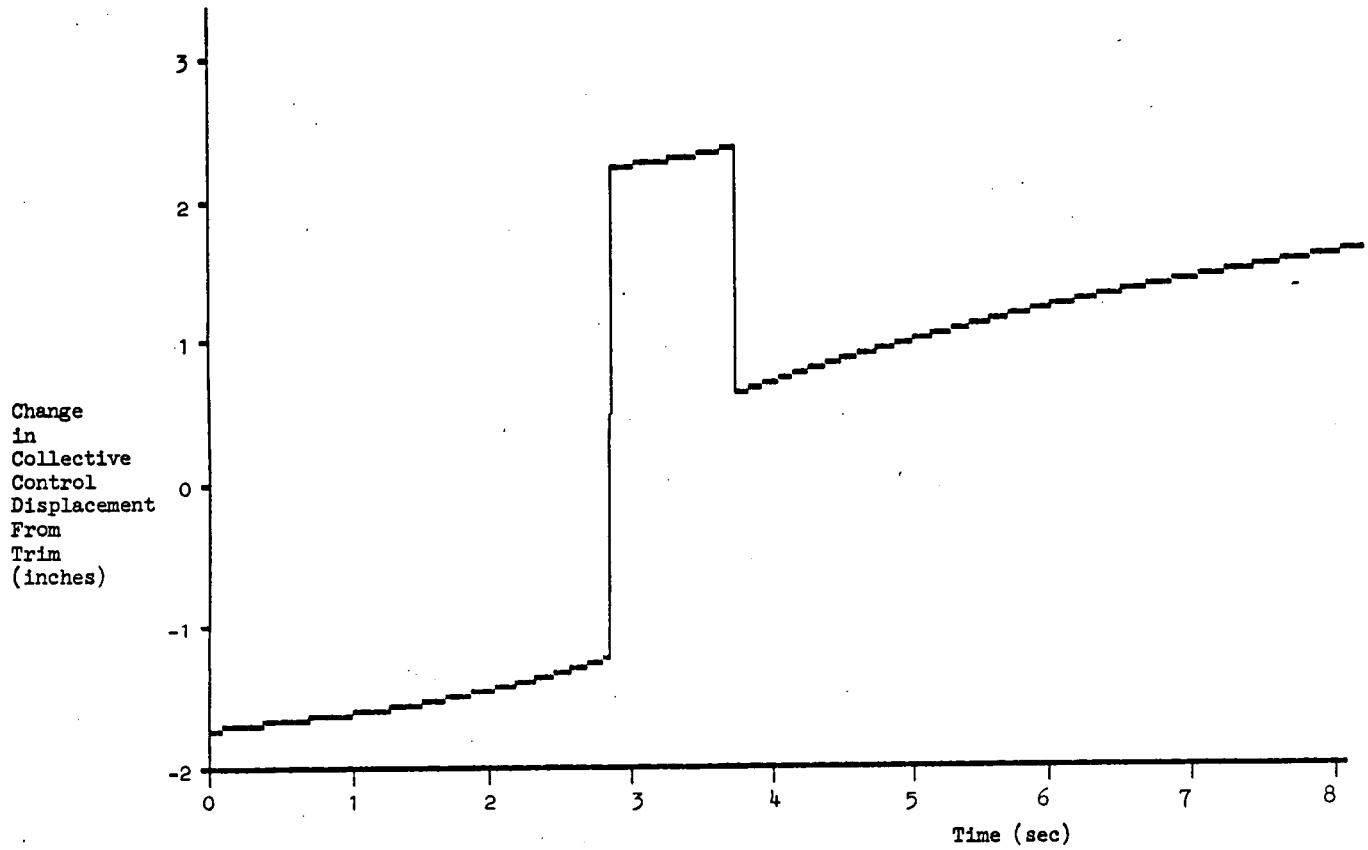

COLL/$\dot{h}_c$ for UH-1H with VCHH; -1.0/sec Headwind-to-Tailwind Shear in Descent

Figure 40. Collective Control Time History with Programmed Vertical Velocity Command Appropriate for a Time Optimal Descent of 50 ft in the Absence of Wind Shear but Applied in the Presence of Wind Shear to VCHH Control Without Integration of Height Error in Wind Shear $\partial u_g/\partial h < 0$

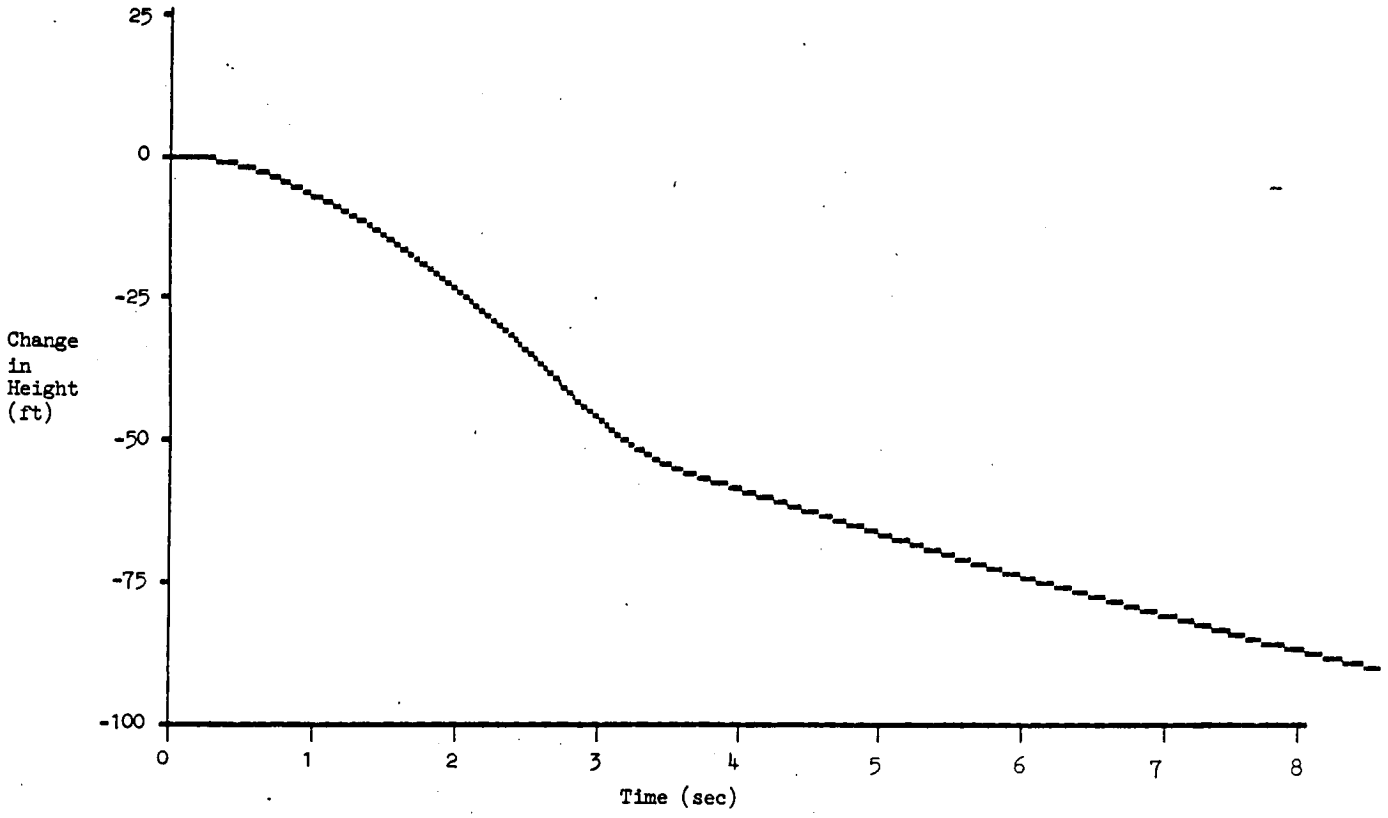

$Y_c = h/\dot{h}_c$ for UH-1H with VCHH; -1.0/sec Headwind-to-Tailwind Shear in Descent

Figure 41. Descent Time History of Height with Programmed Vertical Velocity Command Appropriate for a Time Optimal Descent of 50 ft Showing Stable Drifting Tendency of VCHH Control Without Integration of Height Error in Wind Shear $\partial u_g/\partial h < 0$

(Gradient -1.0/sec = -59.2 kt/100 ft)

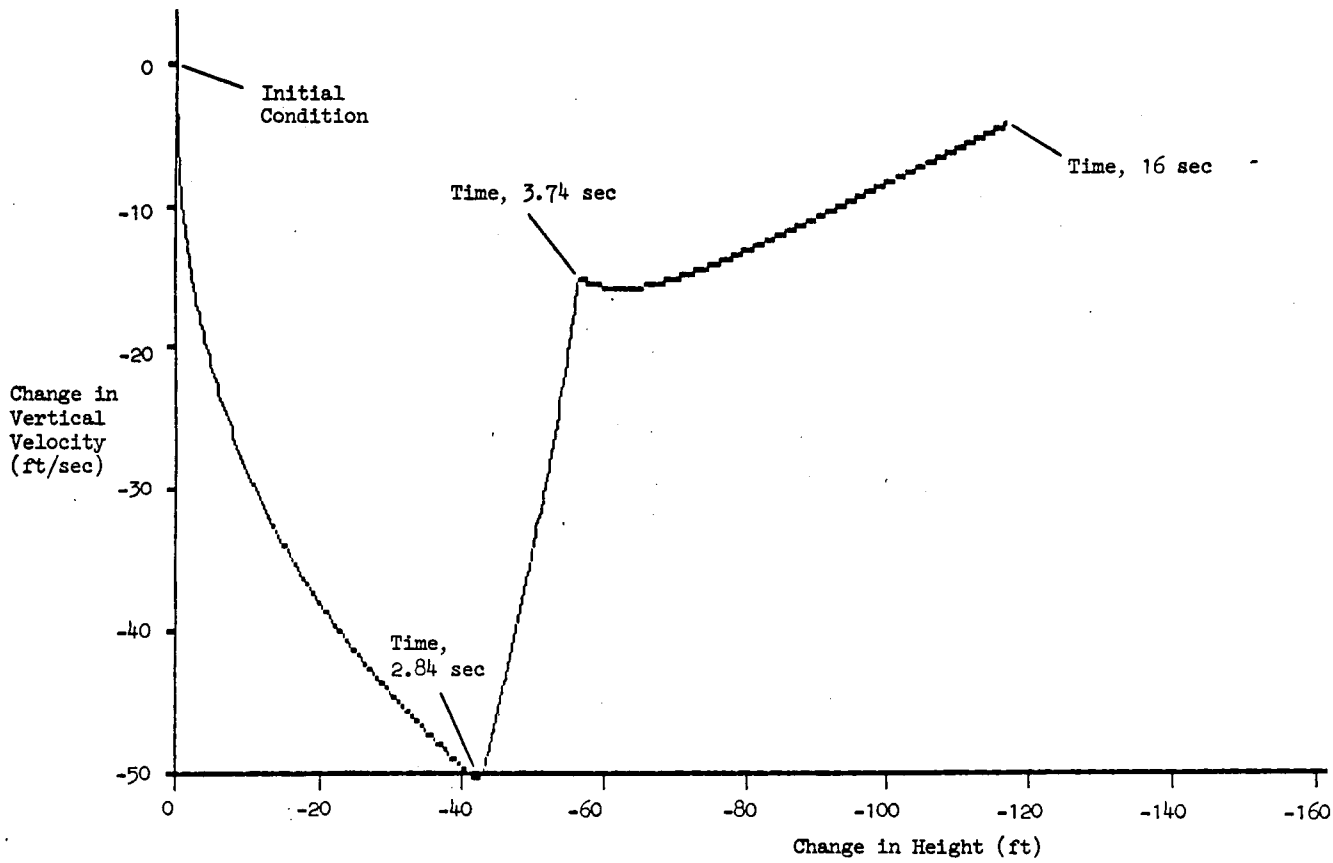

$Y_c = h/\dot{h}_c$ for UH-1H with VCHH; -1.0/sec Headwind-to-Tailwind Shear in Descent

Figure 42. Phase Plane for Descent with Programmed Vertical Velocity Command Appropriate for a Time Optimal Descent of 50 ft Showing Stable Drifting Tendency of VCHH Control Without Integration of Height Error in Wind Shear $\partial u_g/\partial h < 0$

(Gradient -1.0/sec = -59.2 kt/100 ft)

where $a \triangleq 0.862$/sec based on the dimensionless variability* and $a \triangleq 1.0$/sec based on the half-power frequency; but the steady-state gain of the velocity response to a velocity command is less than unity (it is 0.618).

If the high frequency gain ($-Z_{\delta_c} \underline{K}_{\dot{h}_c} = 0.567$/sec) is increased by a factor 1/0.618 = 1.618 to compensate for the reduced gain in Eq. C-11, the new high frequency gain becomes $K_c = 1.618\ (0.567) = 0.917$/sec in Eq. C-11a, and if the amplitude and time intervals of the velocity command are recomputed to account for the increased K_c and increased a in the maneuver urgency factor $K_c M/a^2 A = 1.0$ where $M = |\dot{h}_c|$, then $|\dot{h}_c| \triangleq a^2 A/K_c = (0.862)^2 50/0.917 = 40.51$ ft/sec, where a = 0.862 based on the dimensionless variability; and $T_s = 1.61/1.0 = 1.61$ sec, $T_f = 0.511/1.0 = 0.511$ sec, and $T_c = 2.12$ sec, where $a \triangleq 1.0$/sec based on the half-power frequency. The application of the two different values for a is deliberate because of the form of the modified controlled element in Eq. C-11a, p. C-7, Appendix C.

The modified velocity command ($\dot{h}_c$) is shown as a function of time in Fig. 43. Transient responses of collective and height displacements for this modified (and nearly re-optimized) velocity command are given in Fig. 44 and Fig. 45, respectively. Corresponding velocity response is presented in the phase plane Fig. 46, which confirms that the height and vertical velocity responses have been nearly re-optimized in the absence of wind shear.

---

*"Bandwidth" is a vague term unless the displayed signal spectrum is rectangular. For other spectral shapes, the dimensionless variability can be used to define a rectangular bandwidth equivalent, i.e.,

$$\omega_{i_e} = \frac{\left[\int_o^\infty \Phi_{ii}(\omega)d\omega\right]^2}{\int_o^\infty \left[\Phi_{ii}(\omega)\right]^2 d\omega} \quad \text{(Ref. 27)}$$

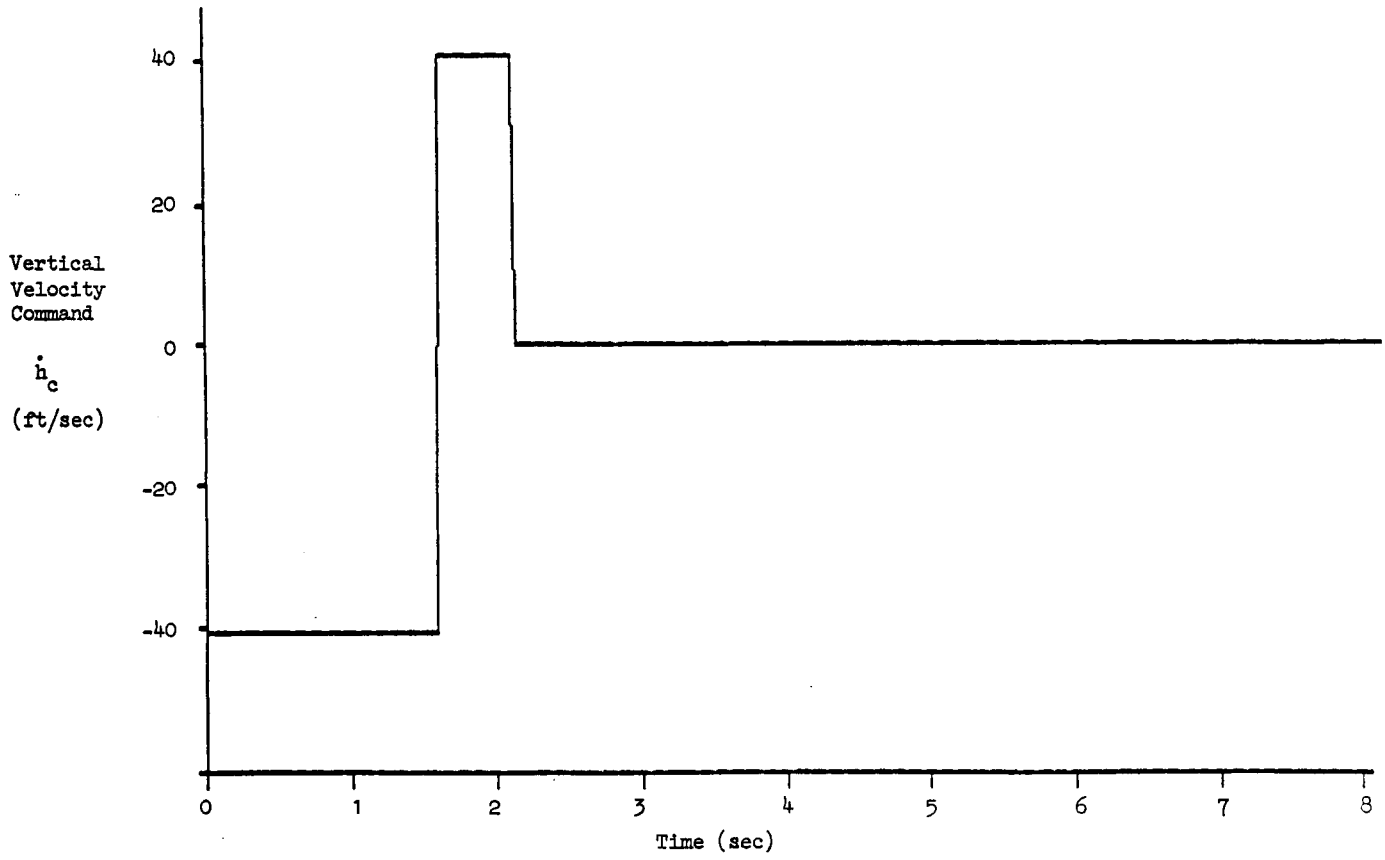

Figure 43. Modified Vertical Velocity Command Representing Redesigned Example Case (e) for VCHH in the Absence of Wind Shear

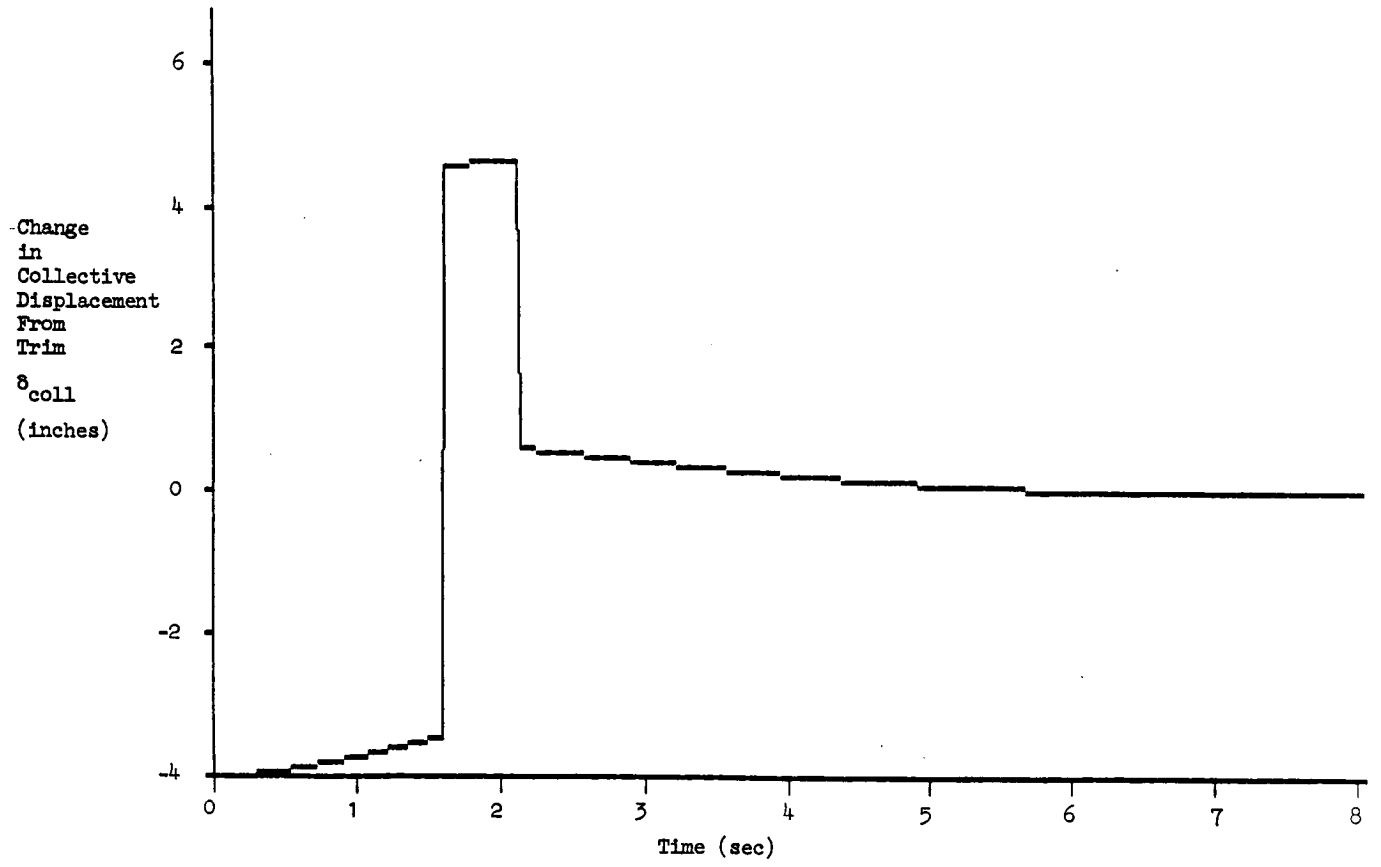

Figure 44. Time History of Change in Collective Displacement From Trim in Response to Modified Vertical Velocity Command Representing Redesigned Example Case (e) for VCHH in the Absence of Wind Shear

(10.7 inches of collective displacement = 100 percent)

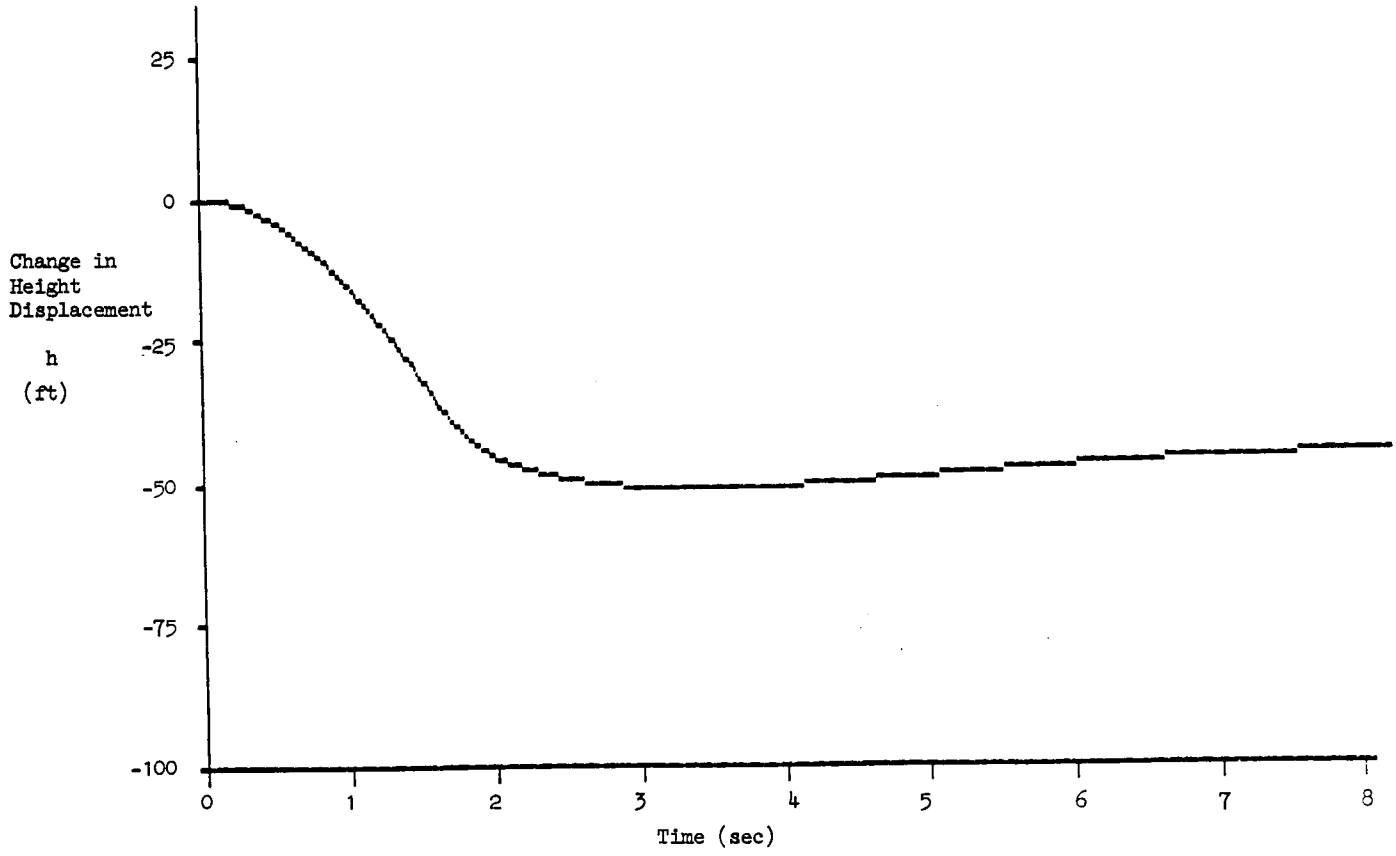

Figure 45. Time History of Change in Height Displacement in Response to Modified Vertical Velocity Command Representing Redesigned Example Case (e) for VCHH in the Absence of Wind Shear

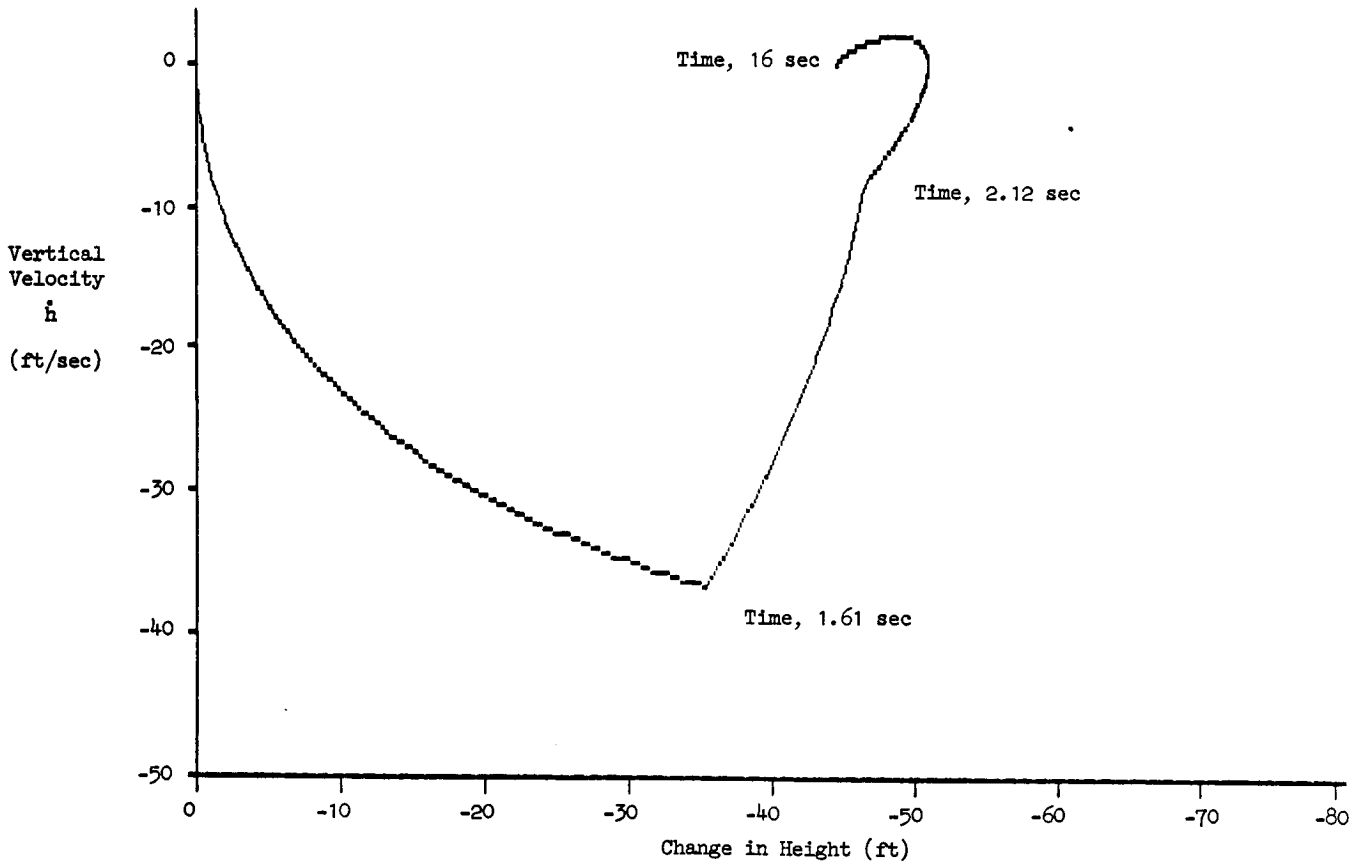

Figure 46. Vertical Velocity and Height Phase Plane for Responses to Modified Vertical Velocity Command Representing Redesigned Example Case (e) for VCHH in the Absence of Wind Shear

g. Conclusion from these examples with VCHH

The worst case design for the wind shear in Example Case (e) is preferable, because it results in a conservative design which can be more easily re-optimized as in Example Case (f) by velocity command amplitude and time interval adjustments in the absence of wind shear.

2. Loss of VCHH Capability

During the rapid response phase of the vertical maneuver without velocity command-height hold capability, the compensatory feedback loop via the pilot or controller to the primary rotorcraft control, in this instance, the collective control, is open. It will therefore be of comparative interest subsequently to examine the effect of a headwind-to-tailwind shear with decreasing height on the time-optimal bob-down during the rapid response phase with open height control loop. This situation would apply in the event of a passive open failure of the height feedback loop in the vertical velocity command-position hold control system, Fig. 32 (p. 75). The three other compensatory loops for longitudinal (Fig. 32) and lateral stationkeeping (Fig. 33, p. 76) and heading-hold are, however, presumed to be closed via the controller (human or automatic) throughout the rapid response phase of the bob-down maneuver. To simply the subsequent analysis, we shall restrict it to consider only the vertical and longitudinal motions by assuming that the controller decouples the lateral-directional motions perfectly.

a. Longitudinal Hovering Position Control in Vertical Unmask and Remask Maneuvers with Open-Loop Height Control

Figure 47 shows the effects while maintaining a longitudinal hovering position, i.e., stationkeeping, with open-loop height control, of varying longitudinal position-to-pitch attitude control high-frequency gain, $K_x^\bullet$, with constant lead compensation, $1/T_{L_x}$ = 0.3 rad/sec on the closed-loop dynamic characteristics of longitudinal translation. Three values of the gain $K_x^\bullet$ and their corresponding closed-loop damping ratio and undamped

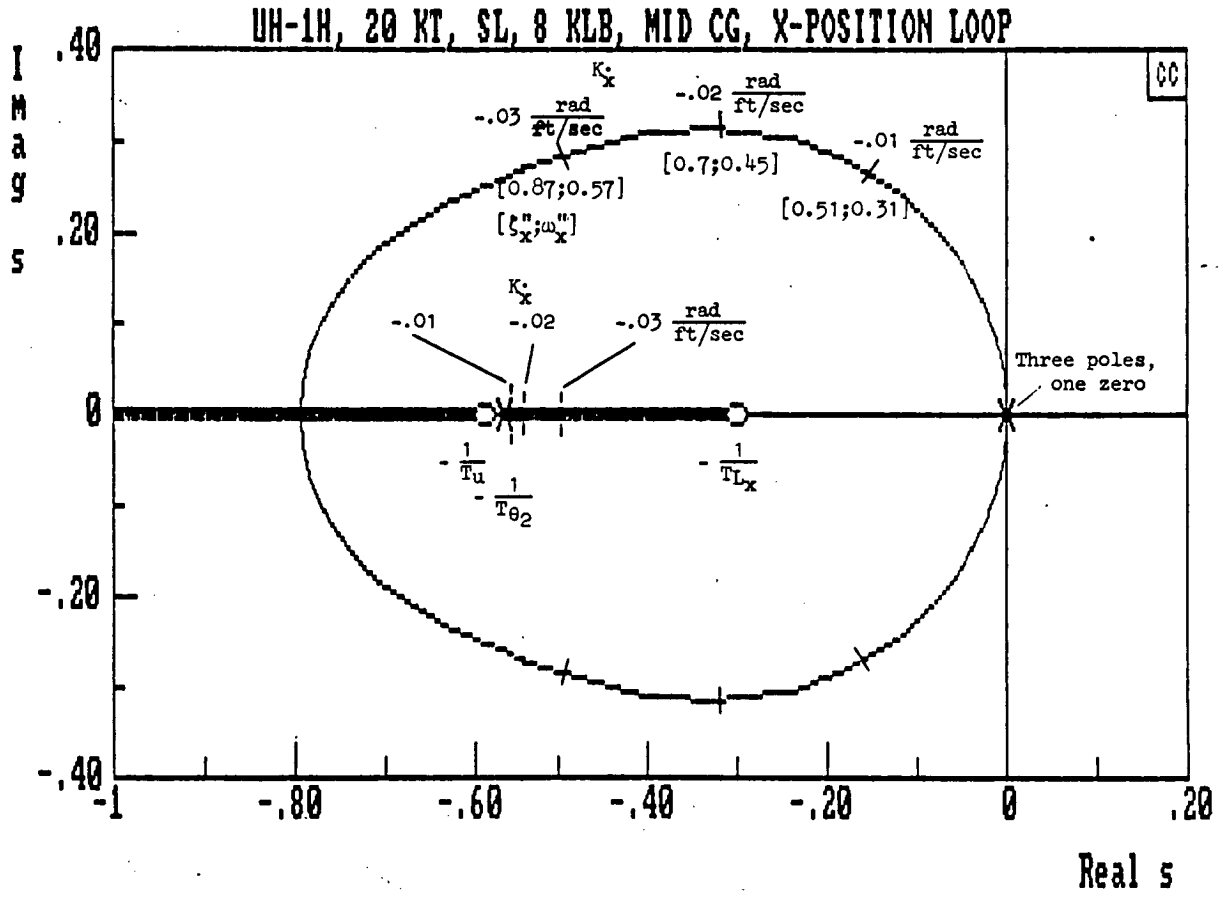

Figure 47. Effects of Varying Longitudinal Position-to-Pitch Attitude Control Loop Gain $K_{\dot{x}}$ with Lead Compensation $1/T_{L_x}$ = 0.3 rad/sec and Without Height Regulation

natural frequencies are identified. There is no time delay in the mathematical model represented in Fig. 47. Likewise, the higher frequency pitch attitude dynamics vested in the residual oscillatory "pendulum component" characterized by the ω_u-ω_p' dipole (refer to Table 6, p. 38, and Appendix D, p. D-4) are not represented in Fig. 47*. The predominant characteristic dynamic mode of longitudinal translation will be of second order, because the heave damping subsidence is suppressed by the translation zero, $1/T_u \doteq 1/T_{\theta_2}$.

The higher frequency attitude dynamics associated with the $\omega_u - \omega_p'$ dipole shown in Table 6 and discussed in Appendix D are nevertheless important, because the amplitude of the residual pendulum oscillation tends to increase and eventually to become objectionable to the pilot as the gain K_x^* increases beyond the range shown in Fig. 47. Criteria for optimizing the gain K_x^*, and its accompanying dynamic effects on translation and attitude are discussed in Refs. 29 through 32 in the context of pilot opinion ratings derived from simulation and flight test experiments.

b. Transient Responses During a Time Optimal Bob-Down Without Wind Shear While Stationkeeping with Open-Loop Height Control

A more complete set of time histories and phase plane portraits during the rapid response phase of a time optimal 50-ft bob-down while stationkeeping in a steady 20 kt head wind (without any shear) is shown in Figs. 48 through 54. There is no VCHH capability. The heave damping

---

*"Higher frequency" refers to the frequency in the complex zero of the "pendulum dipole" represented by

$$\omega_u \doteq \sqrt{\frac{g}{X_{\delta_B}}\left(-M_{\delta_B}\right)}$$

where g is gravitational acceleration and, if δ_B is expressed in terms of swashplate angle in radians, $X_{\delta_B} \doteq g$ in hovering and at low speeds typical of NOE operations.

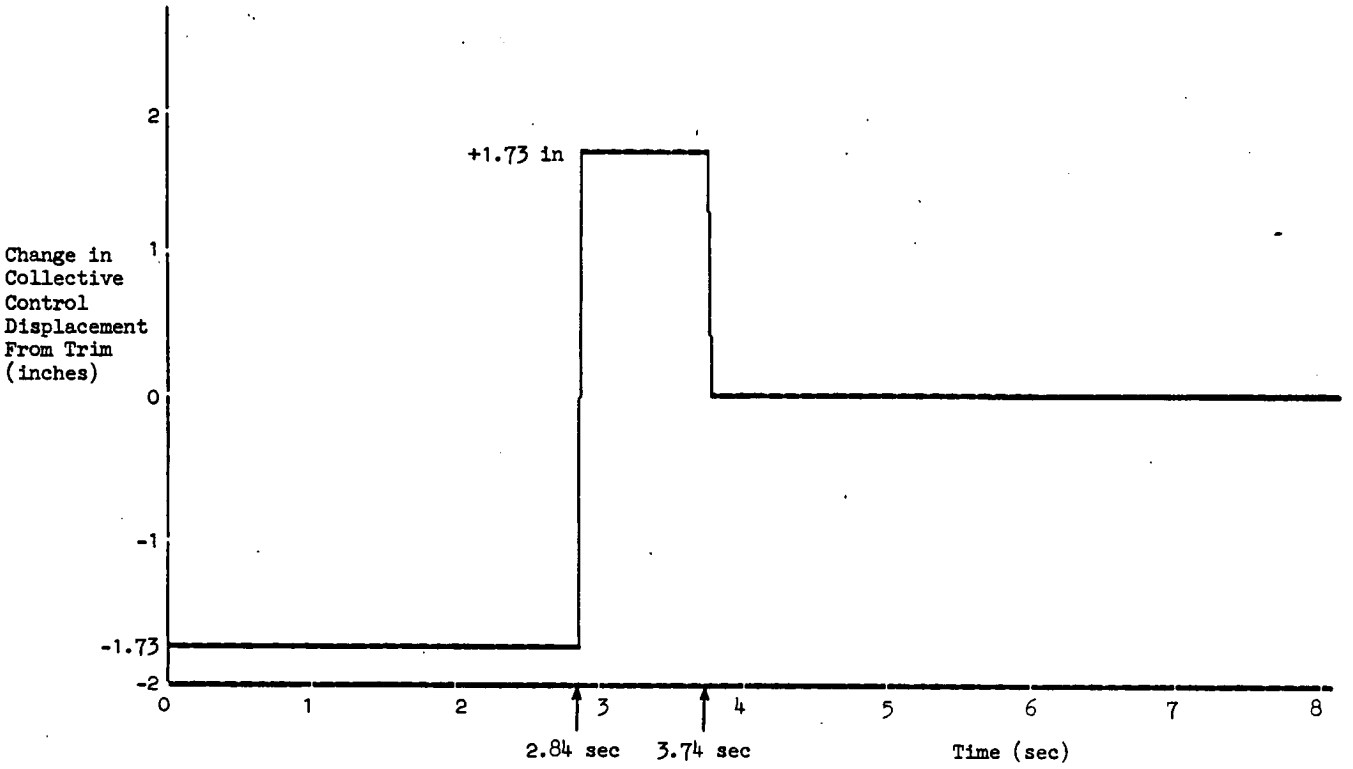

Y_c = h/COLL for the UH-1H; no Shear; 20 kts

Figure 48. Programmed Optimal Time History of Collective Control for 50-ft Descent Controlled Element Transfer Function

$$Y_c(s) = [h(s)/\delta_{COLL}(s)] = [9.29/s(s + 0.567)] \text{ ft/in}$$

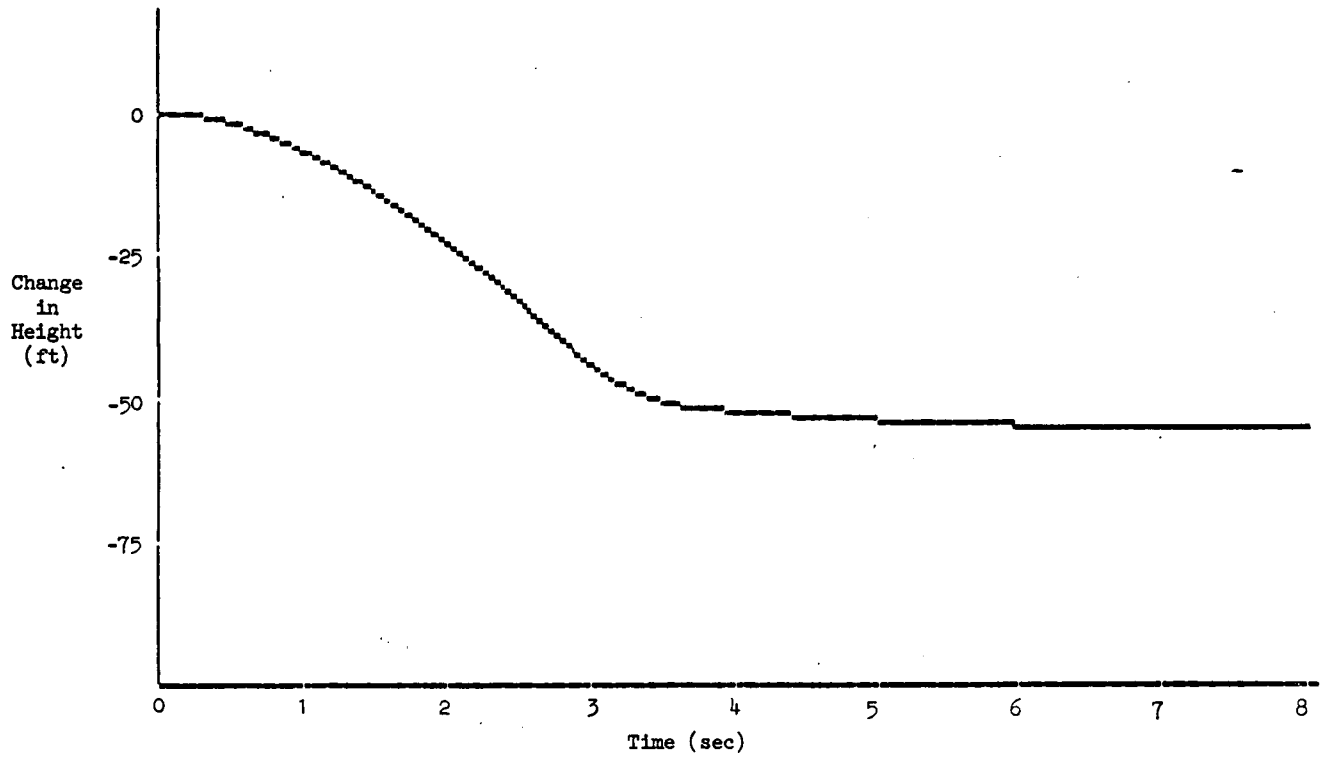

Y_c = h/COLL for the UH-1H; no Shear; 20 kts

Figure 49. Time-Optimal Descent of 50 ft with Programmed Open-Loop Collective Control for Controlled Element Transfer Function

$$Y_c(s) = \left[h(s)/\delta_{COLL}(s)\right] = [9.29/s(s + 0.567)] \text{ ft/in}$$

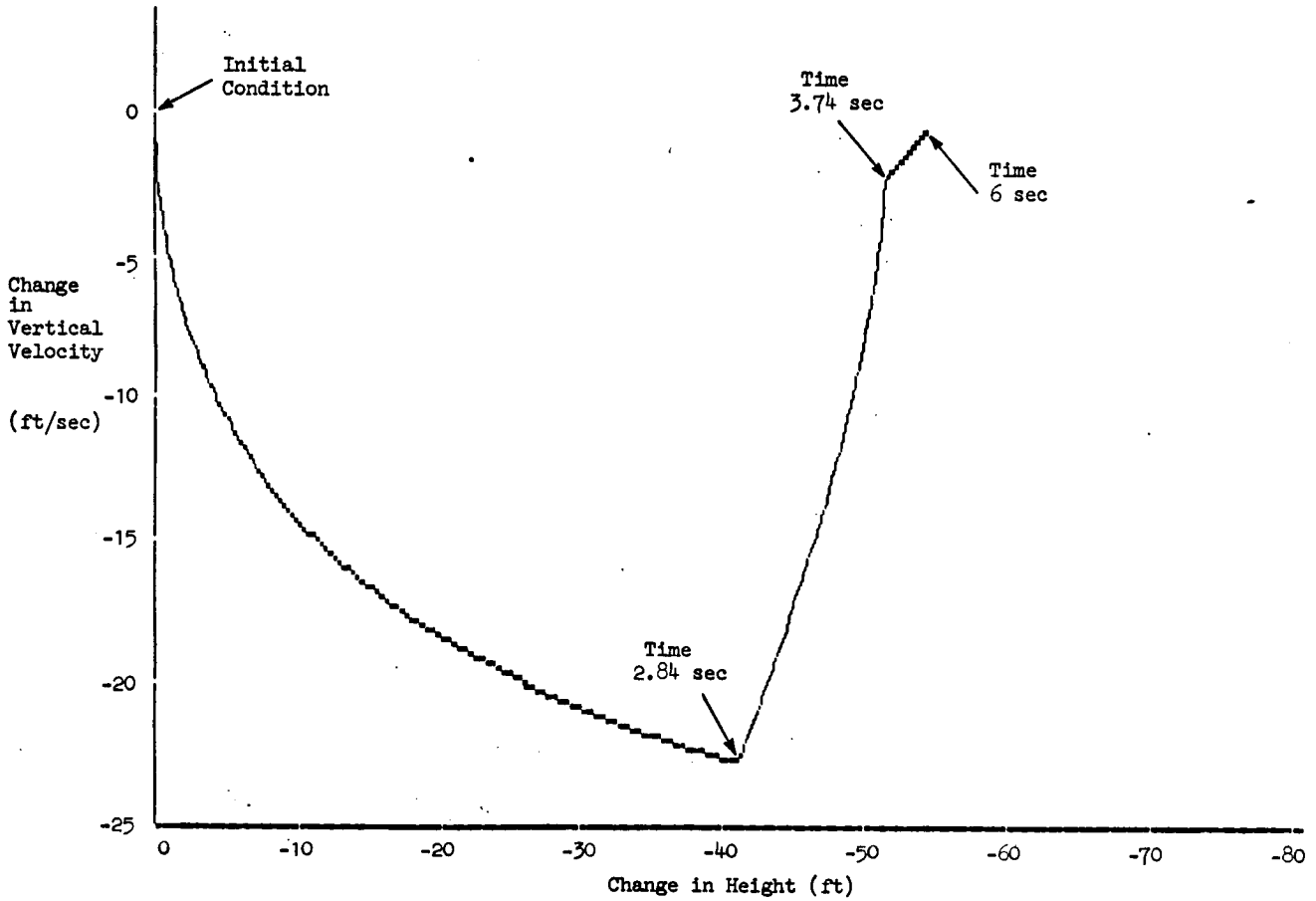

Y_c = h/COLL for the UH-1H; no Shear; 20 kts

Figure 50. Phase Plane for Time-Optimal Descent of 50 ft with Programmed Open-Loop Collective Control for Controlled Element Transfer Function

$$Y_c(s) = \left[h(s)/\delta_{COLL}(s)\right] = [9.29/s(s + 0.567)] \text{ ft/in}$$

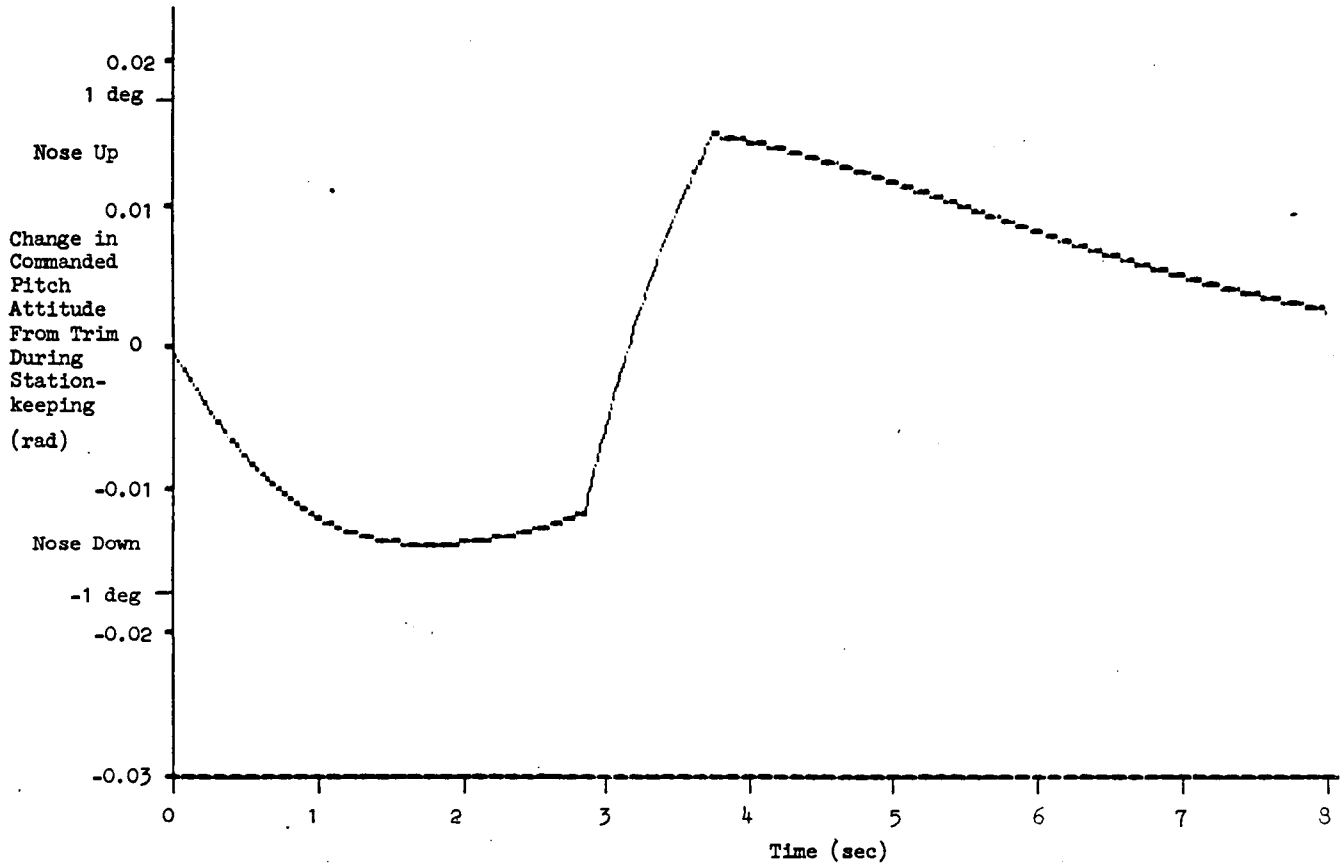

UH-1H at 20 kts, Sea Level, 8000 lbs, mid c.g., no shear.
Closed-Loop Transfer Function of Controlled Element for
$K_x^{\bullet} = -0.02$ rad θ_c/ft/sec and $1/T_{L_x} = 0.3$ rad/sec Without Wind Shear:

$$\frac{N^x_{\delta_{COLL}}}{\Delta''} = \frac{0.01126(s + 0.3)(s - 0.0600)}{(s + 0.543)[s^2 + 2(0.715)(0.449)s + (0.449)^2]} \frac{\text{rad}}{\text{in}}$$

Figure 51. Change in Commanded Pitch Attitude From Trim During Stationkeeping Accompanying Time Optimal Descent of 50 ft with Programmed Open-Loop Collective Control

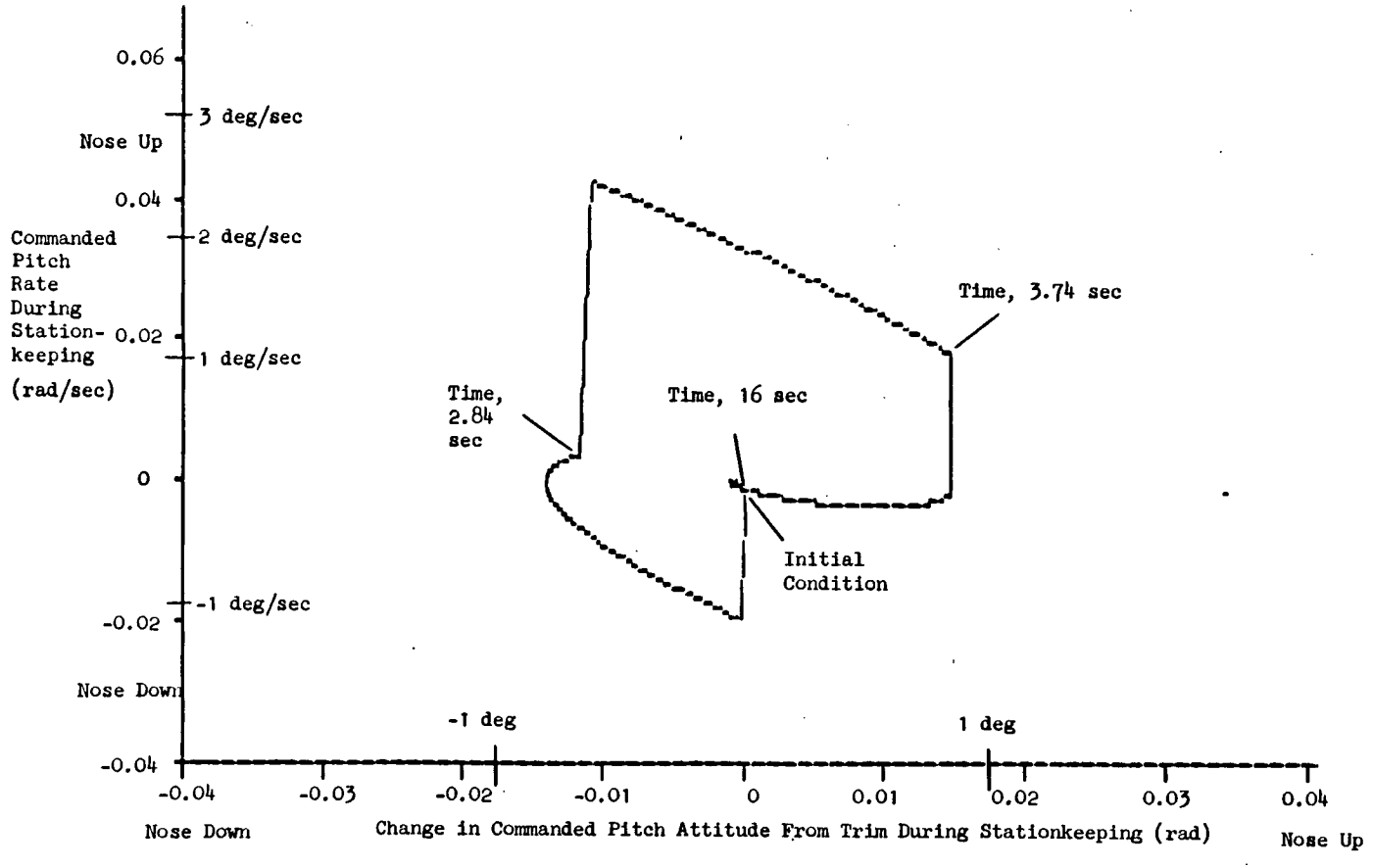

Figure 52. Phase Plane for Change in Commanded Pitch Attitude From Trim During Stationkeeping Accompanying Time-Optimal Descent of 50 ft with Programmed Open-Loop Collective Control. UH-1H at 20 kts, Sea Level, 8000 lbs, No Shear.

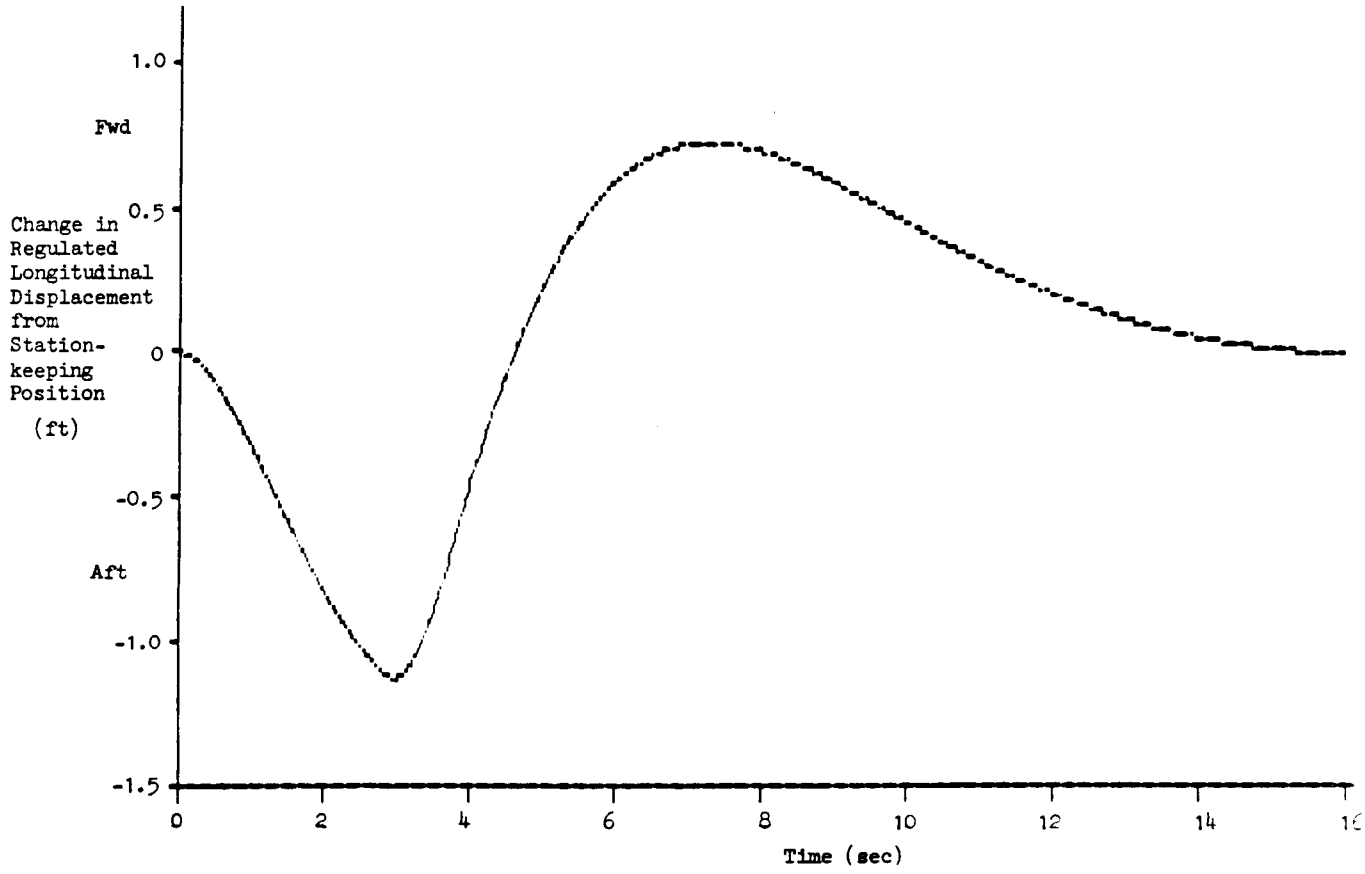

UH-1H at 20 kts, Sea Level, 8000 lbs, mid c.g., no shear.
Closed-Loop Transfer Function of Controlled Element for
$K_x^{\bullet} = -0.02$ rad θ_c/ft/sec and $1/T_{L_x} = 0.3$ rad/sec Without Wind Shear:

$$\frac{N_{\delta_{COLL}}^{x}}{\Delta''} = \frac{0.563s(s - 0.0600)}{s(s + 0.543)\left[s^2 + 2(0.715)(0.449)s + (0.449)^2\right]} \frac{ft}{in}$$

Figure 53. Change in Regulated Longitudinal Displacement From Stationkeeping Position Accompanying Time Optimal Descent of 50 ft with Programmed Open-Loop Collective Control

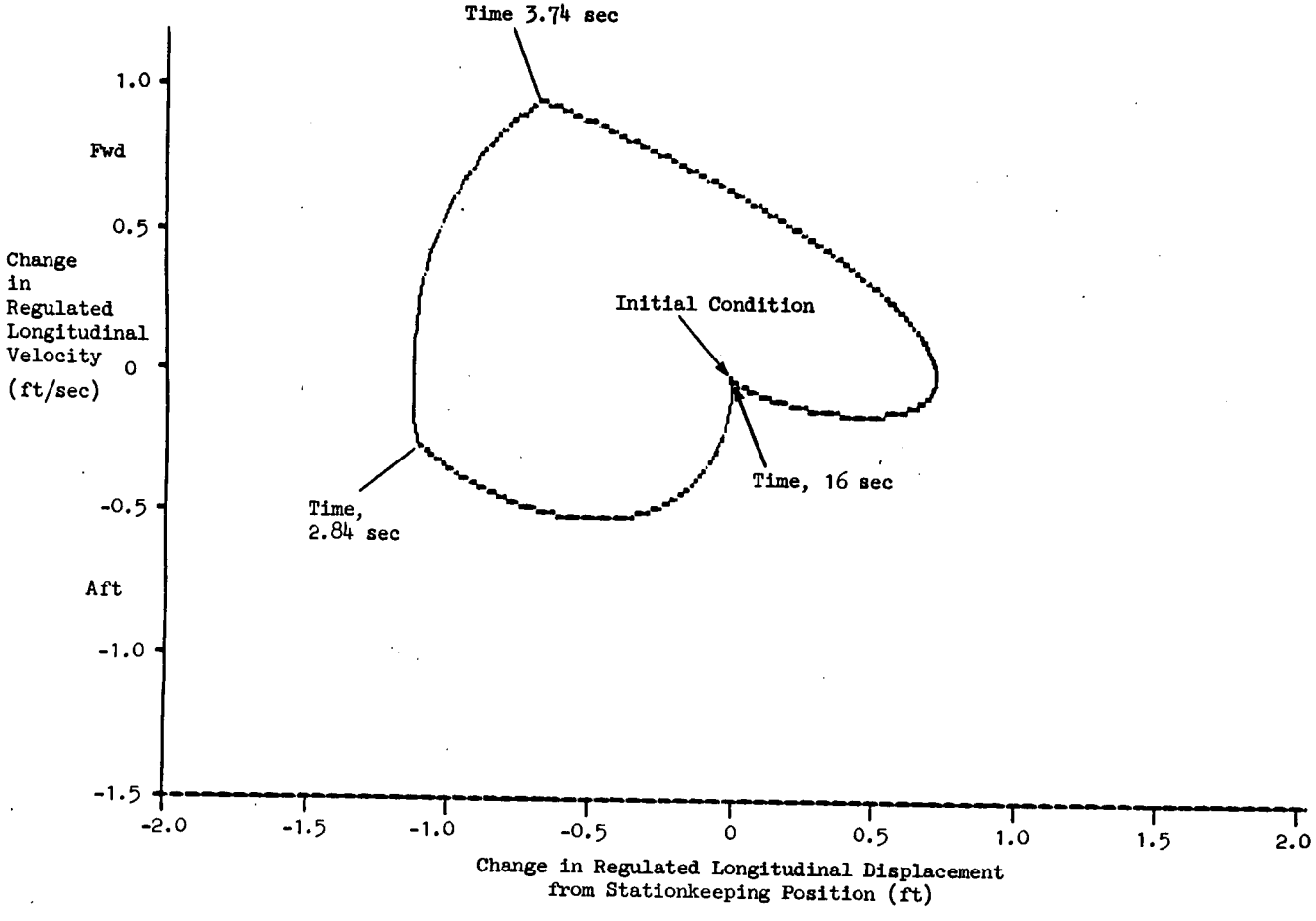

Figure 54. Phase Plane for Regulation of Longitudinal Stationkeeping Accompanying Time-Optimal Descent of 50 ft with Programmed Open-Loop Collective Control. UH-1H at 20 kts, Sea Level, 8000 lbs, No Shear.

($-Z_w$) in the example is 0.567 rad/sec, and the collective control acceleration effectiveness ($-Z_{\delta_c}$) is 9.29 ft/sec^2-in. The maneuver is performed by the open-loop time optimal collective control pulse sequence in Fig. 48, using ± 1.73 inches of collective authority from trim (10.7 inches = 100%). Changes in height and vertical velocity are displayed in Figs. 49 and 50, pitch attitude and rate command required for stationkeeping in Figs. 51 and 52, and transient longitudinal displacement deviation and velocity during stationkeeping in Figs. 53 and 54.

Figures 49 and 50 show that the 50 ft descent is completed in 3.74 sec, with a residual velocity of about -2 ft/sec, which decays to zero at 6 sec even with the compensatory height regulation loop open. The final unregulated height is -54 ft. The peak descent velocity at the collective control reversal time (2.84 sec) is -33.5 ft/sec.

Figures 51 and 52 show that the change in commanded pitch attitude required for automatic longitudinal stationkeeping regulation is within ± 0.9 deg and returns to trimmed attitude within 10 sec. The extreme pitch rates are -1.1 deg/sec (nose down) initially and 2.5 deg/sec (nose up) at the time of collective control reversal (2.84 sec).

Figures 53 and 54 show that the extreme values of displacement from the regulated longitudinal stationkeeping position are -1.1 ft (aft) at 3 sec and 0.7 ft (forward) at 7 sec. The initial stationkeeping position is restored in 16 sec, and the extreme values of regulated longitudinal velocity are -0.5 ft/sec (aft) at 1.5 sec and 0.9 ft/sec (forward) at 3.74 sec, when the descent is completed.

c. Effect of Headwind-to-Tailwind Shear with Decreasing Altitude on Longitudinal Stationkeeping During Bob-Down While Stationkeeping with Open-Loop Height Control

(1) Complex and Bode Root Loci of Closed-Loop Characteristics. Starting with each of the closed-loop characteristics represented in Fig. 47 and Figs. 55 and 56 then show the effect of a headwind-to-tailwind shear with decreasing altitude on the closed-loop stability of the longitudinal position control loop during

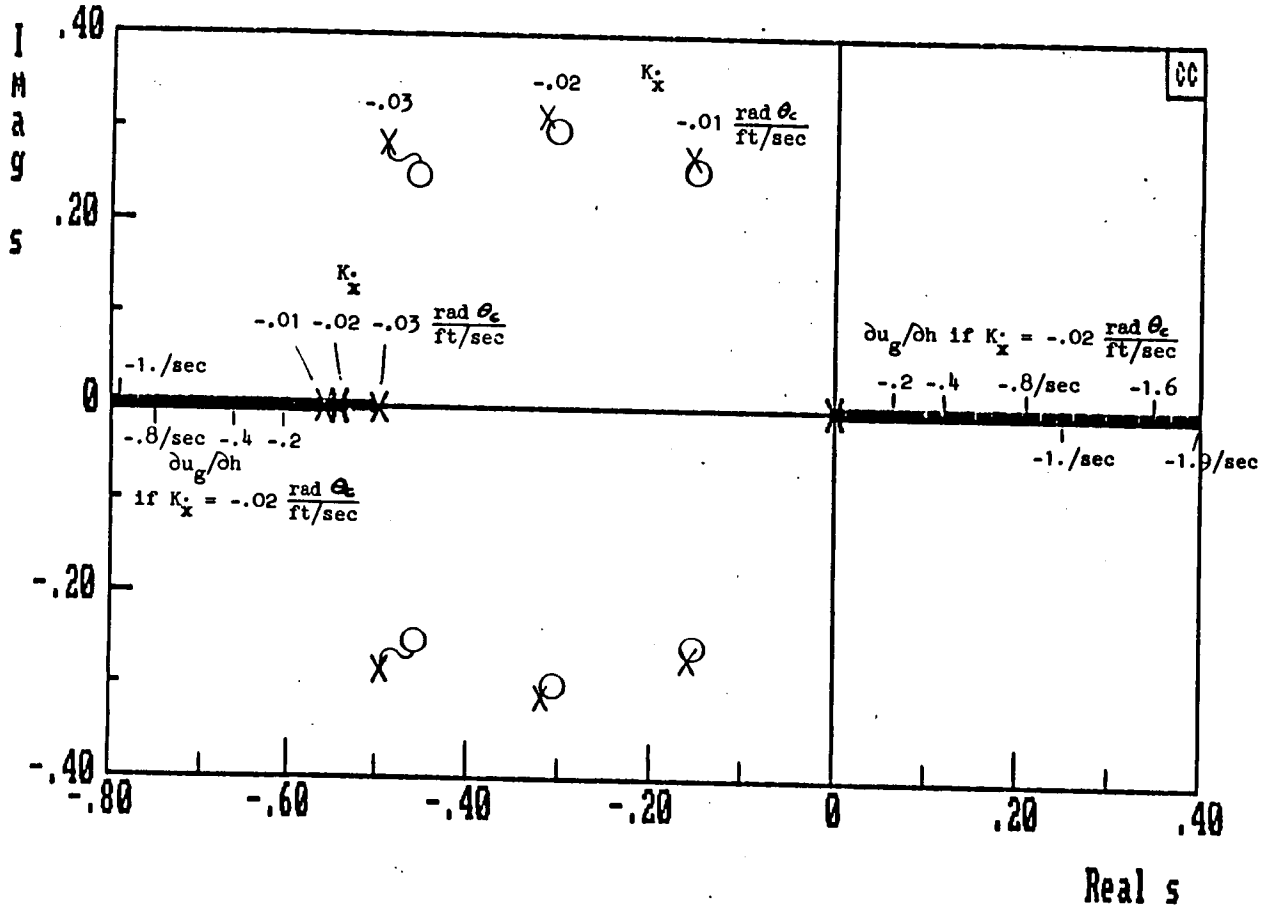

Figure 55. Complex Root Locus Showing Effect of Headwind-to-Tailwind Shear with Decreasing Altitude on Longitudinal Stationkeeping During Bob-Down With Open-Loop Height Control: $\partial u_g/\partial h < 0$. Longitudinal Position Loop Closed with Lead Compensation $1/T_{L_x}$ = 0.3 rad/sec. UH-1H at 20 kts, Sea Level, 8000 lb, mid cg.

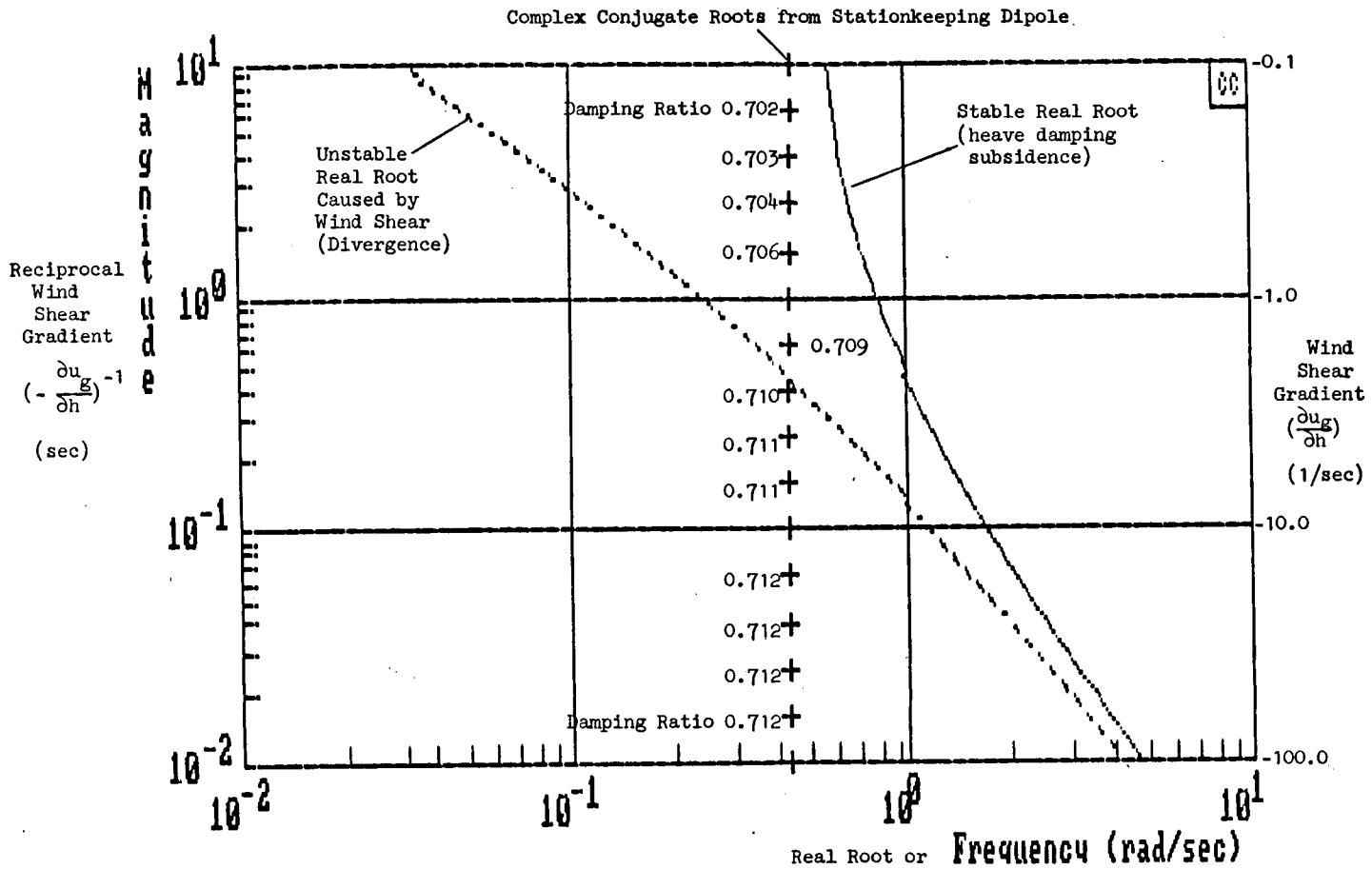

Figure 56. Sigma-Bode Root Locus Showing Effect of Headwind-to-Tailwind Shear with Decreasing Altitude on Longitudinal Stationkeeping During Bob-Down with Open-Loop Height Control: $\partial u_g/\partial h < 0$. Longitudinal Position Loop Closed Via Pitch Attitude with Lead Compensation $1/T_{L_x}$ = 0.3 rad/sec and High Frequency Gain K_x^* = -0.02 rad θ_c/ft/sec. UH-1H at 20 kts, Sea Level, 8000 lb, mid cg.

the rapid response phase with open-loop height control. The shear gradient causes immediate instability when there is no height regulation loop during the bob-down. Values of the divergence poles are shown along the real axis as a function of the gust gradient $\partial u_g/\partial h$ for a particular value of high-frequency gain $K_x^{\bullet} = -0.02$ rad/ft/sec. For example, if the shear gradient $\partial u_g/\partial h$ is -0.4/sec (-23.7 kts/100 ft), the divergence pole will be 0.12 rad/sec, which has a time to double amplitude of about 5.8 sec. If this shear gradient increases to -1.0/sec (-59.2 kt/100 ft), the divergence pole will roughly double to 0.24 rad/sec, which has a time to double amplitude of 2.9 sec. The results in Figs. 55 and 56 are not sensitive to the particular value of high-frequency position loop gain $K_x^{\bullet}$. Likewise, the results in Figs. 55 and 56 are not sensitive to the effects of delay in the longitudinal position loop. In fact, the results in Figs. 55 and 56 are substantially the same as would be obtained with only the attitude loops closed (Ref. 33).

(2) Transient Responses During a Time-Optimal Bob-Down in a Headwind-to-Tailwind Shear with Decreasing Altitude. Time histories and phase plane portraits of the divergent bob-down and station-keeping maneuvers with a shear gradient $\partial u_g/\partial h = -1.0$/sec are shown in Figs. 57 through 63 for comparison with Figs. 48 through 54. Since the 50-ft bob-down requires only 3.74 sec, the effect of the relatively rapid divergence can be nulled by closure of the compensatory height loop at the end of the maneuver. Nonetheless, the previous conclusion from the examples with velocity command-height hold is reinforced, viz., that the designer should try to provide reliable velocity command-position hold capability in all axes for superior immunity to wind shear in an automatic guidance and control system.

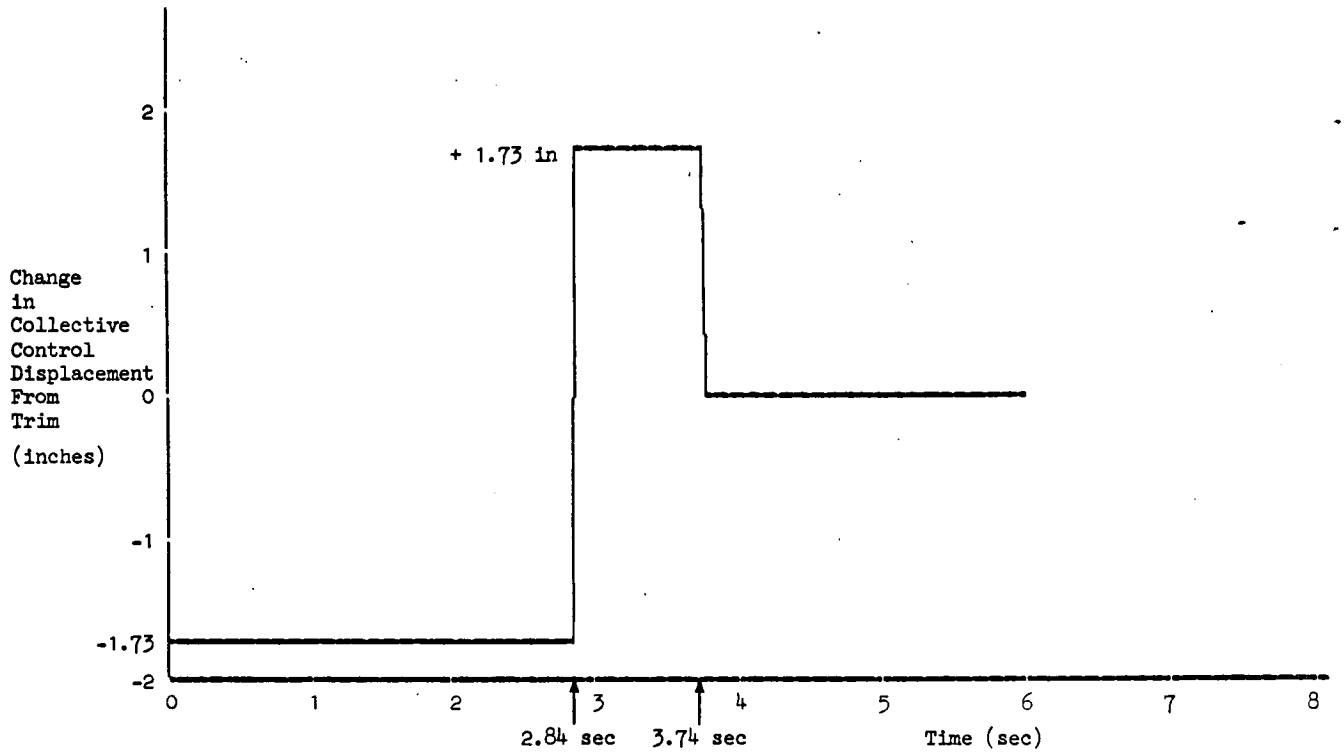

Y_c = h/coll for the UH-1H; -1.0/sec headwind-to-tailwind shear in descent (-59.2 kt/100 ft shear gradient)

Controlled Element Transfer Function

$$Y_c(s) = \left[h(s)/\delta_{coll}(s)\right] = [9.29/(s - 0.243)(s + 0.793)] \text{ ft/in}$$

Figure 57. Programmed Optimal Time History of Collective Control Appropriate for 50-ft Descent in the Absence of Wind Shear but Applied in the Presence of Wind Shear

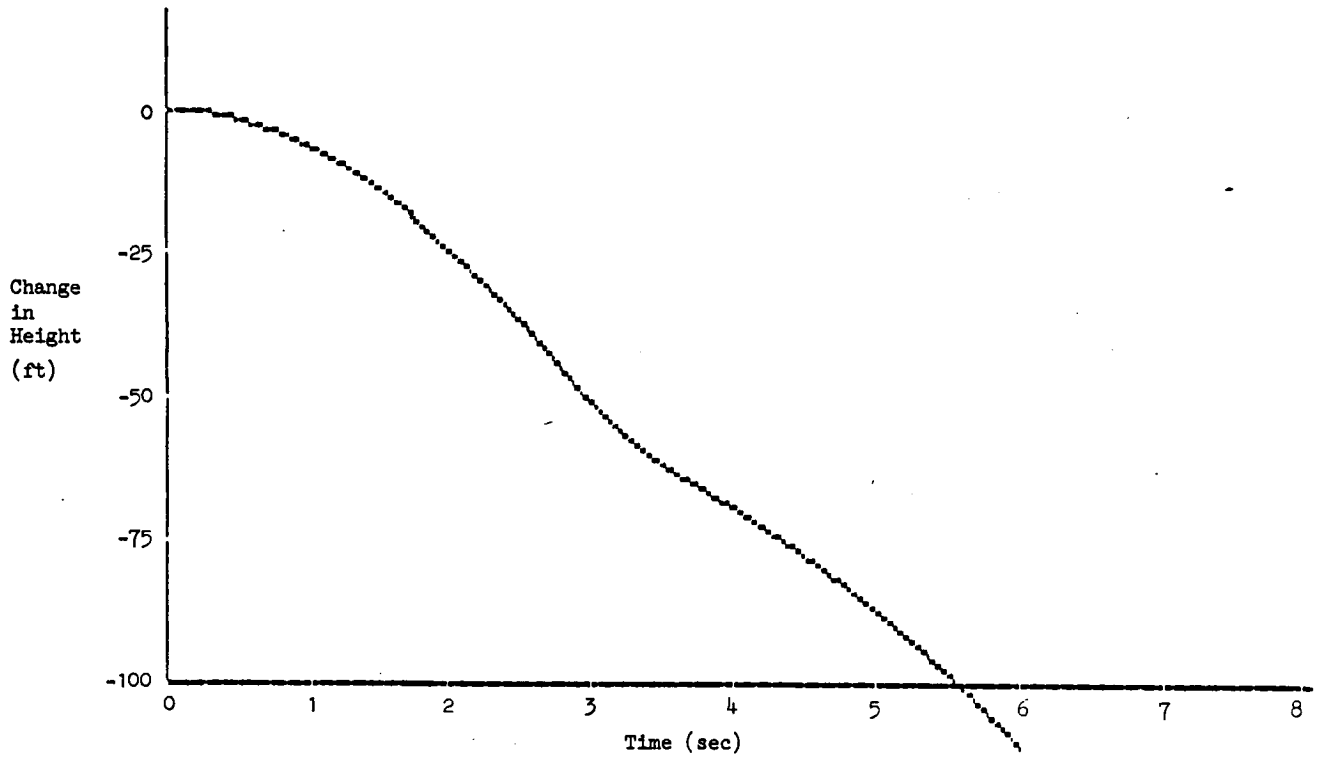

Y_c = h/coll for the UH-1H; -1.0/sec headwind-to-tailwind shear in descent (-59.2 kt/100 ft shear gradient)

Controlled Element Transfer Function

$$Y_c(s) = \left[h(s)/\delta_{coll}(s)\right] = [9.29/(s - 0.243)(s + 0.793)] \text{ ft/in}$$

Figure 58. Descent Time History with Programmed Open-Loop Collective Control Appropriate for a Time Optimal Descent of 50 ft Showing Destabilizing Effect of Wind Shear $\partial u_g/\partial h < 0$

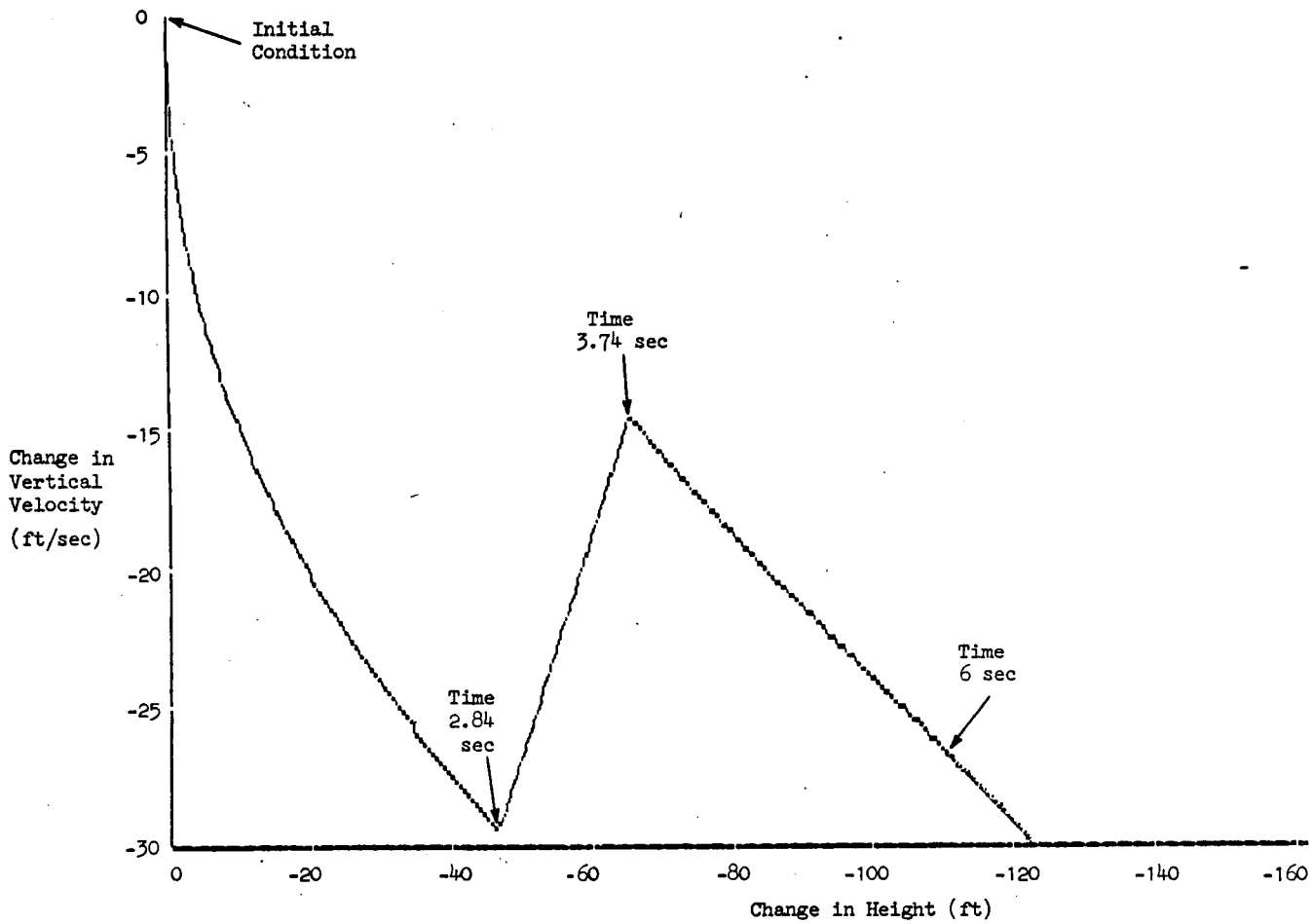

Y_c = h/coll for the UH-1H; -1.0/sec headwind-to-tailwind shear in descent

Controlled Element Transfer Function

$$Y_c(s) = \left[h(s)/\delta_{coll}(s)\right] = [9.29/(s - 0.243)(s + 0.793)] \text{ ft/in}$$

Figure 59. Phase Plane for Descent with Programmed Open-Loop Collective Control Appropriate for a Time Optimal Descent of 50 ft Showing Destabilizing Effect of Wind Shear $\partial u_g/\partial h < 0$

(Gradient -1.0/sec = -59.2 kt/100 ft)

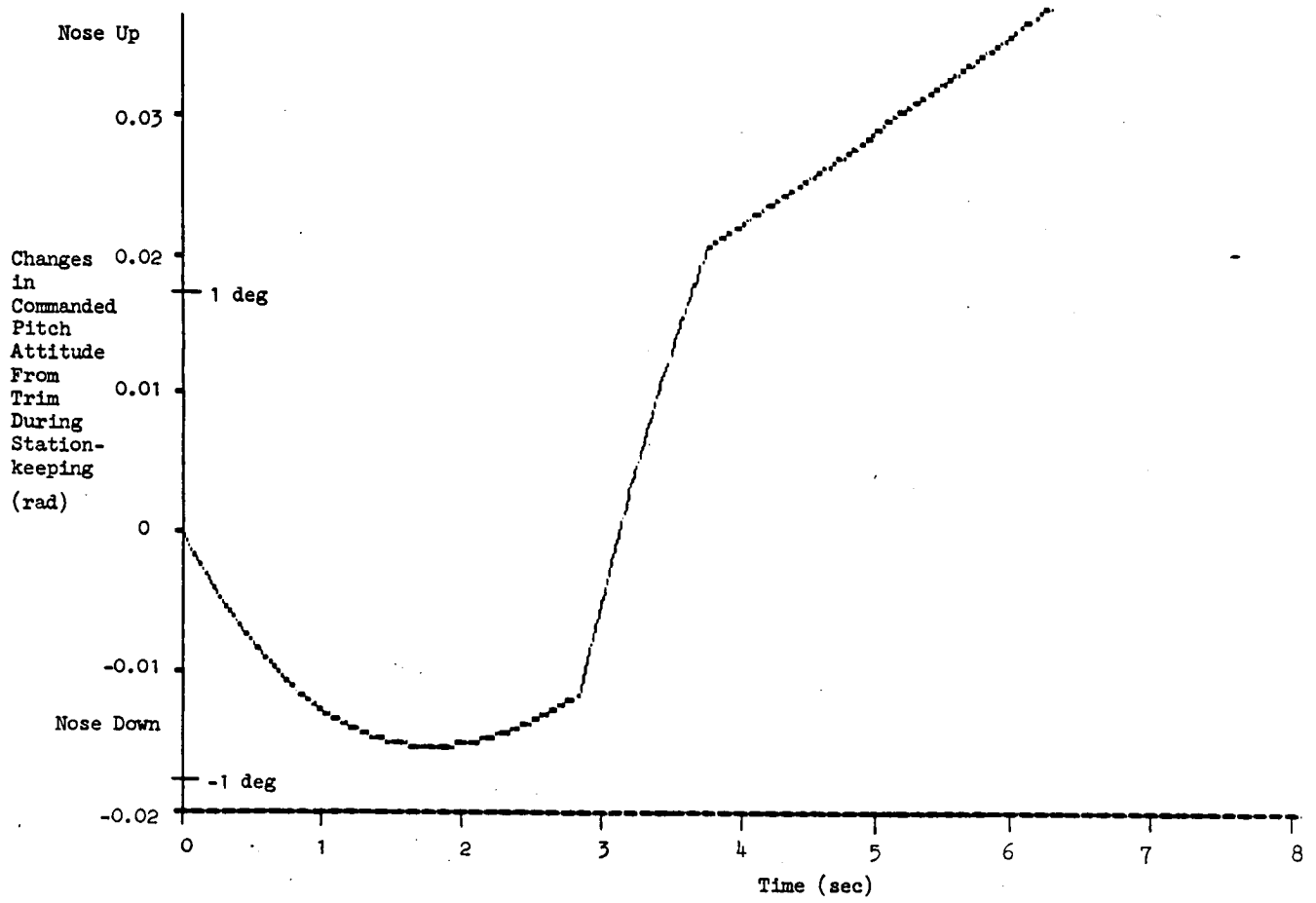

UH-1H at 20 kts, Sea Level, 8000 lbs, -1.0/sec headwind-to-tailwind shear in descent (-59.2 kt/100 ft shear gradient)

Closed-Loop Transfer Function of Controlled Element for $K_x^{\bullet} = -0.02$ rad θ/ft/sec and $1/T_{L_x} = 0.3$ rad/sec Without Wind Shear

$$\frac{N^{x}_{\delta_{coll}}}{\Delta''} = \frac{[0.01126(s + 0.3)(s - 0.4624)(s + 0.5224)]}{(s + 0.243)(s + 0.7934)[s^2 + 2(0.7075)(0.4336)s + (0.4336)^2} \text{ rad/in}$$

Figure 60. Change in Commanded Pitch Attitude From Trim During Stationkeeping with Programmed Open-Loop Collective Control Appropriate for a Time Optimal Descent of 50 ft Showing Destabilizing Effect of Wind Shear $\partial u_g/\partial h < 0$

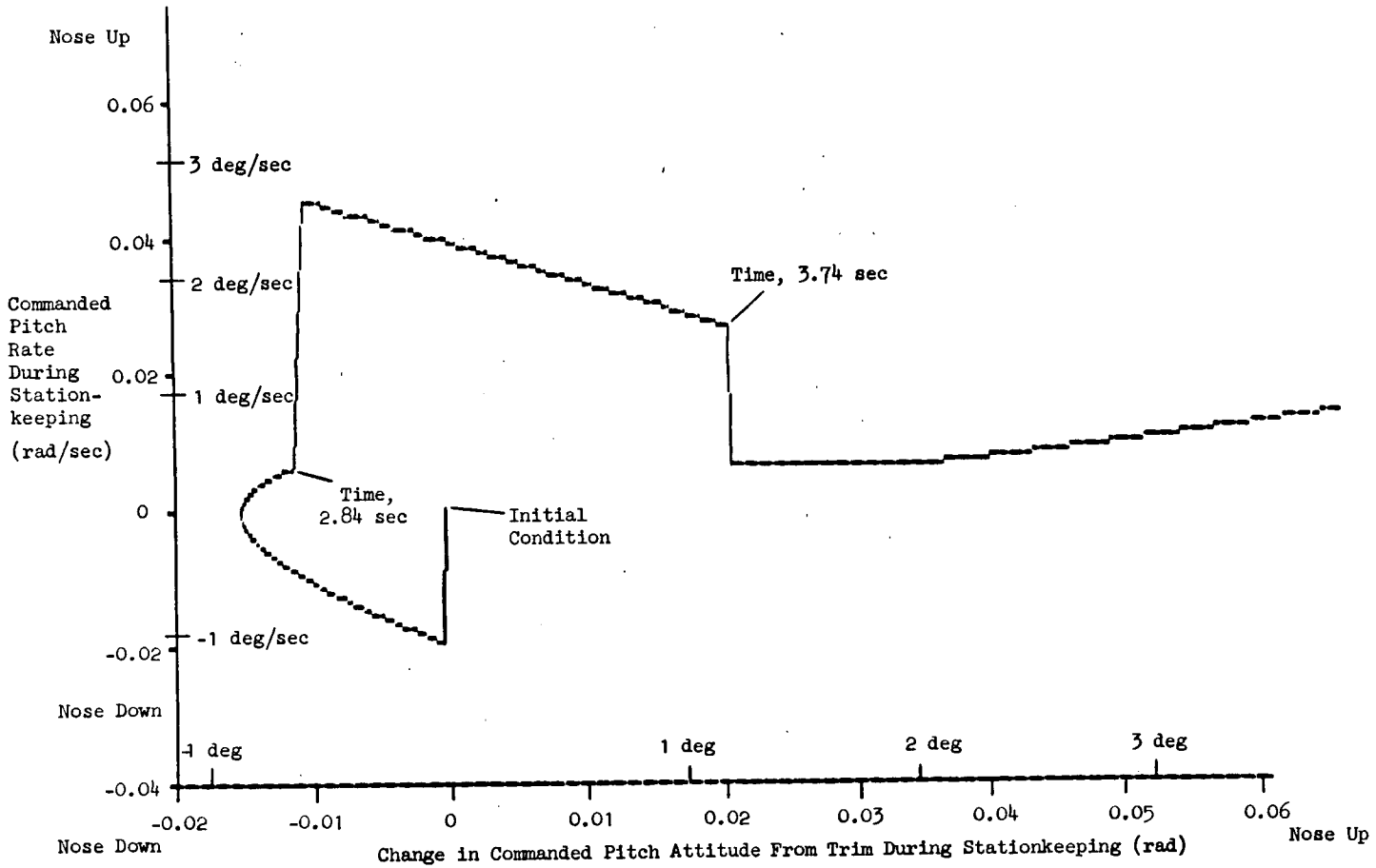

UH-1H at 20 kts, Sea Level, 8000 lbs, -1.0/sec headwind-to-tailwind shear in descent (-59.2 kt/100 ft shear gradient)

Closed-Loop Transfer Function of Controlled Element for
$K_x^{\bullet} = -0.02$ rad θ/ft/sec and $1/T_{L_x} = 0.3$ rad/sec Without Wind Shear

$$\frac{N^x_{\delta_{coll}}}{\Delta''} = \frac{[0.01126(s + 0.3)(s - 0.4624)(s + 0.5224)]}{(s + 0.243)(s + 0.7934)[s^2 + 2(0.7075)(0.4336)s + (0.4336)^2} \text{ rad/in}$$

Figure 61. Phase Plane for Change in Commanded Pitch Attitude From Trim During Stationkeeping with Programmed Open-Loop Collective Control Appropriate for a Time Optimal Descent of 50 ft Showing Destabilizing Effect of Wind Shear $\partial u_g/\partial h < 0$

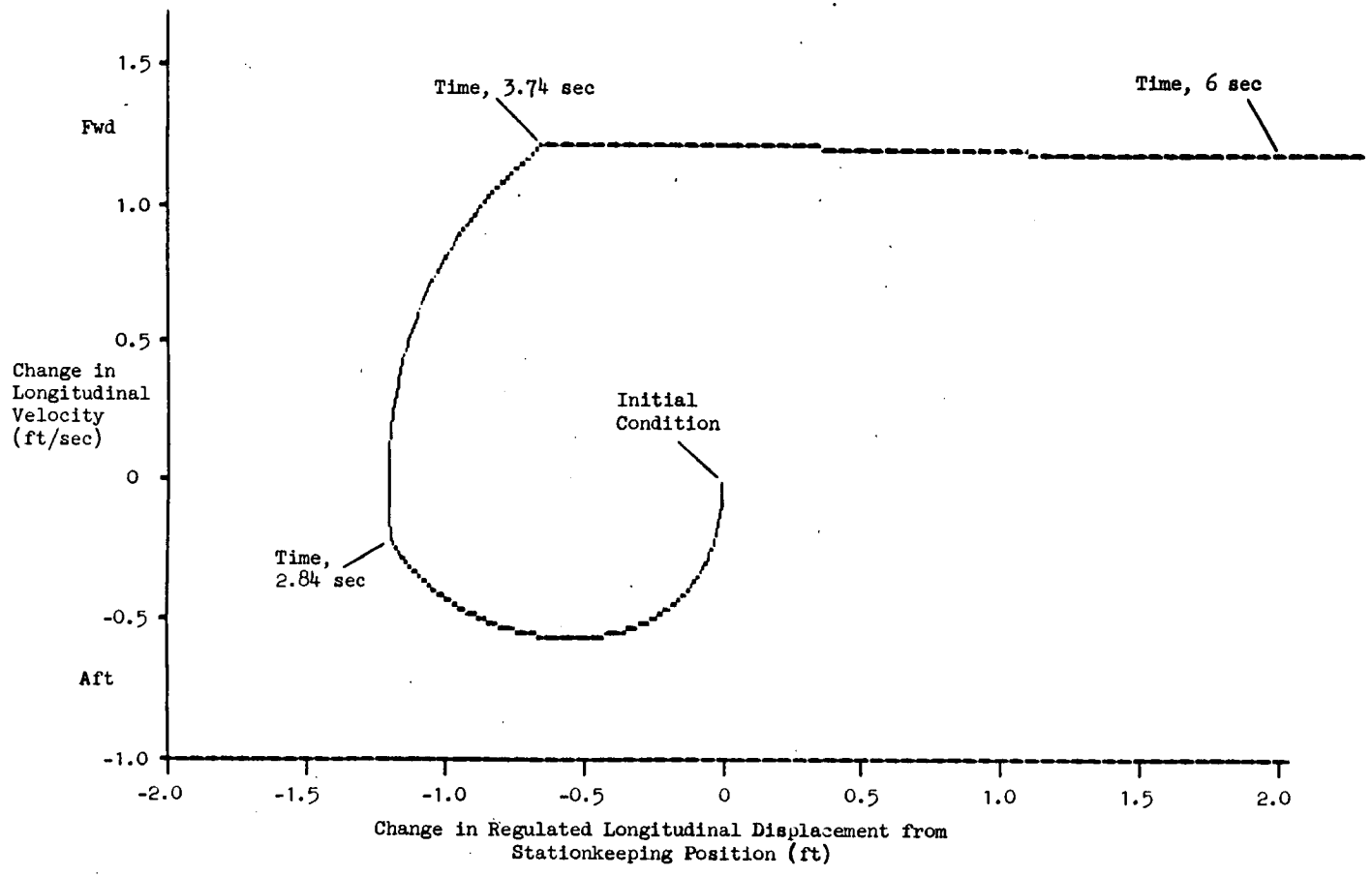

UH-1H at 20 kts, Sea Level, 8000 lbs, -1.0/sec headwind-to-tailwind shear in descent (-59.2 kt/100 ft shear gradient)

Closed-Loop Transfer Function of Controlled Element for
$K_x^{\bullet}$ = -0.02 rad θ/ft/sec and $1/T_{L_x}$ = 0.3 rad/sec Without Wind Shear

$$\frac{N^{x}_{\delta_{coll}}}{\Delta''} = \frac{0.563(s - 0.4624)(s - 0.5224)}{(s - 0.243)(s + 0.7934)[s^2 + 2(0.7075)(0.4336)s + (0.4336)^2} \text{ rad/in}$$

Figure 62. Phase Plane for Regulated Longitudinal Displacement from Stationkeeping Position with Programmed Open-Loop Collective Control Appropriate for a Time Optimal Descent of 50 ft Showing Destabilizing Effect of Wind Shear $\partial u_g/\partial h < 0$

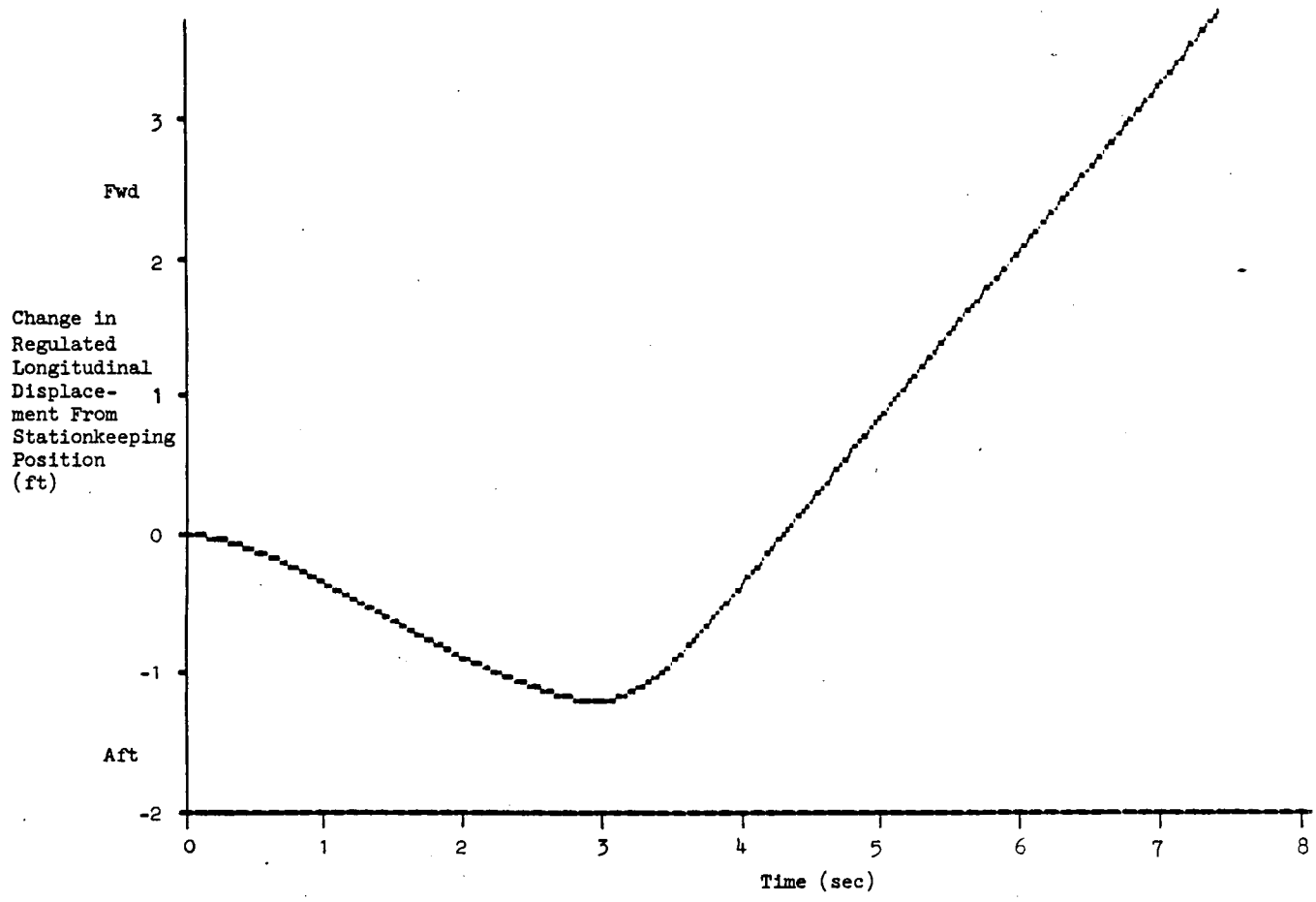

UH-1H at 20 kts, Sea Level, 8000 lbs, -1.0/sec headwind-to-tailwind shear in descent (-59.2 kt/100 ft shear gradient)

Closed-Loop Transfer Function of Controlled Element for $K_x^{\bullet} = -0.02$ rad θ/ft/sec and $1/T_{L_x} = 0.3$ rad/sec Without Wind Shear

$$\frac{N_{\delta_{coll}}^{x}}{\Delta''} = \frac{0.563(s - 0.4624)(s - 0.5224)}{(s + 0.243)(s + 0.7934)[s^2 + 2(0.7075)(0.4336)s + (0.4336)^2} \text{ rad/in}$$

Figure 63. Change in Regulated Longitudinal Displacement from Stationkeeping Position with Programmed Open-Loop Collective Control Appropriate for a Time Optimal Descent of 50 ft Showing Destabilizing Effect of Wind Shear $\partial u_g/\partial h < 0$

C. EFFECT OF HEADWIND-TO-TAILWIND SHEAR WITH FORWARD DISPLACEMENT ON LONGITUDINAL POSITION CONTROL

Figures 64 and 65 show the effect of the headwind-to-tailwind shear with forward displacement, $\partial u_g/\partial x > 0$, on the closed-loop dynamics of the longitudinal position-to-pitch attitude control loop. The lead compensation $1/T_{L_x}$ is constant at 0.3 rad/sec, and the gain $K_x^* = 0.01$ rad θ_c/ft/sec. Note that this is a horizontal displacement-dependent shear; consequently, the longitudinal position control loop tends to resist the gradient of gust velocity with position. Since the horizontal-displacement-dependent shear acts on the vehicle through surge damping (X_u), the very low value of surge damping for this particular example makes the closed-loop characteristics particularly resistant to the effects of this type of shear. Although this shear causes an immediate divergence, the divergence pole is so small, even for extremely large shear gradients, that the time to double amplitude is very long. Even if the surge damping were doubled, half of the gradient shown in Figs. 64 and 65 would produce the same effects on the closed-loop system. Even then, the smallest of the shears is so extraordinarily large as to be extremely rarely encountered.

The conclusion, then, for longitudinal position-to-pitch attitude control is that it provides a virtual immunity to horizontal-displacement-dependent wind shear effects.

This completes our summary of activities on Task III. We shall complete this discussion of all Phase I activities with a summary of findings in Section V for each of the tasks that constitute this phase of the study.

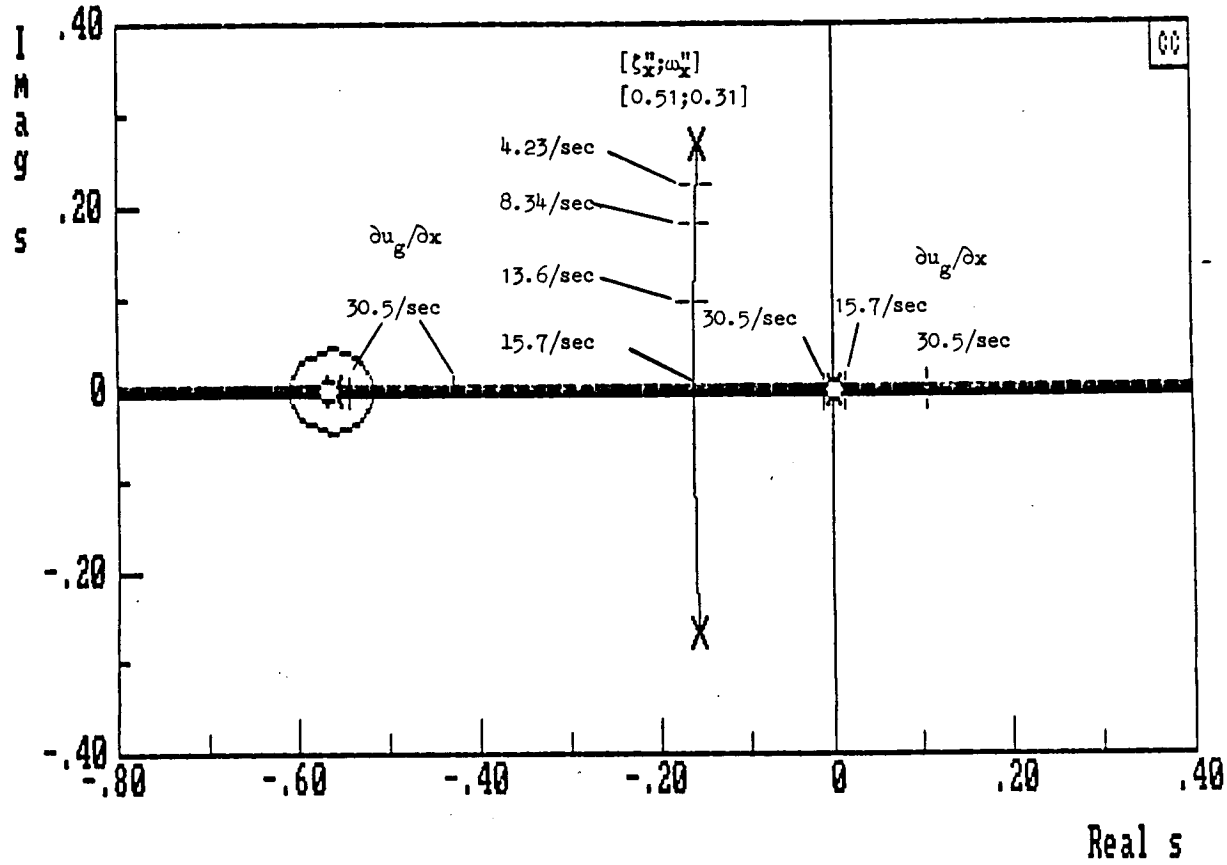

UH-1H at 20 kt, Sea Level, 8000 lb, Mid cg

Longitudinal Position-to-Pitch Attitude Control Closed with Lead Compensation $1/T_{L_x}$ = 0.3 rad/sec and Gain K_x^* = -0.01 rad θ_c/ft/sec

Figure 64. Complex Root Locus Showing Effect of Headwind-to-Tailwind Shear with Forward Displacement on Longitudinal Position Control: $\partial u_g/\partial x > 0$

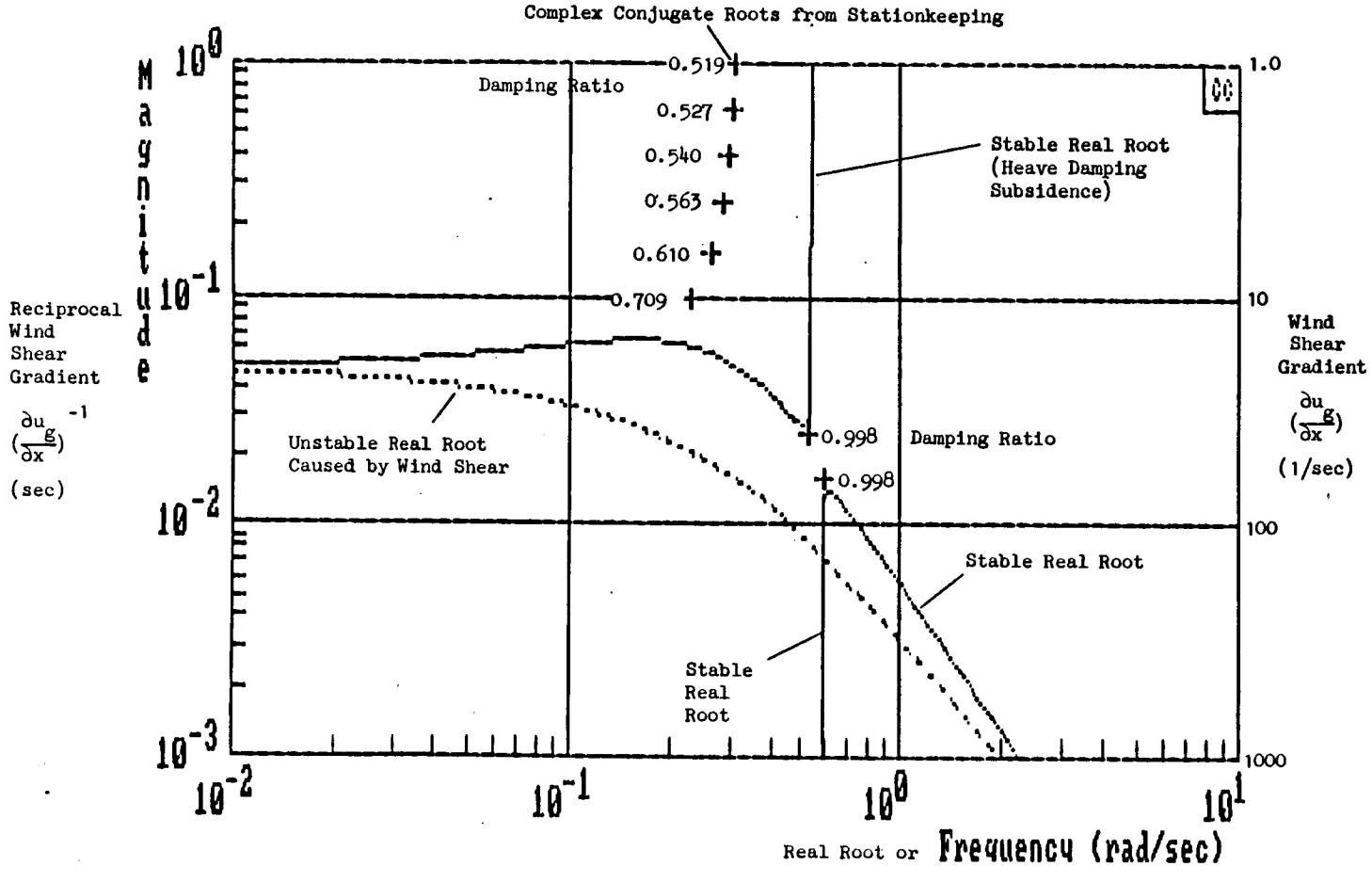

UH-1H at 20 kts, Sea Level, 8000 lbs, mid c.g.; Longitudinal Position-to-Pitch Attitude Control Loop Closed with Lead Compensation $1/T_{L_x}$ = 0.3 rad/sec and Gain K_x^* = -0.01 rad θ_c/ft/sec

Figure 65. Sigma-Bode Root Loci Showing Effect of Headwind-to-Tailwind Shear with Forward Displacement on Longitudinal Position Control: $\partial u_g/\partial x > 0$

SECTION V

SUMMARY OF FINDINGS

This section summarizes the principal findings for each of the tasks that constitute this phase of the study.

A. TASK I: STORAGE AND UPDATING OF TERRAIN PROFILES

The study investigated the representation of the guidance command vector for a planned flight profile in terms of a combination of polynomial and harmonic functions of along-course and across-course coordinates, i.e., a vector of truncated Taylor and Fourier series. Examples of flight profiles were sampled from a 5 km x 5 km digitized terrain model having 1 dm resolution. The examples for which finite Fourier transforms were obtained exhibited effective spatial bandwidths of about 0.2 rad/dm. At 20 kt forward speed, spatial bandwidth in rad/dm and temporal bandwidth in rad/sec are virtually identical. Thus we can expect a typical guidance and control system to follow an offset profile over these samples with good precision of 20 to 40 kt forward speed.

The techniques examined for representing a planned flight profile using Fourier series descriptors achieved data compression ratios between 8:1 and 10:1 for the samples of vertical profiles from the particular terrain data base used. The resulting recommendations for compressing flight profile data storage requirements are summarized in Table 5, p. 27.

A procedure is outlined for updating and modifying the stored guidance command flight profiles in real time to provide unexpected sensed obstacle and threat avoidance using constrained time-optimal maneuver strategy. It remains to develop in the second phase of this study a rationale and procedure for correcting potential conflicts caused by unexpected obstacles and threats and returning to the flight plan safely by means of transition logic between the anticipative trajectory coupler and the constrained time-optimal maneuvers for avoiding obstacles.

B. TASK II: AUTOMATIC GUIDANCE FOR FOLLOWING FLIGHT PROFILES

The automatic guidance algorithms will employ estimates of anticipated vertical, lateral, and longitudinal deviation commands required to follow the desired path, course, and schedule, respectively, with feedforward compensation. Preview of both stored and sensed terrain and obstacle data is therefore essential to compensate for the inevitable and predictable processing delays and rotorcraft response lags.

That part of the guidance error associated with following commands may be reduced by an automatic pursuit feedforward guidance adjustment analogous to that which the pilot will adopt in following a fluctuating curved course if sufficient visual preview of the source slope and curvature are available. If incorporated in automatic guidance, this practical pursuit adjustment will enhance pilot acceptance of automatic guidance in following nap-of-the-earth profiles with precision. A stored data base for the flight profile will provide a practical basis for the preview necessary to implement this pursuit adjustment.

A significant degree of immunity from wind shears and turbulence can be provided by automatic velocity command-position hold guidance and control systems. A closed-loop height response-to-collective control bandwidth of 1.0 rad/sec with 0.7 damping ratio will provide superior immunity against a headwind-to-tailwind shear gradient with decreasing altitude in excess of -50 kt/100 ft, although a bandwidth of only 0.5 rad/sec will be fairly effective in countering lesser gradients. An intermediate range of closed-loop speed subsidence of 0.3 to 0.5 rad/sec will help to provide a more favorably balanced immunity than a higher subsidence in excess of 0.6 rad/sec, because the wind shear gradient $\partial u_g/\partial h < 0$ will itself cause the speed subsidence to increase.

C. TASK III: AUTOMATIC GUIDANCE FOR AGGRESSIVE NAP-OF-THE-EARTH MANEUVERS

Four distinctive multiaxis NOE maneuvers, each involving primarily one of the four rotorcraft controls as a commanded input, are critical to the

success of most NOE missions. These maneuvers include the (1) bob-up and -down, (2) hover turn, (3) dash-quickstop, and (4) sidestep. Recent Black Hawk (UH-60A) flight tests and simulation tests for the purpose of assessing the fidelity of simulated NOE maneuvers have shown that experienced pilots can perform nearly time-optimal bob-ups, hover turns, dash-quickstops, and sidesteps when circumstances require aggressive maneuvers. Time optimality therefore provides a well-defined and validated criterion for corresponding automatically controlled NOE maneuvers, if the pilot is to have confidence in the automated maneuvering technique.

The output of the feedforward element representing the rapid response technique for a skilled pilot is peculiar to each controlled element transfer function form $Y_c(s)$. The form $Y_c(s) = K_c/s(s+a)$ applies to the heading response-to-yaw control inputs in a hover turn with constrained attitude as well as to all four maneuvers with the velocity command-displacement hold guidance and control systems typically required for automatic NOE maneuvers. The optimal control pulse intervals are unequal in duration for performing aggressive maneuvers with controlled elements having the form $K_c/s(s+a)$; the starting pulse is longer than the final pulse when the damping coefficient a is substantial. Necessary constraints that contribute to suboptimality are rotor torque limitations and rotor speed governor recovery capability, control displacement and rate limitations, attitude displacment and rate limitations, and acceleration limitations in uncoordinated maneuvers.

Among the examples of design for time-optimal velocity command-height hold in a wind shear environment, the "worst case" design to preserve heave damping in an extreme wind shear $\partial u_g/\partial h \triangleq -59$ kt/100 ft is preferable, because it results in a conservative design that can be more easily re-optimized by velocity command amplitude and time interval adjustments in lesser gradients or in the absence of wind shear. Thus the designer should try to provide reliable velocity command-position hold capability in all axes for superior immunity to wind shear in an automatic guidance and control system for NOE operations.

The longitudinal position control loop tends to resist the gradient of longitudinal gust velocity with horizontal displacement, $\partial u_g/\partial x$. Since

the horizontal-displacement-dependent shear acts on the vehicle through surge damping (X_u), the very low value of surge damping for rotorcraft makes the closed-loop characteristics particularly resistant to the effects of this type of shear. Although this type of shear causes an immediate divergence, the divergence pole is so small, even for extremely large shear gradients, that the time to double amplitude is very long.

The conclusion, then, for longitudinal position-to-pitch attitude control is that it provides a virtual immunity to horizontal-displacement-dependent wind shear effects.

This completes our summary of findings on Tasks I, II, and III. We shall conclude this discussion of all Phase I activities with a summary in Section VI of pilot-centered considerations for monitoring automatically controlled NOE flight.

SECTION VI

CONCLUDING SUMMARY OF PILOT-CENTERED CONSIDERATIONS FOR MONITORING AUTOMATICALLY CONTROLLED NOE FLIGHT

A. AUTOMATIC-MANUAL CONTROL RESPONSE COMPATIBILITY

Automatic pursuit guidance for NOE operations will improve pilot acceptance of automatic course-and-profile following, because pursuit guidance is compatible with manual piloting technique if sufficient preview of the course-and-profile is available. Automatic guidance of aggressive tactical maneuvers for NOE operations based on principles of time-optimality (with appropriate control rate, attitude rate, and attitude constraints) will improve pilot acceptance, because time-optimality is compatible with measured manual piloting techniques under visual conditions in flight tests. Automatic control algorithms should weight the various motion and position feedback and feedforward signals so that the resulting rotorcraft motions are not disharmonious or dangerous (e.g., no excessive attitude overshoot to correct velocity or position error) but are similar to those experienced under visual manually controlled conditions. It also implies that a flight director be compatible with the automatic system. The control techniques for most NOE operations will be appropriate for speeds below that for minimum power required, viz., $h, \dot{h} \rightarrow \delta_C$; $x, \dot{x}, \theta \rightarrow \delta_B$; $y, \dot{y}, \phi \rightarrow \delta_A$; $\psi, \dot{\psi} \rightarrow \delta_p$

B. STATUS DISPLAYS

Status displays should provide cues similar to those in visual flight and should be compatible with any command display to inspire pilot confidence in an automatic control system. In particular for NOE operations, pursuit displays such as the pole-track (Refs. 34 through 36), channel (Refs. 37 and 38), and their antecedents (e.g., see the review in Ref. 39) will become necessary for course-and-profile following and maneuvering. Pursuit displays will very likely have to be complemented with auditory

command and status information during automatically guided constrained time-optimal maneuvering.

C. DECOUPLED CONTROL RESPONSES

Rotorcraft responses to control inputs are inherently coupled when there is but a single main rotor. The predominant coupled responses are those in yaw, pitch, and roll due to collective control inputs. Depending on the airspeed and the ambient winds, the coupled heading and attitude changes can also be accompanied by unwanted translational motions. The automatic system should compensate for collective coupling by simultaneously applying pedal, lateral stick, and longitudinal stick inputs when moving the collective control.

The prevalent direct and cross-coupled responses to rotorcraft controls are listed in Table 7 for a single main rotor. The columns are as follows: Column 1 identifies the name of the control, Column 2 identifies the direct response, Column 3 identifies the predominant cross-coupled responses, and Column 4 identifies the crossfeed required to decouple the response. Compensation for the cross-coupled responses to control inputs may consist of either or both crossfeeds between the controllers and/or feedbacks of the responses to the controllers. Feedback offers the additional advantage of compensation for responses to unmeasurable disturbances. Feedback also alters the automatic-manual control response compatibility of the vehicle. Using crossfeeds between the controllers reduces the unwanted vehicle response before it has time to build up. Thus the hybrid approach to using both crossfeeds and feedbacks offers a cost effective compromise.

This concludes our recitation of Phase I results. We have demonstrated initially the technical feasibility of the objectives of this research in terms of the specific findings of each task in Phase I.

TABLE 7. COMPENSATION FOR CROSS-COUPLED RESPONSE TO CONTROLS FOR A SINGLE MAIN ROTORCRAFT

Control	Direct Response	Cross-Coupled Responses	Compensating Control Crossfeeds to Suppress Cross-Coupled Responses
Collective, δ_C	Normal Velocity, w	Yaw Rate, r	$\delta_C \rightarrow \delta_P \equiv G_C^P$
		Roll Rate, p	$\delta_C \rightarrow \delta_A \equiv G_C^A$
		Pitch Rate, q	$\delta_C \rightarrow \delta_B \equiv G_C^B$
Yaw, δ_P	Yaw Rate, r	Normal Velocity, w	$\delta_P \rightarrow \delta_C \equiv G_P^C$
		Roll Rate, p	$\delta_P \rightarrow \delta_A \equiv G_P^A$
		Pitch Rate, q	$\delta_P \rightarrow \delta_B \equiv G_P^B$

REFERENCES

1. Grunwald, Arthur J., and S. J. Merhav, "Vehicular Control by Visual Field Cues--Analytical Model and Experimental Validation," IEEE Transactions on Systems, Man, and Cybernetics, Vol. SMC-6, December 1976, pp. 835-845.

2. Anon., Fully Automatic Guidance for Rotorcraft Nap-of-the-Earth Flight, NASA SBIR 85-1/03.08/4675, May 28, 1985.

3. Anon., Automation in Combat Aircraft, National Academy Press, Washington, D. C., 1982.

4. Clement, Warren F., and Wayne F. Jewell, Fully Automatic Guidance for Rotorcraft Nap-of-the-Earth Flight. Initial Briefing, July 11, 1986, STI Working Paper 1239-1, July 1986.

5. Magdaleno, Raymond E., Using FREDA and NIPIP to Model Terrain Via Fourier Series Descriptions, STI Working Paper 1239-2, August 1986.

6. Hanson, Gregory D., and Wayne F. Jewell, Non-Intrusive Parameter Identification Procedure User's Guide, NASA CR-170298, April 1983.

7. Jewell, W. F., and T. M. Schulman, A Pilot Control Strategy Identification Technique for Use in Multiloop Control Tasks, NASA CR-152374, Auguat 1980.

8. Jewell, Wayne F., Data Collection Requirements, A Pilot Control Strategy Measurement Technique and Verification Procedures for the Phase III HUD Program, NASA CR-152294, February 1980.

9. Allen, R. Wade, and Duane McRuer, "The Man/Machine Control Interface--Pursuit Control," Automatica, Vol. 15, No. 6, November 1979, pp. 683-686.

10. Stapleford, Robert L., Velocity Command/Position Hold: A New Flight Control Concept for Hovering VTOL Aircraft, STI Paper 270, August 1980.

11. Sinacori, J. B., The Determination of Some Requirements for a Helicopter Flight Research Simulation Facility, Systems Technology, Inc., Technical Report No. 1097-1, September 1977.

12. Whitbeck, Richard F., and L. G. Hofmann, Analysis of Digital Flight Control Systems with Flying Qualities Applications. Volume II: Technical Report, AFFDL-TR-78-115, September 1978.

13. Whitbeck, Richard F., Wiener-Hopf Approaches to Regulator, Filter/Observer, and Optimal Coupler Problems, ONR-CR215-260-1, January 1980.

14. Heffley, R. K., W. F. Jewell, R. F. Whitbeck, and T. M. Schulman, The Analysis of Delays in Simulator Digital Computing Systems. Volume One: Formulation of an Analysis Approach Using a Central Example Simulator Model, NASA CR-152340, October 1979.

15. Whitbeck, Richard F., Warren F. Clement, and Wayne F. Jewell, The Analysis of Delays in Simulator Digital Computing Systems. Volume Two: Formulation of Discrete State Transition Matrices--An Alternative Procedure for Multirate Digital Computations, Systems Technology, Inc., Technical Report No. 1140-1-II, February 1980.

16. Whitbeck, Richard F., and Dennis G. J. Didaleusky, Multi-Rate Digital Control Systems with Simulation Applications. Volume I: Technical Report, AFWAL-TR-80-3101, September 1980.

17. Whitbeck, Richard F., and Julian Wolkovitch, Optimal Terrain-Following Feedback Control for Advanced Cruise Missiles, Systems Technology, Inc., Technical Report No. 1147-2, January 1982.

18. Whitbeck, Richard F., James C. Smith, and Thomas T. Myers, Flight Test of Advanced Digital Control Concepts, AFWAL-TR-82-3021, March 1982.

19. Whitbeck, Richard F., Elements of Simulation Error Analysis, Systems Technology, Inc., Technical Report No. 1173-1, February 1982.

20. Myers, T. T., D. E. Johnston, and D. McRuer, Space Shuttle Flying Qualities and Flight Control System Assessment Study, NASA CR-170391, June 1982.

21. Ferguson, Samuel W., Warren F. Clement, William B. Cleveland, and David L. Key, "Assessment of Simulation Fidelity Using Measurements of Piloting Technique in Flight," Systems Technology, Inc., Paper No. 347, Presented at the 40th Annual Forum of the American Helicopter Society, Arlington, Virginia, May 1984.

22. Clement, Warren F., William B. Cleveland, and David L. Key, "Assessment of Simulation Fidelity Using Measurements of Piloting Technique in Flight," Systems Technology, Inc., Paper No. 348, Presented at the AGARD Guidance and Control Panel 38th Symposium, Helicopter Guidance and Control Systems for Battlefield Support, Monterey, California, May 1984.

23. Ferguson, Samuel W., Warren F. Clement, Roger H. Hoh, and William B. Cleveland, "Assessment of Simulation Fidelity Using Measurements of Piloting Technique in Flight--Part II," STI P-371, Presented at the 41th Annual Forum of the American Helicopter Society, Ft. Worth, Texas, May 1985.

24. Ferguson, Samuel W., and Warren F. Clement, Assessment of Simulation Fidelity Using Measurements of Piloting Technique in Flight, STI Technical Report 1184-1, August 1984, Revised March 1986.

25. McRuer, D. T., L. G. Hofmann, H. R. Jex, et al., New Approaches to Human-Pilot/Vehicle Dynamic Analysis, AFFDL-TR-67-150, February 1968.

26. Jewell, Wayne F., and Warren F. Clement, Crossfeed Compensation Techniques for Decoupling Rotorcraft Responses to Control Inputs, Systems Technology, Inc., Technical Report No. 1229-1, September 1985.

27. Heffley, Robert K., Wayne F. Jewell, et al., A Compilation and Analysis of Helicopter Handling Qualities Data. Volume One: Data Compilation, NASA CR-3144, August 1979.

28. Blackman, R. B., and J. W. Tukey, The Measurement of Power Spectra, Dover Publications, Inc., New York, 1958, p. 19.

29. Hoh, Roger H., and Irving L. Ashkenas, Development of VTOL Flying Qualities Criteria for Low Speed and Hover, NADC-77052-30, December 1979.

30. Landis, Kenneth H., and Steven I. Glusman, Development of ADOCS Controllers and Control Laws. Final Report--Volume 3: Simulation Results and Recommendations, Boeing Vertol Report D210-12323-3, July 1984.

31. Johns, J. B, S. T. Donley, and J. W. Clark, "Results of Grumman Design 698 Phase III Piloted Simulation," NADC Memorandum dated September 28, 1984.

32. Radford, Robert C., Dominick Andrisani, and John L. Beilman, An Experimental Investigation of VTOL Flying Qualities Requirements for Shipboard Landings, NADC 77318-60, August 1981.

33. Heffley, Robert K., A Compilation and Analysis of Helicopter Handling Qualities Data. Volume Two: Data Analysis, NASA CR-3145, August 1979, p. 117.

34. Nordstrom, L., and H. Arne, Simulator Studies of Methods of Computing and Displaying the Velocity Vector in a Head-Up Display for Low Speed Flight Path Control, ICAS Paper No. 66-16, September 1966.

35. Nordstrom, Lennart, Eye Level Information by a Perspective Pole-Track, SAAB Technical Notes, TN 58, January 1965.

36. Friedberg, U., Basic Consideration About Scale One-to-One Head-Up Displays, Society of Experimental Test Pilots Symposium, September 1971.

37. Wilckens, V., and W. Schattenmann, "Test Results with New Analog Displays for All Weather Landing," Problems of the Cockpit Environment, AGARD CP-55, March 1970.

38. Wilskens, V., On the Design Philosophy and Operations Capabilities of the CHANNEL-Display, DFVLR IB:NR:19-3/71, January 1971; and Wilckens, V., "Improvements in Pilot/Aircraft-Integration by Advanced Contact Analog Displays," Ninth NASA-University-DOT Annual Conference on Manual Control, May 1973, pp. 175-192.

39. Clement, Warren F., Potential Control/Display Configurations for V/STOL Terminal Operations. Volume III: Head-Up Display Requirements, NADC-77030-30, November 1978.

APPENDIX A

MODELS FOR TRANSIENT INPUTS

(Excerpts from Ref. A-1)

A. INTRODUCTION

The simplest nonstationary control situation is one in which a highly trained, but nonalerted, subject operating a constant-coefficient linear controlled element in a compensatory system is confronted with a randomly occurring step input. In spite of the simple circumstances, the overall behavior is complicated when a variety of controlled elements is considered. The skilled operator's output is peculiar to each controlled element form. The system response is, however, less variant in that it tends to duplicate, after a time delay, the forcing function. Thus, the system output to a unit step forcing function shown in Fig. A-1 is typical. This operator response can be analyzed by considering the three phases separately. When described in terms of a block diagram that relates stimulus to response, each temporal phase can be conceived of as having a different system organization. The block diagram structure indicates the dynamics of the association between the pilot's response and the actual or effective inputs that he is operating on to generate that response.

For tracking random inputs with occasional step inputs, a dual-mode model of the operator is appropriate. The basic structure of the model is given in Fig. A-2. The quasilinear steady-state path is the one used for tracking random inputs when the error e is less than or equal to an error threshold e_t, while the feedforward element operates on the random-occurring step inputs when the error e is greater than the threshold e_t. The basic structure thus incorporates mode switches for the two pathways. In terms of the three temporal phases, the successive action structures of the dual-mode model are:

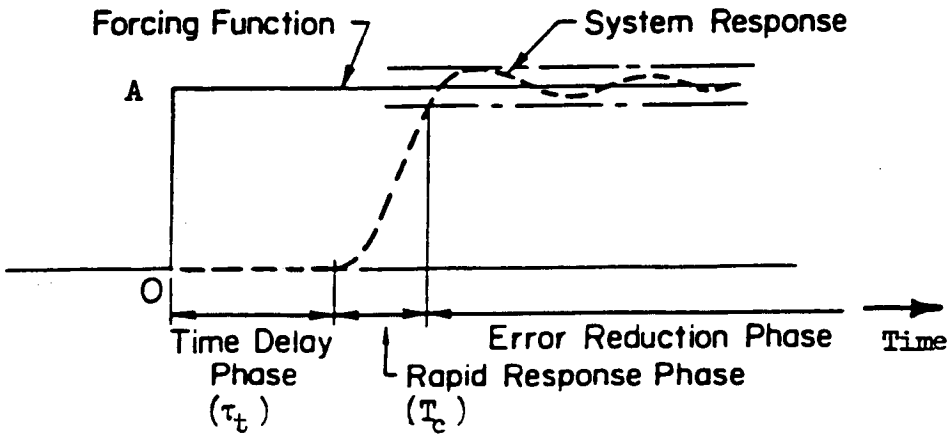

Figure A-1. Typical System Step Response

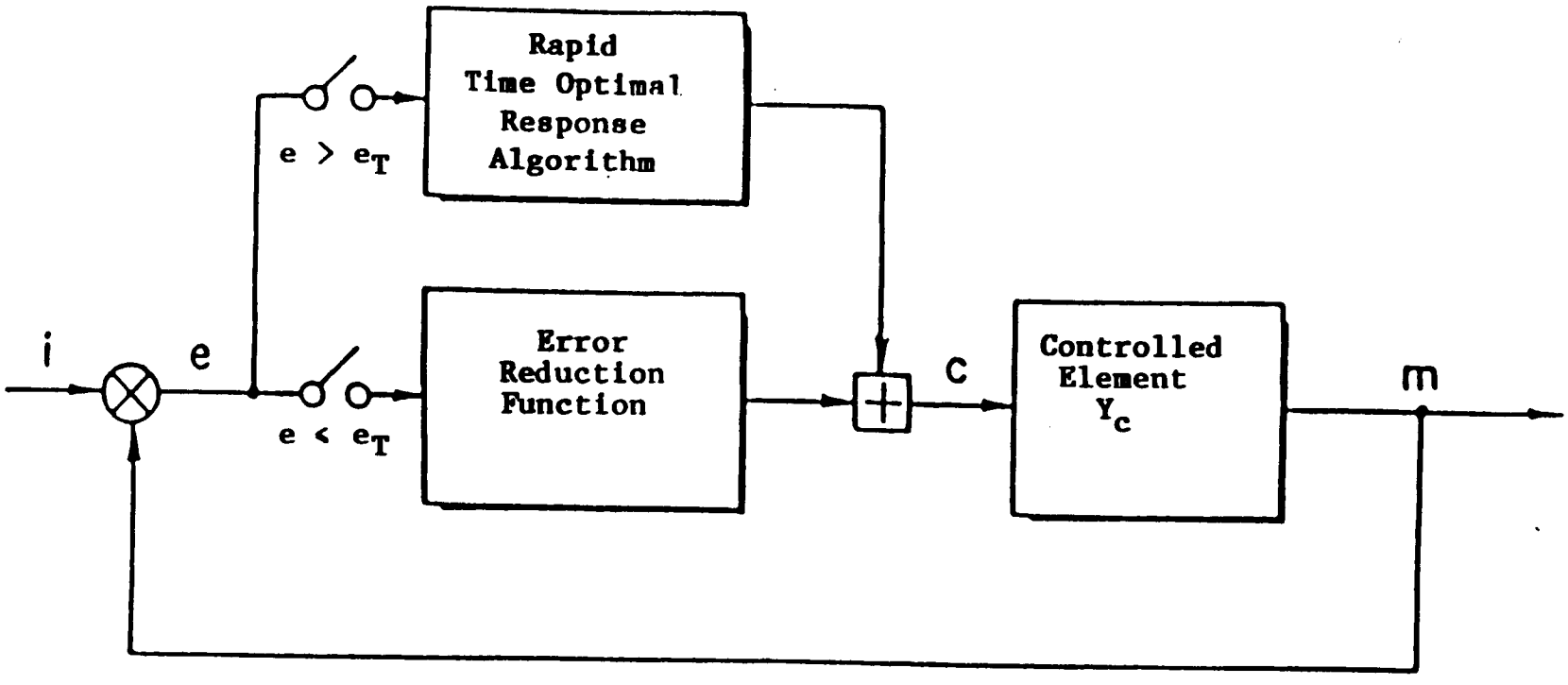

For the bob-up maneuver, e_T is height error threshold, $i = h_i$, $e = h_e$, $c = \delta_{COLL}$, $m = h$, and the error reduction function is Y_{e_h}

Figure A-2. Structure of the Dual-Mode Model

- Transition from quasilinear mode to feedforward mode, corresponding to the time delay phase
- Patterned feedforward response, corresponding to the rapid response phase
- Quasilinear mode, corresponding to the error reduction phase.

The duration of the time delay phase has some minimum value, and its unimodal distribution is therefore skewed toward the larger values. The time delay, τ_t, is generally longer than the steady-state effective time delay, τ_e, in tracking. In particular,

$$\tau_t = \tau_e + \tau_d \qquad \text{(A-1)}$$

where τ_t is the time delay phase duration, τ_e is the effective time delay in steady-state tracking, and τ_d is the decision time. During the decision time, the operator makes the pertinent decisions regarding the shape and magnitudes of the feedforward response. At the end of the time delay phase, the feedforward element generates the proper response to the step input command, giving the rapid response phase. At the end of this period, the error is small, and the operator switches to a quasilinear tracking mode in the error reduction phase.

Much is known about the quasilinear controller; therefore, attention here will be confined to the parallel feedforward path employing the rapid response algorithm used in response to step inputs.

B. A DUAL-MODE CONTROLLER MODEL

An important aspect, obvious from the step response data in Refs. A-1 through A-5, is the bang-bang nature of the stick deflection control movements. This property leads us to the pertinent problem of optimality of the operator and his related performance indices. One explanation is that the operator is optimal or suboptimal relative to the minimum time criterion. Consider an nth order single input single output control system with $|c(t)| \leq M$, where the scalar M may represent either a physical limit on

the stick deflection or, more likely, an implicit restraint imposed by the operator for the given situation. In any case, it represents a magnitude constraint on the control input. For i(t) = constant, the time optimal control has the following properties:

- The control c(t) is bang-bang, i.e., c(t) = +M or -M.
- There are at most (n-1) switchings (i.e., +M or -M or vice versa) for systems with n real eigenvalues.
- The switching logic is dependent on the order of the controlled element. In general, the switching surface is a nonlinear function of the state variables.
- For a given initial condition of the state variables, there is one unique control c(t).

For the problem at hand, there is a specific type of initial condition of the system state vector, namely:

$$e(0) = \text{input height}$$
$$\dot{e}(0) = 0$$
$$\ddot{e}(0) = 0$$
$$\vdots$$

The terminal state is the origin.

In order to characterize the degree to which the available step response data with c(t) = ±M is time optimal, certain invariance conditions, one for each controlled element, are obtained by solving a two-point boundary value problem. These are stated and described in Table A-1 without presenting their derivation; thus, let

T_c = time to complete the force response (i.e., duration of the stick response correction for step inputs)

M = average absolute amplitude (for each Y_c) of the stick response assuming it to be bang-bang with equal positive and negative amplitudes

TABLE A-1

INVARIANCE CONDITIONS FOR TIME OPTIMALITY WITH A STEP INPUT

CONTROLLED ELEMENT, Y_c	INVARIANCE CONDITION FOR TIME OPTIMALITY
K_c/s	$T_c = A/K_cM \quad ; \; T_L = 0$
K_c/s^2 (Square Wave)	$T_c/2 = \sqrt{A/K_cM} \; ; \; T_L = T_c/4$
(Sinusoidal Wave)	$T_c/2 = \sqrt{(\pi/2A)}/K_cM$
$K_c/s(s + a)$	$\begin{cases} \tau_s - \tau_f[2 \exp(-\tau_f)] = \dfrac{a^2A}{K_cM} \\ \tau_s = -\ln\lvert 2 \exp(-\tau_f) - 1 \rvert \end{cases}$ $aT_L = \dfrac{\frac{a^2A}{K_cM} - \tau_s + 1 - \exp(-\tau_s)}{1 - \exp(-\tau_s)}$
K_c/s^3 (Triangular Wave)	$T_c = (32A/K_cM)^{1/3}$

A = amplitude of step input

K_c = controlled element gain

$(\cdot)_o$ = time optimal value of the parameter in parenthesis

Assuming a wide band neuromuscular system (or controller) response, the ideal time-optimal step response character for differing controlled elements is shown in Fig. A-3. Note that the smoothing effect of the neuromuscular system (or controller) would round off the corners in the Fig. A-3 responses. Note further that the control movement starts after the end of the delay time phase, and time optimality pertains to that period of control only. Refs. A-1 through A-5 present a comparison of the actual data to the optimal. On the basis of the comparisons in the cited references, it may be safely concluded that the step response behavior of operators is nearly time optimal.

C. SUMMARY

In conclusion, a time-optimal control model is one possible idealization for the feedforward step response path of the dual-switched-mode model for the operator. The complete model is presented in Fig. A-4, as one explanation of available data. The quasilinear path is the usual operator describing function for compensatory steady-state tracking of random inputs. The feedforward parallel path represents the control plus decision model of the operator in response to step inputs. The nonlinear error sensing blocks in Fig. A-4 automatically route the error signal through the appropriate channel based upon whether $e \gtrless e_T$ (e_T is some threshold magnitude of error unique to the task).

The control logic for each different controlled element, and as a function of the error state $\underline{e}$ [e = col (e, $\dot{e}$, ...)], is given in Table A-2 for time-optimal response. Note that M, the constraint on the control input, is some function of the step input height, controlled element gain, and its order.

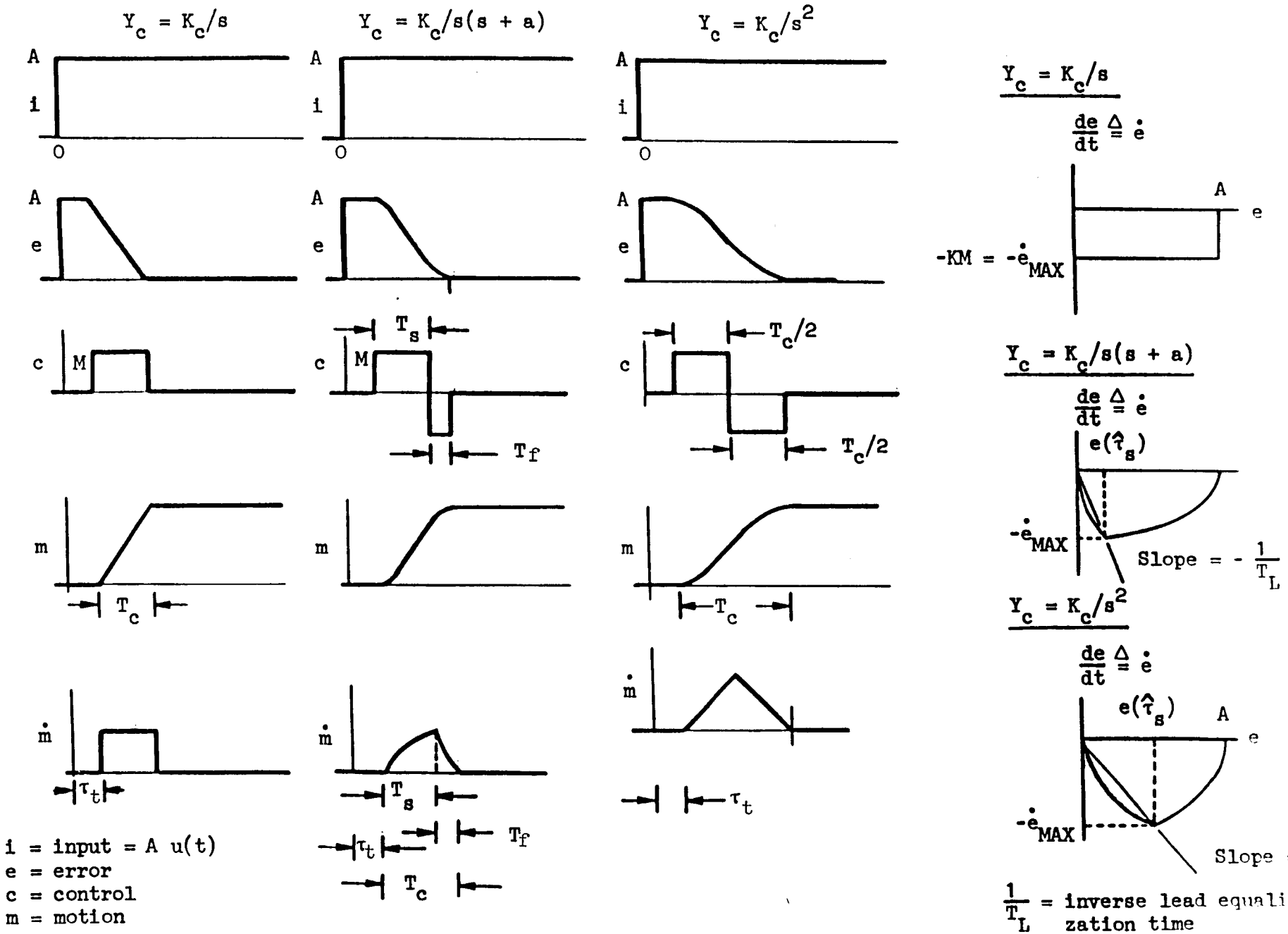

Figure A-3. Ideal Time-Optimal Response Characteristics (T_c = Time to Complete Control Program)

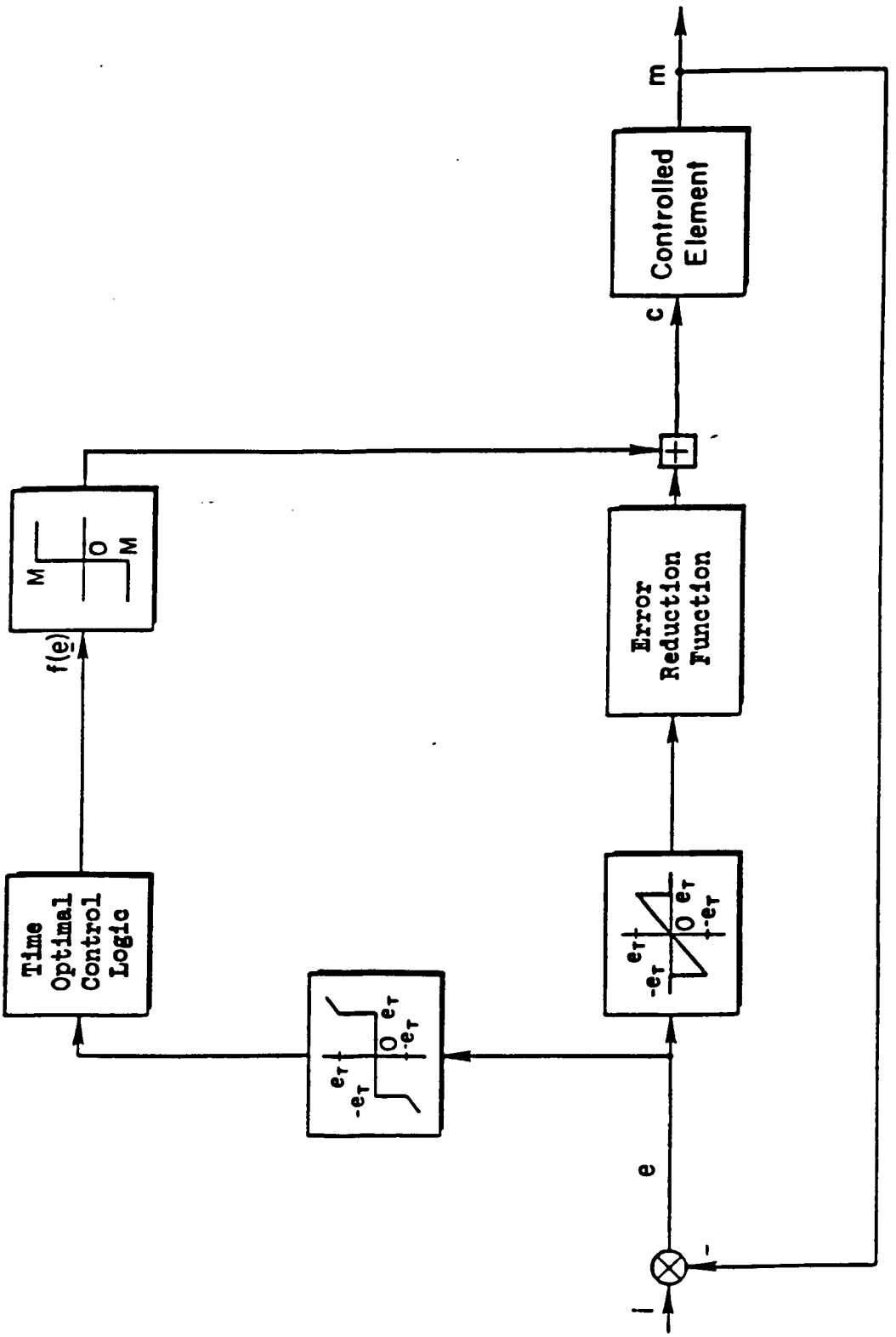

e_T = Error - threshold

Figure A-4. DUAL-MODE CONTROLLER MODEL

TABLE A-2

CONTROL LOGIC FOR VARIOUS CONTROLLED ELEMENTS

CONTROLLED ELEMENT Y_c	CONTROL LOGIC f(e)
K_c	$(A/MK_c)e(t)$
K_c/s	$e(t)$
$K_c/s(s + a)$	$\left[\dot{e} + \frac{\lvert e \rvert}{T_L} \operatorname{sgn} e\right]$ T_L is a transcendental function of a^2A/MK_c (Fig. A-5 and Ref. A-5)
K_c/s^2	$\left[\dot{e} + \sqrt{2MK_c}\lvert e \rvert \operatorname{sgn} e\right]$
$K_c s^3$	$\{e + (1/3)\dddot{e}^3 + W\dot{e}\ddot{e} + W[(1/2)\ddot{e}^2 + W\dot{e}]^{3/2}\}$ $W = +1$ for $[\dot{e} + (1/2)\ddot{e}\lvert\ddot{e}\rvert] > 0$ $= -1$ for $[\dot{e} + (1/2)\ddot{e}\lvert\ddot{e}\rvert] < 0$ (Ref. A-6)

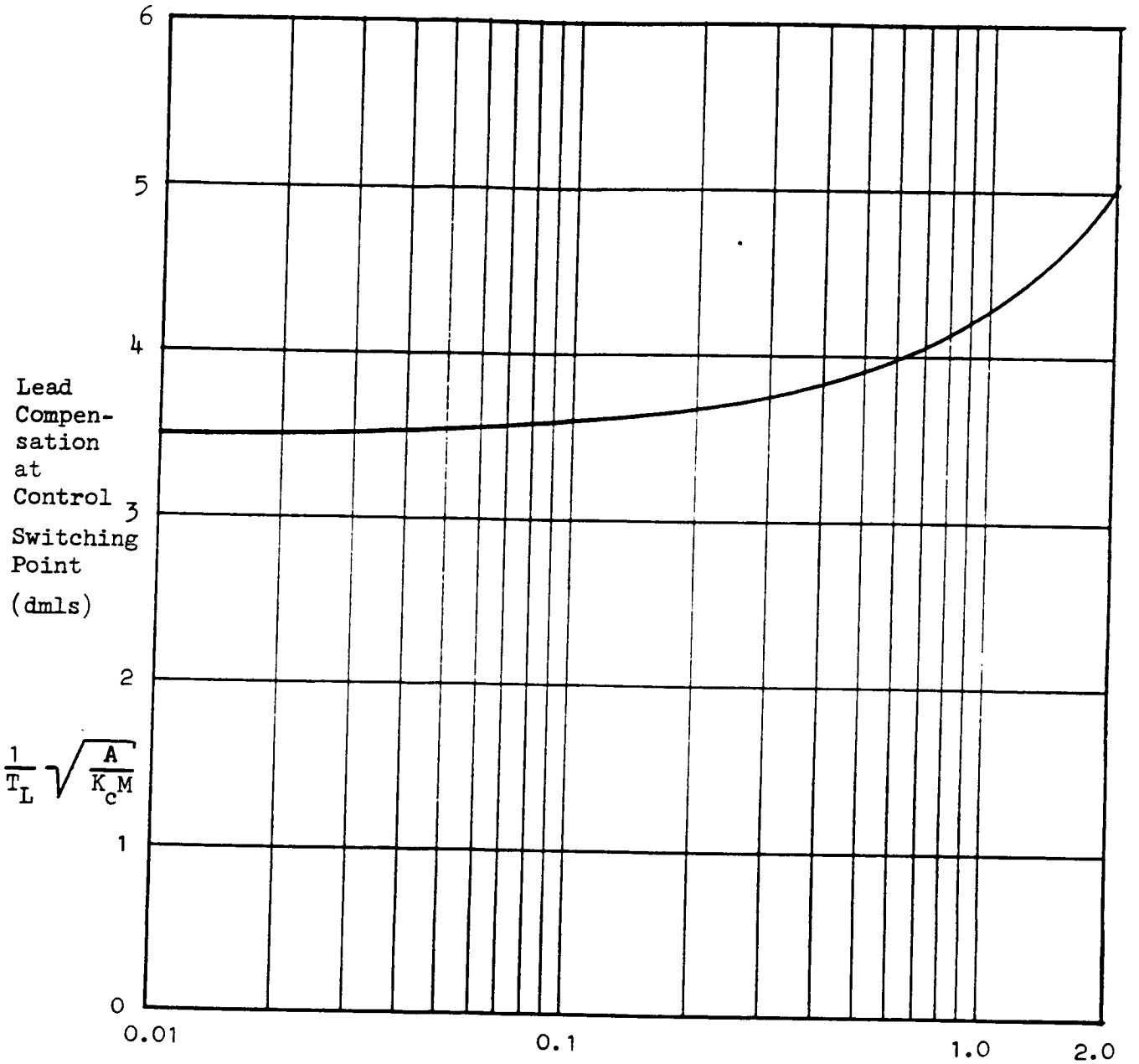

Figure A-5.
Lead Compensation at Switching Point
For Controlled Element $Y_c = K_c/s(s + a)$

The decision logic model for the time-optimal control algorithm behaves like a function switch and accounts for the initial increase in the time delay (beyond that due to quasilinear tracking) in response to a step input.

The model of Fig. A-4 should thus serve as one possible explanation of operator behavior in response to random plus step inputs.

REFERENCES

A-1 McRuer, D. T., L. G. Hofmann, H. R. Jex, et al., New Approaches to Human-Pilot/Vehicle Dynamic Analysis, AFFDL-TR-67-150, February 1968, esp, Section V.

A-2 Ferguson, Samuel W., Warren F. Clement, William B. Cleveland, and David L. Key, "Assessment of Simulation Fidelity Using Measurements of Piloting Technique in Flight," American Helicopter Society, 40th Annual Forum Proceedings, May 1984, pp. 67-92.

A-3 Clement, Warren F., William B. Cleveland, and David L. Key, "Assessment of Simulation Fidelity Using Measurements of Piloting Technique in Flight," Helicopter Guidance and Control Systems for Battlefield Support, AGARD CP 359, May 1984, pp. 25-1 through 25-12.

A-4 Ferguson, Samuel W., Warren F. Clement, Roger H. Hoh, and William B. Cleveland, "Assessment of Simulation Fidelity Using Measurements of Piloting Technique in Flight, Part II," Presented at the American Helicopter Society's 41st Annual Forum, May 1985 (AIAA Data Base Assession No. 86-A-35667).

A-5 Ferguson, Samuel W., and Warren F. Clement, Assessment of Simulation Fidelity Using Measurements of Piloting Technique in Flight, Systems Technology, Inc., Technical Report No. 1184-1, March 1986.

A-6 Flügge-Lotz, I., and H. A. Titus, Jr., "Optimum and Quasi-Optimum Control of Third- and Fourth-Order Systems," Automatic and Remote Control (Proceedings of the Second Congress of International Federation of Automatic Control, Basle, Switzerland, 1963), Vol. 2, Theory, I. V. Broida, et al., (Eds.), Butterworth, Inc., Washington, D. C., 1964, pp. 363-370. (Also published as Air Force Office of Scientific Research Report 2928, June 1962.)

APPENDIX B

EFFECTS OF HORIZONTAL WIND SHEAR GRADIENT ON HEIGHT CONTROL WHILE TRAVELING IN "DOLPHIN" MANEUVERS

The effects on closed-loop characteristics of a headwind-to-tailwind shear gradient, $\partial u_g/\partial h < 0$, with decreasing altitude are shown in Figs. B-1 through B-4. The airspeed regulation subsidence, $\omega_u'' = 0.3$ rad/sec, corresponds with a velocity-to-pitch attitude control high-frequency gain $K_u = -0.01$ rad θ_c/ft/sec in both sets of figures. Figures B-1 and B-2 represent the effects with the lower value of height-to-collective control high-frequency loop gain $K_h^{\bullet} = 0.0245$ in/ft/sec (damping ratio 0.785; undamped natural frequency 0.51 rad/sec); Figs. B-3 and B-4 represent the effects for a higher value of $K_h^{\bullet} = 0.0923$ in/ft/sec (damping ratio 0.7; undamped natural frequency 1.0 rad/sec). The shear gradient $\partial u_g/\partial h$ varies along the complex and real root loci in Figs. B-1 and B-3 as shown in the corresponding logarithmic Sigma-Bode root loci, Figs. B-2 and B-4. The results in Figs. B-1 through B-4 are expanded further in this appendix to represent the effects of two other values of airspeed regulation subsidence, $\omega_u'' = 0.15$ and 0.6 rad/sec, corresponding respectively to two other values of velocity-to-pitch attitude control high-frequency gain, viz., $K_u = -0.005$ and -0.02 rad θ_c/ft/sec. Figures B-5 through B-8 present the results for $\omega_u'' = 0.15$ rad/sec, and Figs. B-9 through B-12 present the results for $\omega_u'' = 0.6$ rad/sec.

Not surprisingly, the higher height control bandwidth in Figs. B-3 and B-4 ($\omega_u'' = 0.3$ rad/sec), Figs. B-7 and B-8 ($\omega_u'' = 0.15$ rad/sec), and Figs. B-11 and B-12 ($\omega_u'' = 0.6$ rad/sec) provides a higher threshold of instability caused by the wind shear gradient. Although the height control bandwidth in Figs. B-3, B-4, B-7, B-8, B-11, and B-12 is only doubled with respect to that in Figs. B-1 and B-2 ($\omega_u'' = 0.3$ rad/sec), Figs. B-5 and B-6 ($\omega_u'' = 0.15$ rad/sec), and Figs. B-9 and B-10 ($\omega_u'' = 0.6$ rad/sec), the wind shear gradient required to cause instability is between 2-1/2 and 3 times greater in Figs. B-3, B-4, B-7, B-8, B-11, and B-12 depending on the speed regulation subsidence.

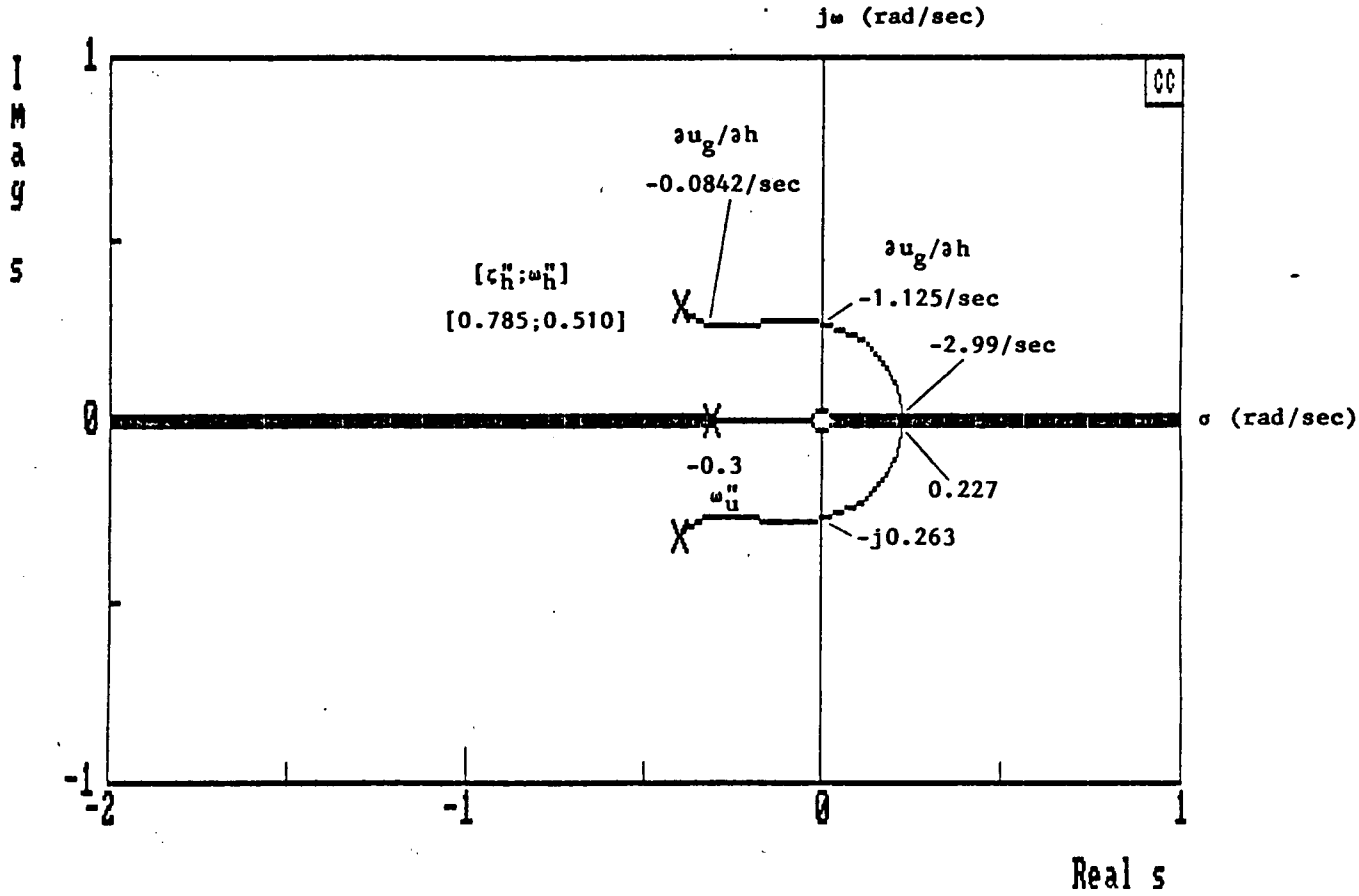

Complex Root Locus of Characteristic Values for the Closed-Loop Determinant Δ"(s) of Height and Airspeed Control Equations While Traveling

$$\Delta''(s) \doteq \left[s + 1/T_{\theta_1} + K_u(X_\alpha - g)\right]$$
$$\left[s^2 + (1/T_{\theta_2} - Z_{\delta_c} K_h^\bullet)s - (Z_{\delta_c} K_h^\bullet / T_{L_h})\right]$$
$$- (\partial u_g/\partial h)s(Z_u - K_u Z_\alpha)$$

$\partial u_g/\partial h < 0$, UH-1H at 20 kt, Sea Level, 8000 lb, mid cg, $K_h^\bullet = 0.0245$ in/ft/sec

$-Z_w = 0.567$ rad/sec $\quad -Z_{\delta_c} = 9.29$ ft/sec^2-in $\quad -X_u = 0.005$ rad/sec

$-Z_u = 0.198$ rad/sec $\quad (X_\alpha - g)K_u \doteq \omega_{c_u}'' \doteq 0.3$ rad/sec $\quad 1/T_{L_h} = 1.13$ rad/sec

Figure B-1. Complex Root Locus of Characteristic Values for the Closed-Loop Determinant of Height and Airspeed Control Equations While Traveling Showing Effects of Headwind-to-Tailwind Shear with Decreasing Altitude

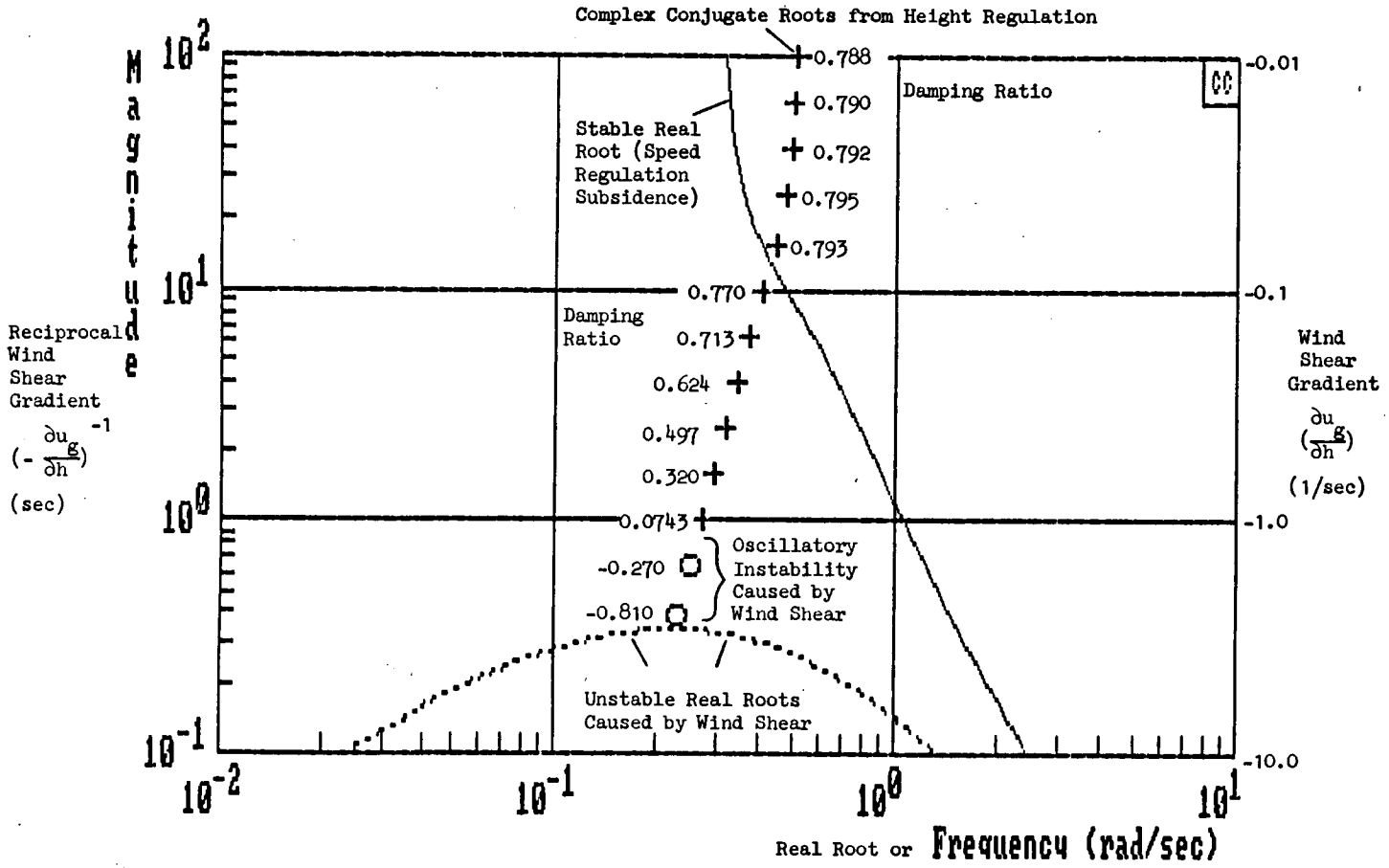

$\partial u_g/\partial h < 0$, UH-1H at 20 kt, Sea Level, 8000 lbs, mid c.g. Height Regulation Loop Closed Via Collective Control with Lead Compensation $1/T_{L_h} = 1.13$ rad/sec Without Delay and High Frequency Gain $K_h^{\bullet} = 0.0245$ in/ft/sec. Speed Regulation Loop Closed Via Pitch Attitude Without Delay and High Frequency Gain $K_u = -0.01$ rad θ_c/ft/sec

Figure B-2. Sigma-Bode Root Locus of Characteristic Values for the Closed-Loop Determinant $\Delta''(s)$ of Height and Airspeed Control Equations While Traveling

$$\Delta''(s) \doteq \left[s + 1/T_{\theta_1} + K_u(X_\alpha - g)\right]\left[s^2 + \left(1/T_{\theta_2} - Z_{\delta_c} K_h^{\bullet}\right)s - \left(Z_{\delta_c} K_h^{\bullet}/T_{L_h}\right)\right] - \left(\partial u_g/\partial h\right)s\left(Z_u - K_u Z_\alpha\right)$$

Showing Effect of Headwind-to-Tailwind Shear with Decreasing Altitude

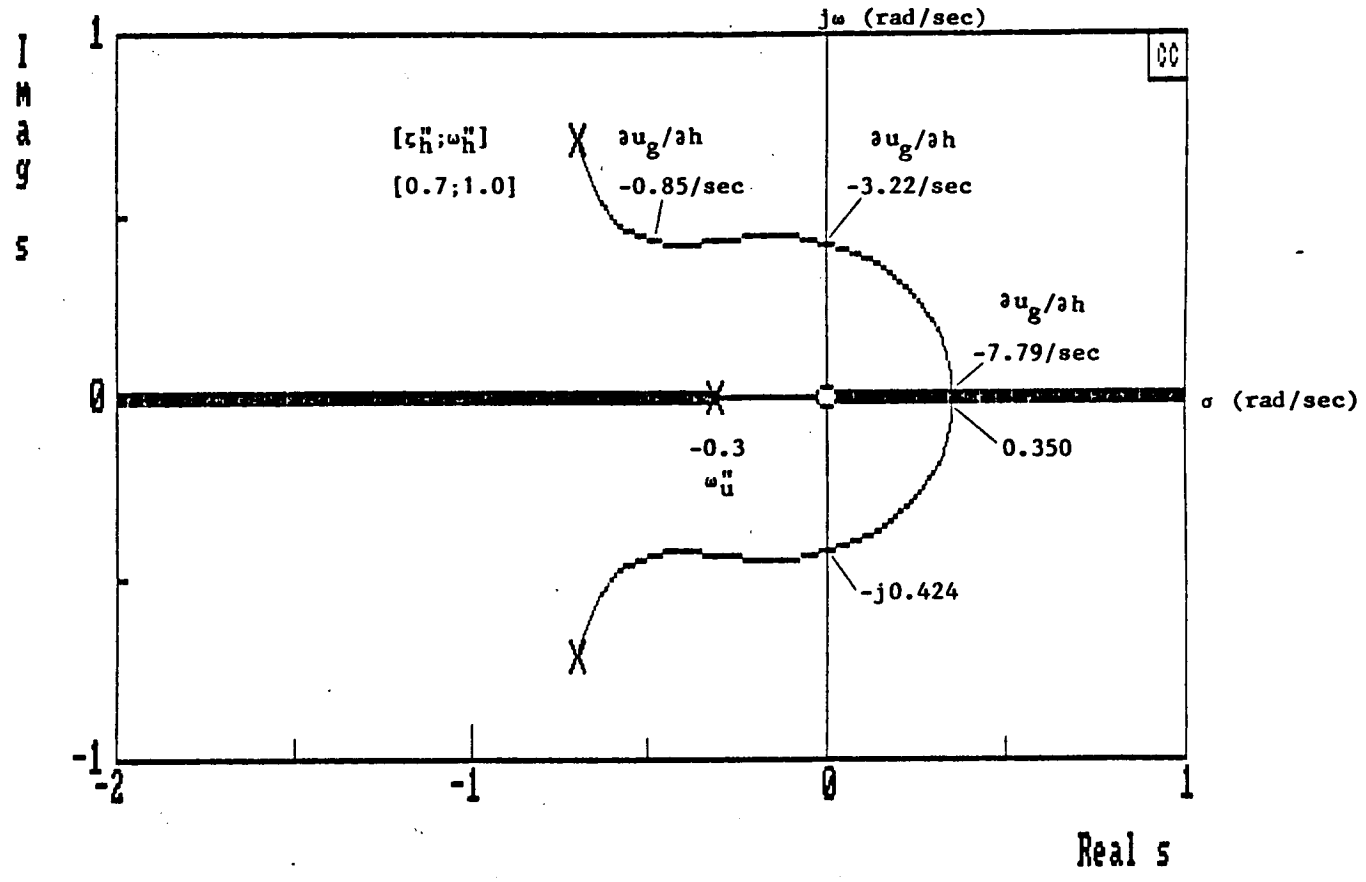

Complex Root Locus of Characteristic Values for the Closed-Loop Determinant Δ"(s) of Height and Airspeed Control Equations While Traveling

$$\Delta''(s) \doteq \left[s + 1/T_{\theta_1} + K_u(X_\alpha - g)\right]$$
$$\left[s^2 + (1/T_{\theta_2} - Z_{\delta_c} K_h^{\cdot})s - (Z_{\delta_c} K_h^{\cdot}/T_{L_h})\right]$$
$$- (\partial u_g/\partial h)s(Z_u - K_u Z_\alpha)$$

$\partial u_g/\partial h < 0$, UH-1H at 20 kt, Sea Level, 8000 lb, mid cg, $K_h^{\cdot} = 0.0923$ in/ft/sec

$-Z_w = 0.567$ rad/sec $-Z_{\delta_c} = 9.29$ ft/sec^2-in $-X_u = 0.005$ rad/sec

$-Z_u = 0.198$ rad/sec $(X_\alpha - g)K_u \doteq \omega''_{c_u} \doteq 0.3$ rad/sec $1/T_{L_h} = 1.13$ rad/sec

Figure B-3. Complex Root Locus of Characteristic Values for the Closed-Loop Determinant of Height and Airspeed Control Equations While Traveling Showing Effects of Headwind-to-Tailwind Shear with Decreasing Altitude

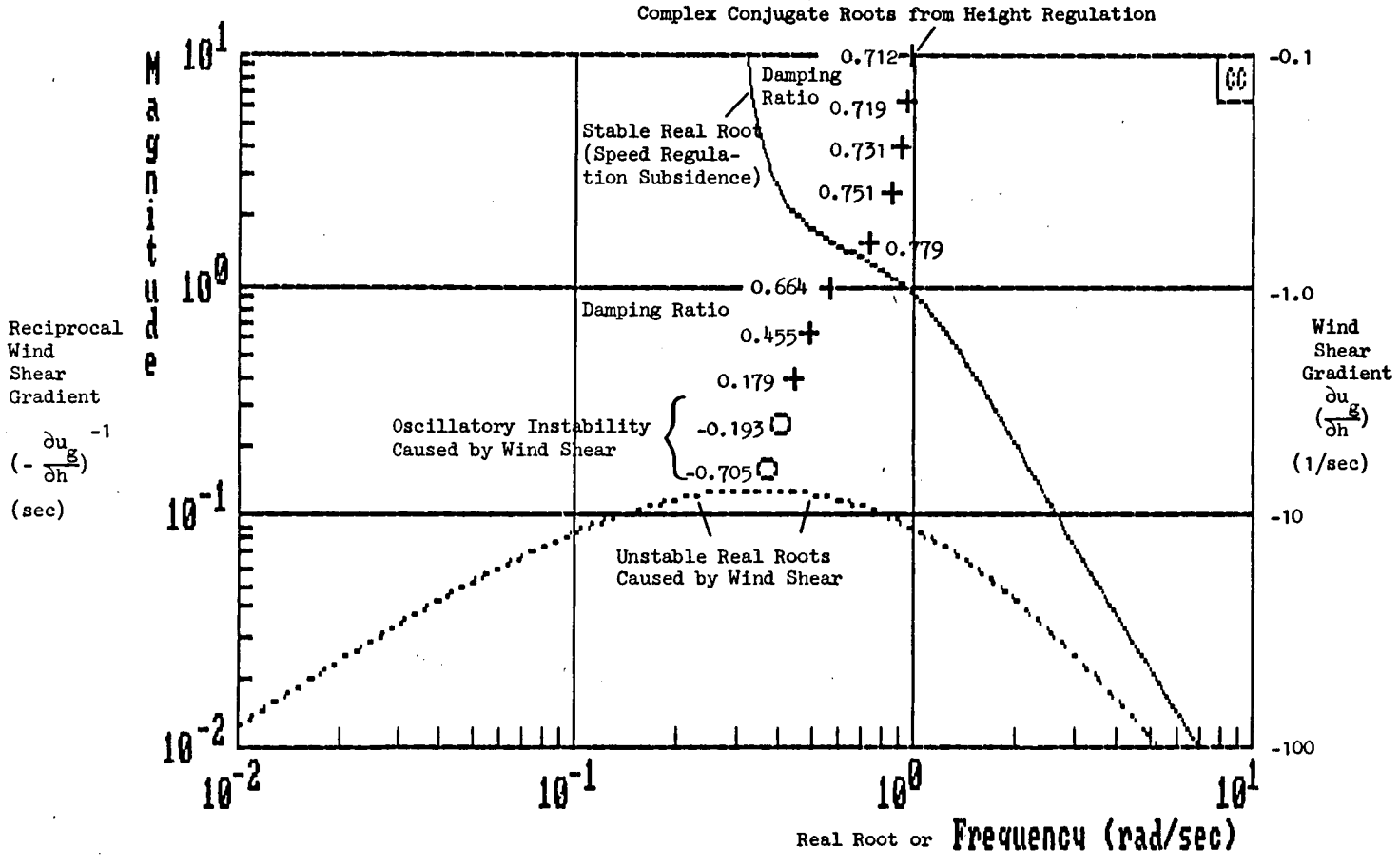

$\partial u_g/\partial h < 0$, UH-1H at 20 kt, Sea Level, 8000 lbs, mid c.g. Height Regulation Loop Closed Via Collective Control with Lead Compensation $1/T_{L_h}$ = 1.13 rad/sec Without Delay and High Frequency Gain $K_h^{\cdot}$ = 0.0923 in/ft/sec. Speed Regulation Loop Closed Via Pitch Attitude Without Delay and High Frequency Gain K_u = -0.01 rad θ_c/ft/sec

Figure B-4. Sigma-Bode Root Locus of Characteristic Values for the Closed-Loop Determinant $\Delta''(s)$ of Height and Airspeed Control Equations While Traveling

$$\Delta''(s) \doteq \left[s + 1/T_{\theta_1} + K_u(X_\alpha - g)\right]\left[s^2 + \left(1/T_{\theta_2} - Z_{\delta_c} K_h^{\cdot}\right)s - \left(Z_{\delta_c} K_h^{\cdot}/T_{L_h}\right)\right] - (\partial u_g/\partial h)s(Z_u - K_u Z_\alpha)$$

Showing Effect of Headwind-to-Tailwind Shear with Decreasing Altitude

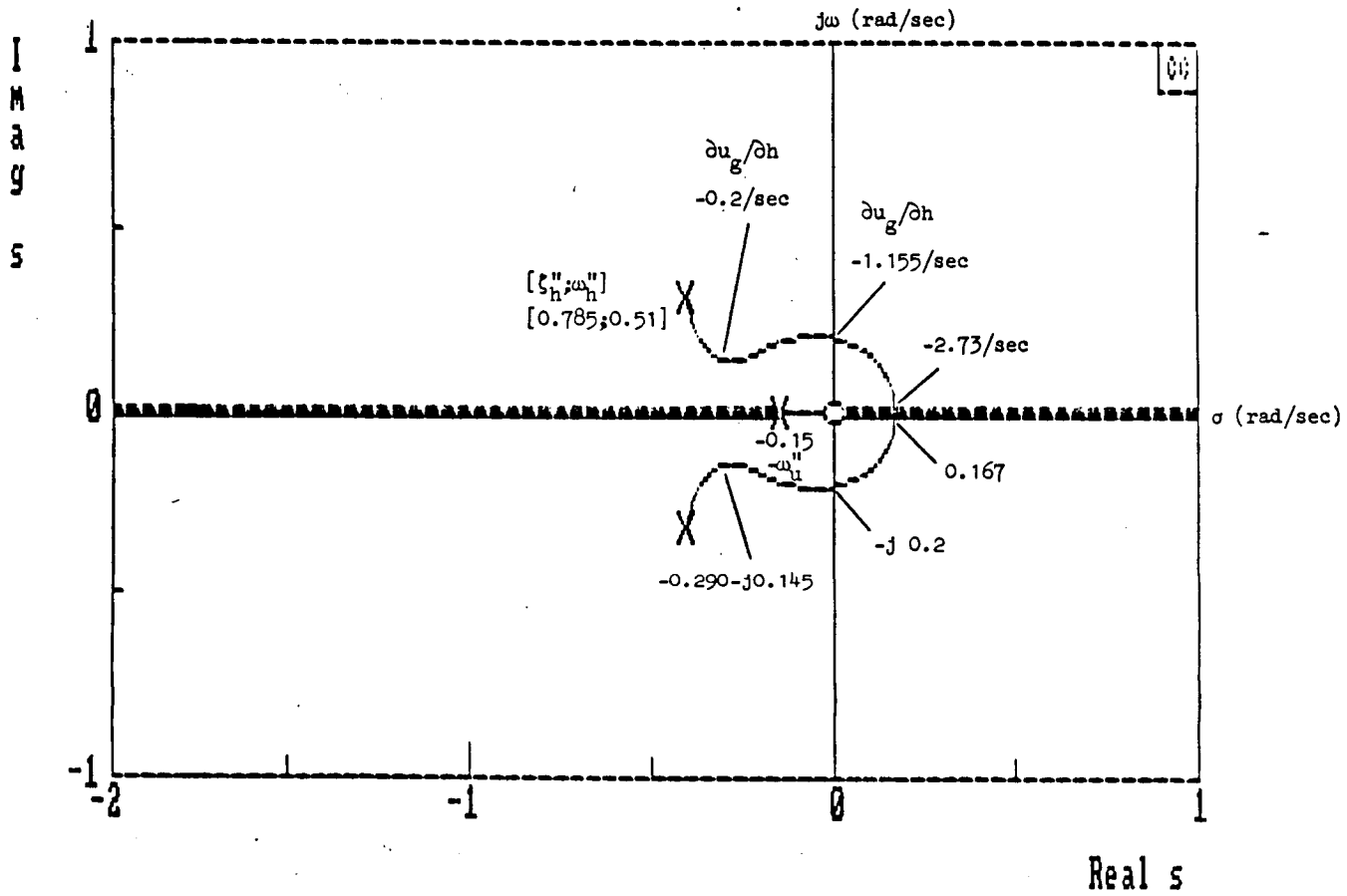

UH-1H at 20 kts, Sea Level, 8000 lbs, mid c.g., $K_h^{\cdot} = 0.0245$ in/ft/sec

$-Z_w = 0.567$ rad/sec $\quad -Z_{\delta_c} = 9.29$ ft/sec^2-in $\quad -X_u = 0.005$ rad/sec

$-Z_u = 0.198$ rad/sec $\quad (X_\alpha - g)K_u \doteq \omega_{c_u}'' \doteq 0.15$ rad/sec $\quad 1/T_{L_h} = 1.13$ rad/sec

$K_u = -0.005$ rad θ_c/ft/sec

Figure B-5. Complex Root Locus of Characteristic Values for the Closed-Loop Determinant of Height and Airspeed Control Equations While Traveling Showing Effects of Headwind-to-Tailwind Shear with Decreasing Altitude $\partial u_g/\partial h < 0$

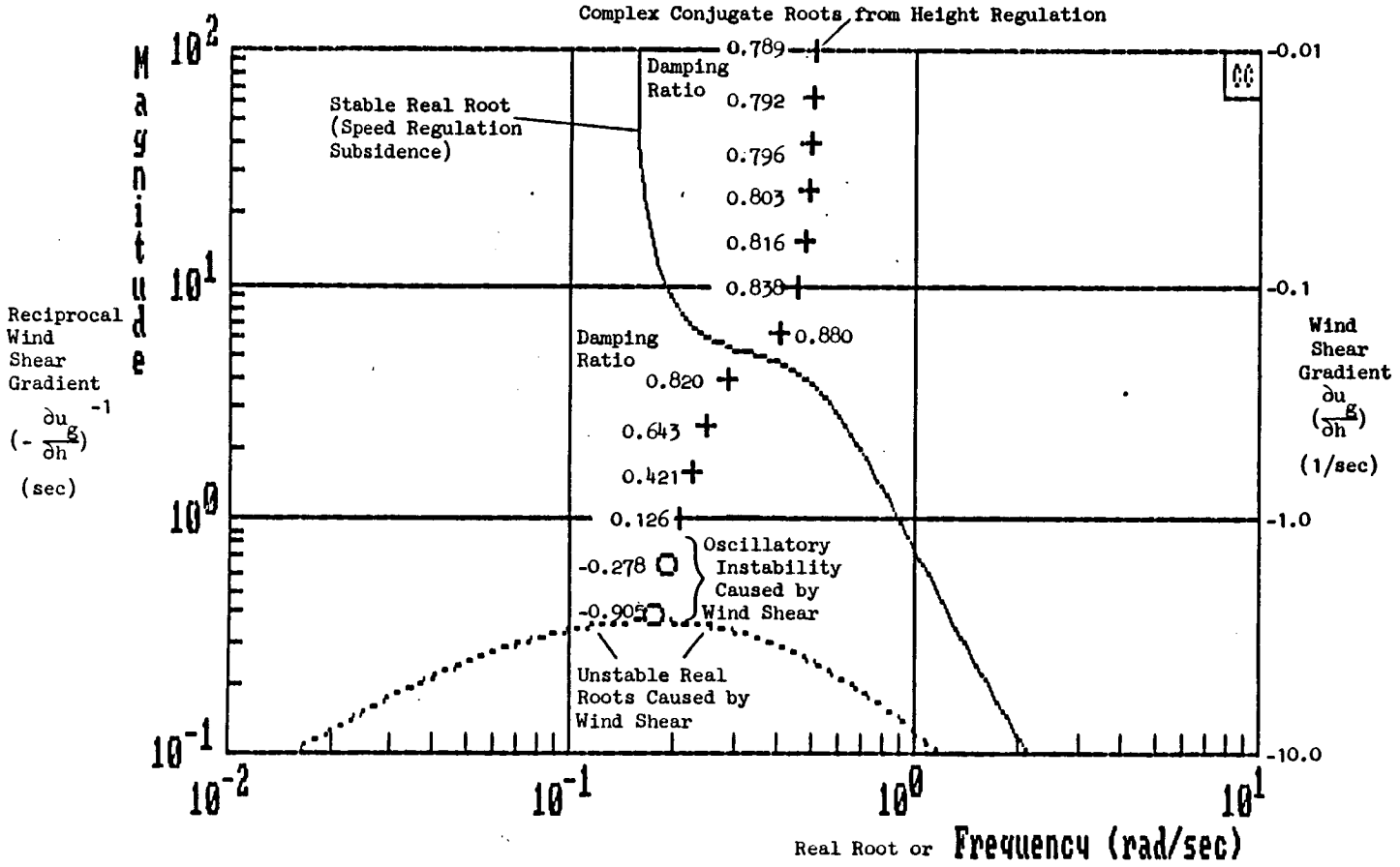

UH-1H at 20 kt, Sea Level, 8000 lbs, mid c.g. Height Regulation Loop Closed Via Collective Control with Lead Compensation $1/T_{L_h}$ = 1.13 rad/sec Without Delay and High Frequency Gain $K_h^{\cdot}$ = 0.0245 in/ft/sec.

Speed Regulation Loop Closed Via Pitch Attitude Without Delay and High Frequency Gain K_u = -0.01 rad θ_c/ft/sec

Figure B-6. Sigma-Bode Root Locus Showing Effect of Headwind-to-Tailwind Shear with Decreasing Altitude: $\partial u_g/\partial h < 0$

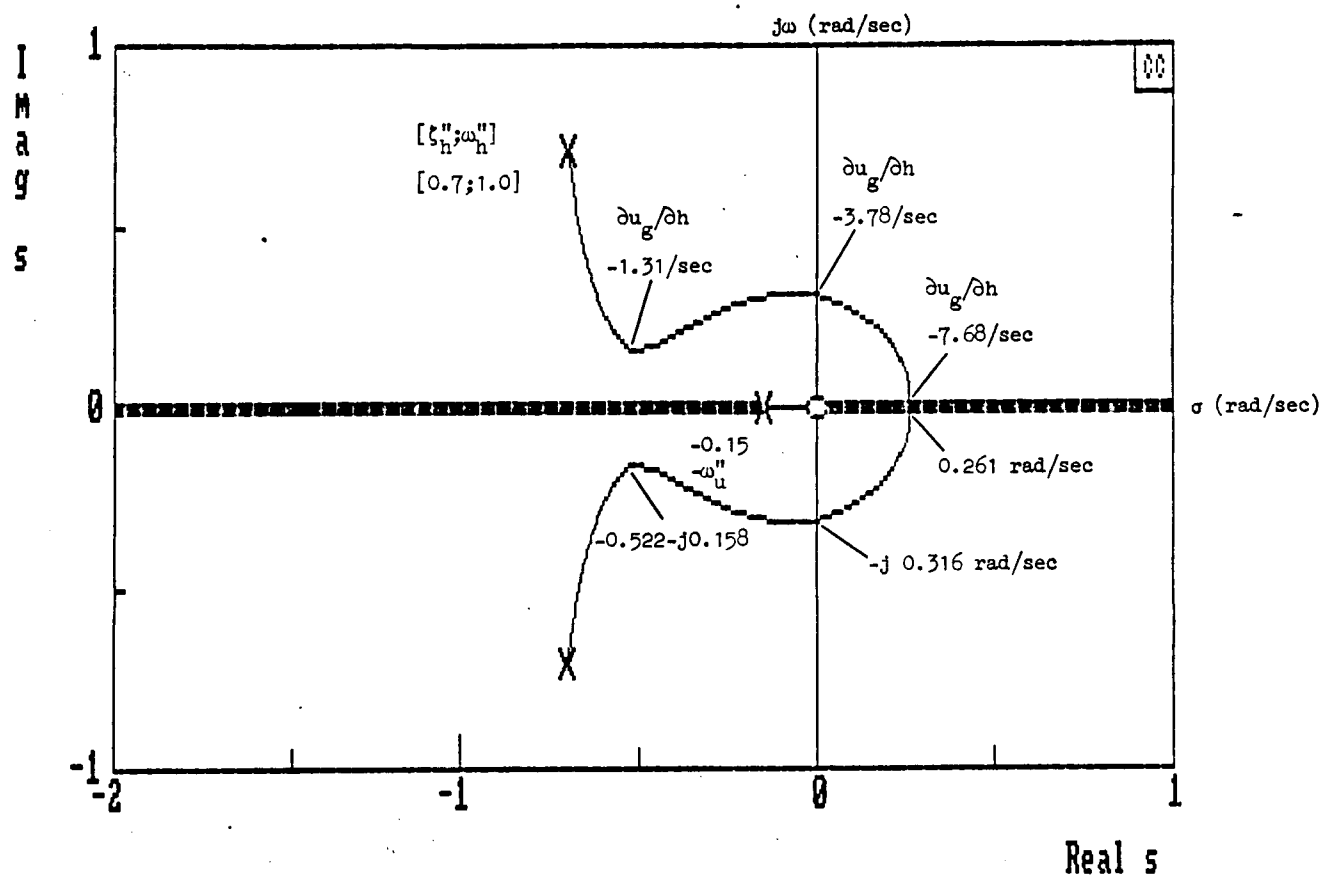

UH-1H at 20 kts, Sea Level, 8000 lbs, mid c.g., $K_h^{\cdot} = 0.0923$ in/ft/sec

$-Z_w = 0.567$ rad/sec $\quad -Z_{\delta_c} = 9.29$ ft/sec^2-in $\quad -X_u = 0.005$ rad/sec

$-Z_u = 0.198$ rad/sec $\quad (X_\alpha - g)K_u \doteq \omega''_{c_u} \doteq 0.15$ rad/sec $\quad 1/T_{L_h} = 1.13$ rad/sec

$K_u = -0.005$ rad θ_c/ft/sec

Figure B-7. Complex Root Locus of Characteristic Values for the Closed-Loop Determinant of Height and Airspeed Control Equations While Traveling Showing Effects of Headwind-to-Tailwind Shear with Decreasing Altitude $\partial u_g/\partial h < 0$

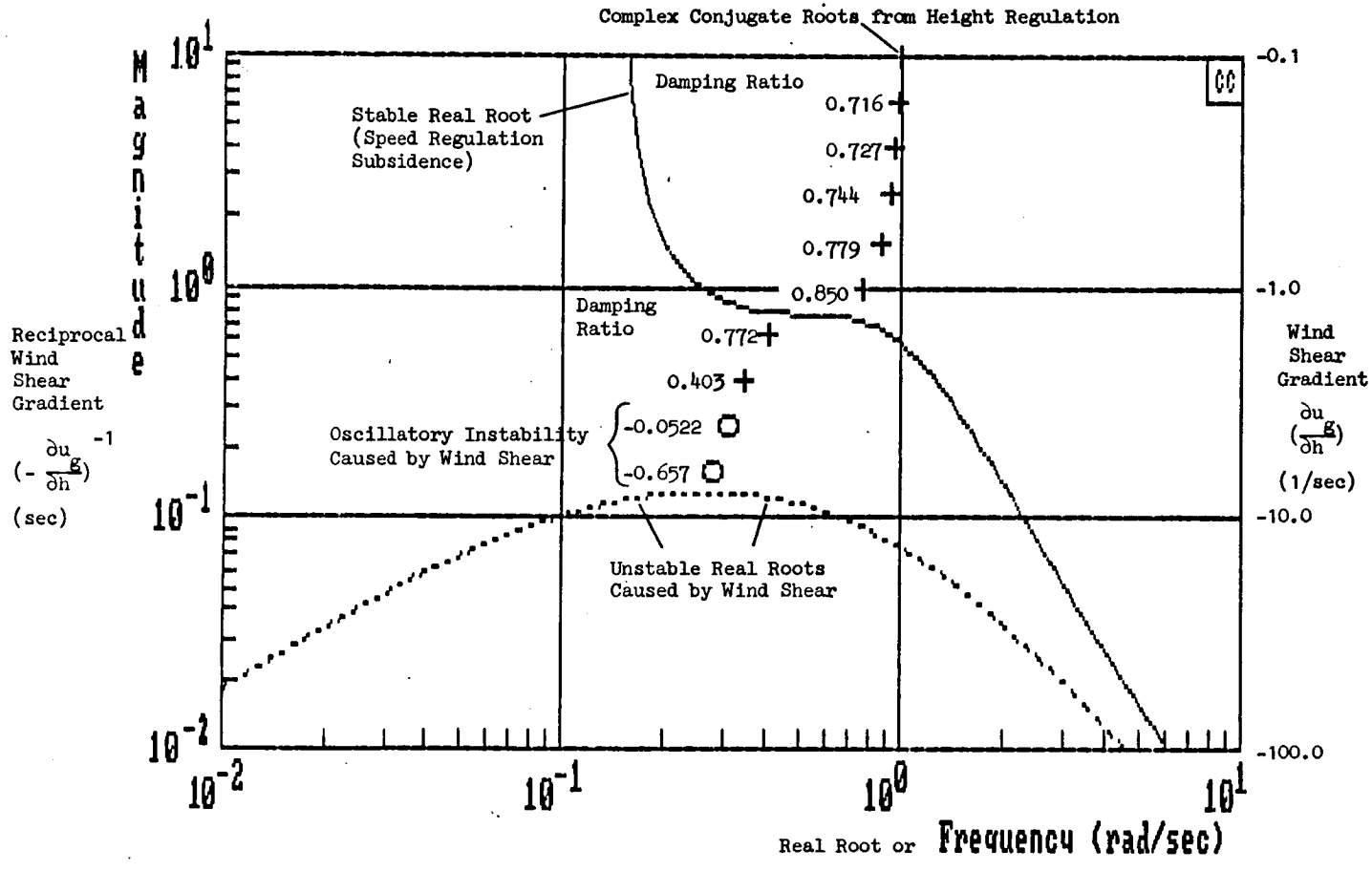

UH-1H at 20 kt, Sea Level, 8000 lbs, mid c.g. Height Regulation Loop Closed Via Collective Control with Lead Compensation $1/T_{L_h}$ = 1.13 rad/sec Without Delay and High Frequency Gain $K_h^{\cdot}$ = 0.0923 in/ft/sec.

Speed Regulation Loop Closed Via Pitch Attitude Without Delay and High Frequency Gain K_u = -0.005 rad θ_c/ft/sec

Figure B-8. Sigma-Bode Root Locus Showing Effect of Headwind-to-Tailwind Shear with Decreasing Altitude: $\partial u_g/\partial h < 0$

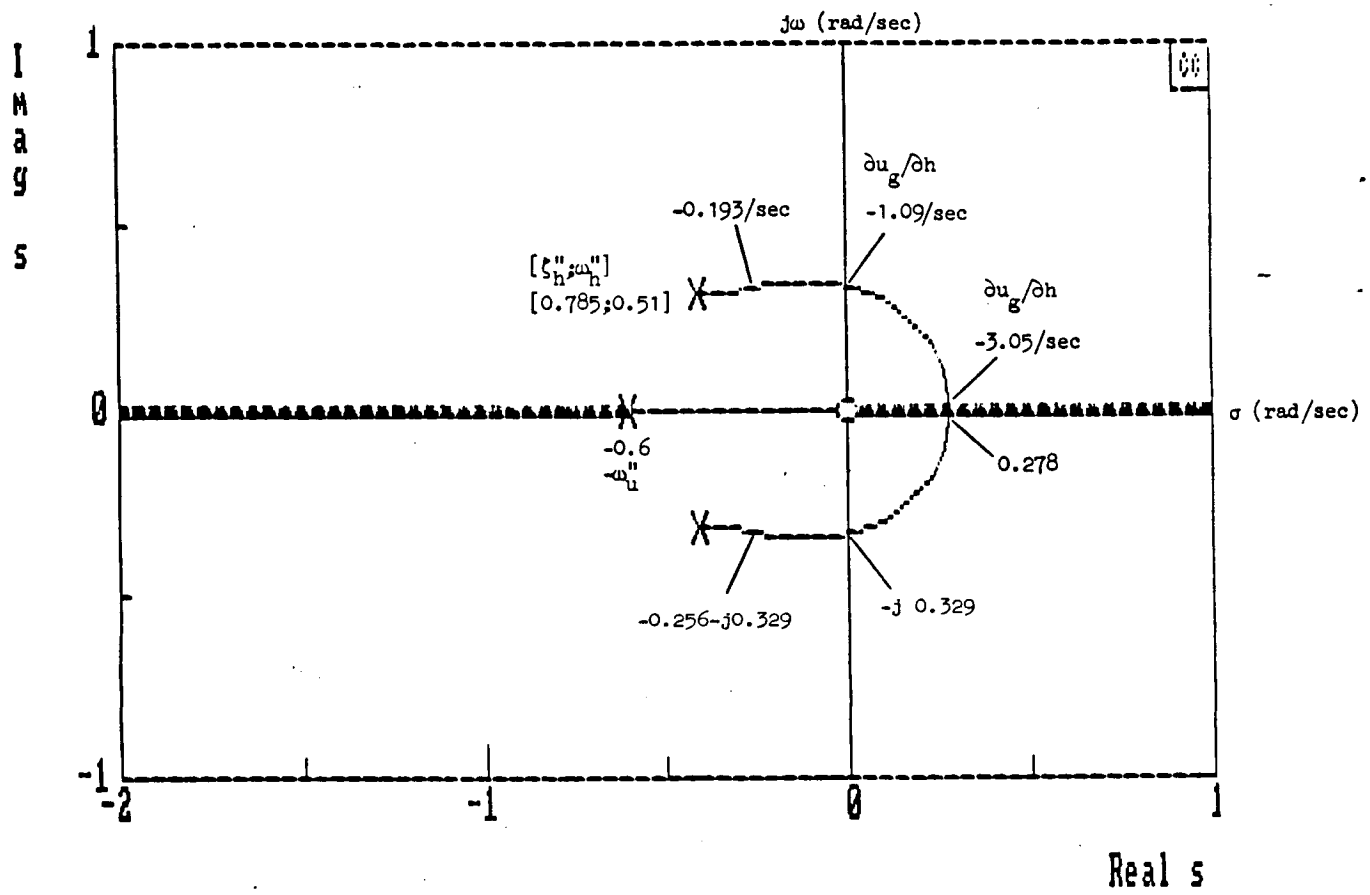

UH-1H at 20 kts, Sea Level, 8000 lbs, mid c.g., $K_h^{\cdot} = 0.0245$ in/ft/sec

$-Z_w = 0.567$ rad/sec $\quad -Z_{\delta_c} = 9.29$ ft/sec^2-in $\quad -X_u = 0.005$ rad/sec

$-Z_u = 0.198$ rad/sec $\quad (X_\alpha - g)K_u \doteq \omega_{c_u}'' \doteq 0.6$ rad/sec $\quad 1/T_{L_h} = 1.13$ rad/sec

$K_u = -0.02$ rad θ_c/ft/sec

Figure B-9. Complex Root Locus of Characteristic Values for the Closed-Loop Determinant of Height and Airspeed Control Equations While Traveling Showing Effects of Headwind-to-Tailwind Shear with Decreasing Altitude $\partial u_g/\partial h < 0$

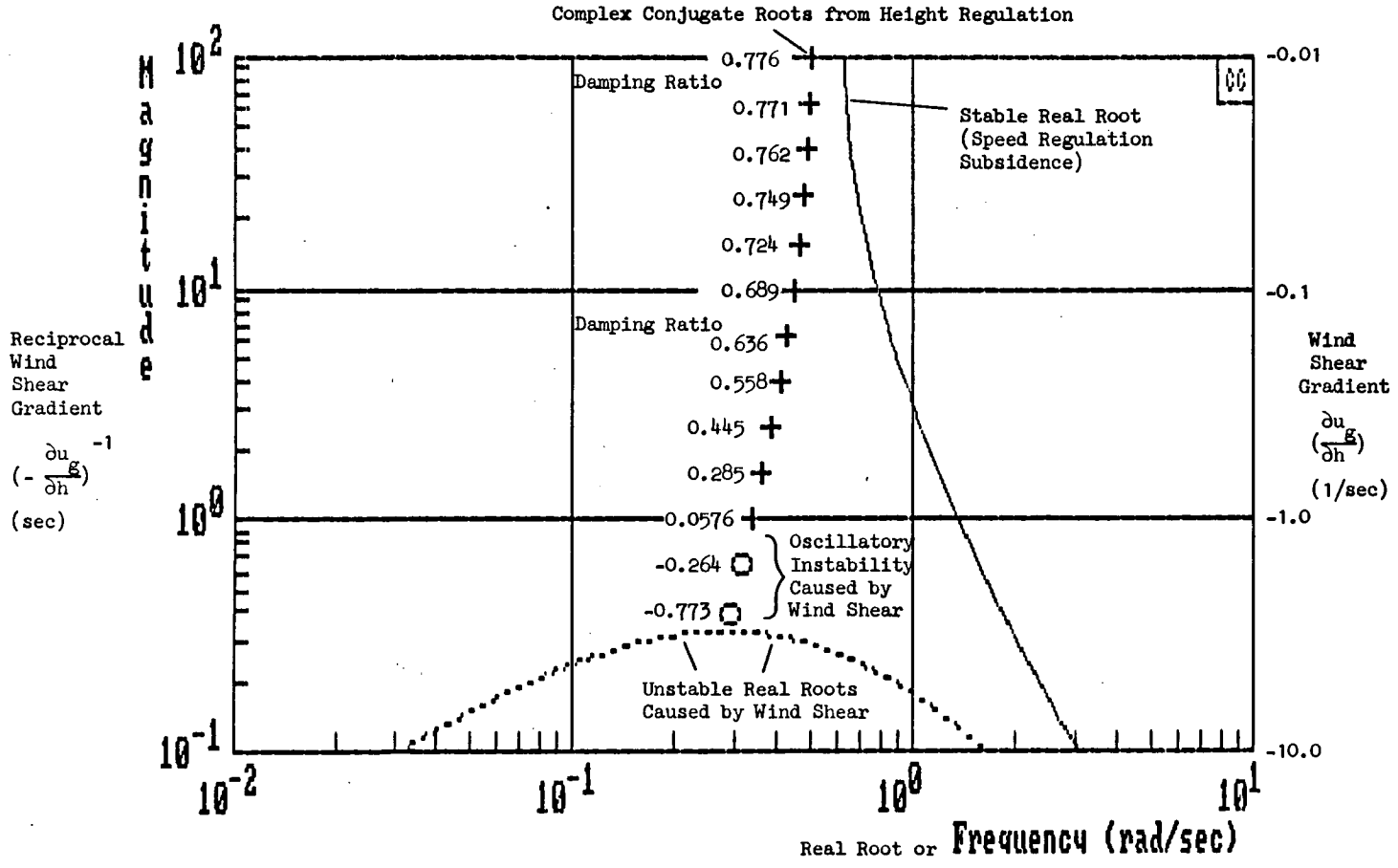

UH-1H at 20 kt, Sea Level, 8000 lbs, mid c.g. Height Regulation Loop Closed Via Collective Control with Lead Compensation $1/T_{L_h}$ = 1.13 rad/sec Without Delay and High Frequency Gain $K_h^{\cdot}$ = 0.0245 in/ft/sec.

Speed Regulation Loop Closed Via Pitch Attitude Without Delay and High Frequency Gain K_u = -0.02 rad θ_c/ft/sec

Figure B-10. Sigma-Bode Root Locus Showing Effect of Headwind-to-Tailwind Shear with Decreasing Altitude: $\partial u_g/\partial h < 0$

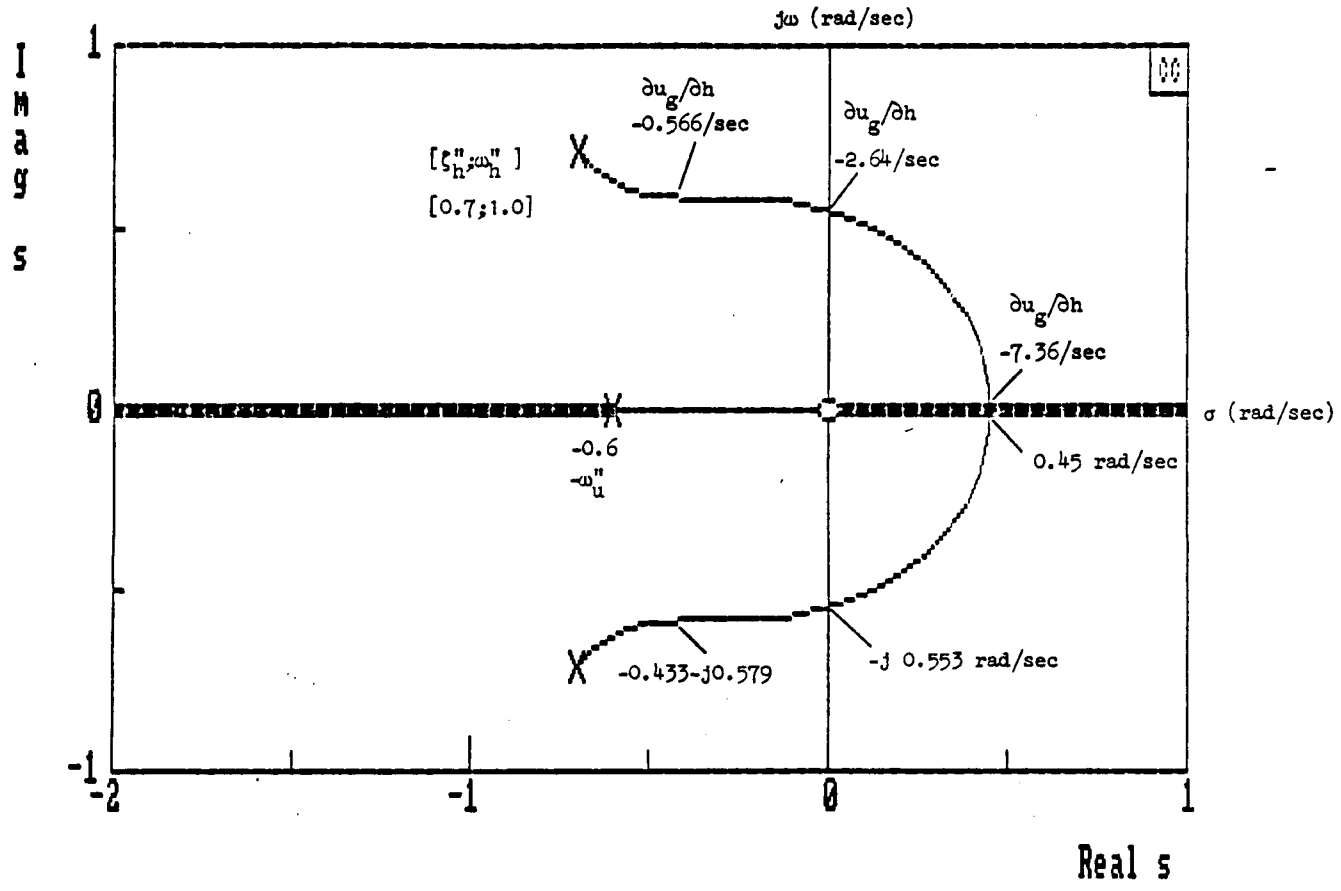

UH-1H at 20 kts, Sea Level, 8000 lbs, mid c.g., $K_h^{\cdot} = 0.0923$ in/ft/sec

$-Z_w = 0.567$ rad/sec $\quad -Z_{\delta_c} = 9.29$ ft/sec^2-in $\quad -X_u = 0.005$ rad/sec

$-Z_u = 0.198$ rad/sec $\quad (X_\alpha - g)K_u \doteq \omega_{c_u}'' \doteq 0.6$ rad/sec $\quad 1/T_{L_h} = 1.13$ rad/sec

$K_u = -0.02$ rad θ_c/ft/sec

Figure B-11. Complex Root Locus of Characteristic Values for the Closed-Loop Determinant of Height and Airspeed Control Equations While Traveling Showing Effects of Headwind-to-Tailwind Shear with Decreasing Altitude $\partial u_g/\partial h < 0$

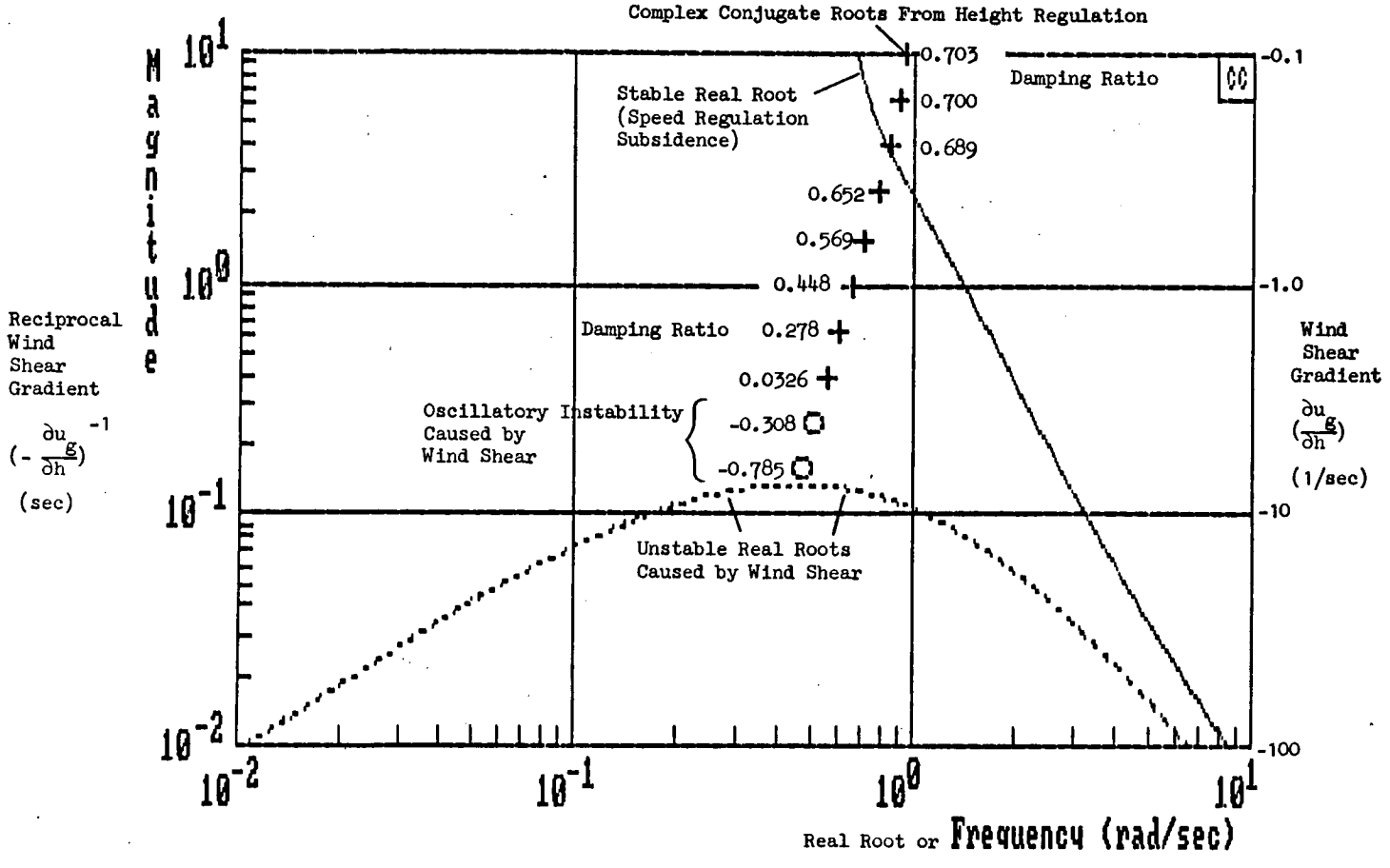

UH-1H at 20 kt, Sea Level, 8000 lbs, mid c.g. Height Regulation Loop Closed Via Collective Control with Lead Compensation $1/T_{L_h}$ = 1.13 rad/sec Without Delay and High Frequency Gain $K_h^{\cdot}$ = 0.0923 in/ft/sec.

Speed Regulation Loop Closed Via Pitch Attitude Without Delay and High Frequency Gain K_u = -0.02 rad θ_c/ft/sec

Figure B-12. Sigma-Bode Root Locus Showing Effect of Headwind-to-Tailwind Shear with Decreasing Altitude: $\partial u_g/\partial h < 0$

If the speed subsidence is smaller (ω_u'' 0.15 rad/sec and 0.3 with ω_h'' = 1.0 rad/sec) than the height control bandwidth, an increasing wind shear gradient of the sense presented causes a monotonic reduction in height control bandwidth but a slight <u>increase</u> in height control damping ratio before it causes loss of damping and instability. This is a more favorable circumstance than if the speed subsidence approaches (ω_u'' = 0.3 with ω_h'' = 0.5 rad/sec and ω_u'' = 0.6 with ω_h'' = 1.0 rad/sec) or exceeds (ω_u'' = 0.6 with ω_h'' = 0.5 rad/sec) the height control bandwidth, whence an increasing wind shear of the sense presented causes simultaneous and monotonic loss of height control bandwidth and damping ratio. In all cases shown, the wind shear causes a monotonic increase in the speed subsidence.

In Figs. B-5 and B-6 (ω_u'' = 0.15 rad/sec) (lower closed-loop height control bandwidth and lowest speed subsidence), a shear gradient of -0.2/sec (-11.84 kt/100 ft) decreases the closed-loop height bandwidth about 36 percent and <u>increases</u> the closed-loop damping ratio about 12 percent. Figures B-5 and B-6 also show that the shear gradient must increase to -1.155/sec (-68.39 kt/100 ft) to cause instability.

The larger closed-loop height bandwidth shown in Figs. B-7 and B-8 (ω_u'' = 0.15 rad/sec) (coupled with the lowest speed subsidence) provides the greatest margin of stability against this particular type and sense of shear gradient among the six examples shown. A shear gradient of -1.31/sec (-77.57 kt/100 ft) reduces the closed-loop height bandwidth about 44 percent and <u>increases</u> the closed-loop damping ratio about 21 percent. Figures B-7 and B-8 show that the shear gradient must increase to -3.78/sec (-224 kt/100 ft) to produce instability.

Consider next the two examples with the intermediate values of the speed subsidence ω_u'' = 0.3 rad/sec. In Figs. B-1 and B-2 (ω_u'' = 0.3 rad/sec) (lower closed-loop height control bandwidth), a shear gradient of only -.0842/sec (-5 kts/100 ft) decreases the closed-loop height bandwidth about 20 percent without altering the damping ratio. Figures B-1 and B-2 also show that there is still a considerable margin of stability vested in the damping ratio, because a shear gradient of -1.125/sec (-66.6 kts/100 ft) is required to produce instability.

The larger closed-loop height bandwidth shown in Figs. B-3 and B-4 ($\omega_u'' = 0.3$ rad/sec) provides a greater margin of stability against the headwind-to-tailwind shear with decreasing altitude. A shear gradient $\partial u_g/\partial h$ of -0.85/sec (-50 kts/100 ft) reduces the closed-loop height bandwidth by about 33 percent without altering the closed-loop damping ratio significantly; whereas, a shear gradient of -3.22/sec (-190 kts/100 ft) is required to produce instability. Consider finally the two examples with the largest value of the speed subsidence, $\omega_u'' = 0.6$ rad/sec.

In Figs. B-8 and B-9 ($\omega_u'' = 0.6$ rad/sec) (lower closed-loop height control bandwidth), the shear gradient causes simultaneous and monotonic decrease in closed-loop height bandwidth and damping ratio. For example, a gradient of -0.193/sec (-11.43 kt/100 ft) reduces the height bandwidth about 19 percent and reduces the damping ratio about 24 percent; whereas, a shear gradient of -1.09/sec (-64.5 kt/100 ft) is required to produce instability. This example provides the smallest margin of stability against this particular type and sense of shear gradient among the six examples shown.

The larger closed-loop height bandwidth shown in Figs. B-11 and B-12 ($\omega_u'' = 0.6$ rad/sec) provides a greater margin of stability against the shear gradient, although the decreases in height bandwidth and damping ratio are again simultaneous and monotonic with increasing gradient. A shear gradient of -0.568/sec (-33.51 kt/100 ft) reduces the closed-loop height bandwidth about 27 percent and reduces the damping ratio about 14 percent; whereas, a shear gradient of -2.64/sec (-156 kt/100 ft) is required to produce instability.

The results from these six examples are summarized in Figs. 26 through 28 in the main body of the text.

APPENDIX C

HEIGHT CONTROL IN THE BOB-UP OR -DOWN RAPID RESPONSE PHASE

Height Control With Vertical Velocity Command-Height Hold (VCHH)

During the rapid response phase of the vertical maneuver with velocity command-height hold capability in Fig. 32 (p. 75) in the main body of the text, the reference for the compensatory height regulation loop via the controller is slewed by the velocity command integration while the height feedback loop remains closed to provide a measure of immunity against disturbances--especially the destabilizing effect of a headwind-to-tailwind shear gradient with decreasing altitude: $\partial u_g/\partial h < 0$. Concurrently, the three other compensatory loops for longitudinal (Fig. 32 in the text) and lateral stationkeeping (Fig. 33, p. 76 in the text) and heading-hold are closed via the controller throughout the rapid response phase of the vertical maneuver. To simplify the subsequent analysis, we shall consider only the vertical and longitudinal motions by assuming that the controller decouples the lateral-directional motions during the vertical maneuver by means of the methods described, for example, in Ref. C-1.

The closed-loop transfer function for height response, h, to a vertical velocity command, $\dot{h}_c$, can be expressed with good approximation at low frequencies which are typical of the guidance bandwidth as in Eq. C-1.

$$\frac{h}{\dot{h}_c}(s) = \frac{N^h_{\dot{h}_c}}{\Delta''}(s) \doteq \frac{-Z_{\delta_c} K^{\dot{h}_c} \left(s + \frac{1}{T_{L_{h_c}}}\right) \lfloor \zeta'_x; \omega'_x \rfloor}{s \lfloor \zeta''_h; \omega''_h \rfloor \quad \lfloor \zeta''_x; \omega''_x \rfloor} \qquad \text{(C-1)}$$

Closely Coupled Stationkeeping Dipole

where $\left[\zeta_h'';\omega_h''\right] \triangleq s\left(s + \frac{1}{T_{\theta_2}}\right) - Z_{\delta_c} K_h^{\cdot}\left(s + \frac{1}{T_{L_h}}\right) - \frac{\partial u_g}{\partial h} Z_u$

(C-2)

$$= s^2 + \left(\frac{1}{T_{\theta_2}} - Z_{\delta_c} K_h^{\cdot}\right)s - Z_{\delta_c} K_h^{\cdot}/T_{L_h} - \frac{\partial u_g}{\partial h} Z_u$$

$$\left[\zeta_x';\omega_x'\right] \doteq \left[\zeta_x'';\omega_x''\right] \doteq s^2 + \left(X_\alpha - g\right)K_{\dot{x}}s + \frac{\left(X_\alpha - g\right)K_{\dot{x}}}{T_{L_x}} + \underbrace{\frac{\partial u_g}{\partial h}\left(X_u - \frac{X_{\delta_c}}{Z_{\delta_c}} Z_u\right)}$$

(C-3)

Not of much practical significance because $(X_u - X_{\delta_c}/Z_{\delta_c} Z_u)$ is so small for rotorcraft

$T_{L_h} \triangleq T_h^{\cdot}$ in Fig. 32

$T_{L_x} \triangleq T_{\dot{x}}$ in Fig. 32

$K_h^{\cdot} \triangleq K_{I_h} T_h^{\cdot}$ in Fig. 32; $K_{\dot{x}} \triangleq K_{I_x} T_{\dot{x}}$ in Fig. 32; $\frac{K_{\dot{x}}}{T_{L_x}} \triangleq K_{I_x}$ in Fig. 32

$\underline{K_{h_c}^{\cdot}} \triangleq K_{I_h} K_{h_c}^{\cdot}$ in Fig. 32; $\frac{\underline{K_{h_c}^{\cdot}}}{T_{L_{h_c}}} = \frac{K_h^{\cdot}}{T_{L_h}} \triangleq K_{I_h}$ in Fig. 32

to provide a unit gain for the closed-loop velocity response to a velocity command at low frequencies in Eq. C-1 in the absence of wind shear gradient $\partial u_g/\partial h$.

$$\frac{1}{T_{L_{h_c}}} \doteq \sqrt{-Z_{\delta_c} \frac{K_h^{\cdot}}{T_{L_h}}}$$

to provide matched lead and lag frequencies in the absence of wind shear gradient $\partial u_g/\partial h$. Therefore,

$$\underline{K_{h_c}^{\cdot}} \doteq -\frac{1}{Z_{\delta_c} T_{L_{h_c}}} \text{ if } \partial u_g/\partial h = 0.$$

The corresponding closed-loop transfer function for the collective control displacement, δ_{coll}, required by a vertical velocity command, $\dot{h}_c$, can be expressed with good approximation for the purpose of guidance as in Eq. C-4

$$\frac{\delta_{coll}}{\dot{h}_c}(s) = \frac{N^{\delta_{coll}}_{\dot{h}_c}}{\Delta''} \doteq \frac{\frac{K_{\dot{h}_c}}{T_{L_{h_c}}}\left(s + \frac{1}{T_{L_{h_c}}}\right)\left[\zeta'_x;\omega'_x\right]\left[s\left(s + \frac{1}{T'_{\theta_2}}\right) - \frac{\partial u_g}{\partial h} Z_u\right]}{s\left[\zeta''_h;\omega''_h\right]\left[\zeta''_x;\omega''_x\right]} \qquad \text{(C-4)}$$

Closely coupled Stationkeeping Dipole

where $\frac{1}{T'_{\theta_2}} \doteq \frac{1}{T_{\theta_2}} \doteq -Z_w$

Example Topic (a) Expanded from Main Text Beginning on Page 74

Example of design for a special case of VCHH with preservation of inherent heave damping, i.e., $1/K_{\dot{h}_c} \triangleq 1/T_{L_{hc}} \doteq 1/T_{L_h} \doteq 1/T_{\theta_2}$ and no wind shear, i.e., $\partial u_g/\partial h = 0$. Therefore, $-Z_{\delta_c} K_{\dot{h}_c} \doteq -Z_{\delta_c} K_{\dot{h}} \doteq \omega''_h \doteq 1/T_{\theta_2}$, where $1/T_{\theta_2}$ is the inherent heave damping, a function of main rotor properties, disc loading, geometry and true airspeed, and Z_{δ_c}, the collective control effectiveness, is also a function of main rotor properties, disc loading, geometry, and true airspeed. The closed-loop height response, h, to vertical velocity command, $\dot{h}_c$, will be from Eq. C-1:

$$\frac{h}{\dot{h}_c}(s) \triangleq \frac{N^{h}_{\dot{h}_c}}{\Delta''}(s) \doteq \frac{\frac{1}{T_{\theta_2}}}{s\left(s + \frac{1}{T_{\theta_2}}\right)} \cdot \frac{\left(s + \frac{1}{T'_{\theta_2}}\right)}{\left(s + \frac{1}{T_{\theta_2}}\right)} \cdot \frac{\left[\zeta'_x;\omega'_x\right]}{\left[\zeta''_x;\omega''_x\right]} \qquad \text{(C-5)}$$

closely coupled dipole

closely coupled stationkeeping dipole

The closed-loop collective control required will be from Eq. C-4:

$$\frac{\delta_{coll}}{\dot{h}_c}(s) \triangleq \frac{N^{\delta_{coll}}_{\dot{h}_c}}{\Delta''}(s) \doteq -\frac{1}{Z_{\delta_c} T_{\theta_2}} \cdot \frac{s\left(s + \frac{1}{T_{\theta_2}}\right)\left(s + \frac{1}{T'_{\theta_2}}\right)\left[\zeta'_x; \omega'_x\right]}{s\left(s + \frac{1}{T'_{\theta_2}}\right)\left(s + \frac{1}{T_{\theta_2}}\right)\left[\zeta''_x; \omega''_x\right]} \qquad \text{(C-6)}$$

closely coupled dipole — closely coupled dipole — closely coupled stationkeeping dipole

Equation C-5 approximates the controlled element form $Y_c = K_c/s(s + a)$ with $K_c = a$ for which the generic time-optimal velocity command and rapid height response to a step command in height has already been described in Figs. 34 and 36 the main text (p. 78 and 80, respectively). Equation C-6 shows that the required collective control displacement will be proportional to and in phase with the vertical velocity command time history as described in Fig. 35 in the main text (p. 79).

Example Topic (e) Expanded From Main Text Beginning on Page 88

Example of redesign of VCHH system to increase tolerance to a wind shear gradient $\partial u_g/\partial h = -1.0/\text{sec}$ (-59.2 kt/100 ft). Redesign $K^{\bullet}_h$ and T_{L_h} in Eq. C-2 so that

$$1/T_{\theta_2} - Z_{\delta_c} K^{\bullet}_h \triangleq 2/T_{\theta_2} \text{ and } -Z_{\delta_c} K^{\bullet}_h/T_{L_h} - \partial u_g/\partial h \; Z_u \triangleq (1/T_{\theta_2})^2,$$

if $\partial u_g/\partial h = -1.0/\text{sec}$

$Z_u = -0.198/\text{sec}$

$-Z_{\delta_c} = 9.29 \text{ ft/sec}^2\text{-in}$

and $1/T_{\theta_2} = 0.567/\text{sec}$

therefore, $-Z_{\delta_c} K^{\bullet}_h \triangleq 1/T_{\theta_2}$ and $1/T_{L_h} = 0.198\ T_{\theta_2} + 1/T_{\theta_2} = 0.916/\text{sec}$.

If $-Z_{\delta_c} K^{\bullet}_{h_c} \triangleq 1/T_{L_h} = 1/T_{\theta_2}$ as in Example Topic (a), the transfer function for height response to vertical velocity command (Eq. C-1) in the presence of the designated wind shear gradient will now be

$$\frac{h}{\dot{h}_c}(s) \triangleq \frac{N^{h}_{\dot{h}_c}}{\Delta''}(s) \doteq \frac{\frac{1}{T_{\theta_2}}}{s\left(s+\frac{1}{T_{\theta_2}}\right)} \cdot \frac{\left(s+\frac{1}{T'_{\theta_2}}\right)}{\left(s+\frac{1}{T_{\theta_2}}\right)} \cdot \frac{[\zeta'_x;\omega'_x]}{[\zeta''_x;\omega''_x]} \qquad \text{(C-9)}$$

closely coupled dipole in wind shear

closely coupled stationkeeping dipoles

Equation C-9 is the same as the height response in Eq. C-5 and Fig. 36 in the text (p. 80) for Example Topic (a), except that the vertical velocity command in Fig. 34 in the text (p. 78) is optimized for the effect of this particular wind shear.

The transfer function for closed-loop collective control required in the presence of the designated wind shear gradient will now be

$$\frac{\delta_{coll}}{\dot{h}_c}(s) \triangleq \frac{N^{\delta_{coll}}_{\dot{h}_c}}{\Delta''}(s) = -\frac{1}{Z_{\delta_c} T_{\theta_2}} \cdot \frac{(s-0.244)(s+0.811)}{s\,(s+0.567)} \cdot \frac{\left(s+\frac{1}{T'_{\theta_2}}\right)}{\left(s+\frac{1}{T_{\theta_2}}\right)} \cdot \frac{[\zeta'_x;\omega'_x]}{[\zeta''_x;\omega''_x]} \qquad \text{(C-10)}$$

closely coupled dipole in wind shear

closely coupled stationkeeping dipole

where $-1/Z_{\delta_c} T_{\theta_2} = 0.0610$ in/ft/sec.

Equation C-10 is, however, different from the collective response required in Eq. C-6 and Fig. 35 in the text (p. 79) for Example Case (a), because Eq. C-10 represents the cost of controlling collective displacement to provide a time optimal height response in the designated wind shear with VCHH. Figure 40 (p. 85) shows the collective time history required by Eq. C-10.

Example Topic (f) Expanded from Main Text Beginning on Page 88

Redesigned Example Case (e) in the absence of wind shear ($\partial u_g/\partial h = 0$). Since the redesign in Example Case (e) is based on such an extreme value of the wind shear gradient, it is necessary also to examine the height and collective response to a vertical velocity command in the absence of wind shear. If $\partial u_g/\partial h = 0$ with the VCHH design gains and lead/lag compensation selected in Example Case (e), Eq. C-9 no longer represents the height response; instead, Eq. C-2 for $[\zeta_h'';\omega_h'']$ changes to have the following values

$$\omega_h'' = \sqrt{\frac{-Z_{\delta_c} K_h^{\bullet}}{T_{L_h}}} = 0.721/\text{sec} \text{ and } \zeta_h'' = \frac{2(0.567)}{2(0.721)} = 0.787 \text{ if } \frac{\partial u_g}{\partial h} = 0$$

and Eq. C-1, in turn, changes to have the values in Eq. C-11 for the height response to a vertical velocity command

$$\frac{h}{\dot{h}_c}(s) \triangleq \frac{N_{h_c}^{h}}{\Delta''}(s) \doteq \frac{0.567(s + 0.567)[\zeta_x';\omega_x']}{s[0.787;0.721][\zeta_x'';\omega_x'']} \qquad \text{(C-11)}$$

closely coupled stationkeeping dipole

The effective controlled element in Eq. C-11 is still approximately of the form $Y_c = K_c/s(s + a)$, where $a \doteq 0.862/\text{sec}$ based on the dimensionless variability* and $a \doteq 1.0/\text{sec}$ based on the half-power frequency; but the

---

*"Bandwidth" is a vague term unless the displayed signal spectrum is rectangular. For other spectral shapes, the dimensionless variability can be used to define a rectangular bandwidth equivalent, i.e.,

$$\omega_{i_e} = \frac{\left[\int_o^{\infty} \Phi_{ii}(\omega)d\omega\right]^2}{\int_o^{\infty} [\Phi_{ii}(\omega)]^2 \, d\omega} \quad \text{(Ref. C-2)}$$

steady-state gain of the velocity response to a velocity command is less than unity; (it is 0.618). The corresponding collective response transfer function in Eq. C-12 is based on Eq. C-4 with appropriate modification of $[\zeta_h'';\omega_h''] = [0.787;0.721]$.

$$\frac{\delta_{coll}}{\dot{h}_c}(s) \triangleq \frac{N^{\delta_{coll}}_{\dot{h}_c}}{\Delta''}(s) \doteq -\frac{1}{Z_{\delta_c} T_{\theta_2}} \cdot \frac{s\left(s+\frac{1}{T_{\theta_2}}\right)\left(s+\frac{1}{T'_{\theta_2}}\right)\left[\zeta_x';\omega_x'\right]}{s\ [0.787;0.721]\ \left[\zeta_x'';\omega_x''\right]} \qquad \text{(C-12)}$$

closely coupled stationkeeping dipole

where $-1/Z_{\delta_c} T_{\theta_2} = 0.0610$ in/ft/sec

$$1/T_{\theta_2} \doteq 1/T'_{\theta_2} = 0.567/\text{sec}$$

If the high frequency gain ($-Z_{\delta_c} K_{\dot{h}_c} = 0.567$/sec) is increased by a factor of $1/0.618 = 1.618$ to compensate for the reduced gain in Eq. C-11, the new high frequency gain in Eq. C-11a is 0.917, and the corresponding high frequency gain in Eq. C-12a is 0.0987

$$\frac{h}{\dot{h}_c}(s) = \frac{1.618N^{h}_{\dot{h}_c}}{\Delta''}(s) = \frac{0.917(s+0.567)\left[\zeta_x';\omega_x'\right]}{s[0.787;0.721]\left[\zeta_x'';\omega_x''\right]} \qquad \text{(C-11a)}$$

Closely Coupled Stationkeeping Dipole

and

$$\frac{\delta_{coll}}{\dot{h}_c}(s) = \frac{1.618N^{\delta_{coll}}_{\dot{h}}}{\Delta''}(s) = \frac{0.0987s(0.567)^2\left[\zeta_x';\omega_x'\right]}{s[0.787;0.721]\left[\zeta_x'';\omega_x''\right]} \qquad \text{(C-12a)}$$

If the amplitude and time intervals of the velocity command are recomputed to account for the increased high frequency gain, K_c, and increased effective heave damping, a, in the maneuver urgency factor $K_c M/a^2 A = 1.0$, where $M = |\dot{h}_c|$, then

$$|\dot{h}_c| \doteq a^2 A/K_c = (0.862)^2 50/0.917 = 40.51 \text{ ft/sec},$$

where $a = 0.862$ based on the dimensionless variability

$T_s = 1.61/1.0 = 1.61$ sec

$T_f = 0.511/1.0 = 0.511$ sec

and $T_c = 2.12$ sec

where $a \doteq 1.0$/sec based on the half-power frequency of the vertical velocity ($\dot{h}$) response to a velocity command ($\dot{h}_c$). The application of the two different values for a is deliberate because of the form of the controlled element in Eq. C-11a.

The modified velocity command is shown as a function of time in the main text, Fig. 43 (p. 89). Transient responses of collective and height displacements for this modified (and nearly re-optimized) velocity command are given in the maintext Figs. 44 and 45 (pp. 90 and 91), respectively. Corresponding velocity response is presented in the phase plane, Fig. 46 (p. 92), which confirms that the height and vertical velocity responses have been nearly re-optimized in the absence of wind shear.

Conclusion from these examples with VCHH

The "worst-case" design for the wind shear in Example Case (e) is preferable, because it results in a conservative design which can be more easily re-optimized as in Example Case (f) by velocity command amplitude and time interval adjustment in the absence of wind shear.

REFERENCES

C-1 Jewell, Wayne F., and Warren F. Clement, Crossfeed Compensation Techniques for Decoupling Rotorcraft Responses to Control Inputs, Systems Technology, Inc., Technical Report No. 1229-1, September 1985.

C-2 Blackman, R. B., and J. W. Tukey, The Measurement of Power Spectra, Dover Publications, Inc., New York, 1958, p. 19.

APPENDIX D

THE LONGITUDINAL SPEED RESPONSE TO PITCHING MOMENT CONTROL OR PITCH ATTITUDE CONTROL FOR ARTICULATED ROTARY-WING AND TILT-ROTOR AIRCRAFT

In this appendix, we shall derive the closed-loop longitudinal speed response for typical rotorcraft based on approximations for the ratio of moduli and the ratio of real parts of the complex dipole in the longitudinal speed response to pitching moment control for articulated rotary-wing and tilt-rotor aircraft. The derivation will be performed for hovering flight, because the simplicity of hovering dynamics will enable us to illustrate all of the essential features of the complex dipole which represents the stabilized "pendulum effect" without introducing the unnecessary algebraic complications caused by higher forward speed. Nevertheless, the results are valid at forward speeds typical of formation station-keeping.

When aerodynamic stability derivatives which are usually small are omitted, the two longitudinal equations of hovering motion which describe the pendulum effect in attitude and speed can be written (Refs. D-1 through D-4) together with a third pitch attitude command and feedback equation with rate augmentation for stabilization as:

$$\begin{bmatrix} s - X_u & g & -X_{\delta_B} \\ -M_u & s(s - M_q) & -M_{\delta_B} \\ 0 & K_q s + K_\theta & 1 \end{bmatrix} \begin{Bmatrix} u \\ \theta \\ \delta_B \end{Bmatrix} = \begin{Bmatrix} -X_u \\ -M_u \\ 0 \end{Bmatrix} u_g + \begin{Bmatrix} 0 \\ 0 \\ K_\theta \end{Bmatrix} \theta_c$$

where

g = acceleration of gravity

K_q = pitching rate feedback gain to the longitudinal pitching moment control in dimensional units of time

C-3

K_θ = dimensionless pitch attitude feedback gain to the longitudinal pitching moment control

M = pitching moment applied to the rotorcraft

M_q = $(1/I_y)(\partial M/\partial q)$

M_u = $(1/I_y)(\partial M/\partial u)$

M_{δ_B} = $(1/I_y)(\partial M/\partial \delta_B)$

s = complex Laplacian operator

X = longitudinal force applied to the rotorcraft

X_u = $(1/m)(\partial X/\partial u)$

X_{δ_B} = $(1/m)(\partial X/\partial_{\delta_B})$

I_y = pitching moment of inertia of the rotorcraft

m = mass of the aircraft

q = pitching rate

u = longitudinal perturbed velocity

u_g = longitudinal atmopsheric gust velocity

δ_B = pitching moment control displacement

θ = perturbed pitch attitude

∂ = partial differential operator

The characteristic equation of this set is called the (stabilized) "hovering cubic" and is given by

$$\Delta = \underbrace{s(s - M_q)(s - X_u) + gM_u}_{\text{"Hovering cubic" of vehicle alone}} + \underbrace{(K_q s + K_\theta)[M_{\delta_B}(s - X_u) + X_{\delta_B} M_u]}_{\text{Contribution from Pitch Attitude Stabilization with Rate Augmentation}}$$

Although the speed stability derivatives X_u and M_u can be rather large, they generally have only a small effect on the stabilized pendulum effect in attitude control in the absence of external disturbances such as longitudinal gust velocity, u_g. Consequently we can further simplify the stabilized hovering cubic by neglecting the small products involving the speed stability derivatives and factoring the characteristic equation approximately into a quadratic representing the stabilized pendulum effect and a subsidence representing a reduced surge damping, $0 < 1/T'_{\theta_1} < (-X_u)$

$$\Delta' \doteq \left[s^2 - M_q s + M_{\delta_B} K_q s + M_{\delta_B} K_\theta\right]\left(s + 1/T'_{\theta_1}\right)$$

$$\doteq \left[s^2 + \left(M_{\delta_B} K_q - M_q\right)s + M_{\delta_B} K_\theta\right]\left(s + 1/T'_{\theta_1}\right)$$

$$\equiv \left[s^2 + 2\zeta'_p \omega'_p s + (\omega'_p)^2\right]\left(s + 1/T'_{\theta_1}\right)$$

where twice the real part of the complex pole is $2\zeta'_p\omega'_p = M_{\delta_B}K_q - M_q$ and the square of its modulus is $(\omega'_p)^2 \doteq M_{\delta_B}K_\theta$.

For articulated rotary wing and tilt rotor aircraft, the corresponding speed response numerator to the pilot's δ_B input in the absence of an external disturbance, u_g, is:*

$$N^u_{\delta_B} \doteq X_{\delta_B}\left(s^2 + 2\zeta_u\omega_u s + \omega_u^2\right)$$

---

*The corresponding speed response numerator to the pilot's pitch attitude command input, θ_c, is

$$N^u_{\theta_c} \doteq K_\theta X_{\delta_B}\left(s^2 + 2\zeta_u\omega_u s + \omega_u^2\right)$$

where twice the real part of the complex zero is:

$$2\zeta_u \omega_u \doteq -M_q$$

and the square of its modulus is:

$$\omega_u^2 \doteq -\frac{g}{X_{\delta_B}} M_{\delta_B}$$

At low forward speeds and in hovering, $\omega_u^2 \doteq -M_{\delta_B}$; therefore,

$$\frac{(\omega_u)^2}{(\omega_p')^2} = -\frac{1}{K_\theta}$$

expresses the ratio of squared moduli of the complex dipole representing the stabilized pendulum effect. Typically $-K_\theta$ is on the order of unity. The ratio of real parts of the complex dipole is

$$\frac{\zeta_u \omega_u}{\zeta_p' \omega_p'} \doteq \frac{-M_q}{M_{\delta_B} K_q - M_q}$$

Since $M_q < 0$ and $M_{\delta_B} K_q > |M_q|$, the ratio of real parts will usually be less than unity; and the amplitude of the residual oscillatory pendulum component in longitudinal speed perturbations will be noticeable (and may be bothersome) to the pilot when he regulates disturbances via θ_c through δ_B.

We can represent the effect of speed regulation by the pilot with the aid of the block diagram below

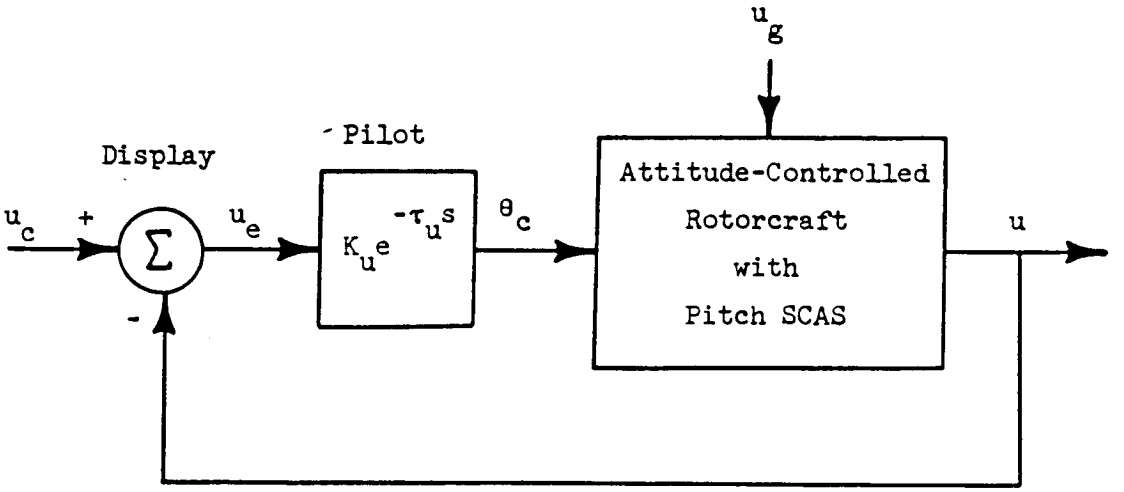

The transfer function for the attitude-controlled rotorcraft with pitch stability and control augmentation system (SCAS) has been derived here as

$$\left[\frac{u}{\theta_c}(s)\right]_{\theta,q\to\delta_B} = \frac{K_\theta X_{\delta_B}}{(s + 1/T'_{\theta_1})} \frac{[s^2 + 2\zeta_u \omega_u s + \omega_u^2]}{[s^2 + 2\zeta'_p \omega'_p s + (\omega'_p)^2]}$$

where $K_\theta \doteq -1$, $X_{\delta_B} \doteq g \doteq 32.2$ ft/sec^2, and $0 < 1/T'_{\theta_1} < -X_u$

EXAMPLE

An effective rotor response delay of 0.1 sec will be added to a pilot's effective delay of 0.33 sec so that $\tau_u \doteq 0.43$ sec by assumption. Typical values for the other singularities are listed below.

$(1/T_{\theta_1})'$	= 0.0257 rad/sec	ζ_u	= 0.0433
ζ'_p	= 0.337	ω_u	= 2.1 rad/sec
ω'_p	= 2.48 rad/sec		

Thus the open-loop transfer function for speed regulation by the pilot will be

$$\left[\frac{u}{u_e}(s)\right]_{\theta,q\to\delta_B} = K_u e^{-\tau_u s}\left[\frac{u}{\theta_c}(s)\right]_{\theta,q\to\delta_B} = \frac{K_u K_\theta X_{\delta_B}[\zeta_u;\omega_u]e^{-\tau_u s}}{(\frac{1}{T'_{\theta_1}})[\zeta'_p;\omega'_p]}$$

$$= \frac{-32.2K_u[0.0433;2.1]e^{-0.43s}}{(0.0257)[0.337;2.48]}$$

where the following abbreviated notation is used for polynomial factors in root locus form:

Real factor $(\frac{1}{T'_{\theta_1}})$ means $(s + \frac{1}{T'_{\theta_1}})$

Quadratic factor $[\zeta;\omega]$ means $[s^2 + 2\zeta\omega s + \omega^2]$

A Bode diagram of this open-loop transfer function is shown in Fig. D-1a attached. Notice the decade-and-a-half (from 0.03 to 1.0 rad/sec) of K/s controlled element characteristics which are favorable to unit gain crossover with ample phase margin. A corresponding complex root locus is shown in Fig. D-1b attached. Closed-loop speed regulation characteristics are identified for a typical range of the pilot's gain $0.0223 \leq -K_u \leq 0.06$ rad/ft/sec in speed regulation tasks demanding high precision.

The rotorcraft's airspeed response numerator, $N^u_{\delta_B}$, provides favorable second-order lead compensation at 2.1 rad/sec, which is nearly equal to the stabilized "pendulum" frequency at 2.48 rad/sec resulting from the pitch attitude closure with rate augmentation in the SCAS. Consequently the pilot's pure gain airspeed loop closure in Figs. D-1a and D-1baccomplishes two desirable results: (1) it increases the closed-loop

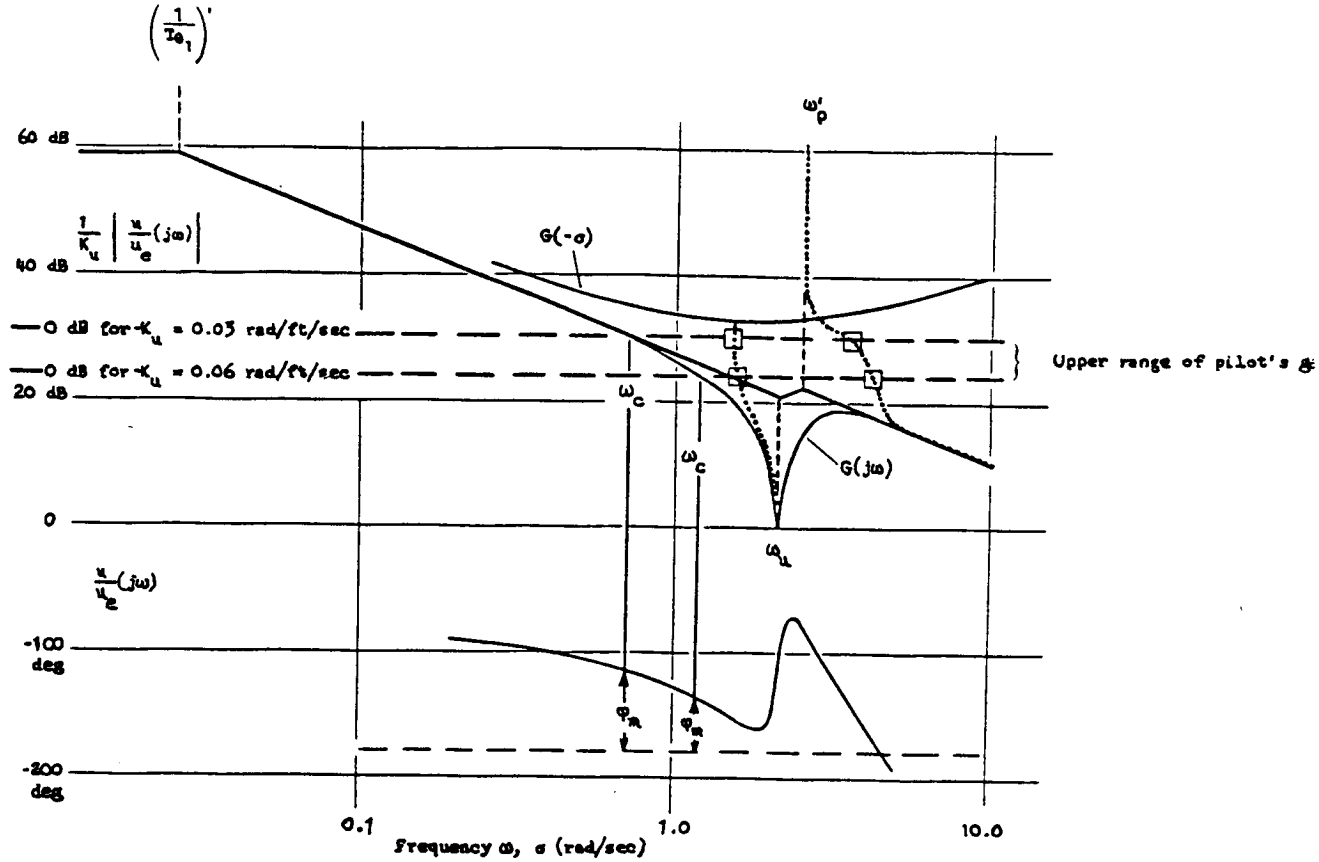

Figure D-1a. Bode Root Locus for Airspeed Outer Loop Closure, $u \rightarrow \theta_c$ with Pitch AFCS

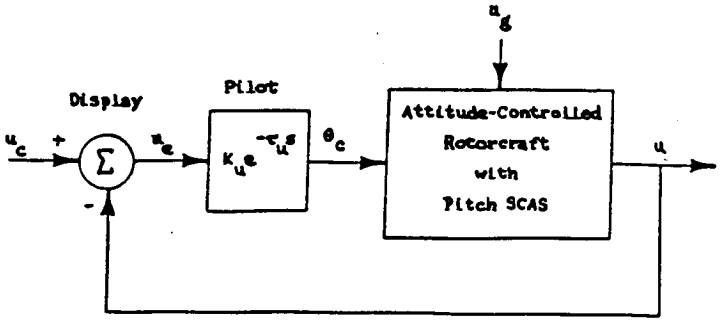

Block Diagram Showing Effect of Airspeed Regulation by the Pilot

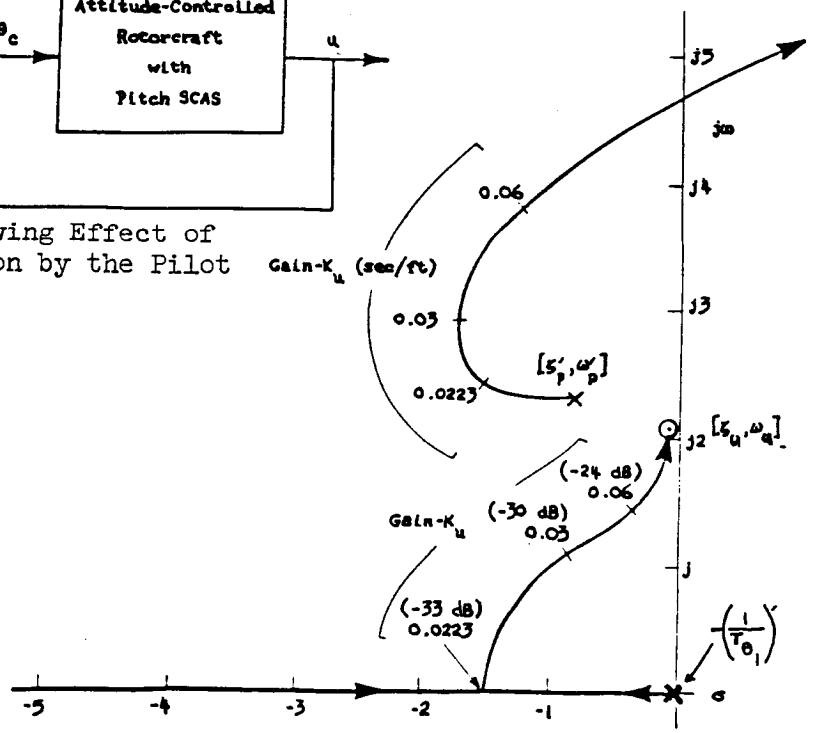

Figure D-1b. Complex Root Locus for Airspeed Outer-Loop Closure, $u \rightarrow \theta_c$ with Pitch AFCS

"pendulum" bandwidth in excess of 3 rad/sec while maintaining an adequate damping ratio in excess of 0.4, and (2) it restores an oscillatory closed-loop "phugoid" with a relatively high undamped natural frequency, 1.5 rad/sec, which is relatively invariant over a wide range of damping ratio, from 0.9 to 0.3, as the pilot's gain is increased. The closed-loop "phugoid" governs the airspeed regulation bandwidth, but will appear to the pilot using a precision display of speed as an oscillatory mode with increasing amplitude as he increases his gain. The airpseed regulation bandwidth is not sensitive to a two-fold variation in the pilot's gain in excess of $-K_u = 0.0223$ rad/ft/sec, which variation primarily affects damping ratio and modal response coefficient. For example, if we hypothesize a step change in commanded airspeed, the transient overshoot associated with the closed-loop "phugoid" will be nil if the pilot's gain $-K_u = 0.0223$ rad/ft/sec, but the overshoot will increase from 6 percent to 28 percent as the pilot's gain, $-K_u$, is increased from 0.03 to 0.06 rad/ft/sec. Thus the net effect of the complex dipole in the speed response is to cause a marked loss in precision of airspeed regulation as the pilot's gain is increased above $K_u \doteq 0.03$ rad/ft/sec, even though the bandwidth is relatively invariant.

Up to this point in the example we have illustrated the effects of a pure gain strategy for airspeed regulation by the pilot. We can next represent the pilot's trimming strategy for speed control by an integral gain, K_x/s, in parallel with the pure gain, K_u, both of which operate on speed error, u_e, as shown in the following block diagram.

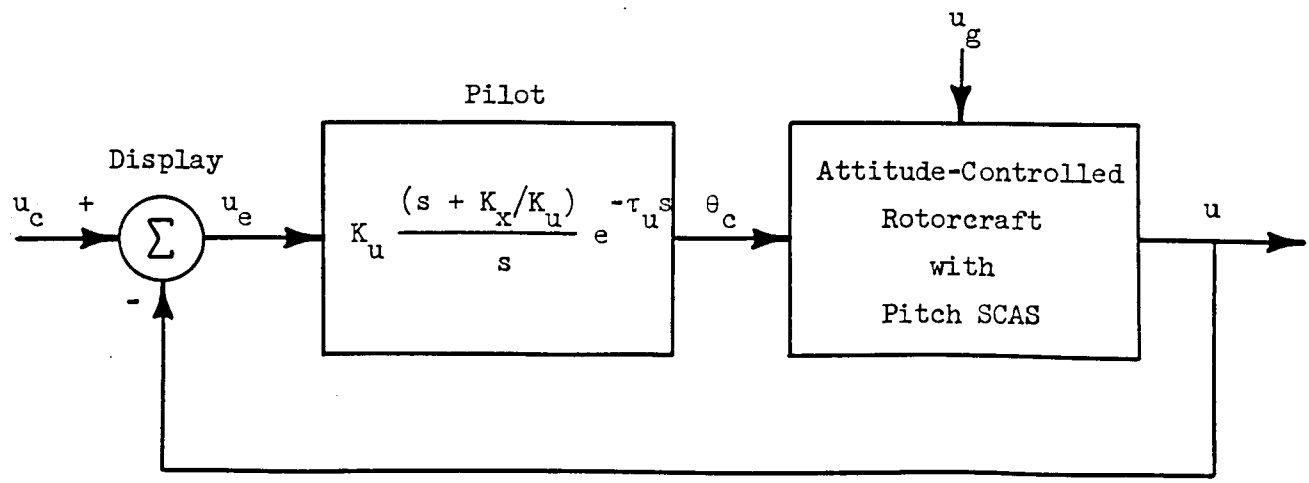

The open-loop transfer function for speed regulation will now become, again using the abbreviated notation for factors,

$$\left[\frac{u}{u_e}(s)\right]_{\theta,q\to\delta_B} = \frac{K_u K_\theta X_{\delta_B} \left(\frac{K_x}{K_u}\right)[\zeta_u;\omega_u]e^{-\tau_u s}}{(0)\left(\frac{1}{T'_{\theta_1}}\right)[\zeta'_p;\omega'_p]}$$

where $K_u K_\theta X_{\delta_B} = -32.2K_u$ as before

From this transfer function it is clear that successful trimming by the pilot requires that $K_x/K_u \doteq 1/T'_{\theta_1}$. Physically this means that the pilot's trimming gain ratio, K_x/K_u, must match the reduced surge damping, $0 < 1/T'_{\theta_1} < (-X_u)$. In terms of the Bode diagram of Fig. D-1a, this will extend the K/s controlled element characteristic to zero (to provide zero steady-state speed error) and create a real closed-loop dipole in the vicinity of $K_x/K_u \doteq 1/T'_{\theta_1}$, which represents the trimming subsidence. Thus, except for this dipole near the origin and the pole at the origin, the complex root locus will be virtually identical to that in Fig. D-1b.

This example can be extended again to illustrate the effects of a hovering strategy by the pilot which is intended to regulate longitudinal position, x. A block diagram for this part of the hovering task is shown below.

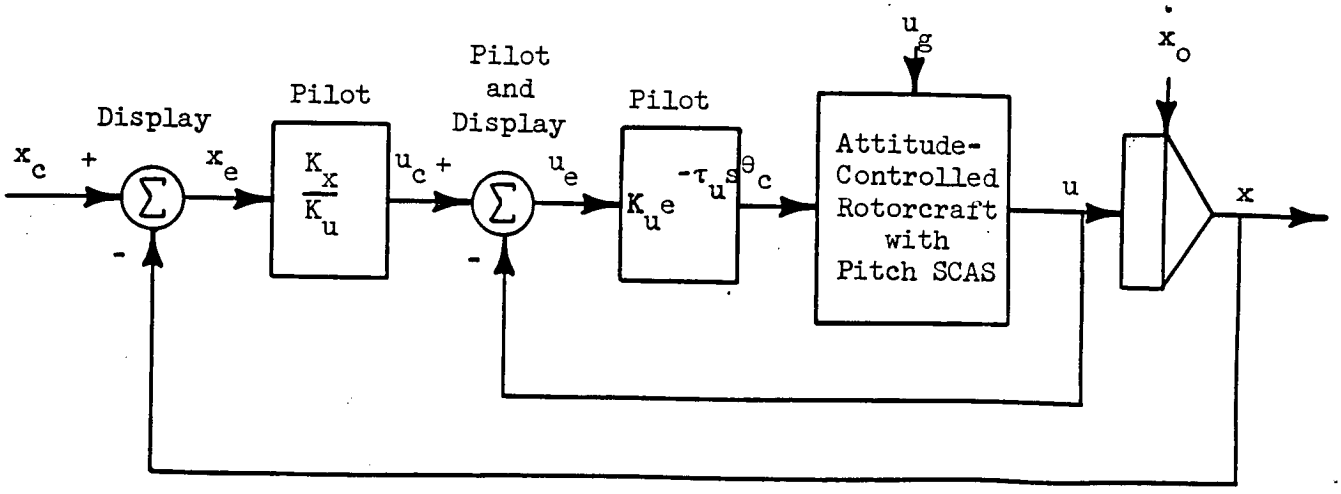

The open-loop transfer function for longitudinal position regulation will become, again using the abbreviated notation for factors,

$$\left[\frac{x}{x_e}(s)\right]_{\theta,q\rightarrow\delta_B} = \frac{K_u K_\theta X_{\delta_B} \left(\frac{K_x}{K_u}\right)[\zeta_u;\omega_u]e^{-\tau_u s}}{(0)\left(\frac{1}{T'_{\theta_1}}\right)[\zeta'_p;\omega'_p]}$$

where $K_u K_\theta X_{\delta_B} = -32.2K_u$ as before

Note the similarity in form to the previous open-loop transfer function for trimming speed regulation. In the present instance, however, the pilot's strategy for his displacement-to-rate gain ratio, K_x/K_u, operating on position error will depend on his relative thresholds of indifference to velocity and displacement cues and his perception of the disturbance environment. Three types of position regulation strategy are depicted in the sketches of complex root loci in the following figures.

In Fig. D-2 , the disturbance environment is presumed to be relatively benign, $K_x/K_u > 1/T'_{\theta_1}$, and, except near the origin, the complex root locus is virtually indistinguishable from that in Fig. D-1b.

In Fig. D-3 the disturbance environment is presumed to be significant, $K_x/K_u >> 1/T'_{\theta_1}$, and the predominant closed-loop "phugoid" bandwidth remains proportional to the pilot's gain, $-K_u$, with a relatively restricted variation in closed-loop damping ratio about the optimum value, 0.707. These closed-loop characteristics enable the pilot to suppress the disturbances as long as his achievable bandwidth (approximately 1 rad/sec) exceeds that of the disturbances. Otherwise his gain (and bandwidth) will necessarily regress.

In Fig. D-4 the pilot is presumed to have adopted too high a gain ratio, K_x/K_u, which results in a lower than desirable closed-loop damping ratio for the "phugoid," regardless of his gain, $-K_u$.

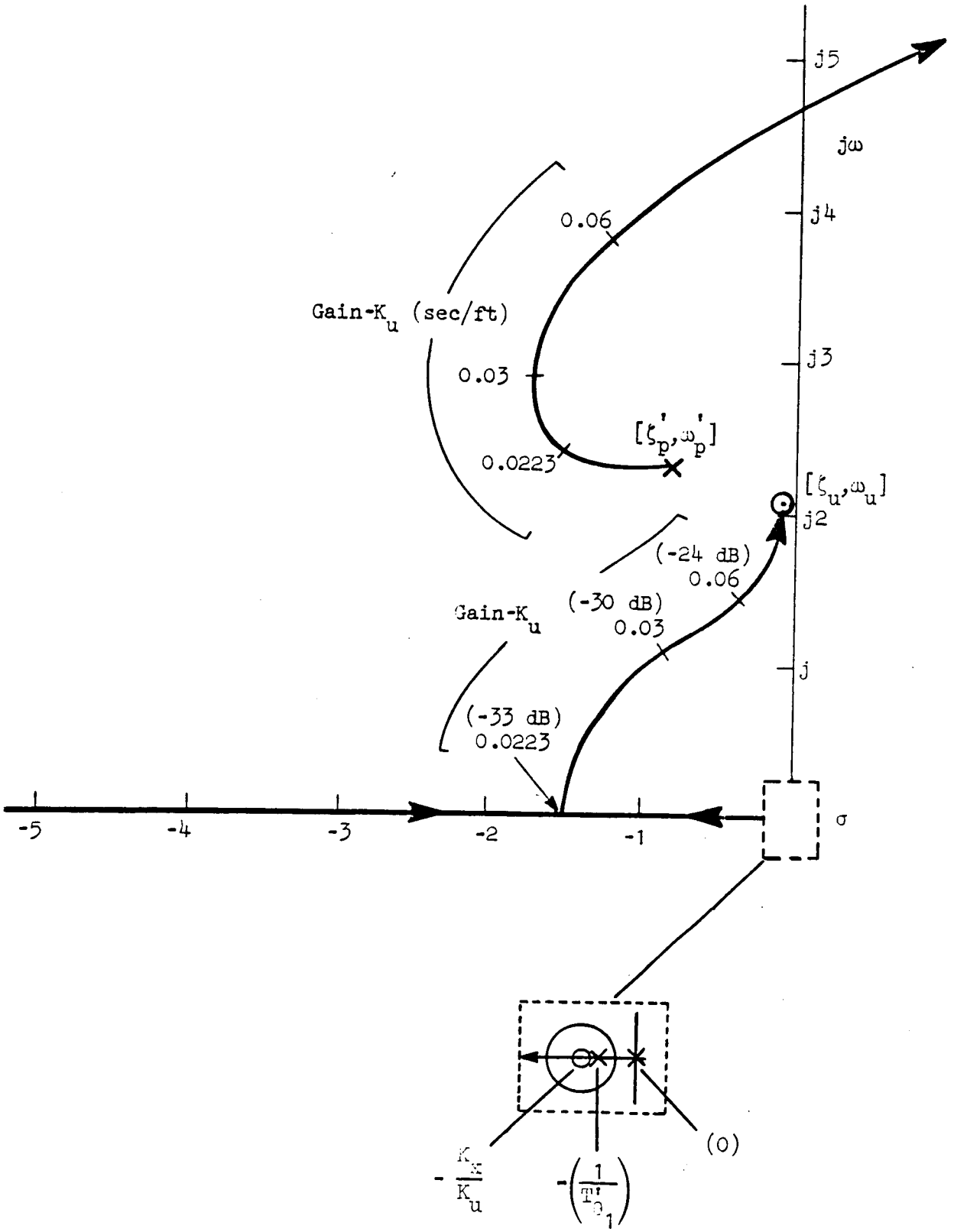

Figure D-2. Complex Root Locus For Longitudinal Position Loop Closure x, u → θ_c in a Benign Disturbance Environment ($K_x/K_u \geq 1/T_{\theta_1}$)

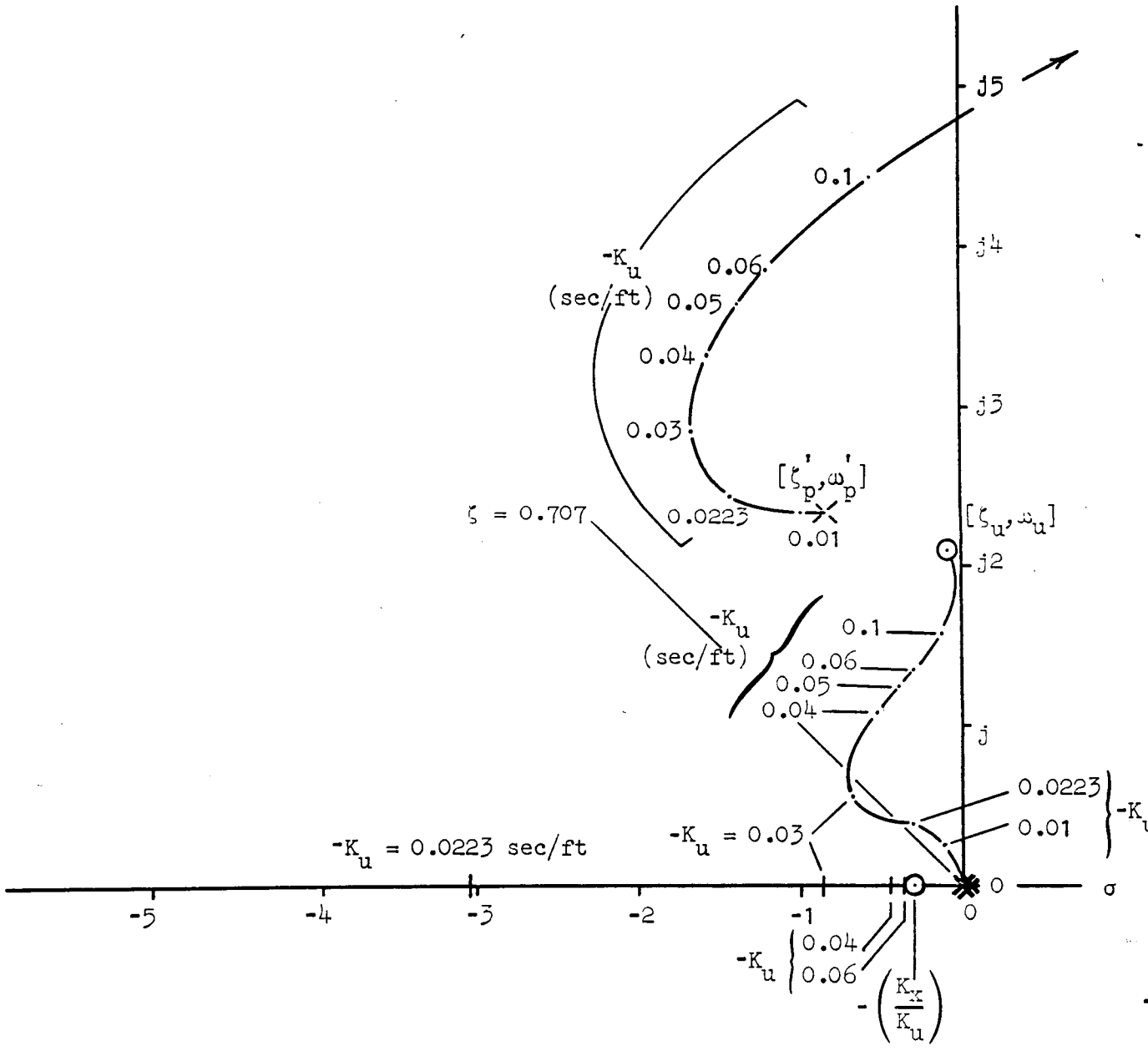

Figure D-3. Complex Root Locus for Longitudinal Position Loop Closure $x, u \rightarrow \theta_c$ in a Disturbed Environment with Gain Ratio K_x/K_u Nearly Optimum ($K_x/K_u = 0.3$)

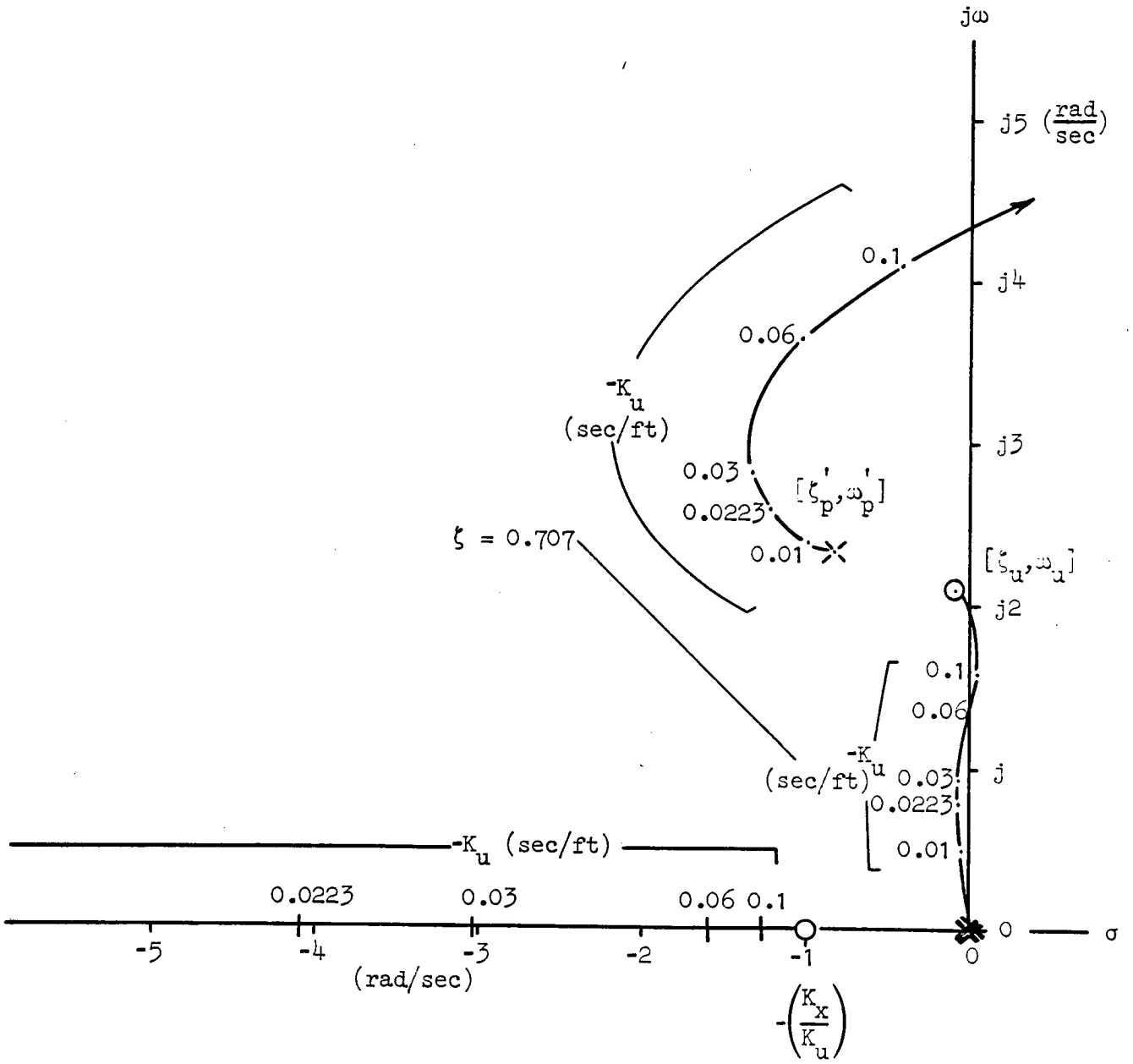

Figure D-4. Complex Root Locus for Longitudinal Position Loop Closure $x, u \rightarrow \theta_c$ with Gain Ratio K_x/K_u too High. $(K_x/K_u = 1.0)$

REFERENCES

D-1. Wolkovitch, J., R. P. Walton, VTOL and Helicopter Approximate Transfer Functions and Closed-Loop Handling Qualities, Systems Technology, Inc., Technical Report No. 128-1, June 1965.

D-2. Stapleford, R. L., J. Wolkovitch, R. E. Magdaleno, C. P. Shortwell, and W. A. Johnson, An Analytical Study of V/STOL Handling Qualities in Hover and Transition, AFFDL-TR-65-73, October 1965.

D-3. Wolkovitch, J., An Introduction to Hover Dynamics, SAE Paper No. 660576, August 1966.

D-4. Walton, R. P., R. L. Stapleford, An Analytical Study of Helicopter Handling Qualities in Hover, Paper presented before the American Helicopter Society Twenty-Second Annual National Forum, Washington, D. C., May 1966.

APPENDIX E

NUMERICAL SOLUTIONS OF THE TRANSCENDENTAL INVARIANCE CONDITIONS FOR TIME OPTIMALITY

Table E-1 provides numerical solutions of the transcendental invariance conditions for time optimality given in Table A-1 in Appendix A for controlled element $Y_c = K_c/s(s + a)$. Definitions of symbols are as follows:

a^2A/K_cM	Controlled element-and-maneuver characteristic (dimensionless inverse maneuver urgency factor)
a	Characteristic damping, rad/sec
A	Amplitude of step function representing command input, units of displacement appropriate to the maneuver
K_c	High frequency gain of the controlled element in appropriate units
M	Average absolute amplitude of the controller response appropriate for each element assuming the controller response to be bang-bang with equal positive and negative amplitudes
T_s	Starting pulse time interval for the controller response, sec
T_f	Final pulse time interval for the controller response, sec
T_c	Time to complete the rapid response maneuver, $T_s + T_f$, sec
T_L	Characteristic lead compensation time at the pulse switching point of the controller, sec

TABLE E-1. INVARIANCE CONDITIONS FOR TIME OPTIMALITY WITH A STEP INPUT AND CONTROLLED ELEMENT

$Y_c = K_c/s(s + a)$

a^2A/K_cM	$\tau_s = aT_s$	$\tau_f = aT_F$	$\tau_s + \tau_f = \tau_c = aT_c$	$\frac{1}{\tau_L} = \frac{1}{aT_L}$
0	0	0	0	∞
ε_o	$2\tau_f$	$\frac{\sqrt{\varepsilon_o}}{\sqrt{3}}\left(1 + \frac{1}{2}\frac{\sqrt{\varepsilon_o}}{\sqrt{3}}\right)$	$3\tau_f$	$\frac{\tau_s - \frac{\tau_s^2}{2!} + \frac{\tau_s^3}{3!} - \cdots}{\varepsilon_o - \frac{\tau_s^2}{2!} + \frac{\tau_s^3}{3!} - \cdots}$
0.01	0.118913	0.05769	0.17660	35.015
0.03	0.21056	0.09975	0.31031	20.395
0.10	0.40194	0.18091	0.58285	11.398
0.25	0.674	0.281	0.955	7.39
0.50	1.03	0.387	1.42	5.53
0.75	1.33	0.458	1.79	4.73
1.0	1.61	0.511	2.12	4.27
1.5	2.15	0.583	2.73	3.79
2.0	2.67	0.626	3.30	3.56
ε_∞	$\varepsilon_\infty + \tau_f$	$\ell n2$	$\varepsilon_\infty + 2\ell n2$	$1/(1 - \ell n2)$

(Continued)

TABLE E-1 (Concluded)

a^2A/K_cM	$T_s\sqrt{\frac{K_cM}{A}}$	$T_f\sqrt{\frac{K_cM}{A}}$	$T_c\sqrt{\frac{K_cM}{A}}$	$\frac{1}{T_L}\sqrt{\frac{A}{K_cM}}$	$\frac{T_c}{4T_L}$
0	$2\sqrt{3}/3$	$\sqrt{3}/3$	$\sqrt{3}$	$2\sqrt{3}$	1.50
⋮	⋮	⋮	⋮	⋮	⋮
ε_o	$\frac{2\tau_f}{\sqrt{\varepsilon_o}}$	$\frac{\tau_f}{\sqrt{\varepsilon_o}}$	$\frac{3\tau_f}{\sqrt{\varepsilon_o}}$	$\frac{\sqrt{\varepsilon_o}}{\tau_L}$	$\frac{3\tau_f}{4\tau_L}$
⋮	⋮	⋮	⋮	⋮	⋮
0.01	1.19	0.577	1.77	3.50	1.56
0.03	1.22	0.576	1.79	3.53	1.58
0.1	1.27	0.572	1.84	3.60	1.65
0.25	1.35	0.562	1.91	3.70	1.77
0.50	1.46	0.547	2.01	3.91	1.97
0.75	1.54	0.529	2.07	4.10	2.12
1.0	1.61	0.511	2.12	4.27	2.26
1.5	1.755	0.476	2.23	4.64	2.57
2.0	1.89	0.443	2.33	5.03	2.85
⋮	⋮	⋮	⋮	⋮	⋮
ε_∞	$\frac{\varepsilon_\infty + \tau_f}{\sqrt{\varepsilon_\infty}}$	$\frac{\ell n2}{\sqrt{\varepsilon_\infty}}$	$\frac{\varepsilon_\infty + 2\ell n2}{\sqrt{\varepsilon_\infty}}$	$\frac{\sqrt{\varepsilon_\infty}}{(1 - \ell n2)}$	$\frac{\varepsilon_\infty + 2\ell n2}{4(1 - \ell n2)}$

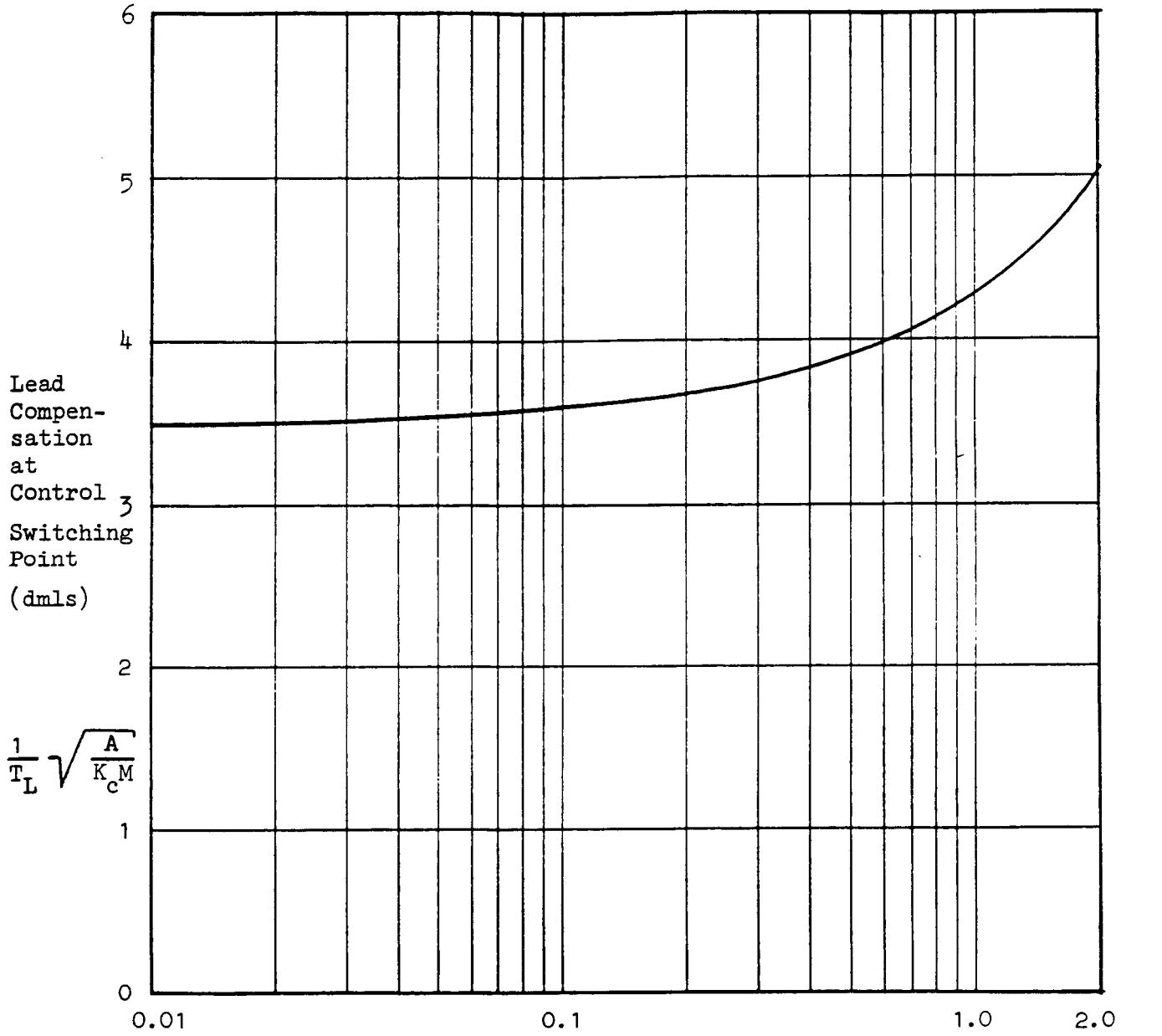

Lead Compensation at Switching Point
For Controlled Element $Y_c = K_c/s(s + a)$

APPENDIX F

EQUATIONS AND METHODS USED FOR VARIANCE ANALYSIS

A. LONGITUDINAL AND VERTICAL

A block diagram of the mathematical models used for variance estimation in height control and longitudinal control tasks is given in Fig. F-1. The pilot's control strategies and divided attention noise sources are represented at the left side of Fig. F-1. Command equalization for velocity control with position hold capabilities are represented across the upper and lower portions of Fig. F-1. Atmospheric turbulence noise sources are shown right of center, and rotorcraft dynamics and kinematics are depicted at the right side of Fig. F-1.

Laplace-transformed linear differential equations of motion for the longitudinal and vertical variance analysis are given in Table F-1, together with symbols not otherwise identified in the block diagram, Fig. F-1.

B. LATERAL AND DIRECTIONAL

A block diagram of the mathematical models used for variance estimation in directional control and lateral control tasks is given in Fig. F-2. The pilot's control strategies and divided attention noise sources are represented at the left side of Fig. F-2. Control equalization for yaw rate command with heading hold capability is represented across the upper portion of Fig. F-2, and control equalization for lateral velocity command with position hold capability is represented across the lower portion of Fig. F-2. Atmospheric turbulence noise sources are shown right of center, and rotorcraft dynamics and kinematics are depicted at the right side of Fig. F-2.

Laplace-transformed linear differential equations of motion for the lateral and directional variance analysis in hover are given in Table F-2, together with symbols not otherwise identified in the block diagram, Fig. F-2.

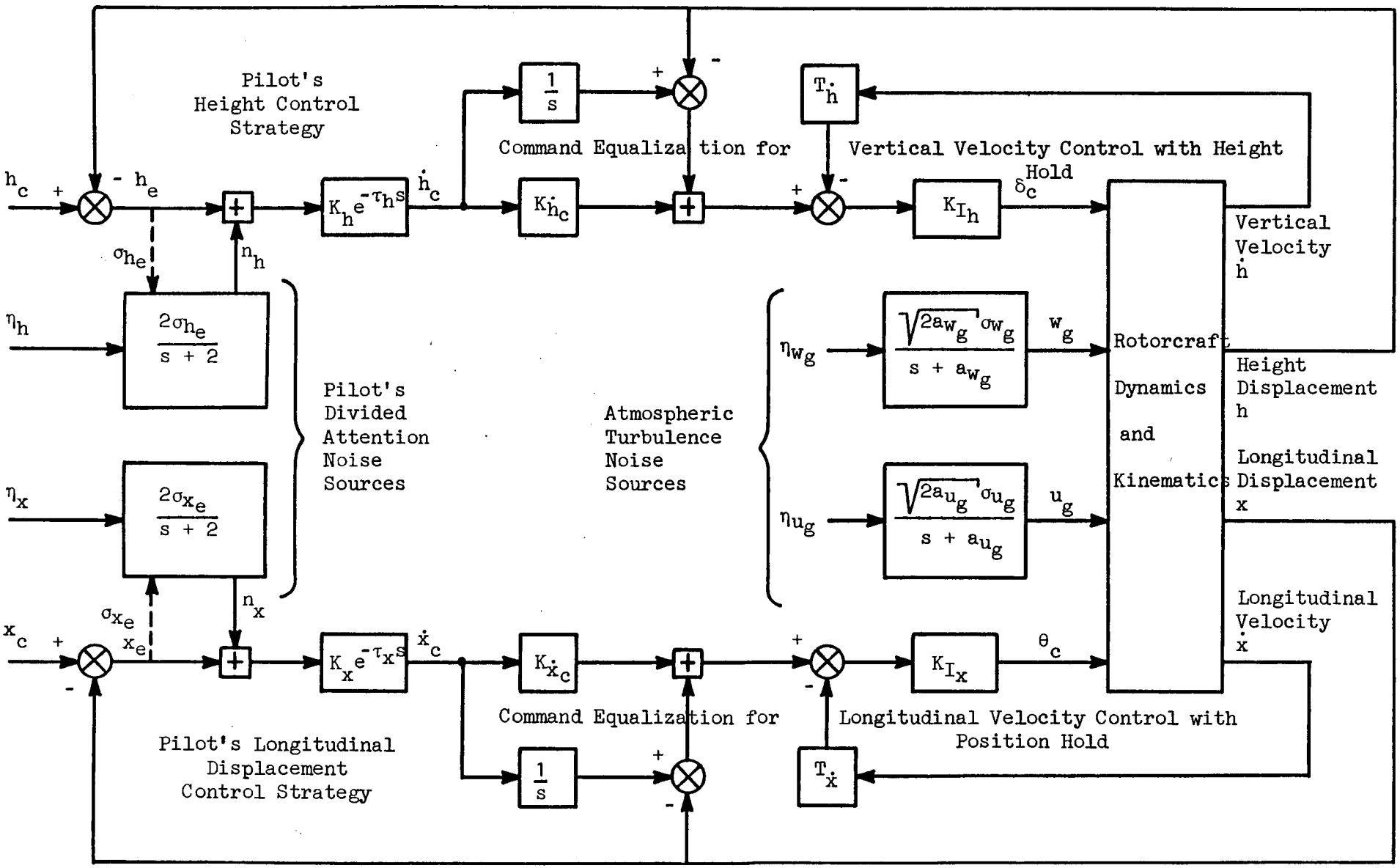

Figure F-1. Block Diagram of Mathematical Models for Covariance Estimation in Height Control and Longitudinal Control Tasks

TABLE F-1. LAPLACE-TRANSFORMED LINEAR DIFFERENTIAL EQUATIONS OF MOTION FOR LONGITUDINAL AND VERTICAL COVARIANCE ANALYSIS

$$
\begin{array}{c}
\\ 1 \\ 2 \\ 3 \\ 4 \\ 5 \\ 6 \\ 7 \\ 8
\end{array}
\begin{bmatrix}
s-\bar{X}_u & \bar{X}_w & -\bar{X}_\theta & -\bar{X}_{\delta_e} & 0 & 0 & \bar{X}_u \frac{\partial u_g}{\partial x} + \bar{X}_w \frac{\partial w_g}{\partial x} & \bar{X}_u \frac{\partial u_g}{\partial h} + \bar{X}_w \frac{\partial w_g}{\partial h} \\
\bar{Z}_u & s-\bar{Z}_w & U_o \bar{Z}_w & \bar{Z}_{\delta_c} & 0 & 0 & -\bar{Z}_u \frac{\partial u_g}{\partial x} - \bar{Z}_w \frac{\partial w_g}{\partial x} & -\bar{Z}_u \frac{\partial w_g}{\partial h} - \bar{Z}_w \frac{\partial w_g}{\partial h} \\
(T_x^{\bullet} s+1)K_{I_x} & 0 & s & 0 & 0 & -(K_{x_c}^{\bullet} s+1)K_{I_x} & 0 & 0 \\
0 & (T_h^{\bullet} s+1)K_{I_h} & 0 & s & -(K_{h_c}^{\bullet} s+1)K_{I_h} & 0 & 0 & 0 \\
0 & 0 & 0 & 0 & [D] & 0 & 0 & K_h[N] \\
0 & 0 & 0 & 0 & 0 & [D] & K_x[N] & 0 \\
1 & 0 & 0 & 0 & 0 & 0 & -s & 0 \\
0 & 1 & 0 & 0 & 0 & 0 & 0 & -s
\end{bmatrix}
\begin{bmatrix}
\dot{x} \\ \dot{h} \\ \theta_c \\ \delta_c \\ \dot{h}_c \\ \dot{x}_c \\ x \\ h
\end{bmatrix}
$$

$$
\begin{array}{c}
\\ 1 \\ 2 \\ 3 \\ 4 \\ 5 \\ 6 \\ 7 \\ 8
\end{array}
=
\begin{bmatrix}
0 & 0 & -X_u & -X_w \\
0 & 0 & Z_u & Z_w \\
0 & 0 & 0 & 0 \\
0 & 0 & 0 & 0 \\
K_h[N] & 0 & 0 & 0 \\
0 & K_x[N] & 0 & 0 \\
0 & 0 & 0 & 0 \\
0 & 0 & 0 & 0
\end{bmatrix}
\begin{bmatrix}
h_c \\ x_c \\ u_g \\ w_g
\end{bmatrix}
$$

TABLE F-1 (CONCLUDED)

SPECIAL SYMBOLS

$$[N] = s^2 - \frac{6}{\tau} s + \frac{12}{\tau^2} \quad \text{where } \tau = \tau_h \text{ in Line 5 or } \tau_x \text{ in Line 6}$$

$$[D] = s^2 + \frac{6}{\tau} s + \frac{12}{\tau^2} \quad \text{where } \tau = \tau_h \text{ in Line 5 or } \tau_x \text{ in Line 6}$$

TRIMMED STABILITY AND CONTROL DERIVATIVES

$$\overline{X}_u = X_u - M_u \frac{X_{\delta_B}}{M_{\delta_B}} \qquad \overline{X}_{\delta_c} = X_{\delta_c} - M_{\delta_c} \frac{X_{\delta_B}}{M_{\delta_B}}$$

$$\overline{X}_w = X_w - M_w \frac{X_{\delta_B}}{M_{\delta_B}}$$

$$\overline{Z}_u = Z_u - M_u \frac{Z_{\delta_B}}{M_{\delta_B}} \qquad \overline{Z}_{\delta_c} = Z_{\delta_c} - M_{\delta_c} \frac{Z_{\delta_B}}{M_{\delta_B}}$$

$$\overline{Z}_w = Z_w - M_w \frac{Z_{\delta_B}}{M_{\delta_B}}$$

$$\overline{X}_\theta = U_o \overline{X}_w - g$$

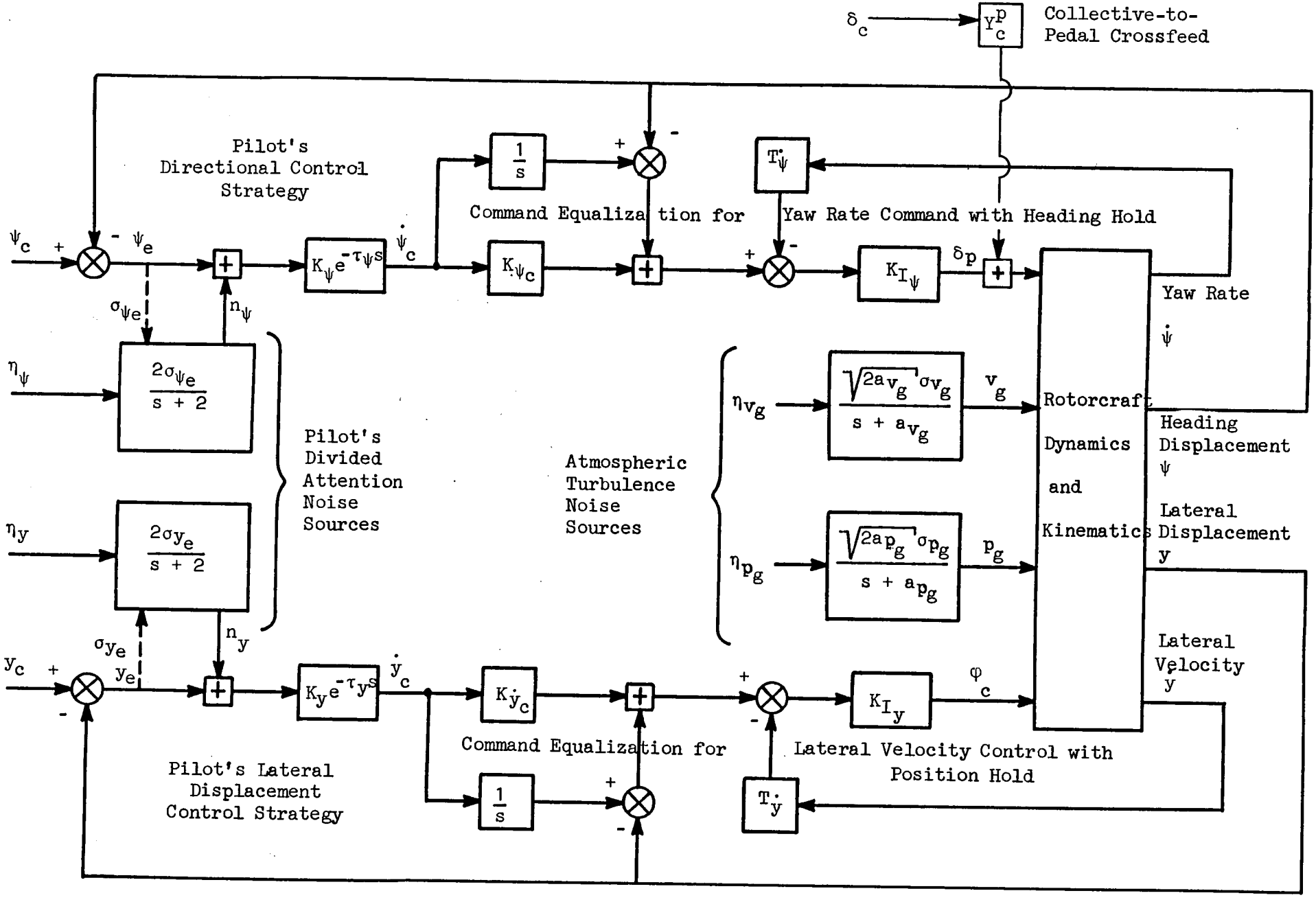

Figure F-2. Block Diagram of Mathematical Models for Covariance Estimation in Directional Control and Lateral Control Tasks

TABLE F-2. LAPLACE-TRANSFORMED LINEAR DIFFERENTIAL EQUATIONS OF MOTION FOR LATERAL AND DIRECTIONAL COVARIANCE ANALYSIS

$$
\begin{array}{c}
\\
1 \\
2 \\
3 \\
4 \\
5 \\
6 \\
7 \\
8
\end{array}
\begin{bmatrix}
s-\bar{Y}_v & -Y_r & -g & -\bar{Y}_{\delta_p} & 0 & 0 & \bar{Y}_v \frac{\partial v}{\partial y}\frac{g}{} + \bar{Y}_r \frac{\partial r}{\partial y}\frac{g}{} & U_o \bar{Y}_v \\
-\bar{N}_v & s-N_r & -N_p s & -\bar{N}_{\delta_p} & 0 & 0 & \bar{N}_v \frac{\partial v}{\partial y}\frac{g}{} + \bar{N}_r \frac{\partial r}{\partial y}\frac{g}{} & U_o \bar{N}_v \\
(T_y^{\bullet}s+1)K_{I_y} & 0 & s & 0 & 0 & -(K_{y_c}^{\bullet}s+1)K_{I_y} & 0 & 0 \\
0 & (T_\psi^{\bullet}s+1)K_{I_\psi} & 0 & s & -(K_{\psi_c}^{\bullet}s+1)K_{I_\psi} & 0 & 0 & 0 \\
0 & 0 & 0 & 0 & [D] & 0 & 0 & K_\psi[N] \\
0 & 0 & 0 & 0 & 0 & [D] & K_y[N] & 0 \\
1 & 0 & 0 & 0 & 0 & 0 & -s & 0 \\
0 & 1 & 0 & 0 & 0 & 0 & 0 & -s
\end{bmatrix}
\begin{bmatrix}
\dot{y} \\ \dot{\psi} \\ \phi_c \\ \delta_p \\ \dot{\psi}_c \\ \dot{y}_c \\ y \\ \psi
\end{bmatrix}
$$

$$
\begin{array}{c}
\\
1 \\
2 \\
3 \\
4 \\
5 \\
6 \\
7 \\
8
\end{array}
=
\begin{bmatrix}
0 & 0 & -Y_v & -Y_r \\
0 & 0 & -N_v & -N_r \\
0 & 0 & 0 & 0 \\
0 & 0 & 0 & 0 \\
K_\psi[N] & 0 & 0 & 0 \\
0 & K_y[N] & 0 & 0 \\
0 & 0 & 0 & 0 \\
0 & 0 & 0 & 0
\end{bmatrix}
\begin{bmatrix}
h_c \\ x_c \\ v_g \\ r_g
\end{bmatrix}
$$

TABLE F-2 (CONCLUDED)

SPECIAL SYMBOLS

$$[N] = s^2 - \frac{6}{\tau} s + \frac{12}{\tau^2} \quad \text{where } \tau = \tau_\psi \text{ in Line 5 or } \tau_y \text{ in Line 6}$$

$$[D] = s^2 + \frac{6}{\tau} s + \frac{12}{\tau^2} \quad \text{where } \tau = \tau_\psi \text{ in Line 5 or } \tau_y \text{ in Line 6}$$

TRIMMED STABILITY AND CONTROL DERIVATIVES

$$\overline{Y}_v = Y_v - L_v \frac{Y_{\delta_A}}{L_{\delta_A}} \qquad \overline{Y}_{\delta_p} = Y_{\delta_p} - L_{\delta_p} \frac{Y_{\delta_A}}{L_{\delta_A}}$$

$$\overline{N}_v = N_v - L_v \frac{N_{\delta_A}}{L_{\delta_A}} \qquad \overline{N}_{\delta_p} = N_{\delta_p} - L_{\delta_p} \frac{N_{\delta_A}}{L_{\delta_A}}$$

1. Report No.	2. Government Accession No.	3. Recipient's Catalog No.
NASA CR-177453		

4. Title and Subtitle	5. Report Date
SOME DATA PROCESSING REQUIREMENTS FOR PRECISION NAP-OF-THE-EARTH (NOE) GUIDANCE AND CONTROL OF ROTORCRAFT	FEB 1987
	6. Performing Organization Code
7. Author(s) WARREN F. CLEMENT, DUANE T. MCRUER AND RAYMOND E. MAGDELENO	8. Performing Organization Report No. TR-1239-1
	10. Work Unit No.
9. Performing Organization Name and Address SYSTEMS TECHNOLOGY, INC. 2672 BAYSHORE PARKWAY, SUITE 505 MOUNTAIN VIEW, CA 94043-1011	11. Contract or Grant No. NAS2-12364
	13. Type of Report and Period Covered CONTRACTOR REPORT
12. Sponsoring Agency Name and Address NASA SBIR PROGRAM WASHINGTON, D.C. 20546	14. Sponsoring Agency Code SBIR85-1/03.08/4675

15. Supplementary Notes
POINT OF CONTACT: LEONARD A. MCGEE MS210-9
AMES RESEARCH CENTER, MOFFETT FIELD, CA 94035
(415) 694-5443 or FTS 464-5443

16. Abstract

Nap-of-the-earth (NOE) flight in a conventional helicopter is extremely taxing for two pilots under visual conditions. Developing a single pilot all-weather NOE capability will require a fully automatic NOE navigation and flight control capability for which innovative guidance and control concepts have been examined. Constrained time-optimality provides a validated criterion for automatically controlled NOE maneuvers if the pilot is to have confidence in the automated maneuvering technique; this is one focus of this study. A second focus has been to organize the storage and real-time updating of NOE terrain profiles and obstacles in course-oriented coordinates indexed to the mission flight plan. A method is presented for using pre-flight geodetic parameter identification to establish guidance commands for planned flight profiles and alternates. A method is then suggested for interpolating this guidance command information with the aid of forward- and side-looking sensors within the resolution of the stored data base, enriching the data content with real-time information, and combining the stored and sensed data for real-time display, guidance, and control purposes. A third focus of this study defined a class of automatic anticipative guidance algorithms and necessary data preview requirements to follow the vertical, lateral, and longitudinal guidance commands dictated by the updated flight profiles and to address the effects of processing delays in digital guidance and control system candidates. The results of this three-fold research effort offer promising alternatives designed to gain pilot acceptance for automatic guidance and control of rotorcraft in NOE operations.

17. Key Words (Suggested by Author(s))	18. Distribution Statement
NOE FLIGHT, AUTOMATIC FLIGHT ROTORCRAFT, HELICOPTERS ANTICIPATIVE GUIDANCE DATA PREVIEW REQUIREMENTS	UNLIMITED

19. Security Classif. (of this report)	20. Security Classif. (of this page)	21. No. of Pages	22. Price*
UNCLASSIFIED	UNCLASSIFIED	194	

*For sale by the National Technical Information Service, Springfield, Virginia 22161